The Angola Current in a Tropical Seasonal Upwelling System

Seasonal Variability in Response to Remote Equatorial and Local Forcing

Dissertation
zur Erlangung des Doktorgrades
der Mathematisch-Naturwissenschaftlichen Fakultät
der Christian-Albrechts-Universität zu Kiel

vorgelegt von

Robert Kopte

Kiel, 2017

C | A | U
Christian-Albrechts-Universität zu Kiel
Mathematisch-Naturwissenschaftliche Fakultät

GEOMAR
Helmholtz-Zentrum für Ozeanforschung Kiel

Erster Gutachter:	Prof. Dr. Peter Brandt
Zweiter Gutachter:	Prof. Dr. Richard J. Greatbatch
Tag der mündlichen Prüfung:	28. September 2017
Zum Druck genehmigt:	28. September 2017

gez. Prof. Dr. Natascha Oppelt, Dekanin

Abstract

In this thesis, the flow and hydrographic characteristics of the boundary circulation off Angola are investigated, with particular emphasis on the mean properties and the seasonal cycle of the Angola Current. Moored velocity observations acquired at the Angolan shelf at 11 °S between 2013 and 2016 reveal a highly variable alongshore flow with velocities in the range of $\pm 40\,\mathrm{cm\,s^{-1}}$ superimposed on a weak poleward mean current with core velocities not exceeding $8\,\mathrm{cm\,s^{-1}}$. These measurements question the former view of a permanently poleward flowing Angola Current, which was based on results from few ship campaigns. During the observational period a mean Angola Current southward transport of 0.32 ± 0.05 Sv is determined. Pronounced annual and semiannual oscillations are found in the alongshore current characterized by distinct baroclinic structures. In the equatorial Atlantic, annual and semiannual oscillations are associated with resonant equatorial basin-modes of the fourth baroclinic mode for the annual cycle and the second baroclinic mode for the semiannual cycle. Equatorial basin-modes represent standing modes in a zonally bounded basin being composed of equatorial Kelvin and Rossby waves. A series of shallow water model experiments differing in the basin geometry and/or the applied forcing show a structural robustness of the corresponding horizontal patterns associated with the annual and semiannual cycles. A substantial part of the observed seasonal Equatorial Undercurrent variability can be explained by the linear superposition of the two dominant basin-modes. The off-equatorial lobes of the basin-modes also impact alongshore velocity at the eastern boundary off Angola. In a suite of shallow water model simulations the remote equatorial forcing related to basin-modes is isolated from the effects of local forcing. The observed annual cycle of alongshore velocity at 11 °S is well reproduced by the remote equatorial forcing. For the semiannual cycle, the inclusion of local forcing improves the agreement between observed and simulated velocity oscillations at 11 °S. Overall, the findings underline the importance of large-scale linear equatorial wave dynamics for the seasonal variability of the boundary circulation off Angola.

Additionally, as part of this study a large data set containing shipboard velocity and hydrographic measurements covering the Angolan shelf on a quasi-semiannual basis since 1995 was post-processed and quality-controlled in a capacity building effort with Angolan scientists. These data substantially contribute to the determination of the seasonal cycles in temperature and salinity at 11 °S, in which the main periods of upwelling in July/August and downwelling in March/April are reflected, but also a secondary upwelling season in December/January is indicated. Mean alongshore sections of velocity reveal a stronger, vertically more confined Angola Current during austral summer compared to austral winter along with a downstream strengthening of the southward flow just north of the Angola-Benguela Front. In light of still existing severe regional biases in coupled climate model simulations and ocean reanalysis products, the derived velocity sections and similar sections of temperature and salinity might turn out valuable for the assessment of model performances in terms of current strength and hydrographic structure off Angola in the future.

Zusammenfassung

In der vorliegenden Arbeit wird die Zirkulation und Hydrographie im östlichen Randstrom vor der Küste Angolas untersucht. Ein Hauptaugenmerk liegt auf der Beschreibung der mittleren Eigenschaften des Angolastroms, sowie auf einem verbesserten Verständnis des saisonalen Zyklus der Strömung. Zwischen 2013 und 2016 wurden Zeitreihen der Geschwindigkeit mittels Verankerungen auf dem angolanischen Schelf bei etwa 11 °S gewonnen. Diese Beobachtungen offenbaren eine stark schwankende küstenparallele Strömung mit Geschwindigkeiten im Bereich von $\pm 40\,\mathrm{cm\,s^{-1}}$. Für den Beobachtungszeitraum ergibt sich eine schwache südwärtige mittlere Strömung mit weniger als $8\,\mathrm{cm\,s^{-1}}$ im Kern des Angolastroms und einem damit verbundenen mittleren südwärtigen Volumentransport von $0.32 \pm 0.05\,\mathrm{Sv}$. Die Messungen widerlegen frühere Annahmen, laut denen es sich bei dem Angolastrom um eine kontinuierlich nach Süden gerichtete Strömung handelt. Die Variabilität des Angolastroms ist von einem ausgeprägten Jahres- und Halbjahresgang bestimmt, verbunden jeweils mit charakteristischen baroklinen Strukturen. Auch die Zonalströmungen entlang des Äquators zeigen einen ausgeprägten Jahres- und Halbjahresgang. Der Jahresgang in der Zonalströmung wird mit einer so genannten resonanten äquatorialen Beckenschwingung der vierten baroklinen Mode in Verbindung gebracht, während der Halbjahresgang mit einer Beckenschwingung der zweiten baroklinen Mode assoziiert wird. Äquatoriale Beckenschwingungen entstehen in einem zonal begrenzten äquatorialen Becken durch die Überlagerung von äquatorialen Kelvin- und Rossbywellen. Die Stabilität der mit Jahres- und Halbjahresgang verbundenen horizontalen Strukturen wird durch eine Reihe von Experimenten mit linearen Flachwassermodellen bestätigt. Die lineare Überlagerung der dominanten Beckenschwingungen erklärt wesentliche saisonale Eigenschaften des Äquatorialen Unterstroms (engl. Equatorial Undercurrent). Die polwärtigen Ausläufer der Beckenschwingungen im Ostatlantik beeinflussen zudem die küstenparallele Strömung vor der Küste Angolas. In einer weiteren Serie von Experimenten mit dem Flachwassermodell wird der äquatoriale Antrieb (welcher äquatoriale Beckenschwingungen erzeugen kann) von einem potentiellen lokalen Antrieb vor Angola isoliert. Der beobachtete Jahresgang im Randstrom vor Angola kann mit einem reinen äquatorialen Antrieb erklärt werden. Die Berücksichtigung von lokalem Antrieb verbessert jedoch die Übereinstimmung von beobachteten und simulierten Halbjahresgang in der Strömung. Im Allgemeinen unterstreichen die Ergebnisse die Bedeutung der linearen äquatorialen Wellendynamik für den saisonalen Zyklus im Randstrombereich vor Angola.

Im Rahmen dieser Studie wurde ein umfangreicher Datensatz in enger Zusammenarbeit mit Wissenschaftlern eines angolanischen Partnerinstitutes prozessiert und aufbereitet. Der Datensatz enthält schiffsgebundene Geschwindigkeits- und Hydrographiemessungen, welche seit 1995 auf halbjährlicher Basis erhoben wurden und den gesamten angolanischen Schelf abdecken. Die Daten tragen wesentlich zur Bestimmung des saisonalen Verlaufs von Temperatur und Salzgehalt bei 11 °S bei, welcher vor allem die Hauptphasen von Auftrieb (engl. Upwelling) im Juli/August und Absinken (engl. Downwelling) im März/April widerspiegelt. Ausserdem finden sich Hinweise

auf eine zweite Auftriebssaison im Dezember/Januar. Mittlere küstenparallele Geschwindigkeitsschnitte zeigen einen stärkeren, vertikal begrenzteren Angolastrom im Südsommer im Vergleich zum Südwinter. Beobachtet wird zudem eine Verstärkung der mittleren Geschwindigkeit stromabwärts mit Maximalgeschwindigkeiten nördlich der Angola-Benguela Frontalzone. Angesichts der starken systematischen Fehler in gekoppelten Klimasimulationen und Ozean-Reanalyseprodukten könnten sich die gewonnenen mittleren Schnitte der Geschwindigkeit, aber auch von Temperatur und Salzgehalt als sehr wertvoll für die Verbesserung der zugrundeliegenden Modelle hinsichtlich der Repräsentation von Strömungen und hydrographischen Strukturen vor der Küste Angolas erweisen.

Contents

Abstract i

Zusammenfassung iii

Table of Contents v

List of Figures ix

List of Tables xi

List of Abbreviations xiii

1 Motivation, aim and outline 1

2 Scientific background 7

2.1 Ocean circulation and water masses in the tropical Angolan system 7

2.2 Theory of eastern boundary circulation 9

2.3 Theory of long equatorial waves and basin mode resonance 10

2.3.1 Equatorial Kelvin waves 13

2.3.2 Equatorial Rossby waves 14

2.3.3 Equatorial basin modes 14

3 The Angola Current: Flow and hydrographic characteristics as observed at 11°S 17

3.1 Introduction 18

3.2 Data and Methods 20

3.2.1 Mooring Data 20

3.2.2 Shipboard and Autonomous Glider Data 21

3.2.3 Auxiliary Data Sets 22

3.2.4 AC Transport Estimation 22

3.2.5 Seasonality of Hydrographic Properties 24

3.3 Results 25

3.3.1 Alongshore Flow and Transport of the AC 25

3.3.2 Seasonality of Hydrographic Properties in the Current Regime 27

3.4 Discussion and Conclusions 29

4 Eastern boundary circulation and hydrography off Angola – building oceanographic capacities in Southwestern Africa 35
4.1 Introduction . . . 36
4.2 The EAF Nansen program . . . 40
4.3 Capacity building efforts . . . 41
4.4 Eastern boundary circulation and hydrography off Angola . . . 43
4.5 Interannual variability of hydrography . . . 49
4.6 Summary and discussion . . . 51

5 Annual and Semiannual Cycle of Equatorial Atlantic Circulation Associated with Basin-Mode Resonance 55
5.1 Introduction . . . 56
5.2 Mooring and CTD data . . . 58
5.3 Model simulations . . . 60
5.4 Results . . . 63
5.4.1 Characteristics of the annual and semiannual cycle . . . 63
5.4.2 Equatorial basin modes as simulated with the reduced-gravity model . . . 65
5.4.3 EUC variability associated with equatorial basin modes . . . 71
5.5 Summary and discussion . . . 74

6 Role of Basin-Mode Resonance for the Seasonal Variability of the Angola Current 79
6.1 Introduction . . . 80
6.2 Observational Data . . . 82
6.3 Shallow water model simulations . . . 84
6.3.1 Basic equations . . . 84
6.3.2 Model setup and forcing . . . 86
6.3.3 Scaling of model-computed modal amplitudes . . . 88
6.4 Results . . . 89
6.4.1 Frequency spectra of observed velocity fields at 23 °W-Equator and 11 °S-Angola . . . 89
6.4.2 Reconstruction of annual and semiannual cycles of zonal velocity at the equator using shallow water model simulations . . . 90
6.4.3 Horizontal structure of annual and semiannual oscillations . . . 94
6.4.4 Observed and reconstructed annual and semiannual cycles of alongshore velocity at 11 °S-Angola . . . 97
6.5 Summary and discussion . . . 99

7 Synthesis 107
7.1 Outlook . . . 113

Bibliography 117

Own Publications 131

Danksagung 133

Erklärung 135

List of Figures

1.1 Seasonal cycle of SST and surface wind in Southeastern tropical Atlantic Ocean. 2
1.2 SST Bias in coupled general-circulation models 3

2.1 Schematic ocean circulation in the Southeast Atlantic Ocean 8
2.2 Sketch of the shallow water model in Cartesian coordinates 12
2.3 Dispersion diagram of equatorial Kelvin and Rossby waves 13

3.1 The study area off Angola 19
3.2 Variability patterns of 11 °S ship sections 23
3.3 Angola Current transport: Observed vs. reconstructed ship sections 24
3.4 Time series of alongshore velocity at 11 °S-Angola during 2013-15 26
3.5 Time series of Angola Current transport at 11 °S during 2013-15 26
3.6 Seasonal cycle of temperature and salinity at 11 °S 28
3.7 θ/S diagram at 11 °S 29
3.8 Seasonal cycles of SST and SLA at 11 °S 30
3.9 Observations vs. ocean reanalysis: Thermal structure and AC strength at 11 °S . 32

4.1 SST and SSS off Angola during FMA and JJA 37
4.2 Hovmöller diagram of mean seasonal cycle of SLA along equator and off Angola 38
4.3 SST anomaly during Benguela Niño 2011 39
4.4 Overview of EAF-Nansen data base off Angola 40
4.5 Meridional sections of alongshore velocity off Angola 44
4.6 Comparison of moored and shipboard alongshore velocity at 11 °S-Angola 45
4.7 Meridional sections of temperature off Angola 46
4.8 Meridional sections of salinity off Angola 46
4.9 Meridional sections of stratification off Angola 47
4.10 Crossshore sections of hydrographic properties off Angola between 10 °S and 12 °S 48
4.11 ABA-Index and interannual subsurface temperature anomalies off Angola 49
4.12 Subsurface temperature anomalies from Argo profiles during warm and cold periods off Angola 50

5.1 Time series of zonal velocity at 23 °W-Equator during 2004-15 58
5.2 Vertical structure functions of the second and fourth baroclinic mode 60

5.3 Seasonal cycle of EUC transport at 23 °W, 10 °W, and 0 ° 61
5.4 Annual cycle of zonal velocity 23 °W-Equator 63
5.5 Frequency and baroclinic mode spectra of zonal velocity from 23 °W-Equator . . 64
5.6 Amplitude and phase patterns of the second and fourth baroclinic mode in TRATL01 66
5.7 Basin mode resonance as function of frequency 67
5.8 Amplitude and phase patterns of the second and fourth baroclinic mode from reduced gravity simulations for a square basin 68
5.9 Amplitude and phase patterns of the second and fourth baroclinic mode from reduced gravity simulations for a realistic coastline domain 69
5.10 Amplitude and phase patterns of the second and fourth baroclinic mode from reduced gravity simulations for a realistic coastline domain and spatially varying wind forcing 70
5.11 Seasonal cycle of EUC transport 72
5.12 Monthly mean EUC transport profiles at various longitudes 73
5.13 Seasonal cycle of EUC properties 75

6.1 Time series of alongshore velocity at 11 °S-Angola during 2013-16 82
6.2 Moored velocity data availability at 35 °W-Equator, 23 °W-Equator, and 11 °S-Angola 83
6.3 Modal decompostion of zonal velocity at 35 °W-Equator and 23 °W-Equator . . 85
6.4 Gravity wave speed optimization 87
6.5 Frequency spectra of zonal and alongshore velocity at 23 °W-Equator and 11 °S-Angola, respectively 90
6.6 Projection coefficients for shallow water simulations 92
6.7 Annual and semiannual cycles of zonal velocity at 35 °W-Equator and 23 °W-Equator 93
6.8 Amplitude structure of annual and semiannual oscillations 95
6.9 Phase structure of annual and semiannual oscillations 96
6.10 Annual and semiannual cycles of alongshore velocity at 11 °S-Angola 98
6.11 Semiannual cycle with amplified fourth baroclinic mode 101
6.12 Semiannual cycle in alongshore velocity at 11 °S-Angola in TRATL01 103
6.13 Baroclinic mode spectra at 35 °W-Equator and 23 °W-Equator for observations, shallow water model, and TRATL01 103
6.14 Amplitude structure of annual and semiannual oscillations derived from TRATL01 105

7.1 Seasonal cycle of internal wave energy at 11 °S off Angola 114
7.2 Observations vs. ocean reanalysis: Salinity at 11 °S 115

List of Tables

5.1 Characteristics of baroclinic modes 1-5 59

6.1 Wind products used for shallow water simulations 86
6.2 Gravity wave speeds for baroclinic modes 1-5 87
6.3 Projection coefficients for shallow water simulations 92
6.4 Amplitude and phase differences between simulations with equatorial forcing and full forcing at 11 °S-Angola 99

List of Abbreviations

ABFZ	Angola-Benguela Frontal Zone
AC	Angola Current
ADCP	Acoustic Doppler Current Profiler
BC	Benguela Current
CTW	Coastally Trapped Wave
EBUS	Eastern Boundary Upwelling System
ESACW	Eastern South Atlantic Central Water
EKW	Equatorial Kelvin Wave
ERW	Equatorial Rossby Wave
EUC	Equatorial Undercurrent
NACW	North Atlantic Central Water
OGCM	Ocean General Circulation Model
PUC	Poleward Undercurrent
SACW	South Atlantic Central Water
SSS	Sea Surface Salinity
SST	Sea Surface Temperature
SECC	South Equatorial Counter Current
SEUC	South Equatorial Undercurrent
SLA	Sea Level Anomaly
SWM	Shallow Water Model
WOCE	World Ocean Circulation Experiment

1 Motivation, aim and outline

To the north of the Benguela upwelling region - one of the four major Eastern Boundary Upwelling System (EBUS) found in the World Oceans (*Carr and Kearns*, 2003; *Chavez and Messié*, 2009) - and separated by the Angola-Benguela Frontal Zone (ABFZ) (*Shannon et al.*, 1987; *Meeuwis and Lutjeharms*, 1990; *Lass et al.*, 2000), the tropical Angolan system represents another highly productive marine ecosystem (*Ostrowski et al.*, 2009). Contrary to the major EBUSs, where persistent alongshore winds drive quasi-permanent coastal upwelling, winds off Angola are generally weak throughout the year (Figure 1.1, *Hellerman* (1980)). Nonetheless, seasonal upwelling occurs in large parts of Angola's coastal zone mainly during austral winter (June to August, Figure 1.1), being of tremendous importance for the country's fishing sector and food security of the coastal population. Previous studies propose that the seasonal conditions on the shelf off Angola are controlled to a large extent by seasonal Coastally Trapped Waves (CTWs) emanating from the equator (*Berrit*, 1976; *Picaut*, 1983; *Ostrowski et al.*, 2009). Satellite altimetry data reveal continuous and recurrent poleward propagations of four CTWs per year along the Angolan coast to at least 15 °S (*Schouten et al.*, 2005; *Lazar et al.*, 2006; *Ostrowski et al.*, 2009; *Rouault*, 2012). Passing times of the first set of one downwelling (March/April) followed by one upwelling (July/August) CTW thereby coincide with the main periods of downwelling and upwelling off the coast of Angola (*Ostrowski et al.*, 2009). The occurrence of a second pair of a downwelling and an upwelling CTW in October and December/January, respectively, is consistent with the idea of a secondary upwelling during December/January (*Berrit and Dias*, 1977), which separates the major downwelling season in March from a secondary downwelling in October.

Ocean circulation in the tropical Angolan system is dominated by the poleward flowing Angola Current (AC). Supplied by the equatorial current system, the AC is assumed to represent a key component in the advection of warm tropical waters towards the northern Benguela, where it converges with the northward flowing Benguela Current (BC) (*Peterson and Stramma*, 1991; *Wacongne and Piton*, 1992; *Rouault et al.*, 2007). Descriptions of the AC exclusively relied on sporadic synoptic observations so far (*Moroshkin et al.* (1970); *Dias* (1983a,b); *Mohrholz et al.* (2001); *Mercier et al.* (2003), see Section 2.1 for a review), leading to the perception of a continuous poleward current, which is stronger during austral summer and weaker during austral winter. However, a detailed assessment of the current's mean properties and associated variability is still pending.

Oceanographic conditions and fish-stock distributions off Angola show large variations on a broad range of time scales that can partly be associated with the occurrence of oceanic warm

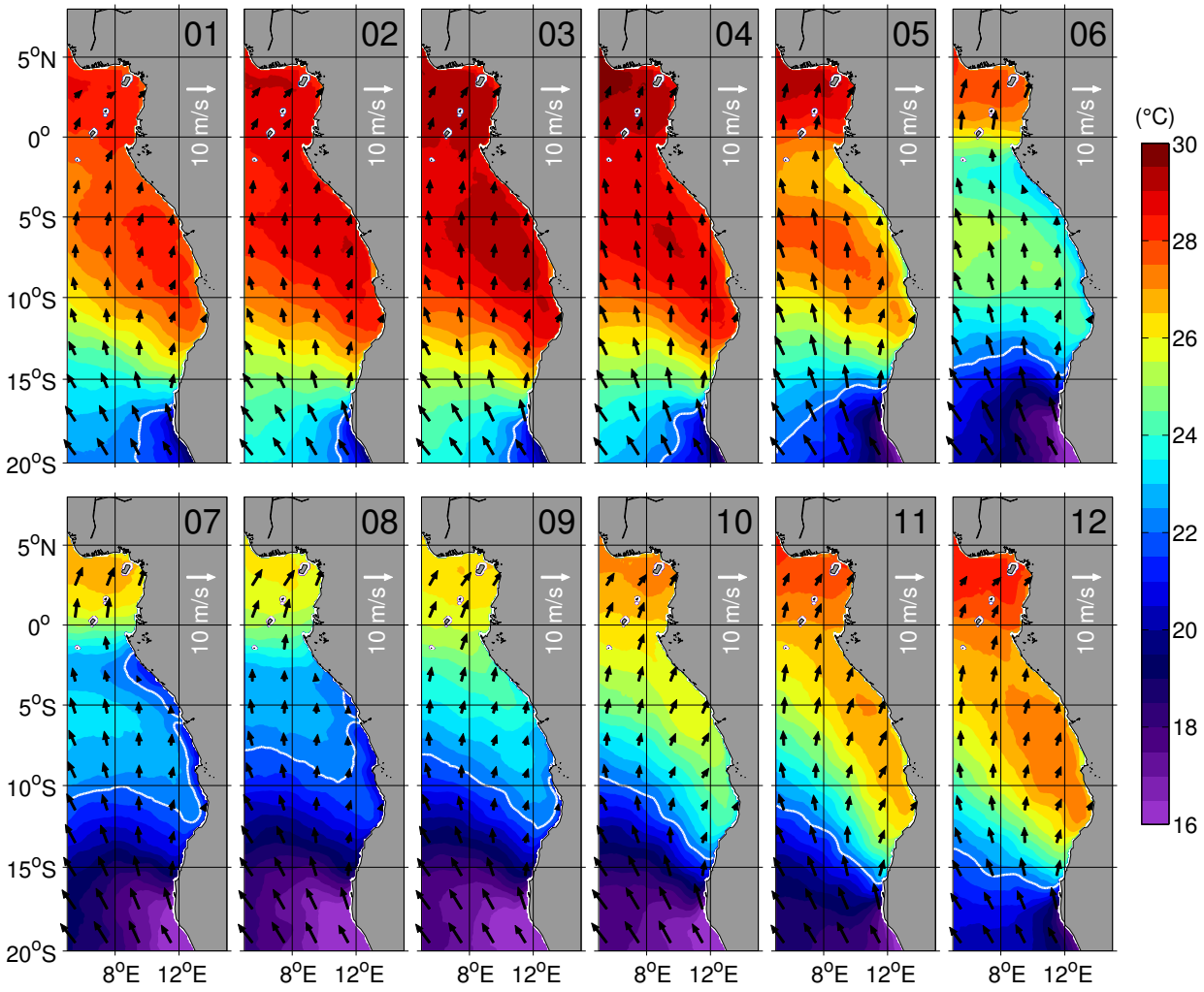

Figure 1.1: Mean seasonal cycle of SST (contour) and surface wind (arrows) derived for the period 2010-2016 from MW Fusion OI-SST and ASCAT altimeter data, respectively (both data sets are available at `http://www.remss.com`). The white contour line corresponds to the 22 °C-isotherm.

events in the region. On interannual time scales these intermittent events are known as Benguela Niños (*Shannon et al.*, 1986) and often are thought to be induced by a wave response to the remote equatorial forcing in the western equatorial Atlantic (*Florenchie et al.*, 2003; *Rouault et al.*, 2007; *Lübbecke et al.*, 2010; *Bachèlery et al.*, 2016). Nonetheless, also local forcing is assumed to modulate the characteristics and strength of these extreme events (*Richter et al.*, 2010). Benguela Niño events are characterized by the poleward intrusion of warm tropical waters into the northern Benguela upwelling region located off Namibia having substantial impact on primary production, fisheries and rainfall rates over adjacent land masses (*Gammelsrød et al.*, 1998; *Rouault et al.*, 2003). In this context, the AC is expected to be a major transport agent for the anomalously strong poleward advection of warm tropical waters (*Rouault et al.*, 2007). In addition to the intrinsic climate variability, Angola's coastal zone faces challenges in response to global climate change. Recent studies suggest that particularly EBUSs will be heavily impacted by different global warming stressors such as increasing temperatures, acidification, and

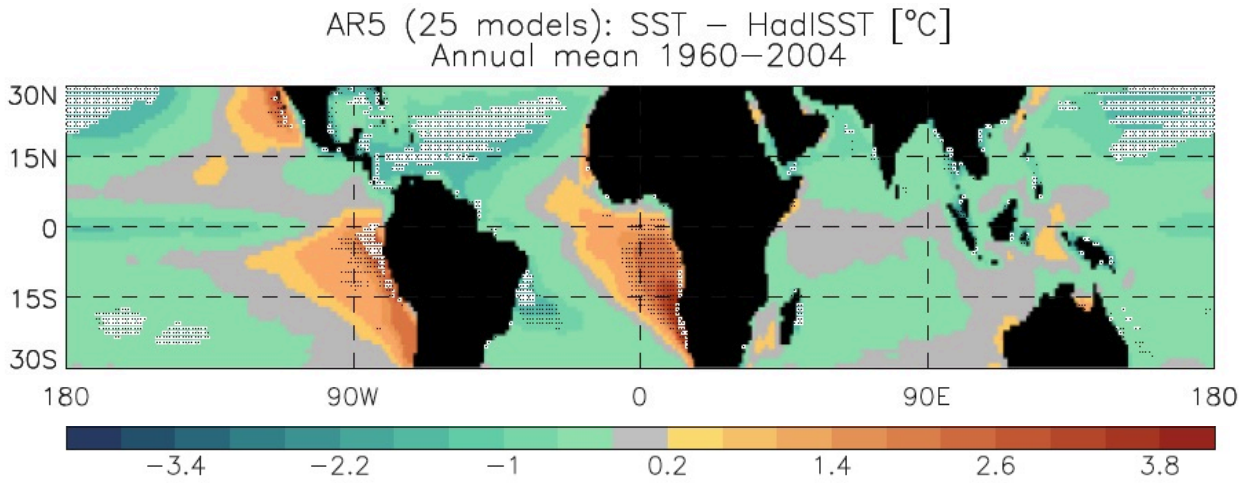

Figure 1.2: Mean SST error in a set of 25 coupled general-circulation models in the CMIP5 (Coupled Model Inter-comparison project 5) ensemble. In areas of white (black) hatching the sign of the error agrees in all (all but one) models (Figure adapted from *Toniazzo and Woolnough* (2014)).

deoxygenation (*Gruber et al.*, 2011).

Together with the eastern equatorial Atlantic, the Southeast Atlantic Ocean exhibits the strongest Sea Surface Temperature (SST) biases seen in many state-of-the-art climate simulations (Figure 1.2, *Davey et al.* (2002); *Richter et al.* (2014); *Toniazzo and Woolnough* (2014)). For coupled models, primarily deficiencies in the atmospheric component have been proposed as source of the bias (e.g. *Huang et al.* (2007); *Patricola et al.* (2012)). Recently it could be shown that a significant bias reduction can be achieved by enhancing the horizontal (*Milinski et al.*, 2016) and simultaneously the vertical (*Harlaß et al.*, 2015) resolution of the atmospheric model component, which results for example in an improved representation of near-coastal winds. However, even widely-used ocean reanalysis data show large biases in the current structure, hydrography, and upwelling strength off the coast of Southwest Africa, pointing to systematic errors in the ocean models potentially contributing to the bias problem (*Large and Danabasoglu*, 2006; *Grodsky et al.*, 2012; *Xu et al.*, 2014). In particular, ocean models tend to have difficulties to represent the sharp thermocline off Angola (*Xu et al.*, 2014) - a problem that usually is accompanied by an erroneous tilt of the equatorial thermocline. Owed to the incorrect thermal structure in the models, too-warm subsurface temperatures are advected southward and subsequently upwelled resulting in too-warm SSTs in the upwelling regions. Furthermore, the representation of the simulated ocean currents off Angola remains rather uncertain as publicly available observational data in the region, which could be used for the validation of the models, are sparse. The model biases in SST off Angola and northern Namibia do not only affect the reliability of future climate projections, but - due to their close spatial resemblance to Benguela Niño events - also hamper the prediction of oceanic warm and cold events in the region (*Xu et al.*, 2014). After all, an improved prediction of these extreme events would be of tremendous importance for the timely activation of suitable adaption strategies carried out by the coastal communities.

Despite the apparent importance of the marine ecosystem off Angola both regionally for the welfare of adjacent countries and globally for example for the improvement of climate change projections, still only little is known about the ocean circulation and hydrographic characteristics in the region. Observational studies off Angola have been restricted to either satellite measurements or synoptic-scale observations taken during sporadic ship surveys. The lack of publicly available observational data thereby has hampered not only the progress in understanding the processes driving the observed variability but also still hinders the evaluation of model biases in the region.

The first goal of this thesis is to provide a detailed description of the eastern boundary circulation and hydrography off the coast of Angola. In July 2013, a mooring array was installed on the continental slope near 11 °S. Being part of the array, two current meters have been profiling velocity in the upper 450 m for the last years yielding the first long-term measurements of both advective and wave signals in the boundary current. These data now for the first time facilitate a robust determination of the mean characteristics and associated variability of the AC, also in terms of volume transport and baroclinic structure (Chapter 3).

Furthermore, the thesis is part of the German BMBF-SPACES (Science Partnerships for the Assessment of Complex Earth System Processes, 2012-2018) and European Union PREFACE (Enhancing prediction of Tropical Atlantic climate and its impacts, 2013-2017) programs, that have fostered the cooperation and capacity building efforts with Angolan partner institutes. Within this framework, an extensive in-situ data set of shipboard velocity and hydrography observations was post-processed and quality-controlled in close cooperation with the Angolan partners. The previously not well-explored data set has been acquired within the EAF-Nansen program, that has been funded by the Food and Agricultural Organization of the United Nations (FAO) and executed by the Norwegian Agency for Development Cooperation (NORAD). First results from the analysis of these data are presented as part of this thesis revealing the seasonal cycle of temperature and salinity at 11 °S (Chapter 3) as well as the large-scale structure of currents and hydrography along the Angolan coast (Chapter 4).

In combination with already existing multi-year moored observations of the circulation in the equatorial Atlantic the newly acquired data set of velocity observations at 11 °S also allows the investigation of the role of remote equatorial forcing for the seasonal variability of the eastern boundary circulation. Seasonal variations of the zonal and alongshore velocities at 23 °W-Equator and 11 °S-Angola, respectively, are dominated by annual and semiannual oscillations. In the equatorial Atlantic, these oscillations are associated with basin-mode resonances of the fourth and second baroclinic mode, respectively (*Claus et al.*, 2016). Equatorial basin modes represent low-frequency standing equatorial modes in a zonally bounded basin that are composed of eastward propagating Equatorial Kelvin Waves (EKWs) and westward propagating Equatorial Rossby Waves (ERWs) (*Cane and Moore*, 1981). Resonances with a forcing at a particular frequency might occur depending on the basin width and the gravity wave speed of the baroclinic mode involved (see also Section 2.3). By exploitation of a top-to-bottom time series of zonal velocity at 23 °W-Equator supported by Shallow Water Model (SWM) simulations, the impact of these resonant

equatorial basin-modes for the seasonal cycle of equatorial Atlantic circulation is investigated (Chapter 5). The off-equatorial lobes of the basin-modes are associated with meridional velocity fluctuations along the eastern boundary presumably also affecting the seasonal variability of the AC. Therefore, the role of these basin-modes and more generally the relative role of the remote equatorial versus the local forcing for the observed seasonality at 11 °S is analyzed by comparing SWM simulations differing in the applied forcing with the acquired observations (Chapter 6).

With this composite of newly acquired and already existing observational data sets at hand, supported by idealized linear wave models, the following main aspects will be addressed in this thesis:

- What are the characteristics of the boundary current flow off Angola locally at 11 °S and along the entire Angolan coastline? (Chapter 3 and Chapter 4)
- How is the seasonal upwelling off Angola reflected in the seasonal cycle of temperature and salinity? (Chapter 3 and Chapter 4)
- What is the importance of basin-mode resonance for the seasonal cycle of the equatorial circulation in the Atlantic? (Chapter 5)
- Given the connection of equatorial and coastal wave-guides, what is the importance of resonant equatorial basin-modes (and remote equatorial forcing in general) for the seasonal cycle of the Angola Current? (Chapter 6)

Chapter 3 through Chapter 6 of this thesis represent individual manuscripts, which either are already peer-reviewed and published in scientific journals, have been submitted and are currently under review for publication, or are in the final stage of preparation for submission. The author of this thesis is either the leading author of the publication (Chapter 3, Chapter 6) or one of the co-authors with significant contributions to the manuscript (Chapter 4, Chapter 5). The current status of each manuscript as well as the detailed contributions of the author to each manuscript are elucidated at the beginning of each chapter. The thesis is complemented by a chapter briefly introducing the scientific background (Chapter 2) and a closing chapter, where a synthesis of the results is presented and an outlook is given (Chapter 7).

2 Scientific background

In the following the scientific background for this study is briefly introduced. Even though winds off Angola are generally weak, present day knowledge shows the large-scale ocean circulation in the region (Section 2.1) being largely consistent with the theory of wind-driven eastern boundary currents (Section 2.2). One major objective of this study is to enhance the understanding of the dynamic response of the boundary current to the remote equatorial forcing, involving propagation of Equatorial Kelvin Waves (EKWs) and Equatorial Rossby Waves (ERWs) as well as Coastally Trapped Waves (CTWs). In this context, the focus will be put on the role of resonant equatorial basin-modes for the seasonal cycle of equatorial Atlantic and eastern boundary circulation off Angola. Therefore, the theoretical background of EKWs and ERWs as well as equatorial basin-modes is briefly given in Section 2.3.

2.1 Ocean circulation and water masses in the tropical Angolan system

The ocean currents off Angola seem to represent a typical eastern boundary circulation system (Section 2.2) that is dominated by the poleward flowing Angola Current (AC) (Figure 2.1). The AC is suggested to be supplied by the eastward flow within the equatorial current system, namely the Equatorial Undercurrent (EUC), the South Equatorial Undercurrent (SEUC), and the South Equatorial Counter Current (SECC) (*Peterson and Stramma*, 1991; *Wacongne and Piton*, 1992; *Rouault et al.*, 2007). At about 16 °S the AC converges with the northward flowing Benguela Current (BC), thereby forming a highly variable thermal boundary known as the Angola-Benguela Frontal Zone (ABFZ) (*Shannon et al.*, 1987; *Meeuwis and Lutjeharms*, 1990). Historically, the velocity structure and transport of the AC had been described exclusively based on synoptic hydrographic data (*Moroshkin et al.*, 1970; *Dias*, 1983a,b; *Mercier et al.*, 2003). These former studies reported subsurface geostrophic southward flow between the surface and 300 to 400 m depth having velocities between 30 cm s^{-1} and 50 cm s^{-1} and subsurface velocities exceeding 50 cm s^{-1} at times. Southward transports of the AC determined by *Dias* (1983a) were 1.2 Sv and 3.7 Sv from data collected in September 1970 and July 1971, respectively. However, *Mercier et al.* (2003) reported an AC transport of 11 Sv from an inverse study making use of World Ocean Circulation Experiment (WOCE) line A13, which was sampled during a major Benguela Niño event in January to March 1995 (*Gammelsrød et al.*, 1998).

During a survey in April 1999 a secondary, offshore branch of southward subsurface flow was identified in shipboard velocity data separated from the coastal branch (*Mohrholz et al.*, 2001). Both pathways were characterized by southward velocities of about 40 cm s^{-1} below the surface. Based on the available synoptic snapshots, the general perception of the AC is that of a continuous poleward current which is stronger in austral summer and weaker in austral winter and plays a key role in the anomalously strong southward advection of tropical waters during Benguela Niño events. Yet, the AC has remained rather unexplored, as a solid description of the current's mean properties and variability has not been feasible with the available data to date.

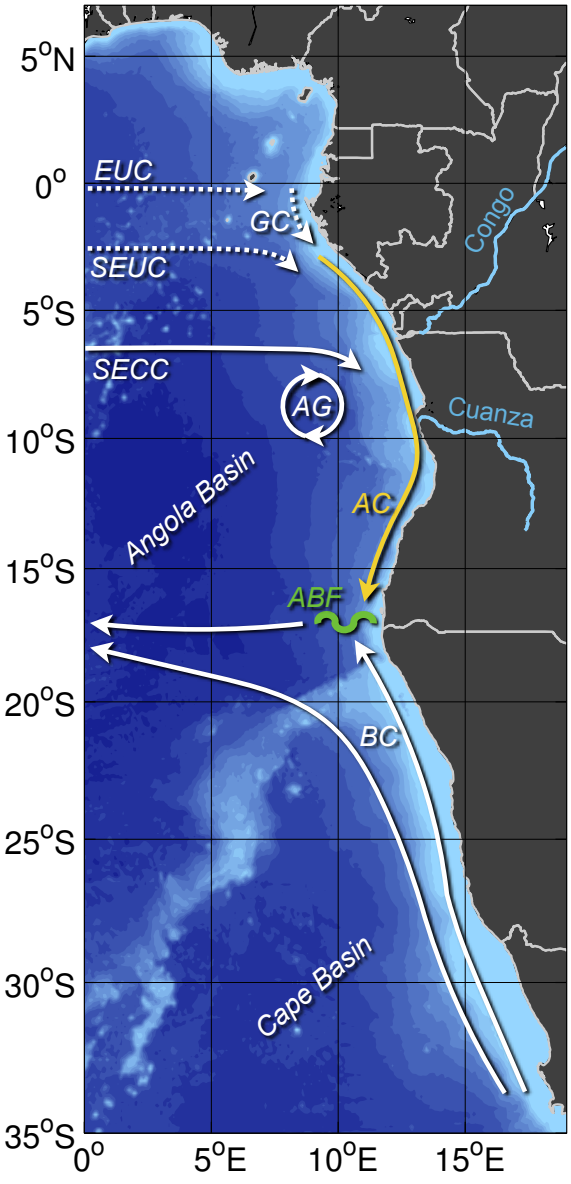

Figure 2.1: Ocean currents in the Southeast Atlantic Ocean (modified from *Rouault et al.* (2007)). Main features are the Equatorial Undercurrent (EUC), South Equatorial Undercurrent (SEUC), South Equatorial Counter Current (SECC), Gabon Current (GC), Angola Gyre (AG), Angola Current (AC), and Benguela Current (BC). The mean position of the Angola-Benguela Frontal Zone (ABFZ) is indicated (see also Figure 3.1a).

Off Angola, one of the most pronounced oxygen minimum zones of the global ocean is found below the productive surface layer. Mainly during austral summer the AC appears to be a key element for the southward spreading of warm, saline, low-oxygen South Atlantic Central Water (SACW) within the upper thermocline. SACW originally is formed in the subtropical convergence of the Brazil-Malvinas Confluence Zone (*Poole and Tomczak*, 1999). It enters the tropical Southeast Atlantic Ocean via the equatorial current system, after being advected through the South Atlantic subtropical gyre. During this journey, SACW properties are constantly altered by continuous remineralization of organic matter causing oxygen depletion and nutrient enrichment plus weak entrainment of North Atlantic Central Water (NACW) within the equatorial current system (*Poole and Tomczak*, 1999). After all these en route modifications an oxygen-poor subtype of SACW with an approximated pseudo-age of 50 years resides in the Angola Gyre (*Mohrholz et al.*, 2008) that finally is advected poleward towards the northern Benguela by the Angola Current. With Eastern South Atlantic Central Water (ESACW) another central water subtype is present in the vicinity of the ABFZ. ESACW is formed in the Cape Basin representing a mixture of SACW from the subtropical gyre and Indian

Central Water that is transferred to the South Atlantic by the Agulhas Current (*Mohrholz et al.*, 2008). From its source region ESACW, which is richer in oxygen than SACW, is transported northward along the Southwest African shelf by the BC. Particularly for the frontal region, the water mass composition, consisting of a mixture of SACW and ESACW, is crucial for the oxygen balance over the shelf (*Mohrholz et al.*, 2008) and strongly depends on the relative strength of the AC and BC.

2.2 Theory of eastern boundary circulation

A number of studies have addressed the theory of wind-driven eastern boundary flows, using numerical or analytical models (*Hurlburt and Thompson*, 1973; *Anderson and Gill*, 1975; *McCreary*, 1981a; *Suginohara and Kitamura*, 1984; *Philander and Yoon*, 1982; *Yoon and Philander*, 1982; *McCreary and Chao*, 1985; *Fennel*, 1999). According to *Philander and Yoon* (1982), the response of an inviscid coastal ocean to the sudden onset of a spatially homogeneous alongshore (equatorward) wind can be divided in three phases:

1. Immediately after the onset of the alongshore wind, an accelerating equatorward coastally trapped jet develops inside the wind band. During this phase the flow is two-dimensional, i.e. no alongshore variations are found. Thus, the offshore Ekman transport associated with the coastal current has to be balanced by coastal upwelling.

2. With the onset of the wind, CTWs were initially excited at the equatorward end of the forced region. Propagating poleward, these waves induce alongshore variations in the flow. After the time period the waves need to reach a certain location within the forced area the acceleration of the coastal jet is stopped at this particular spot, as the wind stress is now balanced by an alongshore pressure gradient. Furthermore, the CTWs introduce a Poleward Undercurrent (PUC) since the vertical structure of the waves differs from that of the surface jet. Another effect of the waves is the reduction of the intensity of the coastal upwelling. In a one-level model, upwelling ceases completely. In an N-layer model in which the Coriolis parameter f is constant, the passage of each baroclinic mode CTW would reduce the upwelling until upwelling has stopped after the the Nth mode has passed (*Philander and Yoon*, 1982). Also, each of the baroclinic modes would modulate the vertical structure of the coastal jet and the PUC. However, since the upwelling has stopped, the Ekman rectification flow supplies the PUC after the passage of the CTWs. Only temporal variations of the wind field can excite new upwelling events (*Fennel*, 1999). In reality, the established balance might also be disturbed by the passage of remotely forced waves (*Strub et al.*, 2013) or coastline irregularities that generate CTWs in a similar manner as alongshore wind variations (*Crépon et al.*, 1984).

3. Considering the spherical shape of the Earth, the response is modified by the β-effect,

i.e. the variation of the Coriolis parameter f with latitude. The final phase to establish equilibrium conditions is then associated with the dispersion of the coastal jet into Rossby waves (*Anderson and Gill*, 1975). Equilibrium conditions are found in the wake of the Rossby waves, which in the case of an inviscid shallow water model forced by uniform alongshore winds would result in no motion at all.

The response of the coastal ocean as described above has to be considered oversimplified. As an example, frictional effects are not taken into account. Steady coastal upwelling is only possible for nonzero friction (*Fennel*, 1999), which limits the propagation distance of the CTWs particularly for higher baroclinic modes. In addition, by considering spatial and temporal variations of the wind field, the response of the coastal ocean becomes more complex. For example, the existence of a wind stress curl (as introduced by spatial variations of the wind stress) alters the coastal circulation and upwelling strength (*Hurlburt and Thompson*, 1973; *McCreary and Chao*, 1985). Contrary to the coastal upwelling, curl-driven upwelling is not affected by CTW propagation, and thus provides a mechanism that is able to maintain upwelling independent of the wave response at the coast.

However, as winds are rather weak off Angola, it seems likely that the response to the local wind as described above is very sensitive to external disturbances like the passage of remotely forced waves. Previous studies have indeed noted that the seasonal conditions on the shelf off Angola appear to be controlled to large extent by remotely forced waves emanating from the equator (*Ostrowski et al.*, 2009; *Rouault*, 2012). Furthermore, intermittent oceanic warm events in the region occurring on interannual time scales have often been explained with a wave response to anomalous wind forcing in the western equatorial Atlantic (e.g. *Florenchie et al.* (2003); *Rouault et al.* (2007); *Lübbecke et al.* (2010); *Bachèlery et al.* (2016)).

2.3 Theory of long equatorial waves and basin mode resonance

It is well-known that the tropical thermocline provides a wave-guide for several types of large-scale ocean waves (e.g. *Gill* (1982)), causing disturbances to remain trapped in the vicinity of the equator. The existence of this wave-guide is owed to the strong mean vertical stratification in the tropical oceans and in particular to the vanishing Coriolis force directly at $0\,^{\circ}$, which leads to the equator acting like a natural boundary analogously to topographic boundaries for coastally trapped waves.

The best-known examples of long equatorial waves are eastward propagating EKWs and westward propagating ERWs that are excited by wind stress variations over the equatorial ocean and can cause thermocline displacements and Sea Surface Temperature (SST) anomalies along their propagation path. Thermocline displacements are thereby mirrored by Sea Level Anomaly (SLA)

(at least for the low baroclinic modes), offering opportunities to track propagating waves from space.

In order to introduce equatorial wave dynamics in the simplest possible context usually linear Shallow Water Models (SWMs) are employed (e.g. *Matsuno* (1966); *Wunsch and Gill* (1976); *Gill* (1982); *Pedlosky* (1987); *Philander* (1990); *Holton* (2004)). In these models a shallow layer of relatively warm (and therefore less dense) water overlies a motionless much deeper layer of cold water. The interface between both layers represents the sharp and shallow tropical thermocline. Linear hydrostatic motion in the upper layer is forced by the wind stress τ_s, which acts on the upper layer as a body force. This motion is associated with a vertical displacement of the interface η. To account for the special case of the Coriolis parameter vanishing at the equator, the equatorial β-plane approximation is used (e.g. *Gill* (1982)). Therefore, the Coriolis parameter f in the momentum equations is replaced by βy, with $\beta = 2.3 \times 10^{-11}\,\mathrm{m^{-1}\,s^{-1}}$ representing the meridional gradient of f in the vicinity of the equator. In a Cartesian coordinate system (see Figure 2.2) considering free wave solutions (i.e. neglecting forcing and dissipation), the shallow water equations on the equatorial β-plane are given by (see Section 6.3.1 for the equations in spherical coordinates):

$$\frac{\partial u}{\partial t} - \beta y v = -g' \frac{\partial \eta}{\partial x} \tag{2.1a}$$

$$\frac{\partial v}{\partial t} + \beta y u = -g' \frac{\partial \eta}{\partial y} \tag{2.1b}$$

$$g' \frac{\partial \eta}{\partial t} + c^2 \left(\frac{\partial u}{\partial x} + \frac{\partial v}{\partial y} \right) = 0 \tag{2.1c}$$

where u and v are the zonal and meridional velocity components, respectively, and $c = \sqrt{g'H}$ represents the gravity wave speed. Because of the stratification, the gravitational acceleration g is effectively reduced to $g' = \frac{\rho_2 - \rho_1}{\rho_1} g$ in Equations (2.1).

From Equations (2.1) a single equation for the meridional velocity component v can be obtained:

$$\frac{\partial}{\partial t} \left(\frac{\partial^2 v}{\partial x^2} + \frac{\partial^2 v}{\partial y^2} \right) + \beta \frac{\partial v}{\partial x} - \frac{1}{c^2} \frac{\partial^3 v}{\partial t^3} - \frac{f^2}{c^2} \frac{\partial v}{\partial t} = 0 \tag{2.2}$$

Waves solutions of the form

$$v = V(y) \exp(ikx - i\omega t) \tag{2.3}$$

where $k = 2\pi/\lambda$ and ω represent zonal wave number and angular frequency, respectively, can be derived by substituting Equation (2.3) into Equation (2.2) yielding the ordinary differential equation

$$\frac{d^2 V}{dy^2} + \left(\frac{\omega^2}{c^2} - k^2 - \frac{\beta k}{\omega} - \frac{\beta^2 y^2}{c^2} \right) V = 0 \tag{2.4}$$

When considering equatorially trapped waves a boundary condition is introduced, forcing the solutions to decay for large values of $|y|$ (*Matsuno*, 1966) , i.e.

$$V \to 0 \qquad \text{as} \qquad y \to \pm\infty \tag{2.5}$$

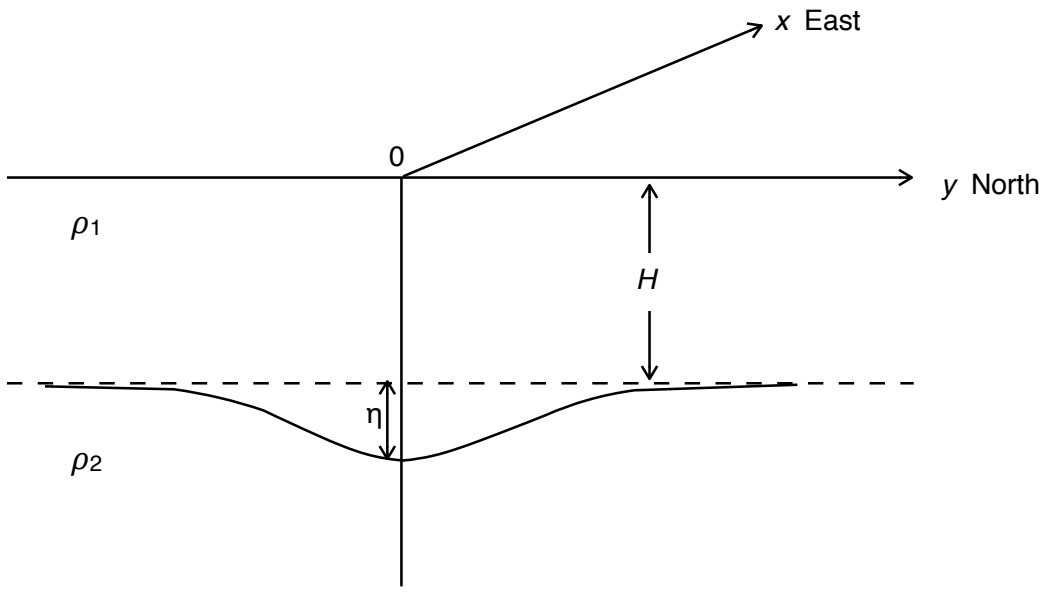

Figure 2.2: A sketch of the shallow water model in the Cartesian coordinate system (adapted from *Philander* (1990).

The meridional extent of the solutions is in fact defined by the equatorial Rossby radius of deformation given by

$$R_{eq} = \sqrt{\frac{c}{\beta}} \tag{2.6}$$

Equation (2.4) together with the boundary condition of Equation (2.5) poses an eigenvalue problem, analogously to Schrödingers equation for a simple harmonic oscillator. The boundary condition is satisfied only for certain discrete values of the meridional wave number n, which leads to the dispersion relation for equatorially trapped waves:

$$\frac{c}{\beta}\left(\frac{\omega^2}{c^2} - k^2 - \frac{\beta k}{\omega}\right) = 2n + 1 \tag{2.7}$$

This dispersion relation permits the description of several types of equatorial waves, including:

- Gravity-inertial or Poincaré waves ($n = 1, 2, 3, ...$)
- Rossby waves ($n = 1, 2, 3, ...$)
- Rossby-gravity or Yanai wave ($n = 0$)
- Kelvin wave ($n = -1$)

In the following the dispersion relation (Equation (2.7)) is explored for EKWs and ERWs (Figure 2.3).

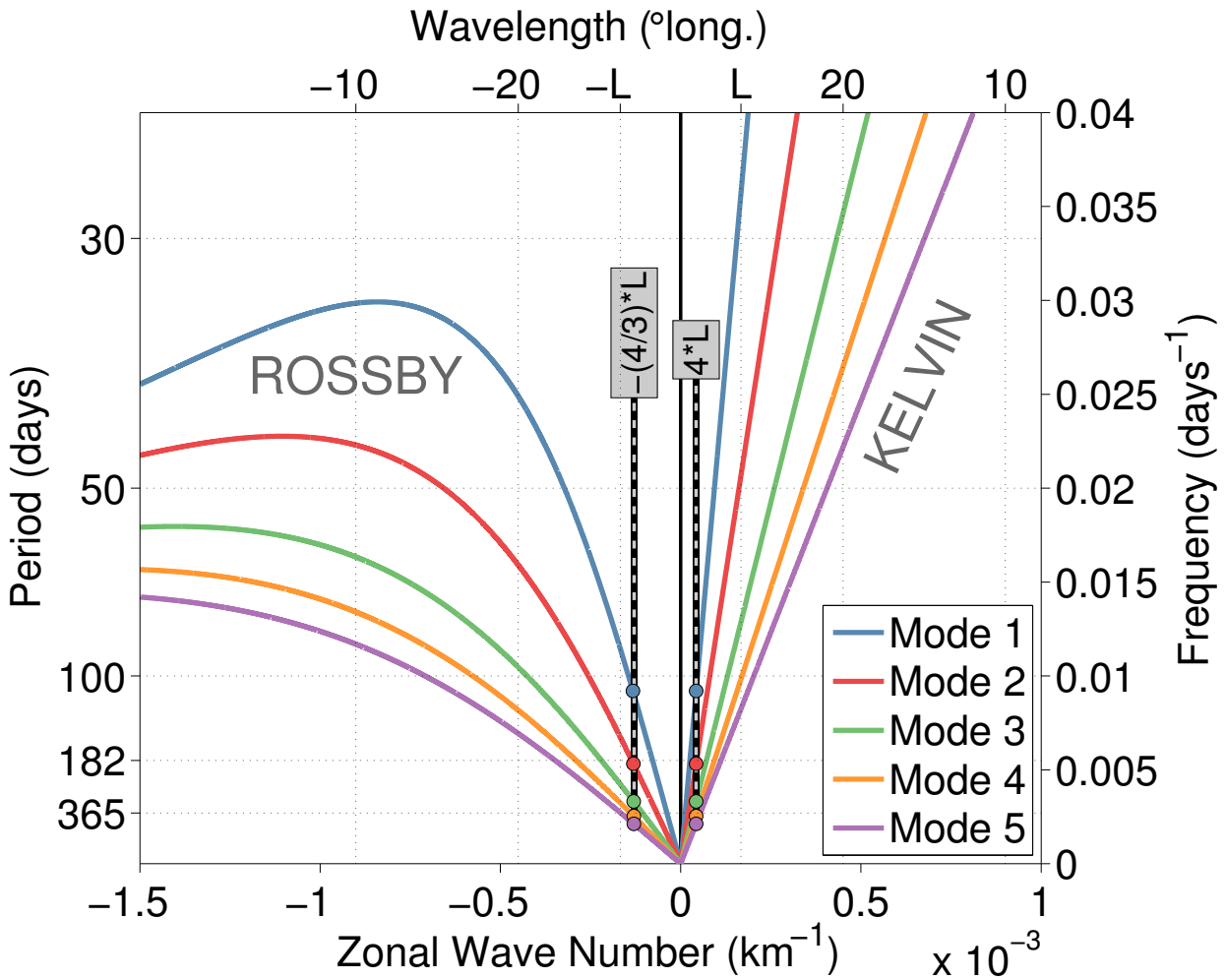

Figure 2.3: Dispersion diagram of equatorially trapped Kelvin and Rossby waves for the first five baroclinic modes (being a function of c in Equation (2.7)), first meridional mode for Rossby waves ($n = 1$ in Equation (2.7)). Positive and negative wave numbers indicate eastward and westward propagation, respectively. L marks the basin width of the equatorial Atlantic corresponding to $52.8\,^\circ \sim 5.8 \times 10^6$ m. Colored dots indicate the wave numbers associated with resonance periods of the corresponding baroclinic mode in the equatorial Atlantic Ocean.

2.3.1 Equatorial Kelvin waves

EKWs represent a special case of the wave solutions, in which the meridional velocity vanishes everywhere. It is the trivial solution of Equation (2.4) for $V = 0$. For the Kelvin wave, represented by $n = -1$, the dispersion relation (Equation (2.7)) reduces to

$$\omega = ck \tag{2.8}$$

Thus, EKWs are non-dispersive propagating waves with constant phase speed corresponding to the gravity wave speed of a particular baroclinic mode (Figure 2.3). Only eastward propagating waves are trapped in the equatorial wave-guide by the Coriolis force, while westward propagation is ruled out as the solution is unbounded at large values of y. Note also the analogy to coastally trapped Kelvin waves, i.e. phase speed equal to gravity wave speed, absence of transverse flow, and decay over a deformation radius.

2.3.2 Equatorial Rossby waves

For low frequencies, ω^2/c^2 can be neglected in Equation (2.7) to obtain

$$\omega = -\frac{\beta k}{k^2 + (2n+1)\beta/c} \tag{2.9}$$

This relationship represents ERWs, characterized by westward phase propagation (Figure 2.3). The frequency has a maximum at $k_{max} = \sqrt{2n+1}/\sqrt{c/\beta} = \sqrt{2n+1}/R_{eq}$, permitting a distinction between *long* ($k \ll k_{max}$) and *short* ($k \gg k_{max}$) ERWs. For long ERWs, group velocity ($\partial\omega/\partial k$) is also westward, while for short ERWs the group velocity is eastward.

Furthermore, for long ERWs the approximation

$$\omega = -\frac{\beta k}{(2n+1)\beta/c} \tag{2.10}$$

is valid, making these waves basically non-dispersive for the wave number range considered. Consequently, their group velocity is given by

$$c_{gr} = -\frac{c}{2n+1} \tag{2.11}$$

Thus, the propagation speed of a long ERW of the first meridional mode is three times slower than that of the corresponding EKW.

2.3.3 Equatorial basin modes

In a zonally bounded basin, equatorial wave propagation and reflection at the zonal boundaries can form standing modes under certain conditions. The modes involve eastward propagating EKWs and westward propagating ERWs and are known as equatorial basin-modes. Equatorial basin-modes have first been analytically discussed for both inviscid dynamics and in the presence of Rayleigh friction by *Cane and Moore* (1981). In the inviscid analytical solution a singularity is found in the centre of the basin due to focussing of the ERWs as a result of beta dispersion (*Schopf et al.*, 1981). This effect is reduced when considering Rayleigh damping in the analytical solution. In the context of a SWM, Rossby wave focusing can be prevented by introducing lateral diffusion and/or mean flow, making solutions more realistic in comparison to observations (*Greatbatch et al.*, 2012; *Claus et al.*, 2014).

The characteristic oscillation period of the gravest basin-mode associated with a particular baroclinic mode (colored dots in Figure 2.3) is set by the time it takes both waves to cross the basin and is given by

$$T = \frac{4L}{c} \tag{2.12}$$

where L represents the basin width and c is the gravity-wave speed of the baroclinic mode considered. According to Figure 2.3, the corresponding wave lengths of EKWs and ERWs associated with the basin-mode frequencies are set by the basin width, independent of the baroclinic mode.

The equatorial basin in the Atlantic Ocean has a zonal width of $\sim 52.8\,^{\circ}$. The wave length of the EKWs and ERWs associated with the gravest basin-modes are approximately $210\,^{\circ}$ and $70\,^{\circ}$, respectively. Therefore, the equatorial basin width L corresponds to about one quarter of the Kelvin wave length and three quarters of the Rossby wave length (Figure 2.3), reflecting the differences in propagation speed between EKWs and ERWs.

Depending on the combination of basin width and wave speed, resonances with a forcing at a particular frequency can occur, which can lead to substantial basin-mode oscillations even though the forcing at this frequency might be weak.

As the previous sections showed, the underlying dynamics of the involved long equatorial waves are linear and a basin-mode can therefore be excited in a linear SWM representing a single baroclinic mode. An oscillatory forcing in the zonal momentum equations is thereby capable of generating the required waves. In this study SWM simulations representing various baroclinic modes are used to study the impact of the basin-modes on the seasonal cycles of both the equatorial Atlantic circulation and the boundary circulation off Angola (Chapter 5 and Chapter 6, respectively).

3 The Angola Current: Flow and hydrographic characteristics as observed at 11°S

The eastern boundary circulation off the coast of Angola has been only sparsely described in the past based on sporadic synoptic-scale measurements. In this chapter the first long-term direct velocity observations of the Angola Current obtained near 11 °S are presented, giving insights in its mean properties and variability. In combination with available shipboard velocity sections an Angola Current transport estimate is derived. Furthermore, an extensive set of shipboard hydrographic observations supplemented by autonomous glider observations allows the determination of the seasonal cycle of temperature and salinity at the shelf break off Angola. The acquired observational data is used for a first assessment of several ocean reanalysis products in terms of current strength and thermal structure off Angola.

The manuscript was published in *Journal of Geophysical Research: Oceans* in February 2017.

Citation: Kopte, R., P. Brandt, M. Dengler, P. C. M. Tchipalanga, M. Macuéria, and M. Ostrowski (2017), The Angola Current: Flow and hydrographic characteristics as observed at 11 °S, J. Geophys. Res. Oceans, 122, 1177–1189, doi:10.1002/2016JC012374.

The candidate designed the study and carried out the analysis of both mooring and shipboard data sets as well as of several reanalysis products. He produced all figures and authored the manuscript from the first draft to the final version.

3.1 Introduction

North of the Benguela upwelling region - one of the world's four major Eastern Boundary Upwelling Systems (Benguela-Canaries-Humboldt-California, e.g., *Carr and Kearns* (2003); *Chavez and Messié* (2009)) - the tropical Angolan system represents another highly-productive ecosystem (*Ostrowski et al.*, 2009). Located en route from the equatorial Atlantic, the region off Angola thereby serves as the gateway for communicating equatorial oceanic variability to the northern Benguela, mainly via poleward propagation of coastally trapped waves (CTWs). At about 16°S the Angola-Benguela Front (ABF) represents a sharp, yet highly variable thermal front, separating at the surface tropical, oligotrophic waters in the north from cold waters,enriched in nutrients by upwelling in the south (*Mohrholz et al.*, 2008). Fluctuations in position and strength of the frontal system range from subseasonal (*Kostianoy and Lutjeharms*, 1999; *Mohrholz et al.*, 2001), via annual (*Meeuwis and Lutjeharms*, 1990), to interannual time scales. The latter are often associated with severe warm events during austral summer being referred to as Benguela Niños (*Shannon et al.*, 1986). Most of the observed interannual variability is induced by wave response via equatorial Kelvin waves and CTWs to the remote equatorial forcing (*Bachèlery et al.*, 2016; *Florenchie et al.*, 2003; *Lübbecke et al.*, 2010; *Rouault et al.*, 2007), yet modulated by local wind forcing (*Bachèlery et al.*, 2016; *Richter et al.*, 2010). Anomalous oceanic conditions in the region have been found to substantially impact precipitation variability over adjacent countries (*Rouault et al.*, 2003) as well as the marine ecosystem and local fisheries (*Gammelsrød et al.*, 1998).

Within the tropical Angolan system, the Angola Current (AC) is one key element in the poleward advection of warm tropical waters. It is suggested to be fed by eastward equatorial currents, namely the Equatorial Undercurrent, the South Equatorial Undercurrent, and the South Equatorial Counter Current, as well as the Gabon Current (Figure 3.1a) (*Peterson and Stramma*, 1991; *Rouault et al.*, 2007; *Wacongne and Piton*, 1992). Its variability in strength is found to be partly controlled by the passage of CTWs (*Ostrowski et al.*, 2009; *Rouault*, 2012). The large-scale properties of the AC have been described exclusively based on synoptic measurements so far. Subsurface southward geostrophic velocities exceeding $50\,\mathrm{cm\,s^{-1}}$ were reported along the Angolan coast between 9 °S and 16 °S during a hydrographic survey in 1968 with southward velocities extending from the surface down to 250–300 m depth (*Moroshkin et al.*, 1970). Current velocities were measured at 12 °S on four occasions between September 1970 and July 1971 (*Dias*, 1983a,b). In March 1971 southward flow was found to be stronger compared to July 1971: $50\,\mathrm{cm\,s^{-1}}$ versus $42\,\mathrm{cm\,s^{-1}}$ at the surface, $70\,\mathrm{cm\,s^{-1}}$ versus $33\,\mathrm{cm\,s^{-1}}$ at 100 m depth, respectively. Southward transports above 400 m depth were calculated in the range of 1.2–3.7 Sv between September 1970 and July 1971 (*Dias*, 1983a). However, results of an inverse model study making use of WOCE line A13, which was sampled during a major Benguela Niño event between January and March 1995 (*Gammelsrød et al.*, 1998), suggest a southward transport of 11 Sv of the AC within surface and thermocline layers (*Mercier et al.*, 2003). During a survey in April 1999 a secondary, offshore branch of southward subsurface flow was identified in shipboard

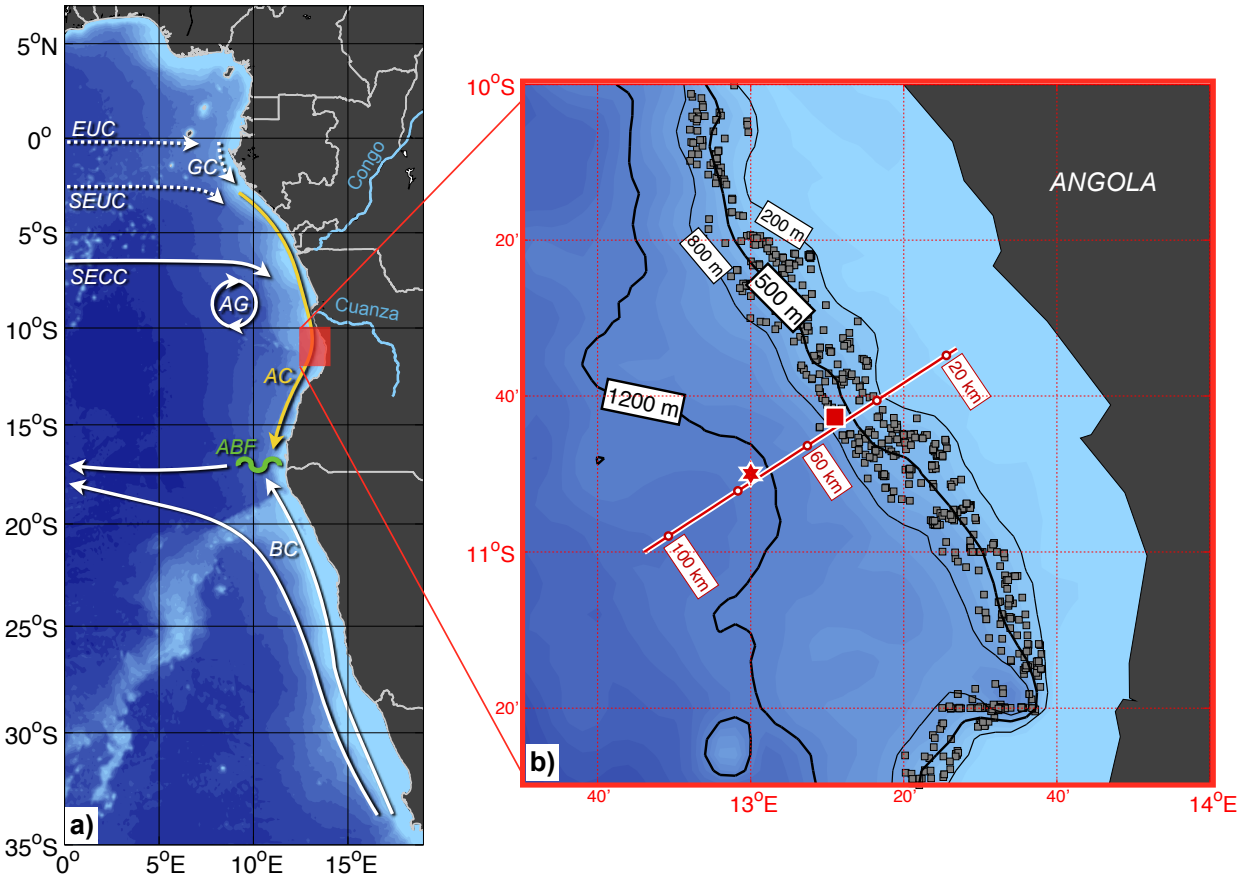

Figure 3.1: (a) Schematic circulation in the Southeast Atlantic Ocean (modified from *Rouault et al.* (2007)). Main features are the Equatorial Undercurrent (EUC), South Equatorial Undercurrent (SEUC), South Equatorial Counter Current (SECC), Gabon Current (GC), Angola Gyre (AG), Angola Current (AC), and Benguela Current (BC). The mean position of the Angola-Benguela Front (ABF) is indicated. (b) Enlargement of the study area indicating the positions of ADCP mooring (red star) and ADCP shield (red square) as well as the ∼11 °S section (solid red line, white dots represent along-section distance to the coast (km)). Gray dots represent positions of all hydrographic profiles used in this study. Bathymetry is extracted from ETOPO2, with black lines representing individual isobaths.

velocity data separated from the coastal branch (*Mohrholz et al.*, 2001). Both pathways were characterized by southward velocities of about 40 cm s^{-1} below the surface. However, below 150 m depth northward currents of 15–20 cm s^{-1} were observed in the coastal branch. Based on the available synoptic snapshots, the general perception of the AC is that of a continuous poleward current which is stronger in austral summer and weaker in austral winter. During Benguela Niños the AC appears to be a major agent in advecting warm tropical waters poleward into the northern Benguela (*Gammelsrød et al.*, 1998; *Rouault et al.*, 2007).

Along with the eastern equatorial Atlantic, the Southeast Atlantic Ocean and particularly the ABF region is subject to the strongest sea surface temperature (SST) biases seen in many state-of-the-art coupled climate simulations (*Davey et al.*, 2002; *Richter et al.*, 2014). A common indicator of the bias is an erroneous tilt of the equatorial thermocline associated with reduced zonal winds, nonetheless the origin of the bias remains highly controversial. Mainly deficiencies

in the atmosphere models have been proposed as source of the bias, such as a misrepresentation of convection over the Amazon and West Africa (*Richter and Xie*, 2008), erroneous localized Bjerknes feedback in the Gulf of Guinea (*Patricola et al.*, 2012), or errors in radiation and low clouds over the upwelling regions (*Huang et al.*, 2007). It could be shown that a reduction of the bias is possible particularly by improving the near-coastal winds when enhancing simultaneously the horizontal and vertical resolution of the atmospheric model in coupled simulations (*Harlaß et al.*, 2015). However, also systematic errors in ocean models potentially contribute to the bias problem (*Grodsky et al.*, 2012; *Large and Danabasoglu*, 2006; *Xu et al.*, 2014). In particular, the representation of the AC and the tropical Angolan system in ocean models as well as reanalysis products have been identified to cause biases in the Southeast Atlantic (*Xu et al.*, 2014). First, based on comparisons with a reference reanalysis product, usually an overshooting of the AC is observed near the ABF causing a southward shift of the front and thus introducing a strong warm SST bias. Second, ocean models tend to have difficulties to simulate the sharp thermocline off Angola, which results in too-warm subsurface temperatures being advected southward into the northern Benguela by a deep continuation of the AC and subsequently upwelled to manifest in too-warm SSTs. In this context the need for in situ ocean observations to validate both AC strength and thermal structure off Angola in ocean models and reanalysis data has been emphasized.

For the first time, moored observations of the boundary circulation at ∼11 °S off the coast of Angola are available between July 2013 and October 2015. They give insight into the mean state and variability of the AC. Furthermore, based on an extensive set of hydrographic measurements from shipboard and autonomous glider measurements covering the period from 1968 to 2015, the seasonality of hydrographic properties at the eastern boundary off Angola is investigated. Finally, the observed thermal structure and alongshore velocities are used to qualitatively assess the performance of various reanalysis products in the boundary current system off Angola.

3.2 Data and Methods

3.2.1 Mooring Data

Multiyear velocity measurements were obtained by a mooring array deployed at ∼11 °S off the coast of Angola for the period from July 2013 to October 2015 (Figure 3.1b). A bottom shield equipped with a 75 kHz Teledyne RDI's Workhorse Long Ranger ADCP, which was sampling every 2.5 min, was located at 500 m water depth (13°11.0'E, 10°42.7'S, 53 km offshore, red square in Figure 3.1b), accompanied by a mooring sitting on the 1200 m isobath (13°00'E, 10°50.0'S, 77 km offshore, red star in Figure 3.1b) with another 75 kHz Long Ranger ADCP being installed at 500 m depth and sampling every hour. Both upward-looking instruments measured the current speed in the overlying water-column up to about 45 m below the sea surface. During data processing, a 40 h low pass filter was applied to hourly-interpolated current data to eliminate tidal currents

followed by a subsampling of the detided data to 12 hourly resolution. The local orientation of the shelf break ($-34\,^{\circ}$) was used for the calculation of the alongshore component of the flow.

Additionally, temperature time series were recorded at the instrument depths.

3.2.2 Shipboard and Autonomous Glider Data

Since 1983, an extensive oceanographic data set from repeated ship surveys carried out in Angolan territorial waters has been acquired within the EAF-Nansen program executed by the Food and Agriculture Organization of the United Nations (FAO) and funded by Norwegian Agency for Development Cooperation (NORAD). Semiannual cruises (austral summer versus austral winter) have been carried out by R/V Dr. Fridtjof Nansen on a regular basis since 1995, collecting data to estimate the abundance and map the distribution of the main commercially important fish species, to perform biogeochemical measurements and to collect hydrographic data. Since 2005, shipboard ADCP measurements from a 150 kHz Teledyne RDI Ocean Surveyor are available.

Recently, shipboard CTD measurements and upper ocean velocities recorded by a 75 kHz Teledyne RDI Ocean Surveyor were collected along a section perpendicular to the topography (red line in Figure 3.1b, hereinafter referred to as "$\sim$11 °S section") during R/V Meteor cruises M98 in July 2013 and M120 in October 2015, when the moorings described in Section 3.2.1 were deployed and serviced, respectively.

Shipboard Current Measurements

From the two data sets described above, we use a total number of 13 upper ocean velocity sections. Eleven sections were acquired within the EAF-Nansen program on a monitoring line perpendicular to the topography near 12 °S (sampling times: March 2007, March 2008, June 2008, March 2009, June 2009, March 2010, July 2010, March 2011, August 2011, February 2014, July 2014), another two stem from samplings of the $\sim$11 °S section by R/V Meteor (sampling times: July 2013, October 2015).

Hydrographic Measurements

A total number of 707 temperature/salinity profiles sampled on the Angolan shelf break within 200 and 800 m water depth between 11.5 °S and 10 °S is used (grey dots in Figure 3.1b), incorporating 644 profiles obtained within the EAF-Nansen program between 1991 and 2015, as well as eight profiles collected during the two R/V Meteor cruises in 2013 and 2015. The majority of these profiles were obtained during March/April, July/August, and October. In particular these data sets do not provide hydrographic information for the December/January period. In order to improve the seasonal coverage, additional historic data were incorporated into the analysis: 52 temperature/salinity profiles were extracted from the input data set for the MIMOC climatology (*Schmidtko et al.*, 2013), originating mainly from the 1980s but as early as 1968; one profile

was taken during R/V Poseidon cruise 250 (April 1999, *Mohrholz et al.* (2001)), one during R/V Meteor cruise 48/3 (September 2000, *Mohrholz et al.* (2008)), and another one during R/V Maria S. Merian cruise 18/4 (August 2011, *Mohrholz et al.* (2014)). Note that the extended data set does contain three profiles for December/January; however, these profiles are limited to the upper 200–450 m depth.

Supplementary to the shipboard hydrographic measurements, we include data from an autonomous Slocum glider (Teledyne Webb Research) that was deployed in the study area from 31 October 2015 to 27 November 2015 (Glider IFM03, deployment-ID: ifm03_depl12). Glider data were internally recorded as time series along the flight path, while for the analysis the data are interpolated onto a regular pressure grid of 1-dbar resolution (see also *Thomsen et al.* (2016) for further details on data processing). During its deployment, the glider sampled along the ∼11 °S section, travelling onshore and offshore five times each thereby acquiring 364 CTD profiles within the section segment between 200 and 800 m water depth.

3.2.3 Auxiliary Data Sets

As the moored ADCP measurements do not provide near-surface velocity observations, we use the delayed-time "all-sat-merged" data set of absolute geostrophic velocities derived from absolute dynamic topography, produced by Ssalto/Duacs and distributed by AVISO, with support from CNES (Version 2014, http://www.aviso.altimetry.fr/duac/). This multimission product is mapped on a $0.25 \times 0.25\,^{\circ}$ grid and provided on daily resolution. However, note that the mapping algorithm takes into account data from a latitude-dependent multiday window using Gauss-Markov weighting (∼12 days at 11 °S, for further details on the mapping procedure see *Pujol et al.* (2016)). Only data from the closest grid point to the mooring positions and corresponding to the mooring deployment period are considered here. A similar extraction is done for sea level anomaly (SLA) data.

For sea surface temperature (SST), we make use of the "Microwave plus Infrared (MW_IR) Optimally Interpolated SST" product provided by Remote Sensing Systems (www.remss.com). This data set combines through-cloud capabilities of microwave sensors (TMI, AMSR-E, AMSR2, WindSat) with high spatial resolution of infrared SST data (Terra MODIS, Aqua MODIS), yielding 9 km horizontal resolution. Using a diurnal model, SST values are corrected to create representative 12:00 LT temperatures (www.remss.com). Daily values from 2006 to 2015, spatially averaged over the Angolan shelf break within 200 and 800 m water depth between 11.5 °S and 10 °S are used here.

3.2.4 AC Transport Estimation

In order to obtain an estimate of the AC transport, a time series of the two-dimensional flow field (as function of distance from coast and depth) is required. Our approach is to apply an

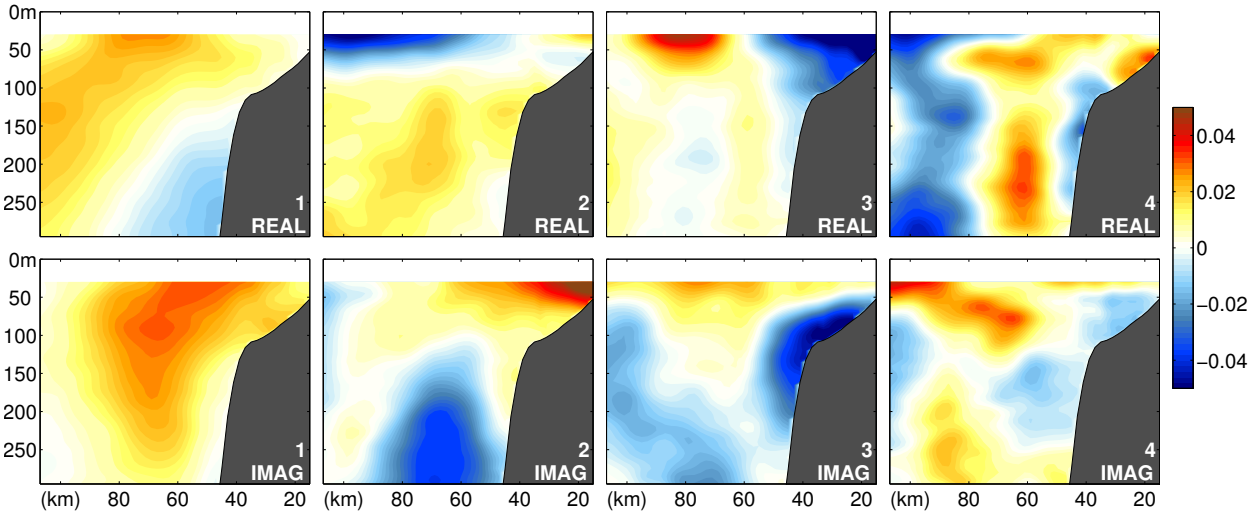

Figure 3.2: HEOF patterns (dimensionless, sign is arbitrary) as calculated from 13 ship sections. Column 1–4 corresponds to HEOF 1–4 with each HEOF consisting of two patterns. Top and bottom plots correspond to the patterns from the real and imaginary HEOF, respectively.

inter/extrapolation scheme to the moored velocity time series described in Section 3.2.1. The inter/extrapolation is based on the variability patterns (Figure 3.2) of 13 shipboard velocity sections collected between ∼11 °S and 12 °S as described in Section 3.2.2. As the topographic slope is very similar for all these sections, we choose a reference bathymetry representing the shelf break at the ∼11 °S section and rearrange alongshore velocity profiles from other sections with respect to depth. Subsequently, the rearranged sections are interpolated on a reference grid. The resulting sections are assumed to give the best estimate of variability contained in the alongshore flow field, although a bias cannot be ruled out considering the sampling times with regard to the seasonal cycle (mainly austral summer and austral winter).

Note that some of the ship sections were limited in their offshore and/or vertical extent. Therefore, before deriving variability patterns, any gaps in these sections were closed by regressing their valid data on the first 20 variability patterns calculated from corresponding section data from the high-resolution OGCM INALT01 (*Durgadoo et al.*, 2013), and subsequently extrapolating the respective ship sections to full offshore and vertical extent.

A Hilbert transformation is applied to the alongshore velocity fields of the ship sections (*Barnett*, 1983; *Brandt et al.*, 2014). Hilbert EOFs (HEOFs), containing real and imaginary patterns, are obtained by applying empirical orthogonal function (EOF) analysis to the Hilbert transform of alongshore velocity.

The summed up contribution of eight real spatial patterns, which were derived from the first four complex EOFs (Figure 3.2), explains 96 % of the variability contained in the ship sections. These eight real patterns are then regressed on the mooring time series of alongshore velocity. Regressed fields are summed up and the resulting time series of the two-dimensional velocity field is integrated in the limits of 15–90 km offshore and 30–200 m depth to obtain a transport time series. The method is validated by reconstructing the ship sections using the variability

patterns (in varying numbers) and the velocity profiles from the ship sections corresponding to the mooring locations. Then the observed AC transport from the ship sections can be compared to the AC transport estimated from the reconstructed sections (Figure 3.3). A balanced compromise has to be found between simplicity and explained variance. Here we decide on using the first four HEOFs (or eight real spatial patterns) for the reconstruction, as they give the lowest RMS between observed and reconstructed AC transport.

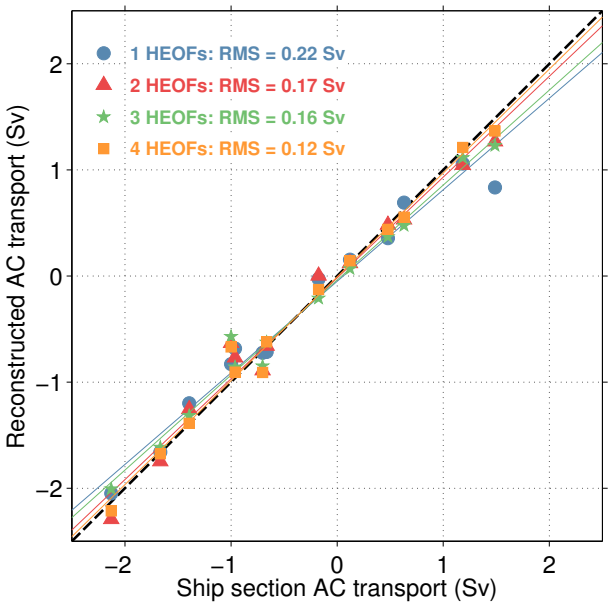

Figure 3.3: Observed versus reconstructed AC transport obtained by regressing various numbers of real pattern derived from HEOF analysis (corresponding to Figure 3.2) on the shipboard velocity profiles measured at the mooring positions. Solid lines are linear regressions with RMS values given in the legend.

3.2.5 Seasonality of Hydrographic Properties

The seasonality of potential temperature and salinity within the current regime is investigated using hydrographic profiles collected within the EAF-Nansen program, and various cruises with R/V Meteor, R/V Maria S. Merian, and R/V Poseidon, supplemented by autonomous glider data as well as historical data (see Section 3.2.2). For each cruise/glider section, a mean potential temperature and salinity profile is derived from all measurements taken between 200 and 800 m water depth along the continental slope near 11 °S. Subsequently, these mean profiles are sorted with respect to the calendar year and are interpolated using a depth-time Gaussian weighting (vertical/temporal half width scale of 5 m/25 days and cutoff scales of 10 m/300 days) to construct a mean seasonal distribution. Note that the chosen interpolation scales leave the amplitude of an annual harmonic almost unaffected, whereas the amplitude of a semiannual harmonic would be reduced by about 20 %. The contribution of the annual cycle to the seasonality is investigated by fitting an annual harmonic to the potential temperature and salinity distribution at each depth level. The effect of potential longterm trends on the seasonality has been evaluated by removing linear trends at each depth level before the interpolation. Trends are strongest but also most uncertain in the near surface layers and have been found to be smaller than 0.4 °C per decade for temperature and 0.15 per decade for salinity. However, removing these trends does not alter significantly the seasonal distribution and particularly the amplitudes of the annual harmonic. Thus, as robust trends are difficult to assess from the available data distribution, particularly when including historical data acquired as early as 1969, and their effect on the seasonality appears to be negligible, we decide on using the nondetrended data set for the analysis of the seasonality.

3.3 Results

3.3.1 Alongshore Flow and Transport of the AC

The alongshore flow observed by the moored ADCPs described in Section 3.2.1 at ∼11 °S is dominated by alternating periods of southward and northward velocities that can last for a couple of months with superimposed high-frequency velocity pulses (Figure 3.4a and c). Stronger velocities were recorded by the onshore ADCP (located 53 km off the coast), with maximum velocities exceeding $\pm 40\,\mathrm{cm\,s^{-1}}$. Considering vertical structure, the offshore ADCP (located 77 km off the coast) measured more depth-independent current profiles. The alongshore component of surface geostrophic velocities from AVISO is found to be coherent with the top-most observations of the ADCPs at about 45 m depth during most of the observation period (significantly correlated at the 95 %-level with $r = 0.49$ for the onshore ADCP and $r = 0.44$ for the offshore ADCP). The mean profile of alongshore velocity from the onshore ADCP, which was derived by first removing the mean seasonal cycle to avoid a seasonal bias due to the record length of 2.5 years, indicates southward flow in the upper 210 m with maximum southward velocities of $8\,\mathrm{cm\,s^{-1}}$ at 50 m depth (Figure 3.4b). Offshore, the mean southward flow extends down to about 160 m depth with maximum velocities of $5\,\mathrm{cm\,s^{-1}}$ also at about 50 m depth (Figure 3.4d). Mean southward surface geostrophic velocities are found to be $5\,\mathrm{cm\,s^{-1}}$ at the onshore and $3\,\mathrm{cm\,s^{-1}}$ at the offshore mooring position.

The mean alongshore velocity across the ∼11 °S section (Figure 3.5a) is obtained from time-averaging the time series of the reconstructed two-dimensional velocity field, which was calculated using both the variability patterns from the shipboard velocity sections and the moored velocity time series (Section 3.2.4). The southward maximum of alongshore velocity is located in 50–60m depth at a distance from the coast close to that of the onshore ADCP, whereas the offshore ADCP appears to monitor the offshore termination of the mean southward flow of the boundary current. Based on the mean flow pattern, a box extending from 15 to 90 km offshore and 30 to 200 m depth is chosen representing the area occupied by the AC. The resulting AC volume transport time series is dominated by submonthly to intraseasonal variability, ranging from 2.2 Sv southward to 1.2 Sv northward (Figure 3.5b). For the observational period, a mean southward transport of 0.32 Sv (standard deviation: 0.59 Sv) is derived. Accounting for the top 30 m by extrapolating moored velocities linearly to surface geostrophic velocities before reconstructing the flow field, yields 0.54 Sv (standard deviation: 0.88 Sv) for the 0–200 m depth range. Four individual transport estimates from available ship sections during the mooring period agree with the reconstructed time series. The inherent submonthly to intraseasonal fluctuations hamper a clear identification of semiannual and annual flow components (Figure 3.5b). However, the semiannual component with amplitude of 0.20 Sv was found slightly stronger than the annual component with amplitude of 0.16 Sv. The superposition of both harmonics suggests March/April and September/October as the periods of maximum southward transport.

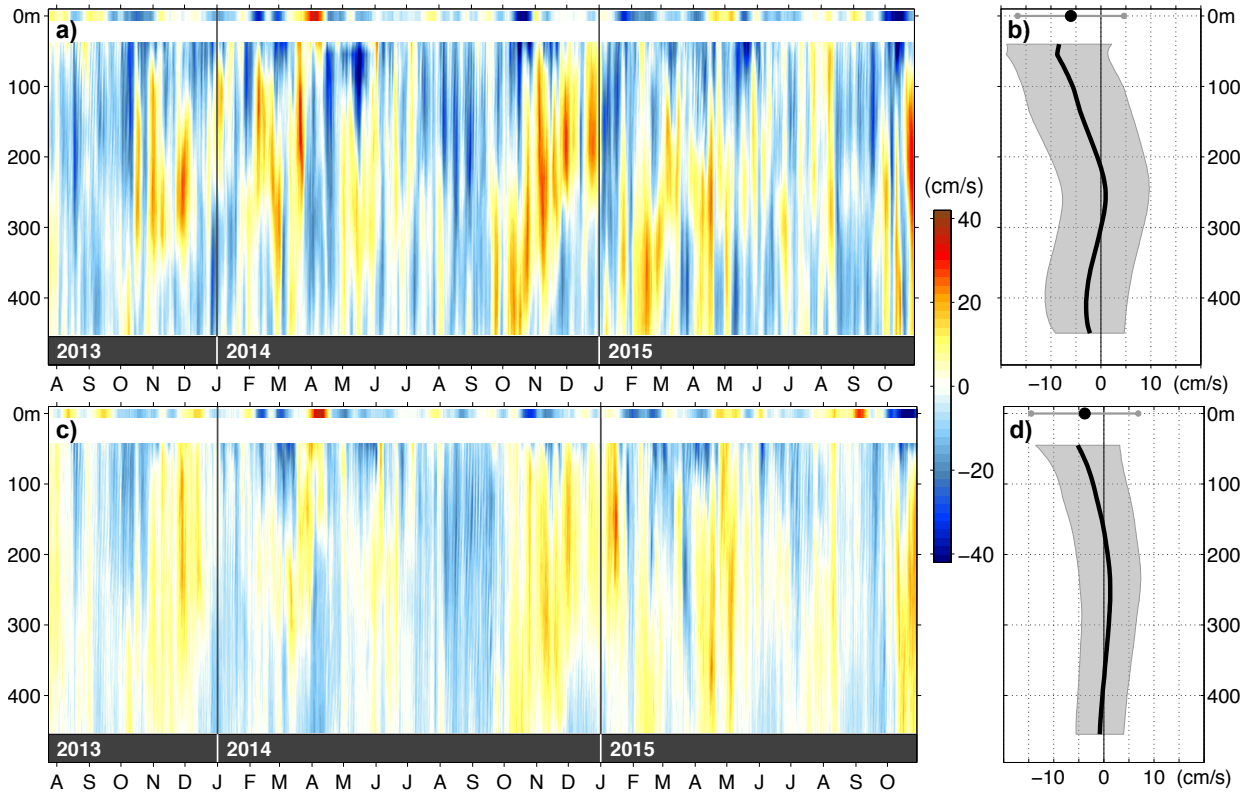

Figure 3.4: Time series of alongshore velocity (−34 °) as measured by (a) the onshore ADCP in the bottom shield and (c) the offshore ADCP in the mooring. Positive values indicate northward and negative values indicate southward flow. Corresponding mean alongshore velocity profiles (thick black lines) and standard deviations (shaded areas) are shown in (b) and (d), respectively. At the surface corresponding AVISO geostrophic alongshore velocities are plotted.

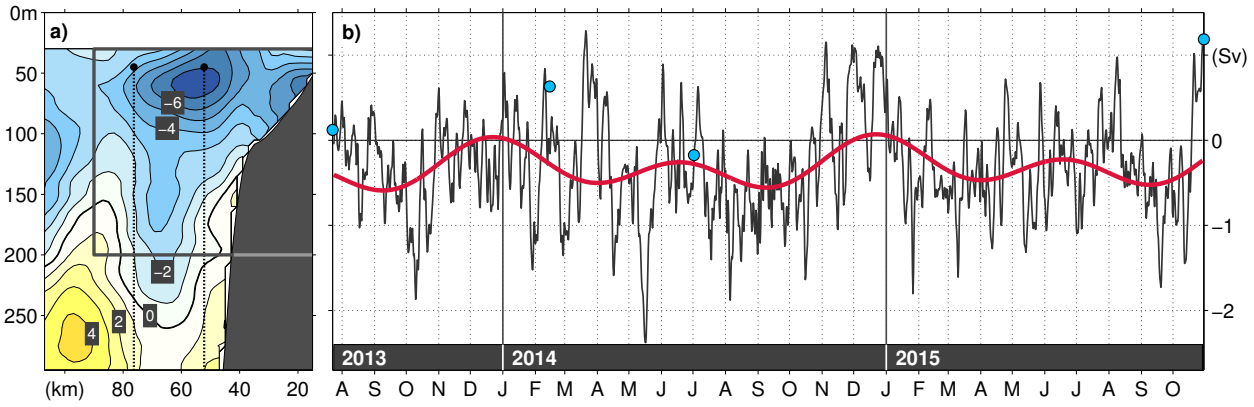

Figure 3.5: (a) Mean alongshore velocity field ($cm\,s^{-1}$) based on the reconstruction of the 3-D flow field using mooring data and eight real pattern from the first four HEOFs. Positive values indicate northward and negative values indicate southward flow. (b) Transport time series (black line) obtained by integrating the alongshore velocity from 30 to 200 m depth and from 15 to 90 km offshore (see grey box in Figure 3.5a). Red line displays sum of semiannual and annual harmonic. Blue dots indicate individual transport estimates based on shipboard velocity sections obtained during the mooring period.

3.3.2 Seasonality of Hydrographic Properties in the Current Regime

The seasonality of potential temperature and salinity at the continental slope at ∼11 °S reflects mainly the major seasons of down and upwelling. Warm/fresh waters occupy the mixed layer during downwelling in March, whereas cold/saline waters prevail during upwelling in August (Figure 3.6a and c). Although December/January are only sparsely sampled and thus are strongly dependent on the chosen interpolation scales, the secondary upwelling during this period is indicated by upward bending isopycnals within the upper 200 m, thereby separating the major downwelling season in March from the secondary downwelling in October/November. By suggesting no more than a weak cooling in December/January, the main periods of down and upwelling are also indicated in the seasonal cycle of SST. At depth, the seasonal distribution of potential temperature derived from the shipboard hydrographic data agrees with the seasonal cycle as recorded by the temperature sensors of the moored ADCPs both in amplitude and evolution over the year (Figure 3.6a), suggesting that the observing period from 2013 to 2015 can be considered as a period with a rather regular seasonal cycle. The individual contributions of both semiannual and annual cycles are inferred by fitting corresponding harmonics to the seasonal distributions of potential temperature and salinity (Figure 3.6b and d, respectively), as well as to the seasonal cycles of SST and temperature as recorded by the ADCP. As noted earlier, the amplitude of the semiannual cycle in the interpolated fields is likely to be reduced by about 20 % due to the chosen temporal interpolation scales. However, in agreement with SST seasonality, the seasonality in the near-surface layers appears to be dominated by the annual cycle. The annual harmonic amplitude of potential temperature is found to be larger than 3 °C for potential temperature, and that of salinity about 0.5. Corresponding semiannual amplitudes do not exceed 1.4 °C for potential temperature and 0.3 for salinity. Within the depth range of the AC (50–200 m depth), the dominance of the annual cycle decreases with depth and amplitudes of semiannual and annual harmonic approach similar levels. Below 200 m depth, there is only weak seasonality with both semiannual and annual amplitudes smaller than 0.5 °C for potential temperature and 0.05 for salinity. Here, semiannual amplitudes are likely being masked by the interpolation, as there is no deep data available for the December/January period. The RMS of the residuals obtained by subtracting the semiannual and annual harmonics from the individual potential temperature and salinity profiles gives a measure of the relative contribution of the derived seasonality to the total variability contained in the hydrographic data and can be compared to the RMS of the sum of semiannual and annual harmonic (Figure 3.6b, d). For potential temperature, the RMS of the residuals is considerably smaller than the RMS of semiannual and annual harmonic in the nearsurface layers, while it is larger for near-surface salinity. Whether intraseasonal or interannual variability dominates the residual fluctuations cannot be resolved with the available hydrographic data. Though, the low-pass-filtered SST time series (cutoff period of 365 days, annual, and semiannual harmonic removed prior filtering) suggests a RMS of 0.46 °C for interannual fluctuations. Correspondingly, for intraseasonal fluctuations the high-pass-filtered version of the SST time se-

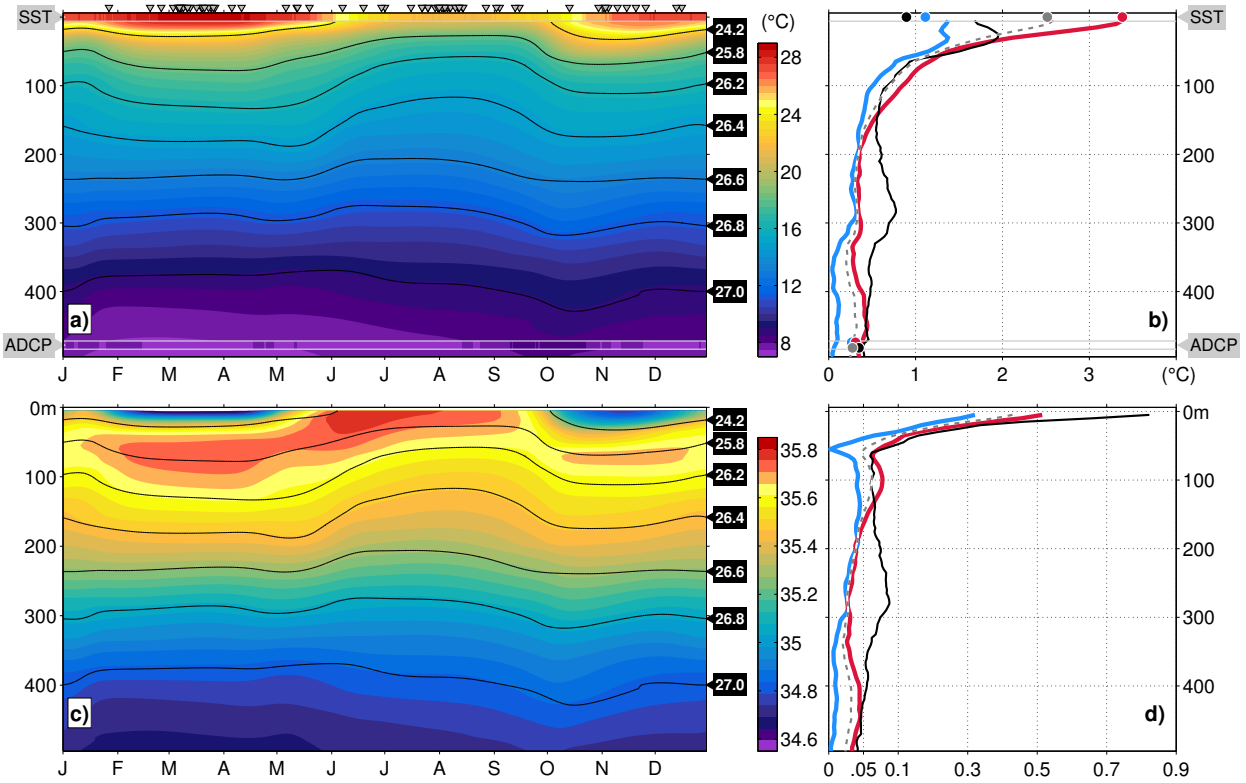

Figure 3.6: Seasonal distribution of (a) potential temperature and (c) salinity derived from available hydrographic measurements in the study area. Sampling times of used profiles relative to the calendar year are indicated by grey triangles at the top of Figure 3.6a. In Figure 3.6a also the seasonal cycles of SST and of potential temperature as recorded by the ADCPs are indicated. Black lines represent isopycnals. On the right, red and blue lines depict amplitudes of the annual and semiannual harmonics, respectively, as fitted to the seasonal distribution of (b) potential temperature and (d) salinity. Solid black lines show the RMS of the residuals derived by subtracting annual and semiannual harmonics from the individual profiles, whereas dashed gray lines show the RMS of the sum of annual and semiannual harmonics.

ries (cutoff period of 365 days) shows a RMS value of 0.66 °C. This indicates slightly higher importance of intraseasonal variability at least for temperature in the near-surface layer. Near the core depth of the AC, the RMS of potential temperature and salinity residuals are found to be in the same range or only slightly larger than the corresponding RMS of the semiannual plus annual harmonic, suggesting the seasonal cycle as an important contributor to the total variability. Below 200 m depth, where semiannual and annual amplitudes are weak anyway, RMS of the residuals generally exceed the RMS of semiannual plus annual harmonic, indicating different time scales dominating the total variability.

While both mixed and upper thermocline layers undergo substantial fluctuations of potential temperature and salinity, the central water layer below remains rather stable on seasonal time scales (Figure 3.7a). At ∼11 °S, it is composed solely of South Atlantic Central Water (SACW, as defined in *Mohrholz et al.* (2008)), clearly distinguishable from the colder and fresher Eastern SACW (ESACW), which stems from the Benguela upwelling region. By investigating the seasonal cycle of salinity anomalies on isopycnals, substantial changes in the water mass contribution

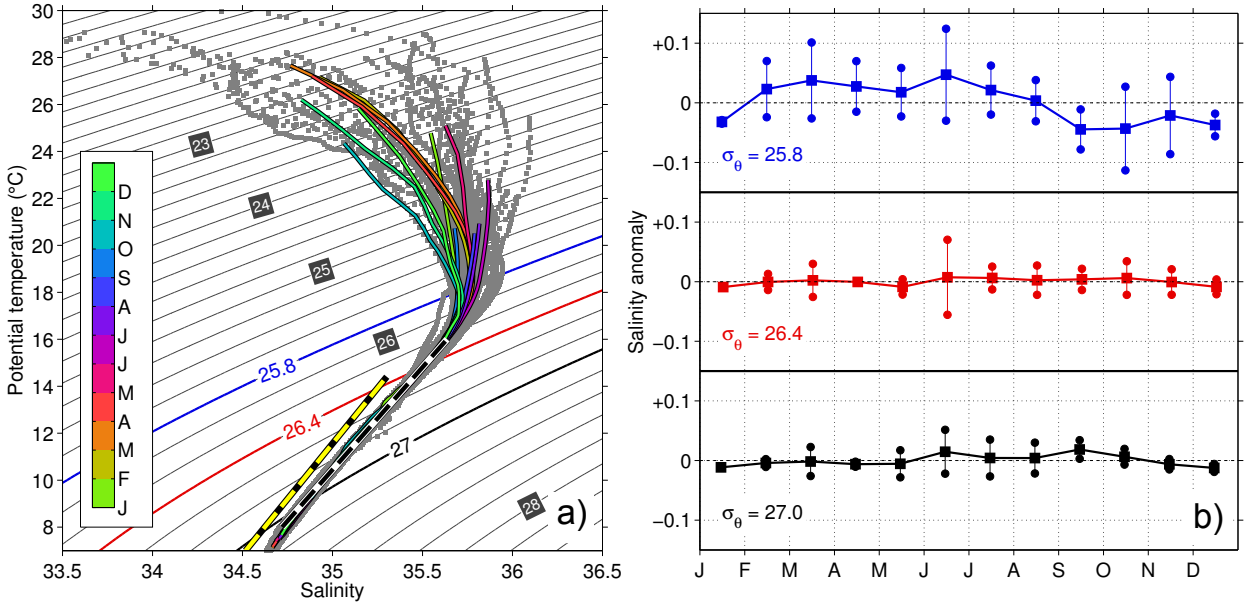

Figure 3.7: (a) θ/S diagram of all available hydrographic measurements (grey dots). Colored lines show monthly mean characteristics derived from the interpolated seasonal distribution. Black-dashed and yellow-dashed lines correspond to the SACW and ESACW characteristics, respectively, as defined in *Mohrholz et al.* (2008). (b) Mean seasonal cycle of salinity anomalies on selected isopycnals. Error bars indicate the corresponding monthly RMS of the residuals derived by subtracting the mean seasonal cycle from individual profiles.

cannot be identified both for upper and lower limits of the central water layer, represented by the 26.4 and 27.0 isopycnal, respectively (Figure 3.7b). Represented by the 25.8 isopycnal, seasonal salinity fluctuations in the upper thermocline are found in the range of ± 0.05 with the annual component being dominant. These seasonal changes in water mass composition in the upper layers are attributed primarily to the annual cycle in surface heat and freshwater fluxes as well as river runoff, as meridional advection cannot account for the observed semiannual cycle of salinity due to rather small meridional advection length scales and weak meridional gradients of salinity on isopycnals.

3.4 Discussion and Conclusions

For the first time, multiyear observations off the coast of Angola are available to describe the eastern boundary circulation. Contrary to the conclusions drawn from historical synoptic measurements, no steady southward flow of the AC is observed at $\sim 11\,^{\circ}$S off Angola. Instead, moored velocity time series of almost 2.5 years duration show strong intraseasonal variability with magnitudes in agreement with previous synoptic measurements (*Dias*, 1983a,b; *Mohrholz et al.*, 2001; *Moroshkin et al.*, 1970). The mean southward alongshore velocity of the AC, however, does not exceed $8\,\mathrm{cm\,s^{-1}}$. A corresponding boundary current transport time series is estimated based on the interpolation/extrapolation of the moored time series using variability patterns derived from a set of 13 shipboard velocity sections. A mean southward transport of 0.32 ± 0.046 Sv

is found for the observation period. Semiannual and annual harmonics are both found to be important within the seasonal cycle having maximum southward transports during March/April and September/October. These periods approximately coincide with the passing times of the semiannual downwelling CTW (*Polo et al.*, 2008; *Rouault*, 2012). By poleward acceleration of the flow, this would result in the southward transport of warm, tropical waters (*Ostrowski et al.*, 2009; *Rouault*, 2012). It should be noted that the mooring observation period did not include a Benguela Niño or Niña, and can therefore be considered as a period with a rather regular seasonal cycle. Expectedly, the corresponding transport estimate from the mooring data is considerable smaller than the AC transport derived during the major Benguela Niño event in 1995 (*Mercier et al.*, 2003).

Based on an extensive set of shipboard hydrographic data and autonomous glider measurements, the seasonality of potential temperature and salinity within the current regime is investigated. The main seasons of downwelling and upwelling in March and August, respectively, are well represented. Also, there are indications for a secondary upwelling in December/January, although this period is only sparsely sampled. The existence of the secondary upwelling was also evidenced in *Berrit and Dias* (1977), based on a 5 year temperature time series acquired at about 12 °S on the shelf in 40 m water depth. Despite a considerable semiannual component in sea level anomalies at the mooring positions indicating the passage of upwelling CTWs in July/August and December/January, SST shows a strong cooling signal only during the major upwelling season in July/August, while only a minor cooling is observed during December/January (Figure 3.8). This dominance of the annual cycle relative to the semiannual cycle in near-surface temperature is most likely related to the annual cycle in surface heat fluxes. However, other processes like seasonal variations in diapycnal mixing might contribute. The upper 20–30 m are characterized by very fresh waters both in October/ November and February/March/April. The freshening off the coast of Angola during austral summer has been previously associated with freshwater outflow from the Angolan rivers (*Mohrholz et al.*, 2001). Strength of Angolan river run-off is controlled by the wet season in the respective drainage areas. Run-off from the Congo and Cuanza rivers reaches its seasonal maximum in December/January (not shown, data for the Congo river published by *Dai et al.* (2009)). Yet, the timing of the freshening most likely is very sensitive to the yearly onset of the wet season. However, also the importance of year-to-year variability in rainfall over the adjacent landmasses and the study area itself must be considered. Revisiting the deep extension of the warm/fresh surface layer in October/November (Figure 3.6), we want to note

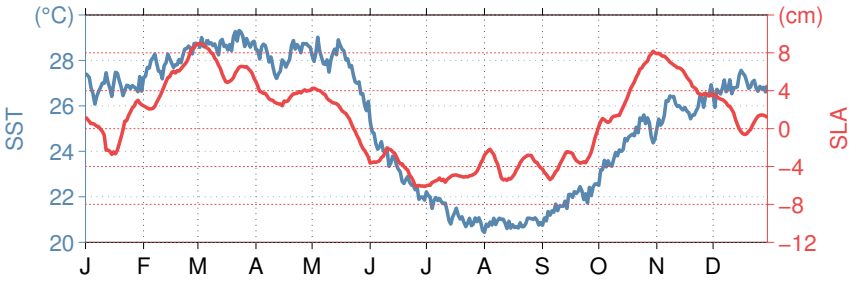

Figure 3.8: Seasonal cycle of SST (blue) and SLA (red) at ∼11 °S averaged over the mooring period (July 2013 to October 2015).

that most of the data in this period stems from a single cruise/glider survey in 2015, when an anomalously strong downwelling was identified in SLA data (SLA amplitude of $\sim$ 17 cm versus 8 cm in the climatology, not shown), most likely associated with the anomalous deepening of the isopycnals.

In order to identify seasonal changes in water mass composition, the mean seasonal cycle of salinity anomalies on selected isopycnals is investigated. Both lateral and vertical mixing as well as meridional advection by the AC are potential impact factors for water mass anomalies in the region. However, below the mixed layer, water mass characteristics appear to be primarily controlled by the annual cycle of surface heat and freshwater fluxes associated with vertical mixing. In particular, no clear connection between water mass composition and the semiannual component of the AC transport can be established. By contrast, in the northern Benguela a seasonal cycle of the central water characteristics is observed, coupled to the seasonality in the alongshore currents and meridional shift of the ABF (*Mohrholz et al.*, 2008). However, at $\sim$11 °S below the near-surface layer, alongshore gradients of hydrographic properties on isopycnals within the AC core are weak and seasonal alongshore advection length scales are small. More specifically, at the AC core depth, the semiannual harmonic amplitude of alongshore velocity that dominates the seasonal variability is 4.5 cm s^{-1} resulting in an advection length scale smaller than $\pm$1 ◦lat. With the isopycnal alongshore gradients of 0.045 °C/°lat for temperature and 0.015 /°lat for salinity, it is obvious that the alongshore advection associated with the seasonal cycle of the AC cannot induce a significant seasonality in water mass composition. The central water layer is composed almost purely of SACW with no seasonal influences by ESACW being identifiable, the latter originating in the Cape Basin.

Most coupled climate simulations exhibit warm SST biases in the coastal upwelling regions of the tropical Southeast Atlantic Ocean (*Davey et al.*, 2002; *Richter et al.*, 2014), particularly strong near the ABF region. While mainly deficiencies in the atmospheric component have been suspected as source of the bias, *Xu et al.* (2014) argue that systematic errors in the ocean models are at least partly responsible for the biases seen in the coupled simulations. Poorly simulated subsurface thermal structures off Angola in combination with an overshooting AC near the ABF have been identified to cause erroneous southward advection of too-warm subsurface waters that are subsequently upwelled causing a warm SST bias in the northern Benguela. Nevertheless, a lack of in situ ocean observations within the boundary circulation and particularly the highly variable frontal region hampers a better understanding of the oceanic contribution to the biases in the region. The data sets presented in this study provide the opportunity for a first assessment of the performance of ocean reanalysis products upstream of the frontal region. Using the monthly output of five publically available reanalysis products (GODAS: 1995–2015, ORAS4: 1995–2014, SODA 2.2.4: 1995–2010, NCEP-CFSR: 1995–2010, NCEP-CFSv2: 2011–2015), we compare observed and simulated alongshore flow, AC transport, and temperature at the mooring array position at $\sim$11 °S (Figure 3.9). The reanalysis products agree in showing a weak mean southward current of 1–3 cm s^{-1} at the AC core depth in about 50 m depth (Figure

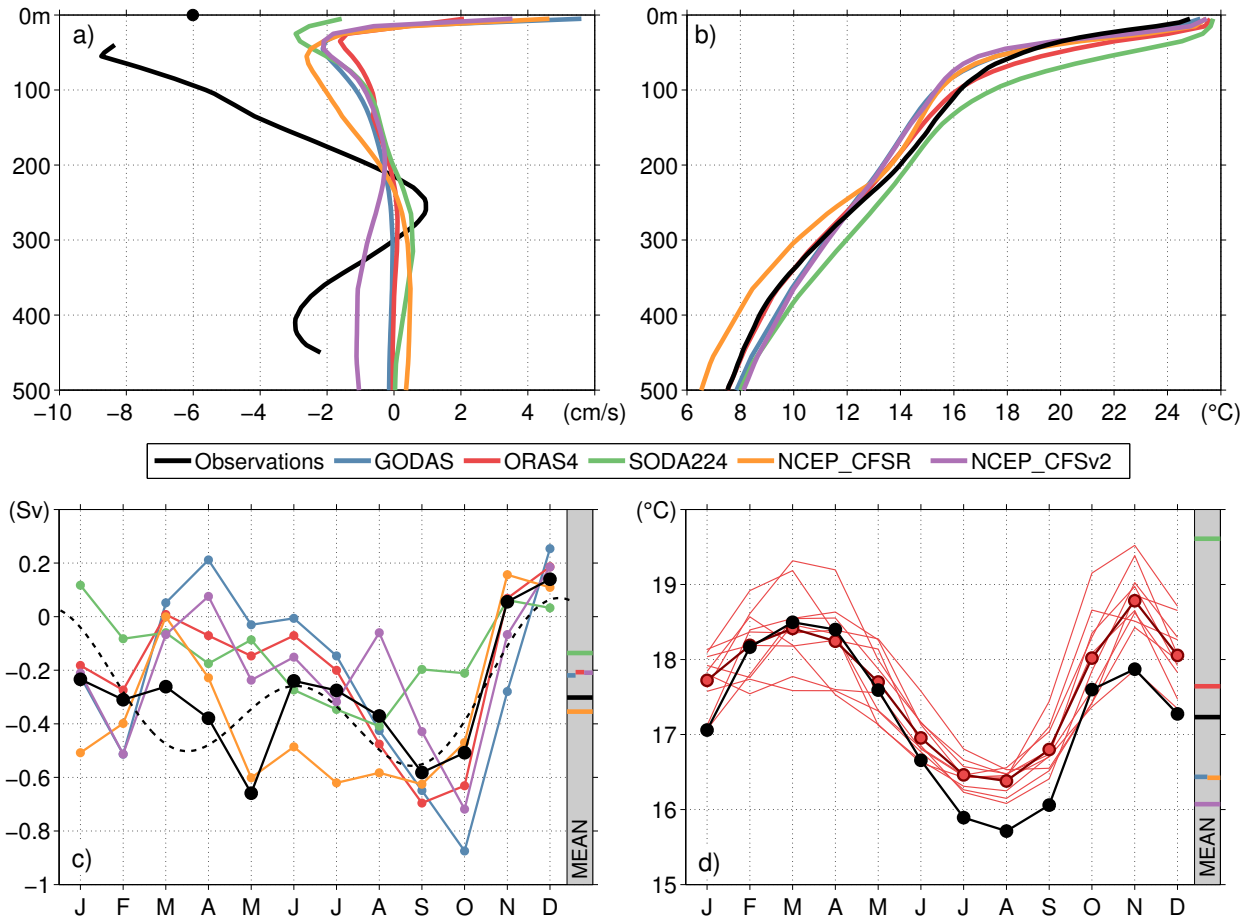

Figure 3.9: Profiles of (a) mean alongshore velocity and (b) potential temperature profiles from observations (black) and various reanalysis products (colors). Seasonal cycle of Angola Current transport from observations (black solid) and reanalysis products (colors) is shown in (c). Black-dashed line shows the sum of semiannual and annual harmonics from Figure 3.5b). Total mean AC transport values are indicated to the right. In (d) the mean seasonal cycle of potential temperature averaged over 50–100 m depth is shown for observations (black) and ORAS4 reanalysis (red). Thin red lines correspond to seasonal cycles derived from individual 2 year segments, while the bold red line shows the mean seasonal cycle derived from the total time series (1995–2014). Corresponding layer-averaged total mean values for both observations and reanalysis products are indicated to the right.

3.9a). However, it should be noted that by confronting these values with observations, point measurements are compared to model results obtained at a horizontal resolution in the range of 0.5–1 °. Therefore, the AC transport estimates from the reanalysis products are based on one or two grid points only. Nevertheless, the mean AC transports from the reanalysis products and observations are similar (Figure 3.9c), indicating that the simulated velocity at the model grid points correspond to the observed section mean velocity rather than the observed velocity at the mooring position. Regarding AC transport seasonality, most of the products reproduce the southward transport maximum in September/October as well as the subsequent decrease, while the second southward maximum in May is generally not captured. Note, that the observed seasonal cycle based on climatological monthly means shows a southward transport maximum in May, while the sum of semiannual and annual harmonics (from Figure 3.5b) suggests a secondary

transport maximum in March/April (black solid versus black-dashed line in Figure 3.9c). This underlines the uncertainty in the estimation of the mean seasonal cycle from the relatively short mooring time series due to the presence of strong intraseasonal fluctuations (Figure 3.5b). Only SODA 2.2.4 clearly reveals an erroneous downward displacement and weakened thermocline, while mean temperatures in GODAS, NCEP-CFSR, and NCEP-CFSv2 tend to be too cold in the AC depth range (Figure 3.9b). Note that all products show too warm near-surface temperatures, suggesting local warm SST biases. In terms of thermal structure ORAS4 appears to be closest to the observations, although showing also a slight downward displacement of the thermocline compared to our observations. The seasonal cycle of potential temperature averaged over the AC core range (50–100 m depth) indicates warm biases mainly during the upwelling seasons in ORAS4 (Figure 3.9d), whereas cold biases in NCEP-CFSR and NCEP-CFSv2 result mainly from a misrepresentation of the major downwelling season in austral autumn (not shown).

There is no indication of a strongly biased thermal structure at $\sim$11 °S in ocean reanalysis products. When comparing observed and simulated alongshore velocities, one has to consider the relatively low horizontal model resolution. Mean velocity profiles from the reanalysis products generally reproduce the observed vertical structure, yet with smaller amplitudes. The simulated velocities correspond rather to the observed section-averaged velocity than to the velocity observed at the mooring with the observed and simulated mean AC transports being similar. However, near the ABF an intensification and overshooting of the AC in similar reanalysis products is described that displaces the front southward and advects warm subsurface water into the northern Benguela (*Xu et al.*, 2014). If there is a local intensification of the AC near the ABF, it appears to be decoupled from the flow further upstream. Observations of processes in the frontal region contributing to cross-frontal exchange are crucial to improve our understanding of the origin of the bias in ocean simulations.

4 Eastern boundary circulation and hydrography off Angola – building oceanographic capacities in Southwestern Africa

The next chapter presents results from an extensive in-situ data set that was analyzed in the framework of a capacity building effort with an Angolan partner institute. The data was acquired within the EAF-Nansen program executed by the Food and Agricultural Organization of the United Nations and funded by Norwegian Agency for Development Cooperation. It provides hydrographic and current data acquired semiannually during the main downwelling and upwelling seasons on the Angolan continental margin covering more than 20 years. It facilitates the description of the mean seasonal structures of alongshore velocity, temperature, and salinity along the entire Angolan coastline. On interannual time scales the data allows the analysis of subsurface temperature anomalies that can be compared with satellite observations of SST with regard to Benguela Niño/Niña events in the last 20 years.

The manuscript is currently being finalized for submission in *Bulletin of American Meteorological Society*. The manuscript presented here is the version as of July 9th, 2017.

Citation: Tchipalanga, P. C. M., M. Dengler, P. Brandt, **R. Kopte**, M. Macuéria, P. Coelho, M. Ostrowski, and N. S. Keenlyside, 2017: Eastern boundary circulation and hydrography off Angola – building oceanographic capacities in Southwestern Africa. To be submitted to Bulletin of American Meteorological Society.

The candidate led the capacity building efforts concerning quality-control and post-processing of shipboard current data during two one-month stays of two respectively three Angolan scientists at GEOMAR. He analysed the post-processed velocity data as well as several satellite products, produced all figures except for figures 4.7, 4.8, and 4.11b. Furthermore, he led the authoring of Section 4.4 and contributed with ideas, discussion and comments to the other chapters of the manuscript.

4.1 Introduction

Angola is located at the Atlantic coast in Southwestern Africa between 5 °S and 17 °20′S with borders to Democratic Republic of Congo in the north and to Namibia in the south. Its coastline stretches over a distance of 1600 km. Due to seasonal upwelling occurring during austral winter in large parts of its coastal zone (Figure 4.1), the Angolan territorial waters represent a highly productive ecosystem. Coupled with a dense coastal population, it plays a key socioeconomical role in the country's development but faces important changes associated with climate variability and global change. Global climate change will particularly impact eastern boundary upwelling regions by a combination of different stresses: increasing temperatures, acidification, and deoxygenation (*Gruber et al.*, 2011). Currently, the fishing sector is third in importance to the national economy after the oil and mining industries and supplies about 25 percent of the total animal protein intake of the Angolan population (*Food and Agricultural Organization of the United Nations (FAO)*, 2014). The impacts of climate-scale variability on eastern boundary upwelling systems and consequently on their fish resources have become widely accepted in recent years (e.g., *Parrish et al.* (2000); *Lehodey et al.* (2006)).

The ocean currents off Angola represent a typical tropical eastern boundary circulation system dominated by the poleward flowing Angola Current (AC). Below the productive ocean surface, thermocline waters are depleted in oxygen concentrations and form one of the most pronounced oxygen minimum zones (OMZ) in the global ocean. Recent observations suggest that the oxygen content of the oceans and particularly in the south eastern Atlantic is declining and that oxygen minimum zones are expanding with some modulations related to the variability of our climate system (*Stramma et al.*, 2008; *Schmidtko et al.*, 2017). Predominately during austral summer, the AC is thought to transport warm, saline, low-oxygen South Atlantic Central Water (SACW) southward into the coastal upwelling region, possibly resulting in hypoxic to anoxic situations on the shelf (*Mohrholz et al.*, 2008; *Monteiro et al.*, 2008). In turn, the AC is suggested to be supplied by the eastward currents in the equatorial region (*Peterson and Stramma*, 1991; *Wacongne and Piton*, 1992; *Rouault et al.*, 2007).

Historically (see insert for a detailed description of the history of physical oceanography in Angola), knowledge of the velocity structure and transport of the AC at the Angolan coast had been gained exclusively from synoptic hydrographic data (*Moroshkin et al.*, 1970; *Dias*, 1983a,b; *Mercier et al.*, 2003). These earlier studies found geostrophic southward flow between the surface and 300 to 400 m depth having velocities between 30 cm s^{-1} and 50 cm s^{-1} and subsurface velocities of similar magnitude. Transport estimates of the AC determined by *Dias* (1983a) were 1.2 Sv and 3.7 Sv from data collected in September 1970 and July 1971, respectively. However, *Mercier et al.* (2003) reported an AC transport of 11 Sv from an inverse study. During a survey in April 1999 a secondary, offshore branch of southward subsurface flow was identified in shipboard velocity data separated from the coastal branch (*Mohrholz et al.*, 2001). Both pathways were characterized by southward velocities of about 40 cm s^{-1} below the surface. However, recent

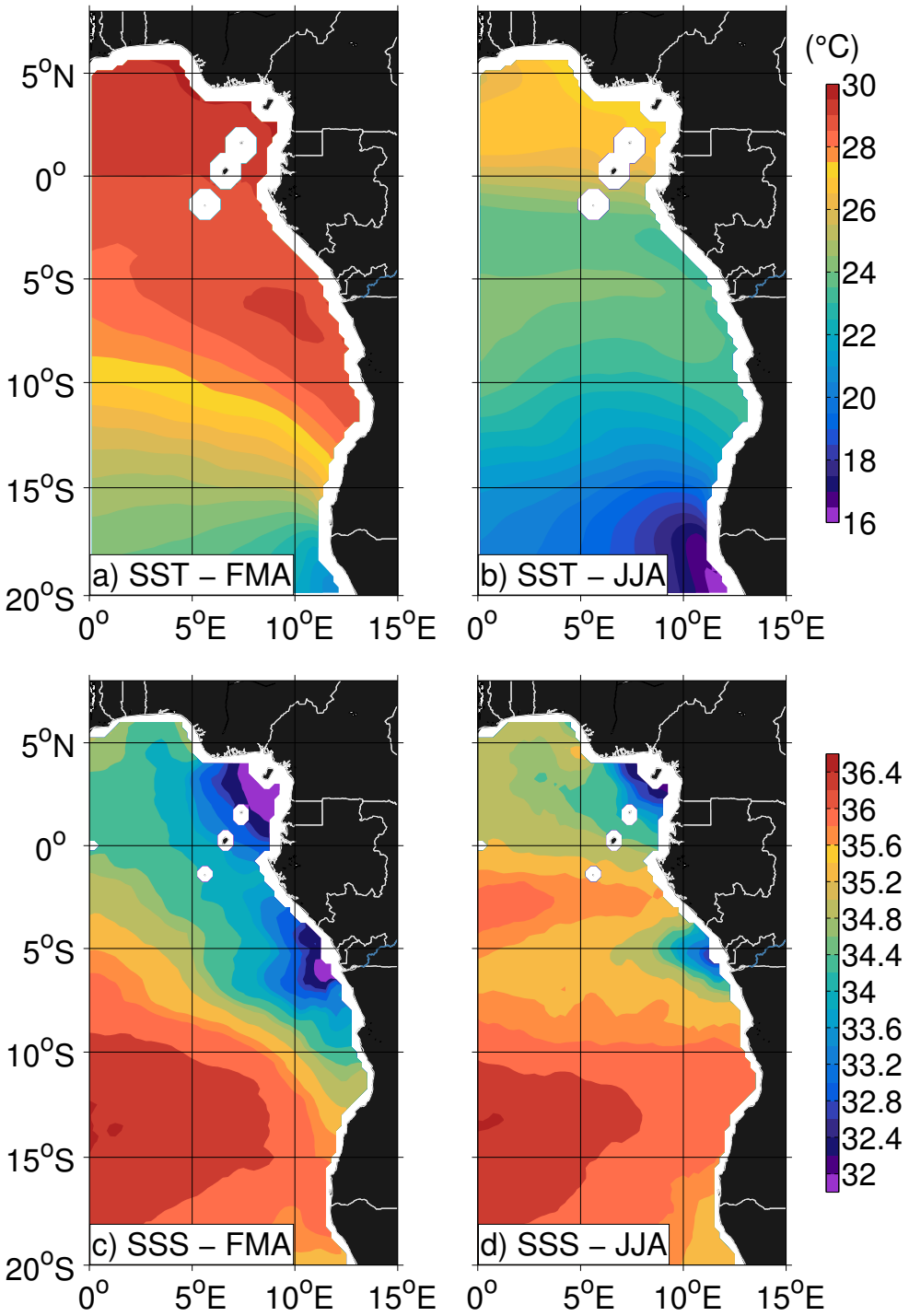

Figure 4.1: Average sea surface temperature and sea surface salinity in February through April (a, c) and in June through August (b, d) determined from Microwave Fusion OI SST (`www.remss.com`) and SMOS L3 v2 (`www.catds.fr`) satellite data, respectively.

direct multi-year velocity observations of the Angola Current by two moorings at 11 °S reveal that the alongshore flow is dominated by alternating periods of southward and northward velocities that can last for a couple of months with superimposed high-frequency velocity pulses (*Kopte et al.*, 2017). Contrary to the conclusions drawn from historical synoptic measurements, no steady southward flow of the AC is observed. Instead, the moored velocity time series of almost 2.5 years

duration showed strong seasonal variability with intraseasonal fluctuations superimposed, having magnitudes in agreement with previous synoptic measurements. However, the mean southward alongshore velocity of the AC in the moored records is weak, with maximum velocities between 5 and 8 cm s^{-1}, and extends from the surface down to about 200 m depth. Its variability in strength appears to be partly controlled by the passage of coastally trapped waves (CTW) (*Ostrowski et al.*, 2009; *Rouault*, 2012; *Kopte et al.*, 2017). These waves communicate equatorial oceanic variability along the continental margin of Angola to the northern Benguela upwelling region. From the analysis of satellite data, four CTW events per year were described to propagate along the southwest coast of Africa as far south as 20 °S (Figure 4.2) (*Schouten et al.*, 2005; *Lazar et al.*, 2006; *Kopte et al.*, 2017). The first downwelling (high sea level) equatorial Kelvin wave and subsequently CTW arrives at the Angolan coast in March, followed by an upwelling (low sea level) CTW in June-July. The second cycle begins with downwelling in October and ends with a weak upwelling signal in December–January.

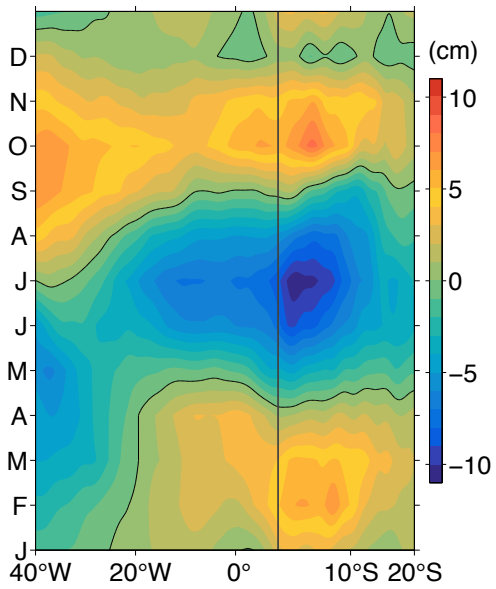

Figure 4.2: Hovmöller diagram of the mean annual cycle of sea level anomaly showing the propagation of upwelling (June) and downwelling (October, February) Kelvin waves (September, December) from west to east along the equator. The equatorial Kelvin wave signal is then carried southward along the eastern boundary by coastally trapped waves. The vertical black line separates the region of eastward propagation along the equator to the left and the region of southward propagation along the coast to the right.

Between 15 °S and 18 °S, the Angola-Benguela Front represents a sharp but variable thermal front, separating tropical, oligotrophic waters to the north from cold, nutrient-rich waters in the south (*Shannon et al.*, 1987; *Lass et al.*, 2000). Across-front temperature differences range from 5 °C to 8 °C. The front fluctuates in position and strength on time scales from intraseasonal (*Kostianoy and Lutjeharms*, 1999; *Mohrholz et al.*, 2001; *Goubanova et al.*, 2013; *Diakhaté et al.*, 2016), annual (*Meeuwis and Lutjeharms*, 1990), to interannual. Interannual variability is often associated with severe warm and cold events during austral summer termed Benguela Niños and Benguela Niñas, respectively (*Shannon et al.*, 1986; *Florenchie et al.*, 2004), in reference to poleward advection of warm waters along the Peruvian coastline during El Niño or enhanced upwelling during La Niña. Benguela Niños are marked by a poleward intrusion of warm equatorial water and reduced upwelling (Figure 4.3). These events are known to have a strong impact on the strength of primary productivity, fisheries, hypoxia and rainfall in the region (e.g. *Rouault et al.* (2007)).

In the past, very little data from field surveys along the Angolan continental margin have been analyzed and published. In fact, due to the lack of publically available data, even widely used ocean reanalysis data, such as simple ocean data reanalysis (SODA) (*Carton and Giese*, 2008) and hybrid coordinate ocean model reanalysis (HYCOM) (*Chassignet et al.*, 2007) show large

biases in the hydrographic data (*Xu et al.*, 2014). Furthermore, due to the lack of observations, understanding of the circulation and its variability is hardly developed and the lack of data and process understanding prohibits satisfactory evaluation of model simulations. However, as described below, it is not that field campaigns in Angolan territorial waters had not been undertaken.

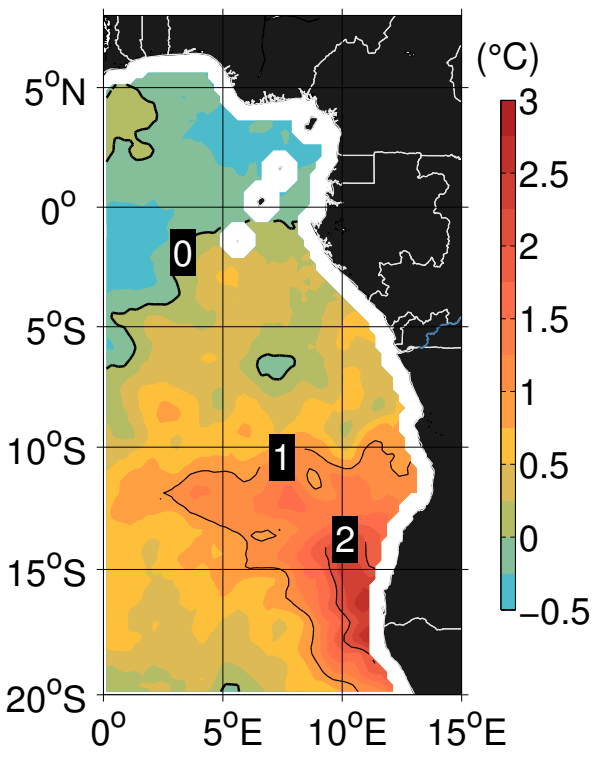

Figure 4.3: Sea surface temperature anomaly during the Benguela Niño event in February 2011 derived from Microwave Fusion OI SST (`www.remss.com`) satellite data. The temperature anomaly was calculated relative to the mean seasonal cycle.

On the other hand, there is a tremendous social and economic interest within the southern African community in the prediction of intraseasonal to interannual rainfall variability. Particularly the Angola Low, a convective hotspot situated over southern Angola/northern Namibia during austral summer, is the source region of the tropical-extratropical cloud bands that bring most of the summer rainfall to subtropical southern Africa. *Reason and Jagadheesha* (2005) demonstrated a link between this land-based convection and winds over the tropical Southeast Atlantic and a dependence on the El Niño/Southern Oscillation phases. However, the prediction of interannual variability as well as of the response to climate change are strongly limited by the presence of an exceptionally large bias of the sea surface temperature in the eastern tropical South Atlantic region in state-of-the-art coupled ocean-atmosphere models (*Wahl et al.*, 2011; *Toniazzo and Woolnough*, 2014; *Zuidema et al.*, 2016). Furthermore, warm sea-surface temperature (SST) biases in the southeastern tropical Atlantic are a common problem in many state of the art and previous generation climate models (e.g. *Toniazzo and Woolnough* (2014); *Xu et al.* (2014)).

The layout of the paper is as follows: We start with a description of the EAF Nansen program providing the database used here (Section 4.2). The further description of observational efforts includes a section about the capacity building efforts in Angola in Section 4.3 as well as an insert about the history of physical oceanography in Angola. Main results of our study are presented in two sections related to the eastern boundary circulation off Angola (Section 4.4) and the interannual variability of hydrography (Section 4.5), before a summary with discussion completes our study.

4.2 The EAF Nansen program

The idea of committing a research vessel to assist newly independent countries in assessing their fish resources dates back to 1960s in Norway. It substantiated a decade later when the Government of Norway and the Food and Agriculture Organisation of the United Nation (FAO) established the Nansen Programme. The first research vessel, named *Dr. Fridtjof Nansen*, was launched in 1974. Since then she and her two successor vessels with the same name (launched in 1994 and 2017, respectively), continue until today to support fisheries and, more recently, ecosystem research and monitoring in developing countries around Africa and elsewhere (*Bianchi et al.*, 2016).

In the Angolan territorial waters, the fish monitoring surveys by RV *Dr. Fridtjof Nansen* have been carried out since 1985 and since 1994 on a regular semiannual basis. The swept area trawl and acoustic fish census surveys dominated the survey designs and data collection (*Saetelsdal et al.*, 1999). Notwithstanding, hydrographic and velocity data from the shipboard acoustic Doppler current profile (ADCP) were also acquired during the cruises.

The semiannual cruises were scheduled during austral summer (February through April) and winter (June through August). Between March 1994 and March 2015, a total of 8818 conductivity-

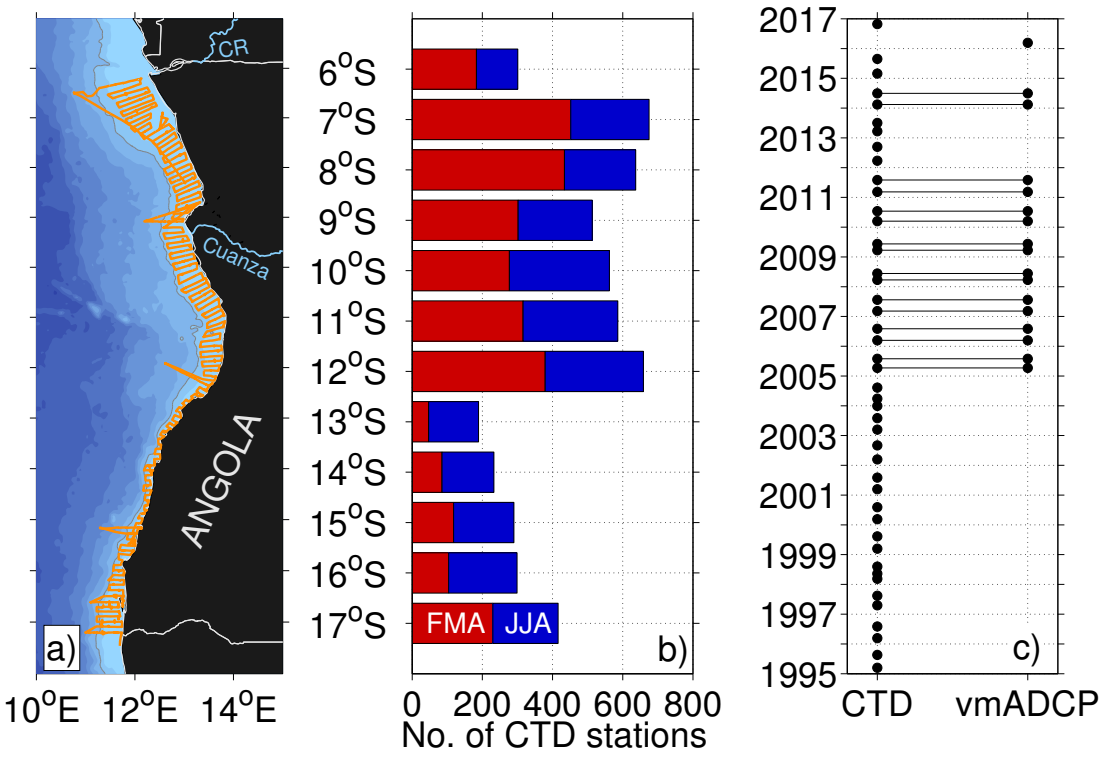

Figure 4.4: (a) Exemplary cruise track of RV *Dr. Fridtjof Nansen* as carried out during June 2014 off the coast of Angola indicating also the location of Nansen monitoring lines. (b) Latitudinal distribution of CTD profiles collected within the EAF-Nansen program between 1995 and 2016 divided in austral summer (red) and austral winter (blue). (c) Timeline of CTD and shipboard ADCP measurements acquired within the EAF-Nansen program.

temperature-depth (CTD) profiles were collected on the shelf and the continental slope off spread along the entire Angolan coast (Figure 4.4b and c). Furthermore, shipboard ADCP measurements from a 150 kHz Ocean Surveyor are available since 2005, and regularly repeated monitoring lines along 6 °S, 9 °S, 12 °S, 15 °S, and 17 °S were established.

By virtue of the Nansen Programme data policies, all collected data had been transferred to and are exclusively owned by the country in which the survey was conducted. As capacities to post-process and interpret the recorded oceanographic data sets in Angola had not been available in the past, the hydrographic and velocity data remained largely unpublished to date.

4.3 Capacity building efforts

Developing sustained cooperation between Angolan and European partners is an integral component of many EU-funded and national-funded programs focusing on ocean research in the Benguela upwelling region. Enhancing capacities in Marine Science in the African countries will improve long-term cooperation and is thus pivotal to the success of cooperative projects. Capacity building in fisheries research and management has been long-term focus of the Nansen Programme and other bilateral cooperation projects between Norway and Angola (*Bianchi et al.*, 2016). However, Angola has also recognized the need for development of local expertise in physical oceanography and its impacts on ecosystem and fisheries dynamics. To address this need, a capacity building program involving training of Angolan scientists and educating students in these two disciplines has been implemented in the frame of the EU PREFACE project. It is jointly developed by Instituto Nacional de Investigação Pesqueira (INIP), Helmholtz-Centre for Ocean Research Kiel, Germany (GEOMAR), Institute for Marine Research Norway (IMR), University of Kiel, Germany (CAU) and University of Cape Town (UCT), South Africa. The program was composed of four elements including (1) training of Angolan scientists at European partner institutions during month-long visits and during surveys of research vessels (2) education of scientists, graduate students and PhD students during summer schools held in African countries (3) short courses for students lectured by European scientists at INIP; (4) collaborative studies for scientists and education for graduate students at the Nansen - Tutu Centre in South Africa.

A central objective of the capacity building program was to scientifically exploit the extensive oceanographic data set from the repeat measurements of the Nansen Programme residing in the hands of Angolan scientists. Training of Angolan scientists focused on calibration and analysis of the data sets at hand. Furthermore, Angolan scientists have maintained fixed oceanographic station at several locations along the Angolan coast (Luanda, Lobito, Ambriz and Moçâmedes - named Namibe between 1985 and 2016). These time series data have neither been quality-controlled nor disseminated. Capacity building efforts thus include quality-control algorithms and data dissemination strategies. Finally, mid-sized research vessels are currently maintained by INIP, but technical skills in instrumental servicing is low. Training of Angolan scientists thus

involved education in strengthening technical skills related to oceanographic instrumentation during recently conducted research cruises.

Sustained long-term involvement in Marine Science capacity building by European scientists beyond the time line of recent programs such as EU-PREFACE, BMBF-SACUS and other currently funded projects is urgently required.

History of Physical Oceanography in Angola

The German Meteor Expedition 1925-1927 might be considered as starting point of physical oceanography studies off Angola. This survey included two trans-Atlantic transects with an inserted port call in Moçâmedes in southern Angola. The observational program included hydrographic measurements providing a general picture of the tropical and South Atlantic water mass and oxygen distribution (*Wüst*, 1935; *Wattenberg*, 1938). A first detailed hydrographic survey off Angola and northern Namibia was carried out by the USSR RV *Akademik Kurchatov* between April and June 1968. The obtained data was used for a first description of the eastern boundary circulation (*Moroshkin et al.*, 1970). At about the time the "Portugal Navy and Bio-oceanographic Fisheries Studies of Angola Institute" was established (MEBPA) which later became the National Research Fisheries Institute (Instituto Nacional de Investigação Pesqueira, INIP). INIP responsibilities included acquisition of oceanographic data at fixed stations, along monitoring lines, and during coastal surveys. Two research vessels, RV *Goa* and RV *Sardinella*, were employed. Starting in 1967, a transect at about 12 °S across the continental slope and shelf were taken 4 to 6 times per year, yielding a first estimate of seasonal variability of the boundary circulation (*Dias*, 1983a). A systematic study covering the shelf of southern Angola started in 1968 with three cruises of RV *Goa* per year. Daily data acquisition was performed at the Lobito time series station (12 °19′S, 13 °35′E) at about 40 m water depth. These measurements, including several physical and biogeochemical parameters, started in 1968, stopped in 1975 and were restarted in 1978. They are running until today, although showing many gaps and a general reduction in the parameter range compared to the early measurements. Early data were used to demonstrate the seasonal march of temperature indicating the presence of primary and secondary upwelling and downwelling seasons off Angola (*Berrit and Dias*, 1977). Similar time series stations were established at 13 °45′S (Santa Marta) and 15 °S (Moçâmedes), both discontinued in 1975.

The turmoil of the war for independence in 1975 saw the most difficult period in the history of the Angolan oceanography. Most of the infrastructure, instruments and equipment were lost and much of the collected literature, reports and data were dispersed. Notwithstanding, some sporadic research surveys were still taking place carried out either with the RV *Goa* or with Cuban and USSR research vessels.

The arrival of the Nansen Programme to Angola in the mid-eighties marked the beginning of new era in the monitoring of the Angolan coastal ocean and its living resources. The surveys with the RV *Dr. Fridtjof Nansen* were first conducted in 1985. Since 1994, these surveys have been carried out twice annually, in February/March and July/August, covering the entire extent of the Angolan continental shelf.

The regional cooperation among Angola, Namibia and South Africa was improved through the programs BENEFIT (Benguela Environment Fisheries Interaction & Training, 1999-2009) and BCLME (Benguela Current Large Marine Ecosystem, 2002-2008 – Now Benguela Current Commission, BCC), which particularly addressed climate variability with extreme environmental events, including the sustained warming of the ocean also called Benguela Niños. Under the umbrella of BENEFIT, several research cruises with German RV *Poseidon*, *Meteor*, *Petr Kottsov*, and *A. v. Humboldt* and the South African RV *Africana* were carried out. Also a new monitoring program was established along a section off Moçâmedes with 11 surveys completed until now and still ongoing. Different bilateral agreements allowed frequent visits by research vessels from different countries, mostly from Germany, Spain, Portugal, Great Britain, Russia and Cuba.

More recently, the NansClim project (2009-2014) was implemented between Norway, Angola, Namibia, and South Africa (*Jarre et al.*, 2015). By using data collected through the Nansen Program and other relevant regional data, the project aims at studying ocean and climate variability and corresponding changes in marine biodiversity. The cooperation between Germany, Angola, Namibia, and South Africa was fostered through GENUS (Geochemistry and Ecology of the Namibian Upwelling System, 2009-2015) and SPACES (Science Partnerships for the Assessment of Complex Earth System Processes, 2012-2018) programmes including additional cruises with RV *Maria S. Merian* and *Meteor* as well as first direct velocity observations from moorings in the Angola Current (*Kopte et al.*, 2017). The latter was performed also in cooperation with the EU PREFACE (Enhancing prediction of Tropical Atlantic climate and its impacts, 2013-2017) project having 28 partners across 18 countries in Europe and Africa.

4.4 Eastern boundary circulation and hydrography off Angola

Upper ocean velocity data acquired with RV *Dr. Fridtjof Nansen*'s 150-kHz Ocean Surveyor between 2005 and 2016 for the first time allow a description of the large-scale characteristics of the eastern boundary circulation off Angola. As the cruises have been carried out on a quasi-regular semiannual basis, the dataset facilitates the comparison of the mean current structure along the Angolan coast during the main downwelling and upwelling periods in February through April and June through August, respectively (Figure 4.5).

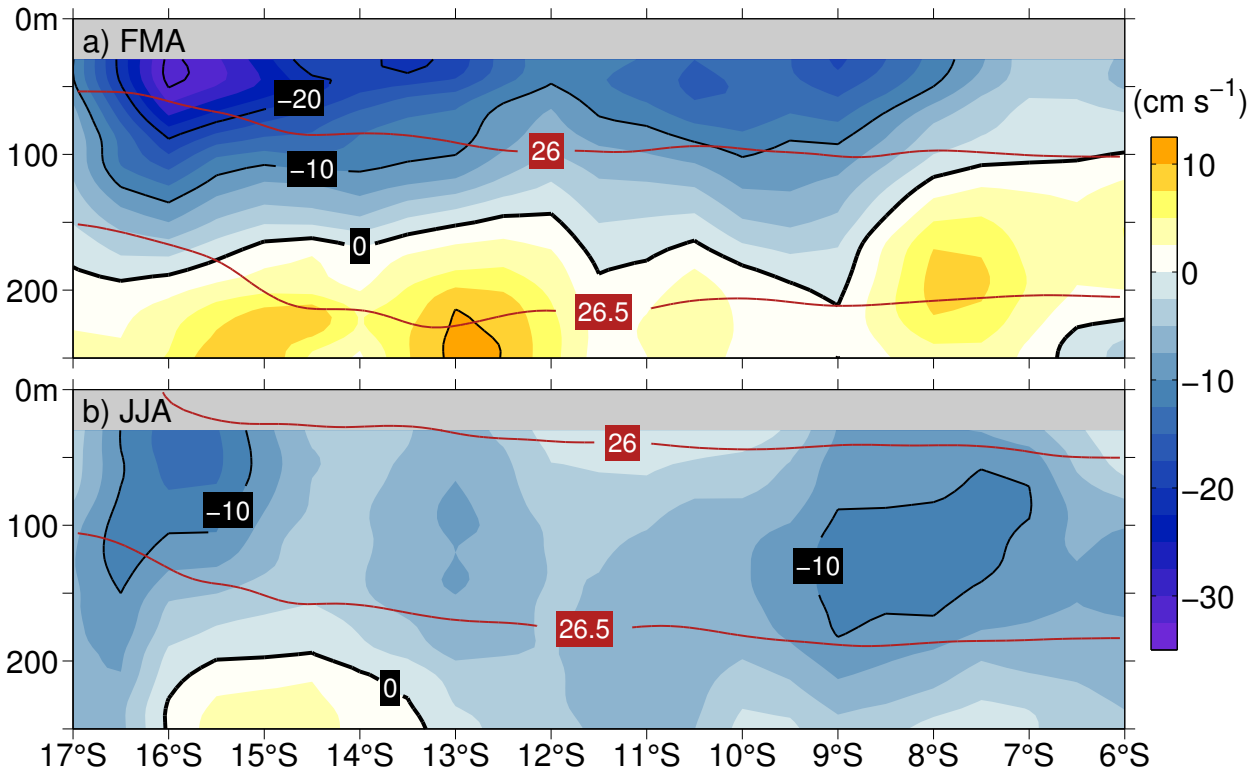

Figure 4.5: Average alongshore velocity (cm s^{-1}) during austral summer (a, February through April) and austral winter (b, June through August). Negative alongshore flow indicates poleward velocities. Mean alongshore velocity components were calculated by averaging all velocity data acquired in the depth range between 100 m and 1000 m depth. The local orientation of the shelf break was used to determine the along-shore flow component. Altogether upper ocean velocity data from 17 EAF Nansen cruises were used, 9 were conducted during summer and 8 during winter.

During the main downwelling period in austral summer, the Angola Current is restricted to the upper 120 m in the north and gradually deepens to 200 m depth at 17 °S south. Below the Angola Current, a weaker northward return flow is observed. Maximum poleward velocities exceeding 30 cm s^{-1} are found just north of the Angola-Benguela Front at 16 °S and the flow generally strengthens downstream. This downstream flow divergence illustrates that the water masses carried poleward cannot solely be supplied from the north. Entrainment of waters from offshore must occur, perhaps as part of an offshore recirculation cell. This entrainment is also supported by the downstream shoaling of isopycnals (Figure 4.5a). During austral winter poleward velocities of the Angola Current do not exceed 15 cm s^{-1}. However, the poleward flow extends to greater depth (Figure 4.5b).

The seasonal differences in the strength and vertical structure of the current are most likely explained by coastal trapped waves (Figure 4.2) (e.g. *Rouault et al.* (2007); *Ostrowski et al.* (2009); *Kopte et al.* (2017)). The passage of the semiannual downwelling CTW in austral winter causes enhanced poleward flow. In contrary, the semiannual upwelling CTW weakens poleward flow during June through August.

Seasonally averaged velocity profiles from a current meter array installed at the continental

slope near 11 °S between July 2013 and October 2015 (*Kopte et al.*, 2017) compare well with the corresponding velocity profiles extracted at the mooring positions (Figure 4.6). The seasonal differences in maximum southward velocity and the baroclinic structure of the mean vertical velocity profiles are consistently reproduced by the independent data set. However, the generally stronger flow in the shipboard observations representing the period from 2005 to 2016 suggests that the period of moored observations from 2013 to 2015 might correspond to a period of an anomalous weak Angola Current.

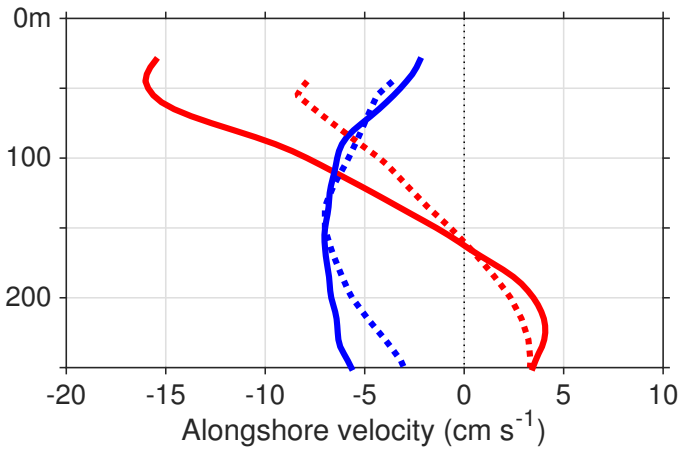

Figure 4.6: Mean profiles of alongshore velocity near 11 °S off Angola for austral summer (February through April, red) and austral winter (June through August, blue) derived from vessel-mounted ADCP data (solid, 2005 to 2014) and moored ADCP data (dashed, July 2013 to October 2015).

CTD data from the Nansen cruises were used to construct average hydrographic sections for the austral summer and winter seasons. All Nansen CTD profiles collected in water depths deeper than 100 m but restricted to a coastal band extending to 0.6 ° offshore of the 100 m-isobath were incorporated into the analysis. Due to the stretched shelf north of 8 °S, the longitude range for averaging was enlarged extending to 1.5 ° offshore of the 100 m-isobath for this northernmost region. Between 1995 and 2016, more than 5700 CTD profiles complied with these specifications. The total number of profiles is distributed nearly equally between the summer and winter season (Figure 4.4b).

During austral summer temperatures in the near-surface layer are above 20 °C along the entire section (Figure 4.7a), while a shoaling of isotherms is observed during austral winter along with an outcropping of the 20 °C-isotherm at about 12.5 °S (Figure 4.7b). During austral summer a thin surface layer with temperatures exceeding 25 °C and salinities below 35 spreads south as far as 13 °S (Figure 4.7a and Figure 4.8a). This surface layer is completely absent in austral winter (Figure 4.7b and Figure 4.8b). Likewise, the upper thermocline, represented by the density range between $\sigma_\theta = 26.0\,\mathrm{kg\,m^{-3}}$ and $\sigma_\theta = 26.5\,\mathrm{kg\,m^{-3}}$, undergoes seasonal variations in depth. The outcropping of the 26.0-isopycnal at the southern edge of the section during austral winter (Figure 4.7b, Figure 4.8b) is an indicator for the seasonal march in latitude of the Angola-Benguela frontal zone (*Meeuwis and Lutjeharms*, 1990). Below the thermocline only minor changes in the water mass composition are found between the seasons. The near-constant water mass composition in the central water layer with regard to the seasonal cycle has been noted also by *Kopte et al.* (2017).

Associated with the seasonal changes in temperature and salinity, there is a substantial variability in the stratification represented by the buoyancy frequency in Figure 4.9. Near-surface

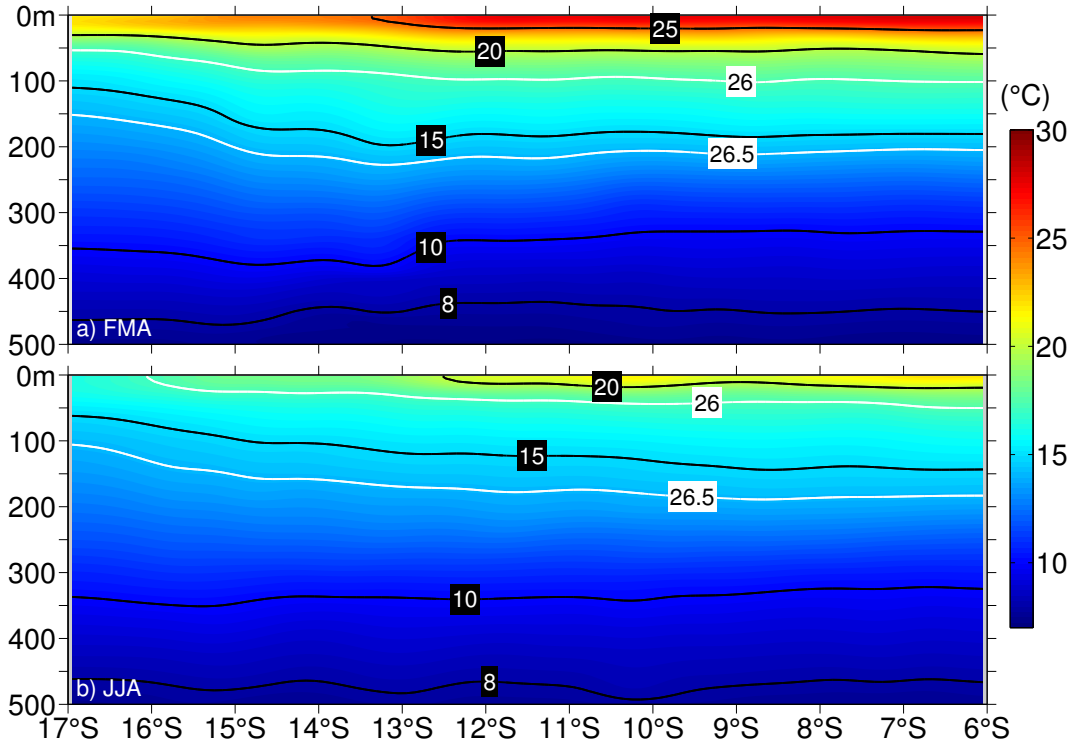

Figure 4.7: Latitude-depth distribution of temperature along the continental margin of Angola during austral summer (a) and austral winter (b).

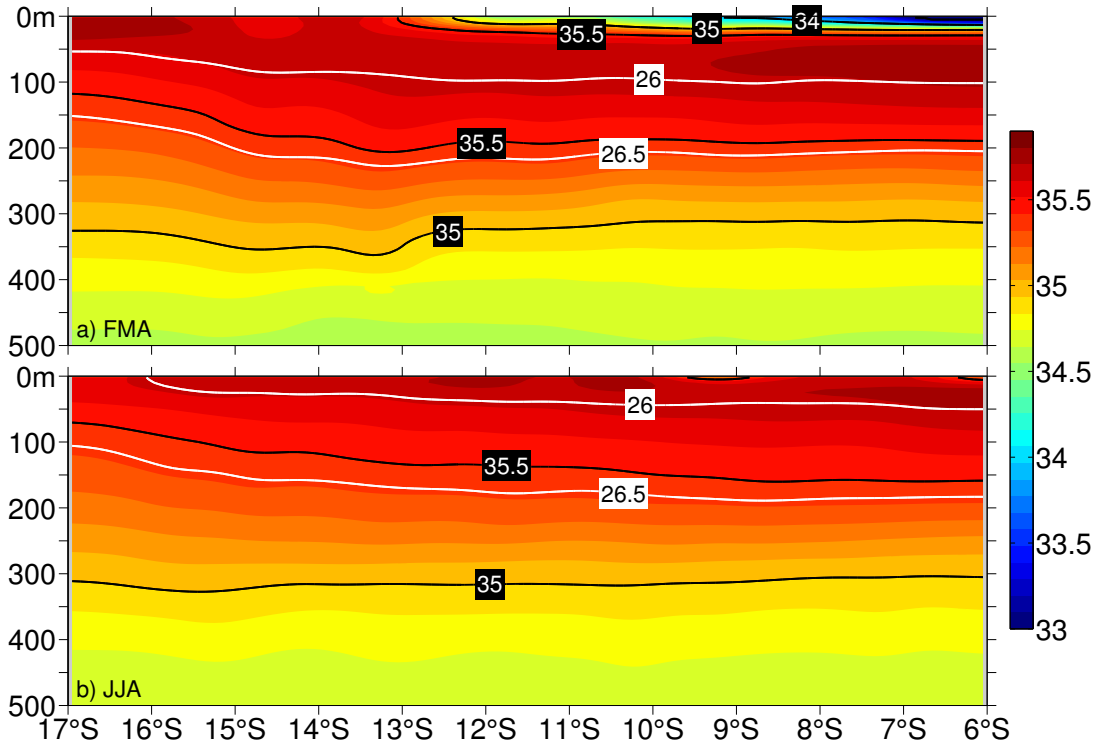

Figure 4.8: As Figure 4.7, but for salinity.

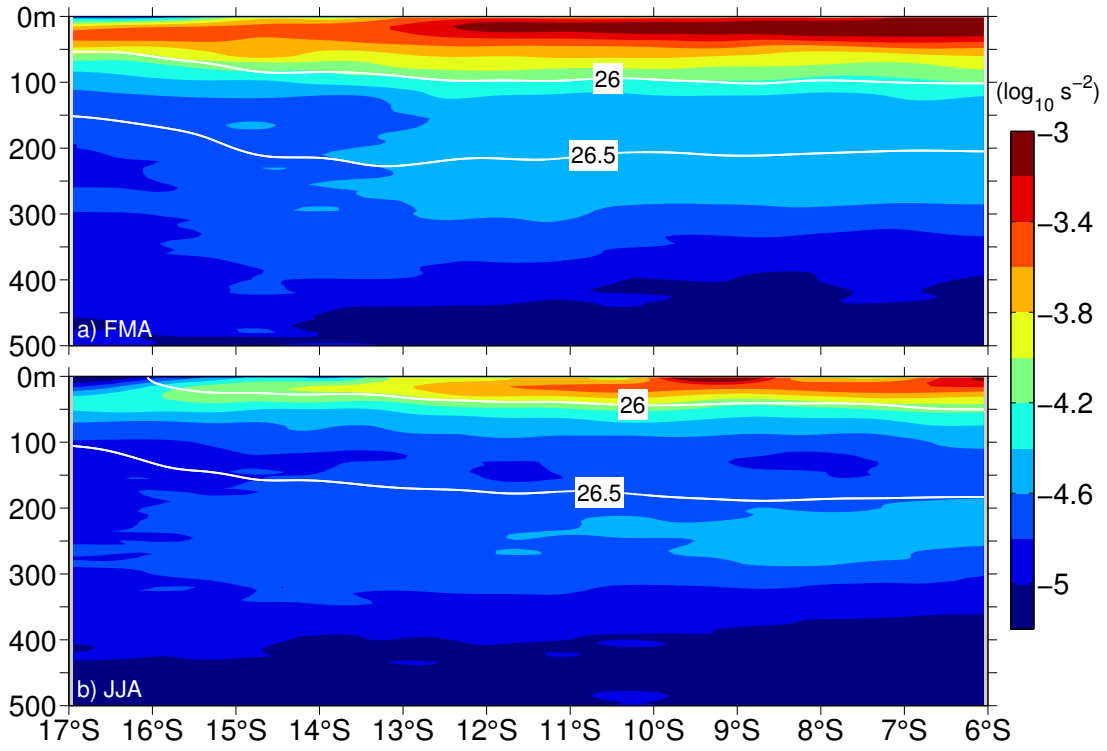

Figure 4.9: As Figure 4.7, but for $\log_{10}$ of buoyancy-frequency squared (N^2).

stratification is an important parameter for the supply of nutrients to the euphotic zone by turbulent mixing processes, with increased stratification during austral summer acting to suppress mixing. Moreover, the seasonal changes of upper-ocean stratification also plays a crucial role for the amount of tidal energy transmitted onto the shelf by internal waves due to tide-topography interaction at the continental slope (e.g. *Hall et al.* (2013); *Lamb* (2014)). Internal wave related mixing processes on the continental slope and shelf are thought to represent a critical physical controlling factor for productivity in Angolan waters (*Ostrowski et al.*, 2009).

Exemplary upper-ocean cross-shore sections of alongshore velocity averaged between 10 °S and 12 °S (Figure 4.10) show the core of the Angola current between 50 and 60 km offshore during both seasons. This distance roughly corresponds to the 500 m-isobath. The flow is stronger and confined to shallower depths during austral summer while it is and weaker but deeper reaching during austral winter (Figure 4.10a, b). Temperature and salinity as well as stratification across this section are rather uniformly distributed. The warm, low salinity surface layer is found throughout the section during austral summer (Figure 4.10c, e), which is absent during austral winter (Figure 4.10d, f). Near-surface isopycnals show some indication of down- and upwelling. During austral summer, these isopycnals are bended downwards toward the shore suggesting downwelling, while during austral winter the same isopycnals are tilted upwards as they approach the shore, indicating upwelling.

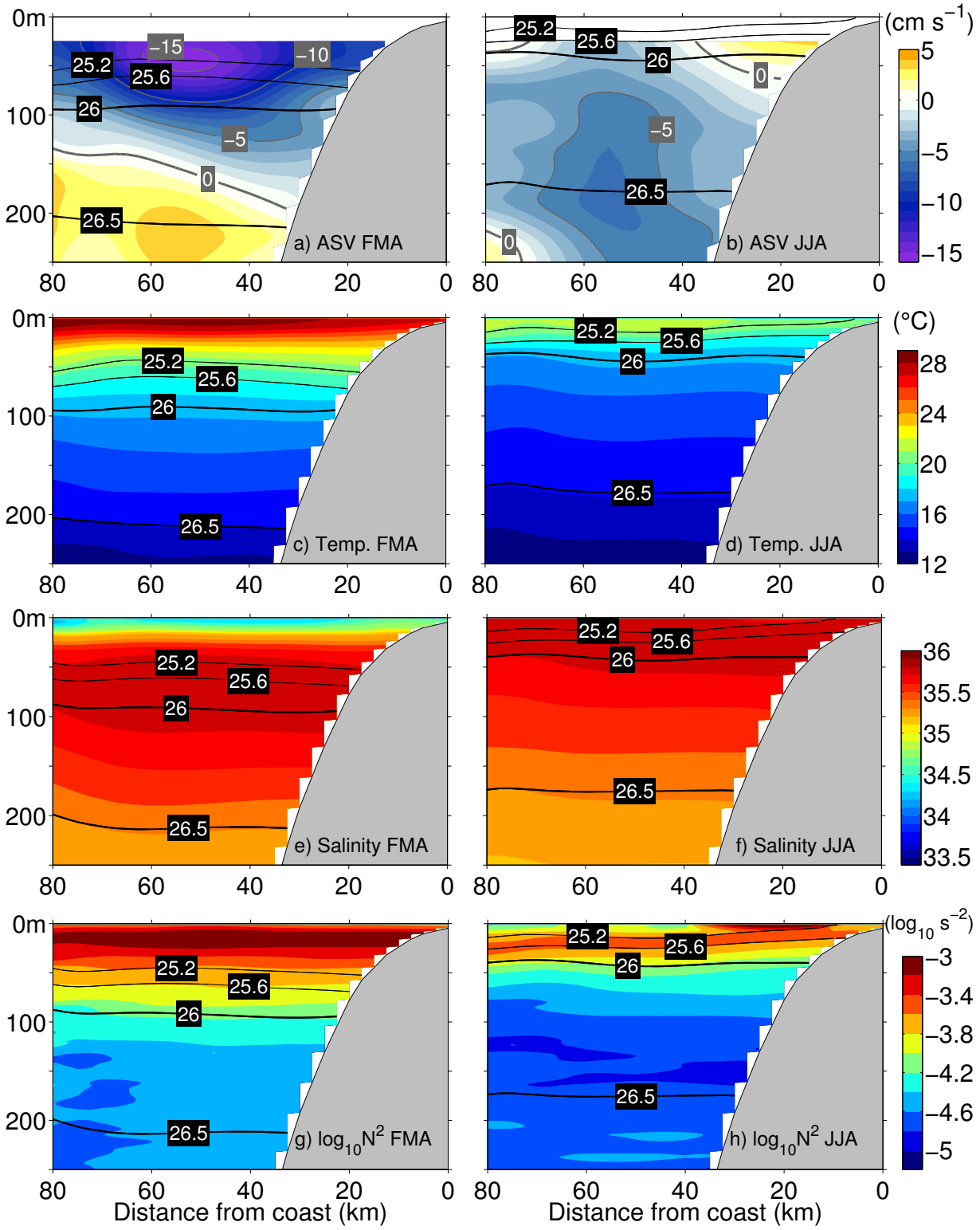

Figure 4.10: Average sections of alongshore velocity (ASV, a and b), temperature (c and d), salinity (e and f), and $\log_{10}$ of buoyancy-frequency squared (g and h) for austral summer (left column) and austral winter (right column) calculated from all available Nansen data between 10 °S and 12 °S.

4.5 Interannual variability of hydrography

Local temperature anomalies calculated on isopycnals can be used to analyze the presence of different central water masses in the upper thermocline. The South Atlantic Central Water (SACW) and the fresher but well-oxygenated Eastern SACW (ESACW) are the two main central water masses found off the southwest African coast. SACW is formed in the subtropical convergence of the Brazil-Malvinas Confluence Zone (*Poole and Tomczak*, 1999). On its way through the South Atlantic subtropical gyre and the equatorial current system towards the Angola Gyre the properties of SACW are constantly altered. Continuous remineralization of organic matter causes oxygen depletion and nutrient enrichment. Furthermore, weak entrainment of North Atlantic Central Water (NACW) within the equatorial current system modifies the properties of SACW (*Poole and Tomczak*, 1999). To account for these en route modifications of SACW, *Mohrholz et al.* (2008) defined an Angola Gyre subtype of SACW that finally is advected poleward towards the northern Benguela by the Angola Current. ESACW originates in the Cape Basin and represents a mixture of SACW from the subtropical gyre and Indian Central Water that is transferred to the South Atlantic by the Agulhas Current (*Mohrholz et al.*, 2008). From its source region ESACW is transported northward along the Southwest African shelf by the Benguela Current.

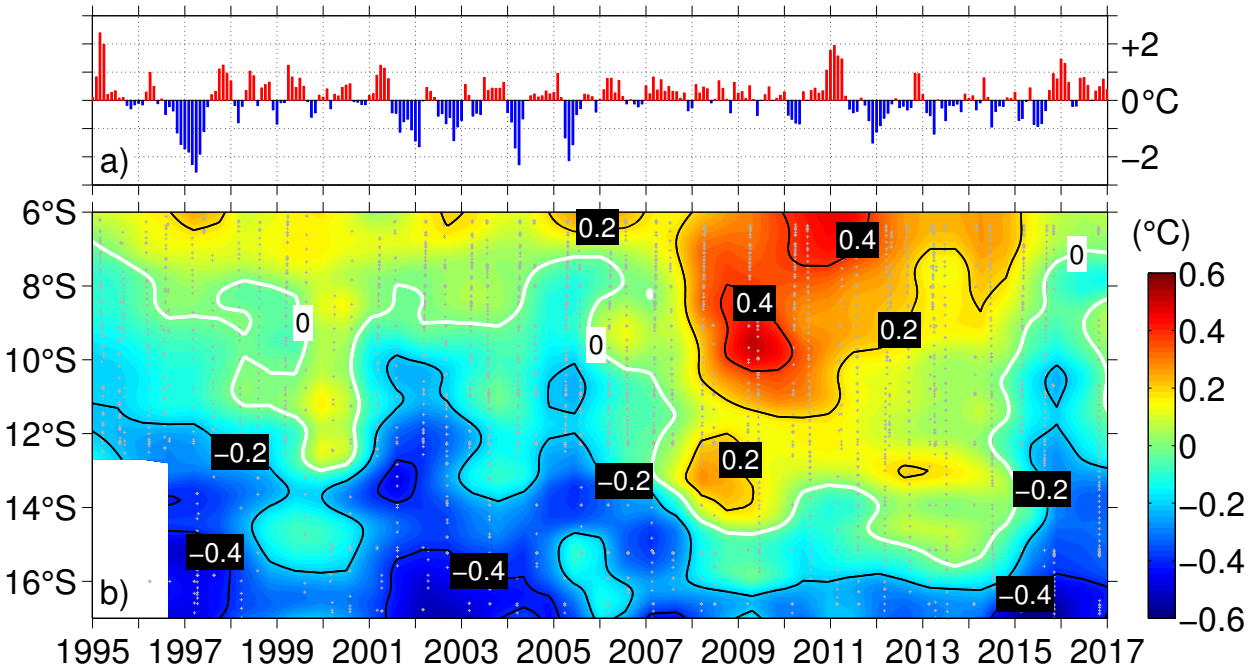

Figure 4.11: (a) Angola Benguela Area (ABA) SST Index from 1995 to 2017 determined from NOAA-OISST (V2) data. SST is averaged between 10 °S and 20 °S and east of 8 °E. The anomaly is calculated relative to the mean seasonal cycle. (b) Interannual variability of temperature anomaly along the continental slope off Angola in the upper thermocline. Temperature was averaged between the isopycnal $\sigma_\theta = 26.0\,\mathrm{kg\,m^{-3}}$ and $\sigma_\theta = 26.5\,\mathrm{kg\,m^{-3}}$. Altogether, 2987 CTD and uCTD profiles collected from March 1995 to November 2016 were used. The depth of the upper and lower isopycnal boundary varies between 0 and 100 m and between 80 and 250 m, respectively. Average isopycnal depths are indicated in Figure 4.7-9.

The CTD data collected during 24 RV *Dr. Fridtjof Nansen* cruises and three RV *Meteor* cruises along the Angolan continental margin from March 1995 to November 2016 exhibit elevated interannual to decadal variability of heat and salt content in the upper thermocline (Figure 4.11b). Warmer water masses were found further to the south between 1999 and 2001 as well as between 2008 and 2013, while colder water masses, likely associated with enhanced contributions of ESACW, were displaced further to the north between 1996 and 1998, from 2002 to 2006 and since 2015.

These warm and cold anomalies in the upper thermocline have some similarities with anomalies of the sea surface temperature in the Angola-Benguela area (20 °S to 10 °S, 8 °E to 15 °E) (Figure 4.11a). Often, thermocline anomalies precede the respective sea surface temperature signal. The known Benguela warm events in 2001 and 2011 are well represented in the subsurface data and occurred during anomalous warm temperatures in the upper thermocline. Similarly, the thermocline was anomalously cold during the Benguela Niña event in 1996. Notably, the presence of a subsurface warm anomaly present two years before Benguela Niño in 2011 suggests that thermocline heat anomalies may serve as a preconditioning for the occurrence of Benguela Niños/Niñas. However, during the Benguela Niño in 1995, right at the beginning of our time series, no similar positive heat anomaly in the upper thermocline was observed. This may suggest different roles of subsurface temperature anomalies during the preconditioning, evolution and mature phase of specific Benguela Niñas. A possible explanation of the elevated interannual

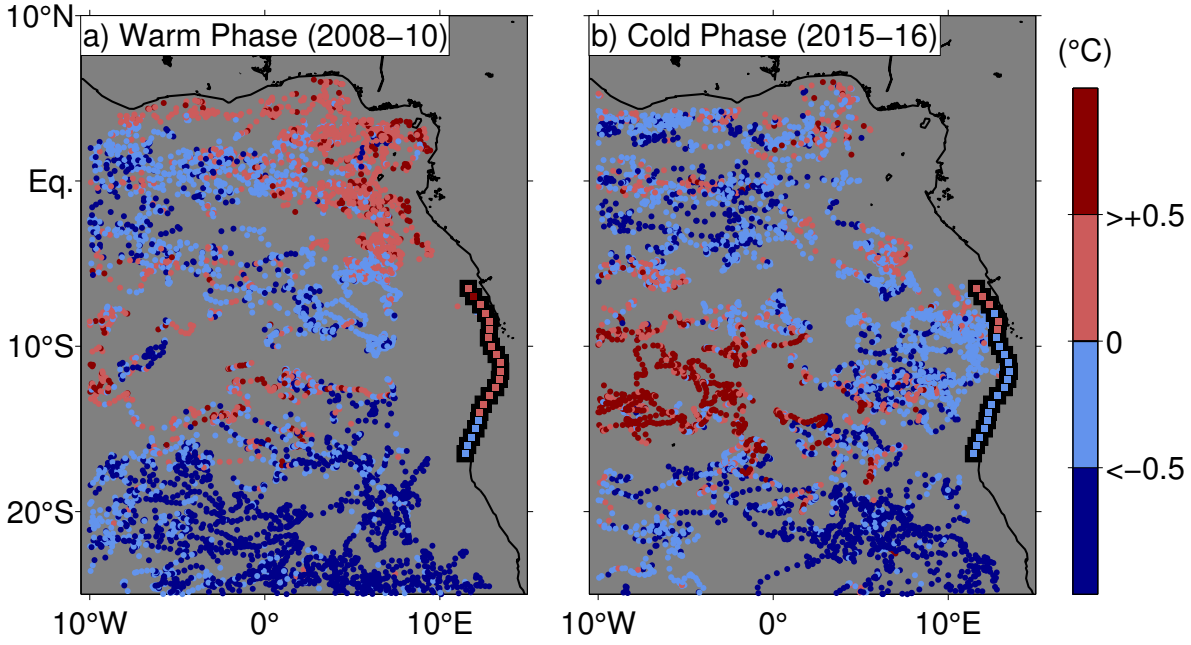

Figure 4.12: Subsurface temperature anomalies from Argo profiles (colored dots) and Nansen CTD data (colored squares) for the periods of (a) a warm (2008-2010) and (b) a cold (2015-2016) subsurface temperature anomaly off the coast of Angola (compare Figure 4.11b). Temperature were averaged in the density range $26.0\,\mathrm{kg\,m^{-3}} \leq \sigma_\theta \leq 26.5\,\mathrm{kg\,m^{-3}}$ and anomalies were derived with respect to a reference temperature corresponding to the total mean of all available Nansen data shown in the latitude-time distribution of Figure 4.11b.

subsurface variability is anomalous heat advection within the Angola Current. The distribution of water mass anomalies in the thermocline of the eastern tropical Atlantic suggests that the water mass anomalies found during the subsurface warm anomaly off Angola during 2008-2010 were transported from the eastern equatorial Atlantic poleward along the Angolan coast (Figure 4.12a), which might be associated with an anomalously strong Angola Current during this period. Likewise, the subsurface cold anomaly during 2015-2016 was associated with colder water masses in the upstream eastern equatorial Atlantic suggesting similarly a role of the Angola Current (Figure 4.12b).

4.6 Summary and discussion

We have presented the current status and the history of physical oceanography in the Angolan territorial waters. Until recently, understanding of the eastern boundary circulation off Angola was derived from a few ship campaigns delivering synoptic geostrophic circulation pattern as well as some time series measurements on the Angolan shelf. The advances of knowledge from these observations were surely limited given the importance of the circulation variability for the highly productive marine ecosystem and associated fisheries (*Gammelsrød et al.*, 1998) as well as for regional and remote climate variability (*Rouault et al.*, 2003).

Within the Nansen programme executed by the Food and Agricultural Organization of the United Nations (FAO) and funded by the Norwegian Agency for Development Cooperation (NORAD) a large number of hydrographic and upper-ocean velocity measurements were acquired during semiannual cruises carried out with the RV *Dr. Fridtjof Nansen* since 1975. As the result of the joint the Angolan and European institutional effort in the frame of the EU PREFACE project this extensive time-series could be first exploited and shared with the scientific community. Here, we presented the main aspects emerging from a first analysis of the dataset. The mean structure of the Angola Current is characterized by a downstream strengthening of the poleward flow between 6 °S and its maximum just north of the Angola-Benguela Front. The semiannual cruise schedule allows a description of the Angola Current during the main downwelling and upwelling seasons. During downwelling season in austral summer (February to April) a shallow and pronounced Angola Current is observed, while during upwelling in austral winter (June to August) the current is weaker and deeper-reaching. The seasonality of the Angola Currents is most likely explained by coastal trapped waves. We also noted the good agreement of the Nansen ship-board velocity data and velocity data from a recently established mooring array at about 11 °S (*Kopte et al.*, 2017).

There is a strong seasonality in near-surface temperature and salinity off Angola. During February to April the upper ocean off Angola is fresh and warm, while during June to August it is much saltier and cooler. Monthly flux climatologies (e.g. *Praveen Kumar et al.* (2013)) suggest evaporation to exceed precipitation during the whole season (e.g. *Lüdke* (2016)) leaving river run

off as the only explanation of the fresh water anomaly in austral summer. Moreover, transport by the Congo river, the only significant continental fresh water source in this region, peaks from November to January (*Dai et al.*, 2009). Excess evaporation over precipitation in austral autumn then degrades the fresh water anomaly. A secondary but weaker near-surface freshening from November to December was recently described by *Kopte et al.* (2017) from a hydrographic data set collected at 11 °S that confirmed early results gained from time series measurements on the Angolan shelf (*Berrit and Dias*, 1977). This semiannual variability corresponds to the semiannual variability of downwelling and upwelling coastal trapped waves causing secondary downwelling and upwelling seasons during October/November and December/January respectively.

Despite the importance of physical processes for the seasonality of primary productivity and its long-term variability, many gaps in our understanding of the tropical upwelling system of Angola remain. This data set and previous studies suggest that seasonal upwelling and downwelling off Angola is mostly associated with the propagation of coastal trapped waves. However, the forcing of these waves, either remotely from the equator or by winds at the eastern boundary, is not fully understood. *Kopte et al.* (2017, submitted manuscript, see Chapter 6) suggests that the annual cycle is dominantly forced remotely at the equator, while the semiannual cycle is strongly modified by winds at the eastern boundary. Furthermore, the impact of these waves on the processes that supply nutrients to the euphotic zone and thus lead to primary productivity remains elusive. As discussed by *Ostrowski et al.* (2009), the tropical upwelling season off Angola coincides with the seasonal minima of alongshore winds. Upwelling due to Ekman divergence is thus not adequate to explain the primary productivity maximum in austral winter. Other processes such as internal wave induced mixing were suggested to contribute to the nutrient supply to the near-surface layers. It is interesting to note the change in stratification of the deeper waters (100 – 400 m depth), most likely associated with the propagation of coastal trapped waves, that is observed in the hydrographic data. Stratification controls the transfer of tidally induced internal wave energy onto the shelf (e.g. *Hall et al.* (2013)) that fuels diapycnal nutrient fluxes on the shelf (e.g. *Schafstall et al.* (2010)). Process studies are needed to resolve these issues in the future.

On interannual timescales, we detected strong variability of subsurface upper-ocean heat content in isopycnal layers. The warm and cold periods that are persisting for several years are most likely due to the variability of Angola Current transport. During periods of strong southward flow, warmer and more saline central water masses from the eastern equatorial waters are transported farther to the south, while during periods of weak southward flow, cooler waters originating south of the Angola-Benguela Front may penetrate into the Angolan upwelling system. The potential of the subsurface heat content anomalies to precondition Benguela Niños or Niñas remains an open question.

Another aspect regards the interannual variability in the near-surface stratification associated with freshwater input due to precipitation and river outflow. On the one hand increased stratification can result in an enhanced surface warming due to reduced mixing (possibly even further enhancing the near-surface stratification), on the other hand near surface stratification also affects

the onshore propagation of internal waves thereby affecting mixing and upward nutrient supply on the shelf. With sea surface salinity data from satellite remote sensing becoming available during recent years in combination with frequent shipboard observations, it should be possible to address the impact of interannually varying near-surface stratification on the nutrient supply and biological productivity more rigorously.

A better understanding of the processes at work will help to improve numerical simulations of the eastern boundary circulation by reducing the still substantial biases in the velocity structures, stratification and upwelling strength. It will ultimately improve coupled climate models and thus the prediction of warm and cold events, which would be of tremendous socioeconomic importance for Angola and particularly its coastal communities. The further development of the capacities in Angola to observe the ocean and to analyze physical and biogeochemical observations taken during ship campaigns or at time series stations in combination with satellite remote sensing will be pivotal to make progress in addressing the impact of climate change and climate variability in a so far generally under-sampled region of the World ocean.

5 Annual and Semiannual Cycle of Equatorial Atlantic Circulation Associated with Basin-Mode Resonance

In this chapter the impact of resonant basin modes for the seasonal cycle of equatorial Atlantic circulation is examined. Dominant baroclinic modes are identified in a multi-year top-to-bottom time series of zonal velocity from the central equatorial Atlantic. These modes are associated with characteristic basin-wide structures corresponding to basin mode resonance. Subsequently the impact of the dominant basin modes on several characteristics of the Equatorial Undercurrent is investigated.

The manuscript was published in *Journal of Physical Oceanography* in October 2016.

Citation: Brandt, P., M. Claus, R. J. Greatbatch, **R. Kopte**, J.M. Toole, W.E. Johns, and C.W. Böning, 2016: Annual and Semiannual Cycle of Equatorial Atlantic Circulation Associated with Basin-Mode Resonance. J. Phys. Oceanogr., 46, 3011–3029, doi: 10.1175/JPO-D-15-0248.1.

The candidate contributed to the analysis of observational data sets and the calculation of vertical structure functions and carried out the analysis of the OGCM output. He produced all figures but 5.7, 5.8, 5.9, 5.10, unified all figures for publication and contributed to the discussion and interpretation of the results.

5.1 Introduction

The mean tropical Atlantic circulation manifests a superposition of the wind-driven and thermohaline circulations that are focused in the upper ocean and near the western boundary (*Schott et al.*, 2004, 2005). At the equator, below the surface wind drift associated with the equatorial easterlies, the Equatorial Undercurrent (EUC) flows eastward along the equator, contributing to the Atlantic meridional overturning circulation and to the wind-driven subtropical cells (*Hazeleger and de Vries*, 2003; *Hazeleger et al.*, 2003). The EUC is among the strongest currents in the tropical Atlantic and flows down the depth-dependent eastward pressure gradient. While nonlinearities contribute to its mean characteristics (*Charney*, 1959; *Qiao and Weisberg*, 1997), the EUC is essentially governed by linear dynamics with the meridional momentum equation being approximated by the geostrophic balance (*Stommel*, 1959; *McCreary*, 1981b).

The main focus of the present study is the seasonal cycle of the zonal velocity that is the dominant variability in the upper layer of the central equatorial Atlantic, particularly modulating the mean eastward flow of the EUC. A question to be addressed is whether the flow variations can be understood as a linear wave response to annual and semiannual wind forcing. Using a general circulation model (GCM), *Philander and Pacanowski* (1986) found that the western part of the equatorial Atlantic is dominated by a local response to the annual wind forcing, while the central and eastern Atlantic shows a stronger semiannual cycle only partially attributable to the local wind forcing. The downward propagation of energy supplied by periodic wind forcing at the sea surface can be conceptually described by equatorial beams. Eastward- and westward-propagating beams are found analytically as the sum of low-order baroclinic mode equatorial Kelvin and Rossby waves, respectively (*McCreary*, 1984). In the tropical Atlantic, such beams are most pronounced at the annual period; the associated upward phase propagation can be identified in direct current observations as well as in highresolution GCM simulations (*Brandt and Eden*, 2005). In relation to the relative strength of the annual and semiannual wind forcing of the tropical Atlantic, the semiannual cycle of the velocity field is enhanced compared to the annual cycle. Using idealized and realistic simulations of the tropical Atlantic, *Thierry et al.* (2004) found that the propagation of second baroclinic mode equatorial Kelvin and long Rossby waves is in resonance with the semiannual wind forcing. Because of the downward energy propagation and the generally dissipative character of the basin resonance, bottom reflections or the presence of the Mid-Atlantic Ridge do not appear to affect the general structure of the semiannual cycle of the velocity field. The spatial and temporal structure of such resonance phenomena are best described by equatorial basin modes (*Cane and Moore*, 1981). These modes are low-frequency standing equatorial modes composed of equatorial Kelvin and long Rossby waves in the context of a shallow-water model with a given gravity wave speed characteristic of a specific baroclinic mode. The total travel time of both types of waves across the basin defines the period of the gravest basin mode. In the inviscid case, the analytical solution by (*Cane and Moore*, 1981) has a singularity in the midbasin due to Rossby wave focusing. The introduction of lateral diffusion

and/or mean flow can prevent such focusing, which makes solutions more realistic in comparison to observations (*Greatbatch et al.*, 2012; *Claus et al.*, 2014).

The concept of equatorial basin modes has been applied to explain the dynamics of observed intraseasonal, seasonal, and interannual variability in the three equatorial basins (see, e.g., *Johnson and Zhang* (2003); *Fu* (2007); *Ding et al.* (2009)). At the semiannual time scale, variability in both the Atlantic and Indian Oceans appears consistent with a resonance of the second baroclinic mode that can be approximated by an equatorial basin mode (*Jensen*, 1993; *Han et al.*, 1999; *Thierry et al.*, 2004; *Ding et al.*, 2009). A subsequent study of basinmode resonance in the Indian Ocean by *Han et al.* (2011) highlighted the influence of wave damping and the shape of the equatorial basin on the spatial structure of these modes, while the existence of equatorial basin modes was found to be a robust feature in simulations with models of different complexity.

In the present paper, we explore the role of the gravest equatorial basin modes of different baroclinic modes in shaping the seasonal cycle of equatorial Atlantic zonal velocity with a particular focus on the EUC. While a basin-mode description of semiannual variability was discussed in previous studies, we will show evidence of a resonant basin mode at the fourth baroclinic mode, annual period.

During the recent decade, an enhanced equatorial observing system consisting of subsurface current meter moorings deployed in cross-equatorial arrays at different longitudes, that is, 23 °W, 10 °W, and 0 °, has been maintained, and the resulting data has been used to document the seasonal behavior of the Atlantic EUC (*Brandt et al.*, 2014; *Johns et al.*, 2014). Some of the identified characteristics, such as the annual cycle of EUC deepening and shallowing and the semiannual cycle of EUC core velocity, have not been dynamically explained so far. Here, we use full-depth velocity observations taken at the equator, 23 °W, to analyze the vertical structure of the seasonal cycle. Further, we compare these results to simulations with a primitive equation numerical model that reveals the horizontal structure of the dominant baroclinic modes in a realistic setting. The obtained horizontal structure resembles that of equatorial basin modes as simulated with a reduced-gravity model. The gravest equatorial basin modes have their strongest zonal velocity oscillations on the equator in midbasin and might thus be well sampled by the 23 °W moored observations. The reduced-gravity model is further used to study the structural dependence of the basin modes on the basin geometry (i.e., square basin vs realistic coastlines) and forcing (i.e., spatially uniform vs realistic wind forcing). The skill of the linear reduced-gravity model in replicating the dominant features of the seasonal cycle of the zonal velocity in the equatorial Atlantic demonstrates that a large part of the seasonal variability may be explained by equatorial wave dynamics associated with just two equatorial basin modes.

The layout of the paper is as follows: In Section 5.2, the moored velocity and shipboard conductivity–temperature–depth (CTD) data are introduced. The model hierarchy, composed of a GCM in a realistic setting and an idealized reduced-gravity model applied for different levels of complexity, is described in Section 5.3. The results section includes a characterization of the annual and semiannual variations as obtained from the mooring data and from the GCM (Section

5.4.1), a comparison between the GCM simulation and the idealized reduced-gravity simulations fitted to moored velocity data from the equator at 238W (Section 5.4.2), and an analysis of the variability of the EUC and its dependence on resonant equatorial basin modes (Section 5.4.3). Summary and discussion are presented in Section 5.5.

5.2 Mooring and CTD data

The zonal velocity observations were obtained from current meter moorings deployed at the equator, 23 °W, from February 2004 to April 2014 (Figure 5.1). This dataset represents an update of that published by *Brandt et al.* (2011, 2012). Here, we use mooring data from seven successive deployment periods of approximately 1.5-yr duration. The moorings were equipped with two ADCPs. The upper one was a 300 or a 150 kHz ADCP installed at 100 to 230 m depth and profiled upward from just below the EUC. The lower instrument was a 75 kHz ADCP that either profiled downward from just beneath the upper instrument or upward from about 600 to 650 m depth. We applied a 40-hour low-pass filter to hourly interpolated current data (ADCP sampling rates varied typically between 0.5 and 1 h^{-1}, but it was set to about 3 samples per day

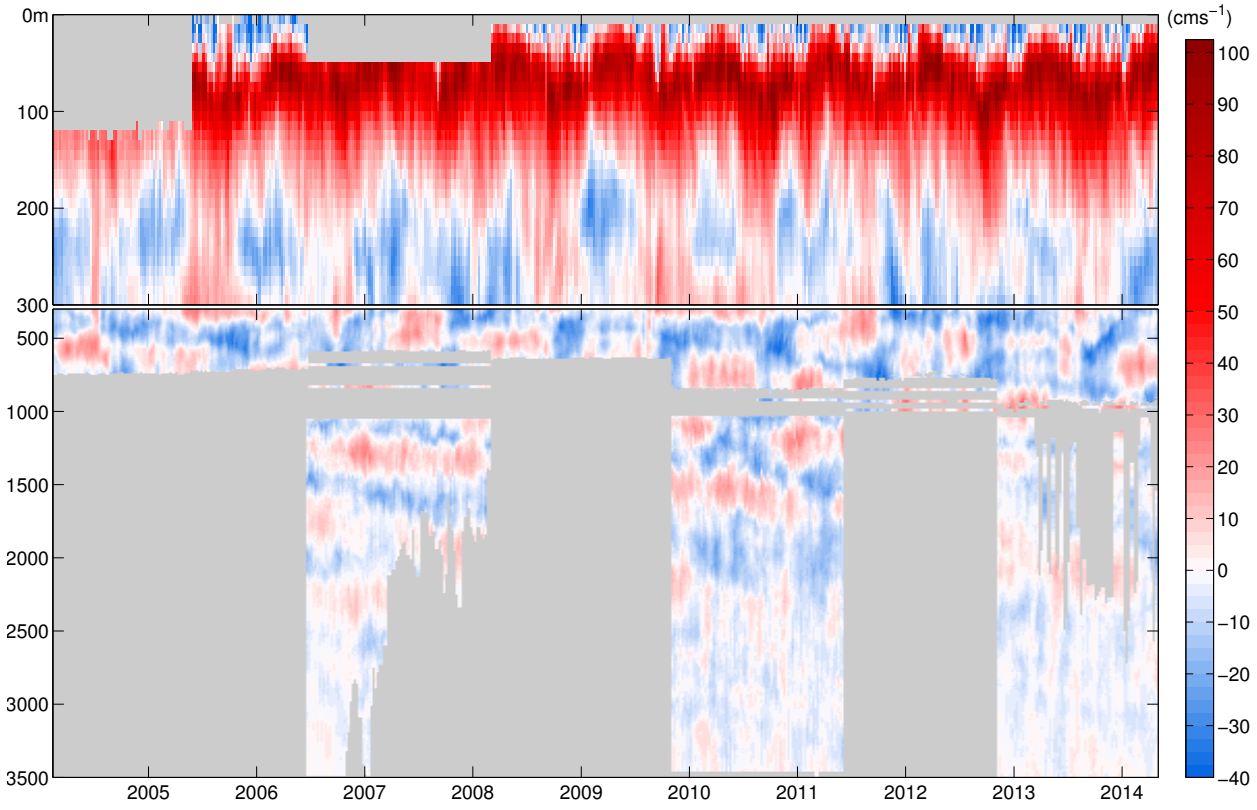

Figure 5.1: Observed zonal velocity from the equator, 23 °W, and above 3500 m depth. Velocity data above about 600 m are from moored acoustic Doppler current profilers; those between 600 and 1000 m are from single-point current meters, and those below 1000 m are from moored profilers. The grey areas mark depths not sampled by the deployed instrumentation. The upper 300 m are enlarged compared to the deeper part of the time series.

during one mooring period) to eliminate tidal currents, and the detided data were subsequently subsampled to 12-hourly resolution.Between 600 and 1000 m during several mooring periods, a few single-point current meters of a different type were installed.

Deeper in the water column, a McLane Moored Profiler (MMP) was programmed to sample the depth range between 1000 and 3500 m. The installed profilers acquired data during three of the seven mooring periods, with a somewhat reduced measurement range during the third and seventh mooring periods (see Figure 5.1). The MMPs were programmed to occupy profiles in bursts of two one-way traverses every 4 or 6 days, with the one-way profiles initiated 6 h apart. No temporal filter was applied to the acquired velocity data. Given the length of the time series, the impact of measurement noise on the derived amplitude of the annual and semiannual cycles can be regarded as negligible.

The time series has so far been used to study equatorial deep jets (EDJs) that are visible as bands of eastward and westward velocity characterized by downward phase propagation and a periodicity of about 4.5 yr (*Brandt et al.*, 2011) as well as the seasonal and interannual variability of the EUC (*Brandt et al.*, 2014). Here, we further exploit the data to study the seasonal circulation variability taking particular advantage of the nearly full-depth velocity measurements to decompose the velocity field according to baroclinic modes at selected frequencies.

For the decomposition of the moored velocity data into baroclinic modes, we used vertical structure functions for a flat bottom derived from a mean Brunt–Väisälä frequency profile that was obtained by averaging individual Brunt–Väisälä frequency profiles calculated from shipboard CTD measurements taken during the mooring service cruises. The structure functions of the low baroclinic modes change only marginally when taking into account the variability about the mean Brunt–Väisälä frequency profile; however, some variations in the depth of zero-crossings of the profiles result when considering different ocean depths. To have a consistent analysis regarding the vertical structure of observed and simulated velocity variability, we decided to use one set of structure functions derived from the observed mean Brunt–Väisälä frequency profile for a water depth of 4500 m for both the analysis of the zonal velocity from moored observations as well as from the GCM.The main characteristics of the baroclinic modes are given in Table 5.1; the two modes of

Baroclinic mode	Phase velocity c ($\mathrm{m\,s^{-1}}$)	Gravest basin-mode period (days)	Depth of first zero-crossing (m)	Depth of second zero-crossing (m)
1	2.47	109	1410	-
2	1.32	203	295	2220
3	0.95	284	85	795
4	0.74	361	65	400
5	0.57	473	50	270

Table 5.1: Characteristics of the baroclinic modal decomposition using a mean Brunt–Väisälä frequency profile derived from CTD casts during mooring service cruises. The gravest basin mode period ($4L/c$) is calculated for a width of $L = 5.8 \times 10^6$ m $\sim 52.8^\circ$ (i.e., the width of the rectangular basin).

particular interest in the present study, that is, the second and fourth baroclinic mode, together with the mean zonal velocity in the upper 300 m derived from the moored time series are presented in Figure 5.2.

Figure 5.2: Normalized vertical structure function of the second (blue) and fourth (red) baroclinic mode as derived from a mean Brunt–Väisälä frequency profile from the equator, 23 °W. Normalization is performed with regard to the standard deviation of the structure functions. In the enlarged upper 300 m depth range the mean zonal velocity (yellow) is also shown.

5.3 Model simulations

The GCM builds on a global configuration [Tropical Atlantic Nest at 1/10 ° (TRATL01)] of the Nucleus for European Modeling of the Ocean (NEMO) code (*Madec*, 2008) in which the grid resolution of 0.5 ° is refined to 0.1 ° in the Atlantic Ocean between 30 °N and 30 °S via two-way nesting (*Debreu and Blayo*, 2008). It includes 46 vertical levels, with increasing thickness from 6 m at the surface to 250 m at depth. With an interannually varying forcing given by the Coordinated Ocean–Ice Reference Experiments (CORE; *Griffies et al.* (2009)) reanalysis data over the period 1948–2007, the TRATL01 configuration was used by *Duteil et al.* (2014) to study the circulation mechanisms responsible for the ventilation of the oxygen minimum zone in the eastern tropical Atlantic. A particular finding of that study was the improved realism of the equatorial current system, owing to the higher resolution of the TRATL01 model compared to a 0.5 ° resolution model. Here, we use the output from the TRATL01 simulation over the period 1995–2007, as well as 3-yr subsets of the time series, to assess the strength of the interannual variability that might be present in the moored observations covering periods of at least 3 yr at the different longitudes. We compare the results of the TRATL01 simulations with observational results that are based on current meter moorings along meridional sections at 23 °W, 10 °W, and 0 °, deployed from October 2007 to June 2011 (*Johns et al.*, 2014). The comparison focuses on the mean and the seasonal cycle of the EUC transport (Figure 5.3). As the time period of the TRATL01 simulation and the observations only marginally overlap, we examined the stability of the mean EUC seasonal cycle for different time periods using the dataset of the ECMWF Ocean Reanalysis System 4 (*Balmaseda et al.*, 2013). We found that in the reanalysis, the mean

seasonal cycle of the EUC for 1995–2007 is similar in amplitude and phase to that of 2007–11, justifying our comparison of TRATL01 simulations with observations from different periods.

The moored data show that at 23 °W, the strongest EUC transport is found in boreal autumn during the period of maximum easterly wind stress that varies dominantly at annual period. At 10 °W, the EUC transport shows a semiannual cycle with maxima in boreal spring and autumn. Farther to the east, the wind forcing is dominated by its semiannual component. However, the observed EUC transport at 0 ° has only a single maximum in boreal spring. The comparison of simulated and observed EUC transports (Figure 5.3) shows that (i) the model's annual-mean EUC transport is generally overestimated and decreases more with distance from west to east as compared to observations (the interannual variability, delineated by the successive 3-yr subsets of the time series, is not able to account for these differences); (ii) within the seasonal cycle, the timing of the boreal autumn maximum in the EUC transport is well represented at 23 °W and 10 °W; and (iii) there is only a weak simulated seasonal cycle at 0 ° with the observed boreal spring maximum not represented. At 23 °W, the simulation is found to capture the main characteristics of the seasonal velocity variability observed on the equator, including the amplitude and phase of the annual harmonic of zonal velocity (Figure 5.4) and the spectral behavior (Figure 5.5). In particular, the reasonable representation of the observed seasonal cycle of zonal velocity in the central equatorial Atlantic, that is, close to midbasin where velocity oscillations of the gravest equatorial basin mode are strongest (*Cane and Moore*, 1981), encourages us to focus on a baroclinic modal decomposition analysis at the annual and semiannual period.

To further the dynamical understanding, we consider single baroclinic mode solutions by applying a linear reduced-gravity model in spherical coordinates. For governing equations and further details of the model, see *Greatbatch et al.* (2012). The internal gravity wave speeds of the

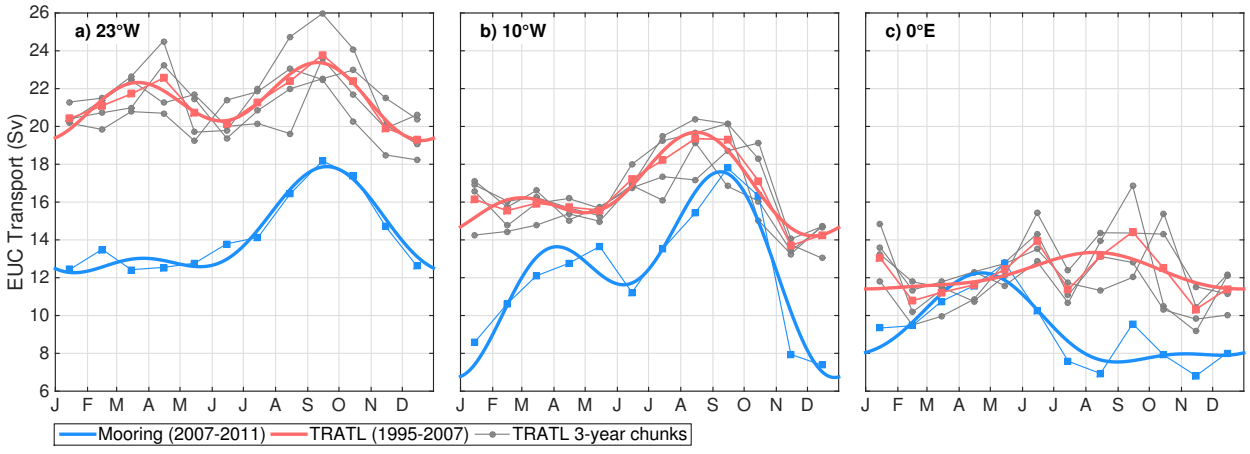

Figure 5.3: Monthly means (squares) of the 30–300 m EUC transport at 23 °W, 10 °W, and 0 ° from observations taken from October 2007 to June 2011 (*Johns et al.* (2014), blue) and the TRATL01 model output derived for the whole model period 1995–2007 (red) as well as for four successive 3-yr subsets of the time series (grey). Thick solid lines represent the mean seasonal cycles derived from annual and semiannual harmonic fits of the observations (blue) and simulations (red).

reduced-gravity model are taken from the baroclinic modal decomposition of the observed mean Brunt–Väisälä frequency profile described above (Table 5.1). The lateral eddy viscosity is set to $300\,m^2\,s^{-1}$, which yields the most realistic results with regard to the meridional structure of high baroclinic mode waves (*Greatbatch et al.*, 2012; *Claus et al.*, 2014). However, model simulations with reduced eddy viscosity, that is, $100\,m^2\,s^{-1}$, give similar results. The governing equations are applied to a rectangular as well as a realistic coastline domain with northern and southern boundaries at 20 °N/S, respectively. Sponge layers at the northern and southern boundaries prevent Kelvin wave propagation along those boundaries. The latitudes of the northern and southern boundaries in the reduced-gravity model are chosen to be far enough away from the equator to have little influence on the structure of the simulated equatorial basin modes. The horizontal resolution is the same as that used in the GCM ($1/10^\circ$ in both longitude and latitude).

Periodic wind stress forcing is applied to the momentum equations (either annually or semiannually), and all simulations with the reduced-gravity model are run for 100 yr in order to obtain a stable, periodically oscillating solution. We note that the resulting oscillation amplitude will depend on different aspects of the model configuration, including the applied damping, the basin geometry, the strength of the basin mode resonance, and, most importantly, the projection of the wind forcing onto the different baroclinic modes. Here, we use similar wind coupling coefficients as, for example, in *Shankar et al.* (1996) or *Han et al.* (1999). However, the annual and semiannual oscillation amplitudes derived from the linear reduced-gravity model are scaled using the ratio of observed and simulated amplitudes of the annual and semiannual oscillations on the equator at 23 °W. This adjustment was performed to counter any misrepresentation of damping or forcing in the reduced-gravity model with respect to the simulated oscillation amplitude. The reduced-gravity model is then used to quantify the horizontal structure of the amplitude and phase of the annual and semiannual cycle throughout the tropical Atlantic.

Three sets of reduced-gravity model simulations are presented. The first uses an idealized rectangular domain with a basin width of 52.8 ° in longitude forced by spatially uniform zonal wind stress at the annual or semiannual period. The second set of simulations is identical except that the model domain is defined by the observed 1000 m isobath of the equatorial Atlantic basin at the eastern and western boundaries. Note that we used a slightly different basin width for the rectangular domain from that used by *Greatbatch et al.* (2012); in that case 55 ° in longitude) in order to ensure that the resonance periods in the model simulations with a rectangular basin and a basin with realistic coastlines are basically the same. For both sets of simulations having spatially uniform wind forcing, in addition to the amplitude scaling, a spatially uniform phase shift is applied to the simulated annual and semiannual oscillations over the whole domain to achieve agreement between simulated and observed phases on the equator at 23 °W. Following this approach, the adjusted model output is independent of the amplitude and phase of the wind forcing. The third set of simulations is the same as the second (i.e., both sets using realistic coastlines), except that we use a spatially varying, harmonically oscillating wind forcing derived from the NCEP–DOE AMIP-II reanalysis product (*Kanamitsu et al.*, 2002). In this third set of

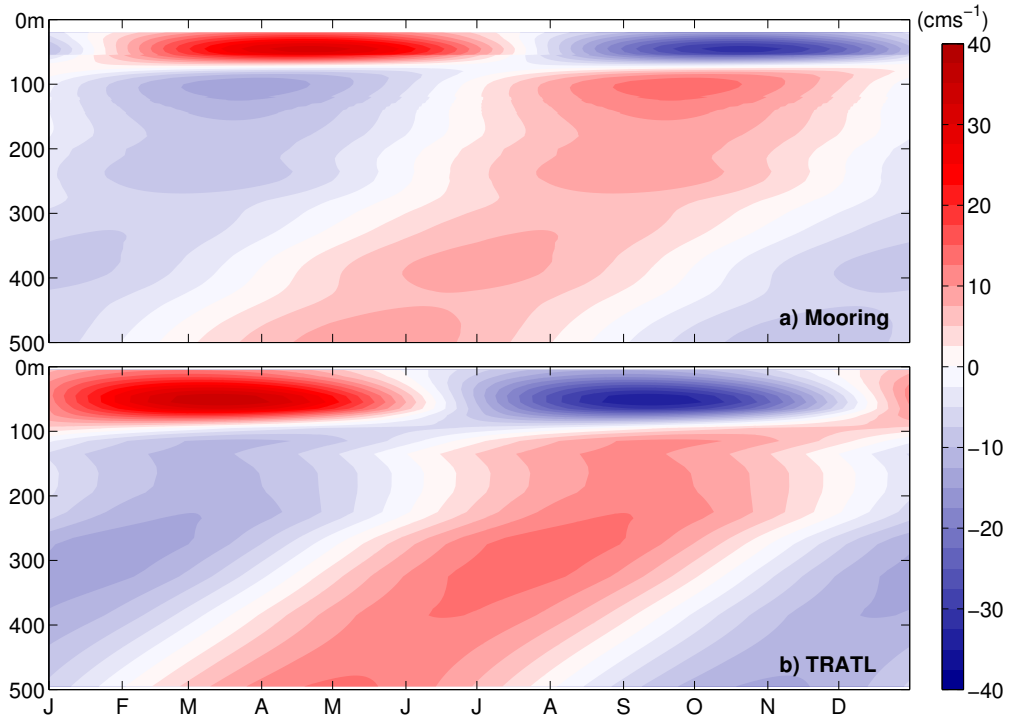

Figure 5.4: Annual cycle of zonal velocity (cm s^{1}) from the equator, 23 °W, as reconstructed using only (a) the annual harmonic fit applied to moored velocity data and (b) the TRATL01 model output.

simulations, we use zonal and meridional wind forcing. Specifically, the amplitude and phase of the annual and semiannual wind forcing are obtained by harmonic fits at the corresponding periods. In this most realistic set of simulations with the reduced-gravity model, only the amplitudes of simulated velocity oscillations are scaled according to the observed values on the equator at 23 °W; no phase adjustment is done, as we expect the phase of the oscillations to be well determined by the applied wind forcing.

5.4 Results

5.4.1 Characteristics of the annual and semiannual cycle

The dominant signals in the zonal velocity field observed at the 23 °W equatorial mooring (Figure 5.1) are the seasonal cycle and the interannual variations associated with the equatorial deep jets. By analyzing an early subset of the mooring data, *Brandt et al.* (2006) identified strong annual cycle amplitudes above and below the mean core depth of the EUC that are in phase opposition. Deeper in the water column, sizable annual amplitudes were also found. A reconstruction of the mean annual cycle from a harmonic fit of the moored velocity data (Figure 5.4a) shows a clearly visible phase jump at about 70 m depth associated with zero amplitude. Around 100 m depth, another maximum in the annual amplitude is found corresponding to the lower part of the EUC. This pattern represents the upward and downward movement of the EUC velocity core

during the year, being shallowest in boreal spring and deepest in autumn. Below the EUC, upward phase propagation is evident that is, according to linear equatorial wave theory, associated with downward energy propagation. The simulation with the TRATL01 model (Figure 5.4b) shows a very similar behavior. Main differences compared to the observations are the slightly deeper depth of the phase jump and the larger amplitude (with a maximum at about 300 m) below the EUC core. Note that the depth of maximum eastward velocity of the annual-mean EUC at 23 °W is about 70 m in the observations and about 85 m in the TRATL01 simulation, which following *McCreary* (1981b) is indicative of too large vertical diffusion in the TRATL01 simulation.

To derive a frequency spectrum from the irregularly sampled moored velocity dataset, we performed harmonic fits of the available data at each depth and averaged the derived amplitude vertically over the whole depth range (Figure 5.5a). The obtained spectrum clearly shows distinct peaks at annual and semiannual periods with another weaker peak at about 120 days. The broad amplitude maximum at the 4–5 yr period is associated with the EDJs (*Brandt et al.*, 2011; *Ascani et al.*, 2015). The strong peaks in the zonal velocity amplitude suggest the presence of strong forcing at these periods and/or a resonant behavior or, possibly, indicate influence from flow instabilities (not discussed further here). Similar calculations performed using the TRATL01 model velocity data also reveal spectral peaks at annual, semiannual, and 120-day periods with the peak at the annual period being substantially stronger by a factor of 2 to 3 compared to observations. Enhanced amplitudes at interannual time scales are missing in the TRATL01 solution, pointing toward a well-known deficiency of such models in representing the EDJs (*Ascani et al.*, 2015).

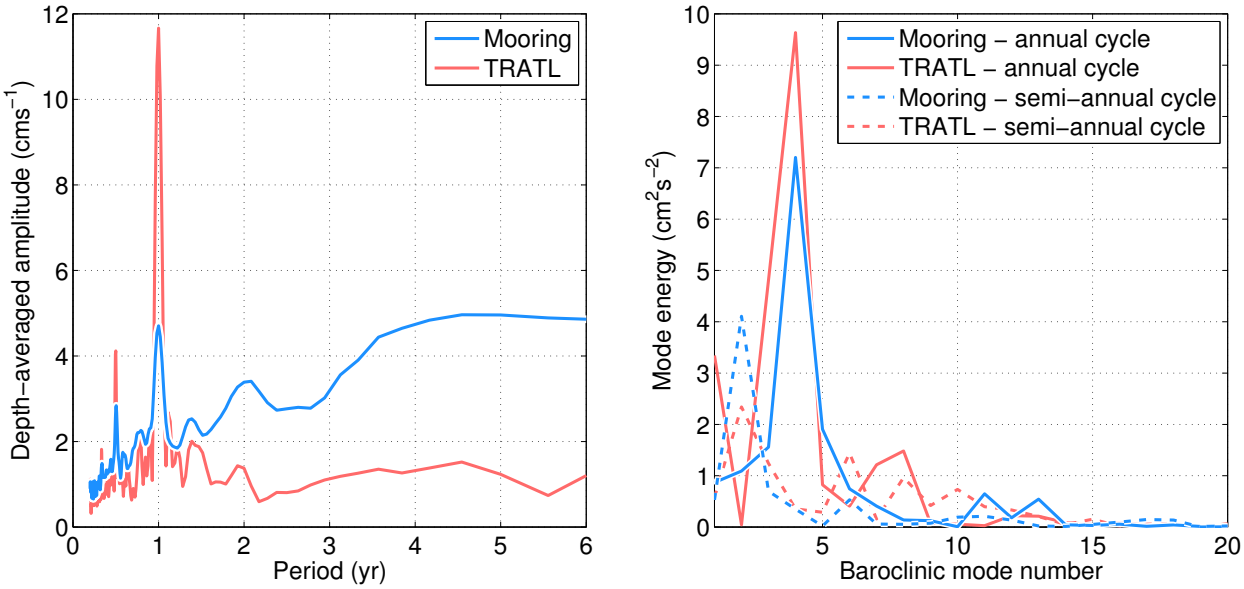

Figure 5.5: (left) Frequency spectra of observed zonal velocity from the equator, 23 °W, and (right) baroclinic mode spectra of the annual (solid) and semiannual (dashed) cycles derived from the equatorial mooring (blue) and the TRATL01 model (red). The spectra of observed zonal velocity in the left panel were derived by fitting harmonic functions to the available data at each depth level, followed by vertical averaging.

To analyze the vertical structure of the annual and semiannual cycle, we performed a baroclinic modal decomposition of the reconstructed annual and semiannual cycles (Figure 5.5b) at each discrete time step. The mode energy was then obtained by averaging the square of the derived coefficients over a whole cycle. As expected from previous studies (*Thierry et al.*, 2004; *Ding et al.*, 2009), the semiannual energy density peaks at the second baroclinic mode. More surprising is the strong peak of the annual cycle at the fourth baroclinic mode. The vertical structure function of the fourth baroclinic mode has its first zero-crossing at 65 m depth (Table 5.1), which is close to the depth of the mean EUC core (Figure 5.2). Thus, the phase shift of the annual cycle within the EUC (Figure 5.4a) is associated with the dominance of this baroclinic mode. Note the weak annual amplitudes at about 400 m depth (Figure 5.4) that correspond to the second zero-crossing of the fourth baroclinic mode (Table 5.1) suggesting also a significant contribution of that baroclinic mode to the velocity variability below the EUC.

The TRATL01 simulation shows very similar characteristics: The peak of the second baroclinic mode, semiannual cycle, is slightly weaker than observed, and the peak of the fourth baroclinic mode, annual cycle, is slightly stronger (Figure 5.5b). We also note that the amplitude of the third/fifth baroclinic mode, annual cycle, is higher/lower in the TRATL01 simulations compared to the observations, which indicate a shift of the simulated annual cycle to lower modes having deeper first zero-crossings compared to higher modes (Table 5.1). This is consistent with our findings from the comparison of reconstructed annual cycles (Figure 5.4), where the phase shift in the annual cycle between the upper and lower part of the EUC is deeper in the simulations compared to the observations.

In a next step, the TRATL01 output (which reproduces the main characteristics of the seasonal velocity variability on the equator at 23 °W) is taken to calculate the horizontal pattern associated with the second baroclinic mode, semiannual cycle, and the fourth baroclinic mode, annual cycle (Figure 5.6). These patterns reveal (i) an elongated amplitude maximum along the equator in midbasin, (ii) general westward phase propagation off as well as on the equator, and (iii) a meridionally broader pattern of the semiannual cycle relative to the annual cycle. Both patterns have similarities with equatorial basin modes as theoretically described by *Cane and Moore* (1981) but reveal at the same time an asymmetry with respect to the equator. We next compare patterns simulated using TRATL01 with idealized simulations using the reduced-gravity model.

5.4.2 Equatorial basin modes as simulated with the reduced-gravity model

The reduced-gravity model was next applied to study the resonance behavior of the equatorial ocean forced with spatially uniform zonal forcing of fixed amplitude but different oscillation periods. The simulations were performed for the square basin as well as for the basin with realistic coastlines. Following previous studies (*Greatbatch et al.*, 2012; *Claus et al.*, 2014), we chose the root-mean-square (RMS) of the zonal velocity along the equator calculated in the stable,

periodically oscillating state to identify the resonance of the equatorial basin modes (Figure 5.7). Here, the estimate is taken over the final complete oscillation cycle. The simulations indicate resonance of the second baroclinic mode near the semiannual period at about 210 days and resonance of the fourth baroclinic mode almost exactly at the annual period. At the resonance periods, the amplitudes of the zonal velocity oscillations are somewhat reduced in the case of a basin with realistic coastlines compared to a square basin. This likely is the result of the

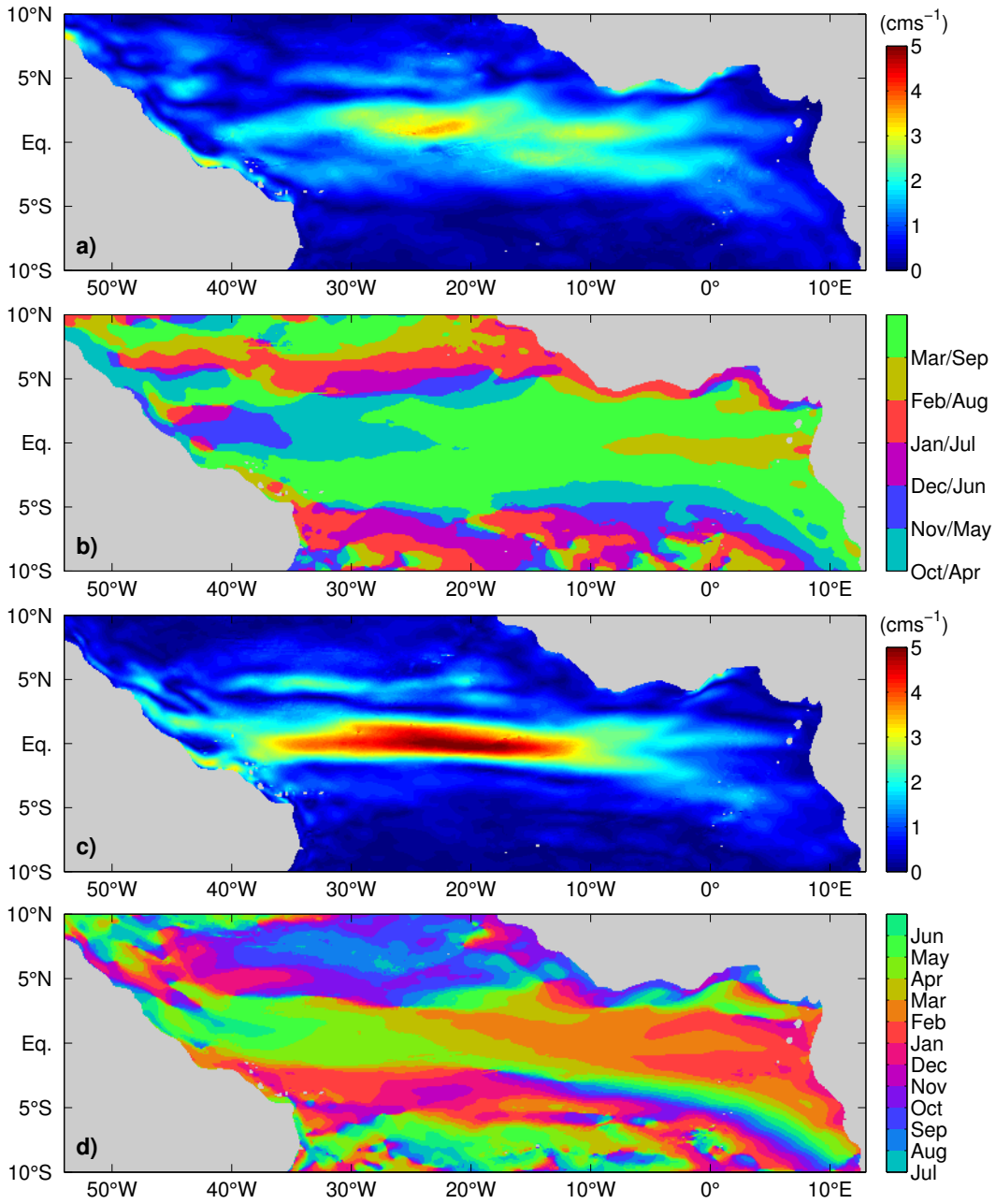

Figure 5.6: The (a),(c) amplitude and (b),(d) phase of the (a),(b) second baroclinic mode, semiannual cycle, and of the (c),(d) fourth baroclinic mode, annual cycle, of zonal velocity from the TRATL01 model. To derive the 3D zonal velocity field associated with the specific baroclinic mode, the amplitudes have to be multiplied by the corresponding vertical structure functions shown in Figure 5.2. The phase is given in month of the year when maximum eastward velocity occurs at the surface.

slanting western boundary reducing the amplitude of the reflected Kelvin wave in comparison to a straight meridional boundary (*Cane and Gent*, 1984) and possibly also a consequence of the Gulf of Guinea coastline shape in the east. Note that Figure 5.7 indicates secondary resonances near 100 days for the second baroclinic mode and near the semiannual period for the fourth baroclinic mode. Several effects that could impact the resonance periods are neglected in the reduced-gravity model. For example, in the real ocean the resonance periods may be reduced in comparison to the idealized simulation presented here due to the presence of a mean flow as shown for equatorial basin modes of higher baroclinic modes (*Claus et al.*, 2014) or due to the nonlinear increase of the propagation speed of equatorial waves (*Boyd*, 1980; *Greatbatch*, 1985).

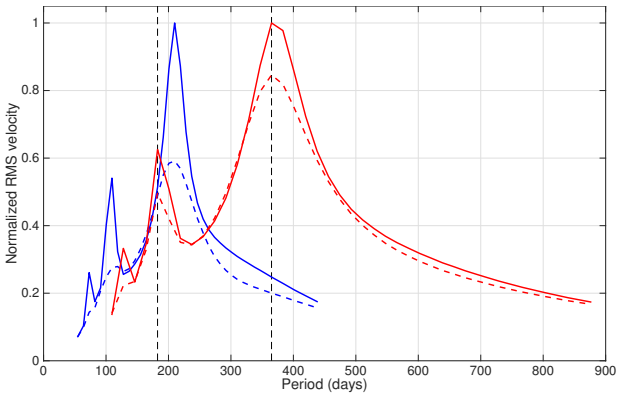

Figure 5.7: Normalized RMS of the zonal velocity along the equator calculated for the final complete oscillation cycle as a function of the period of the applied spatially uniform zonal forcing for simulations with the reduced-gravity model. Simulations are performed for the square basin (solid lines) as well as for the basin with realistic coastlines (dashed lines). The velocity in the ordinate for the second (blue) and fourth baroclinic mode (red) simulation is normalized by the maximum RMS of the respective simulations for the square basin. Vertical dashed lines mark the period of the semiannual and annual cycles.

Different runs with the reduced-gravity model sought to identify the structure of the basin modes in a uniformly forced rectangular ocean and to study the influence of realistic coastlines and wind forcing. Similar to the TRATL01 simulation, the amplitude and phase of the second baroclinic mode, semiannual cycle, and the fourth baroclinic mode, annual cycle, in the reduced-gravity model shows an elongated amplitude maximum along the equator in midbasin and generally westward phase propagation (Figure 5.8-Figure 5.10). The solutions of the reduced-gravity model for a square basin and spatially uniform zonal forcing are symmetric with respect to the equator. The main difference between the solutions for the second baroclinic mode, semiannual cycle (Figure 5.8a,c), and the fourth baroclinic mode, annual cycle (Figure 5.8b,d), is the meridionally broader pattern of the second baroclinic mode, semiannual cycle; in the case of the semiannual cycle, regions farther away from the equator are more affected by the basin mode oscillations than for the annual cycle.

The introduction of realistic coastlines and the associated change of basin geometry induce an asymmetry in the meridional structure of the basin modes; that is, in the western part of the domain, the amplitude maximum is shifted northward, whereas in the east the amplitude in the southern lobe is enhanced, while that in the northern lobe is reduced. Consistent results were found for the basin mode of the second baroclinic mode, semiannual cycle, using a GCM with realistic basin geometry (*Thierry et al.*, 2004) that showed notable meridional asymmetry in the deeper circulation pattern. Here, the second baroclinic mode, semiannual cycle, is more strongly influenced by the introduction of realistic coastlines compared to the fourth baroclinic

mode, annual cycle. This could be expected because of the smaller meridional scale associated with the fourth baroclinic mode compared to the second baroclinic mode. Interesting to note are the amplitude maxima at the northeastern boundary (Figure 5.9a,b) that are likely associated with the propagation of coastally trapped waves around the Gulf of Guinea. Somewhat similar maxima are also found in the TRATL01 solution (Figure 5.6), especially for the second baroclinic mode, semiannual cycle, case.

A final set of simulations with the reduced-gravity model was performed that used a realistic spatial pattern of annual and semiannual wind forcing. In contrast to the first two sets of

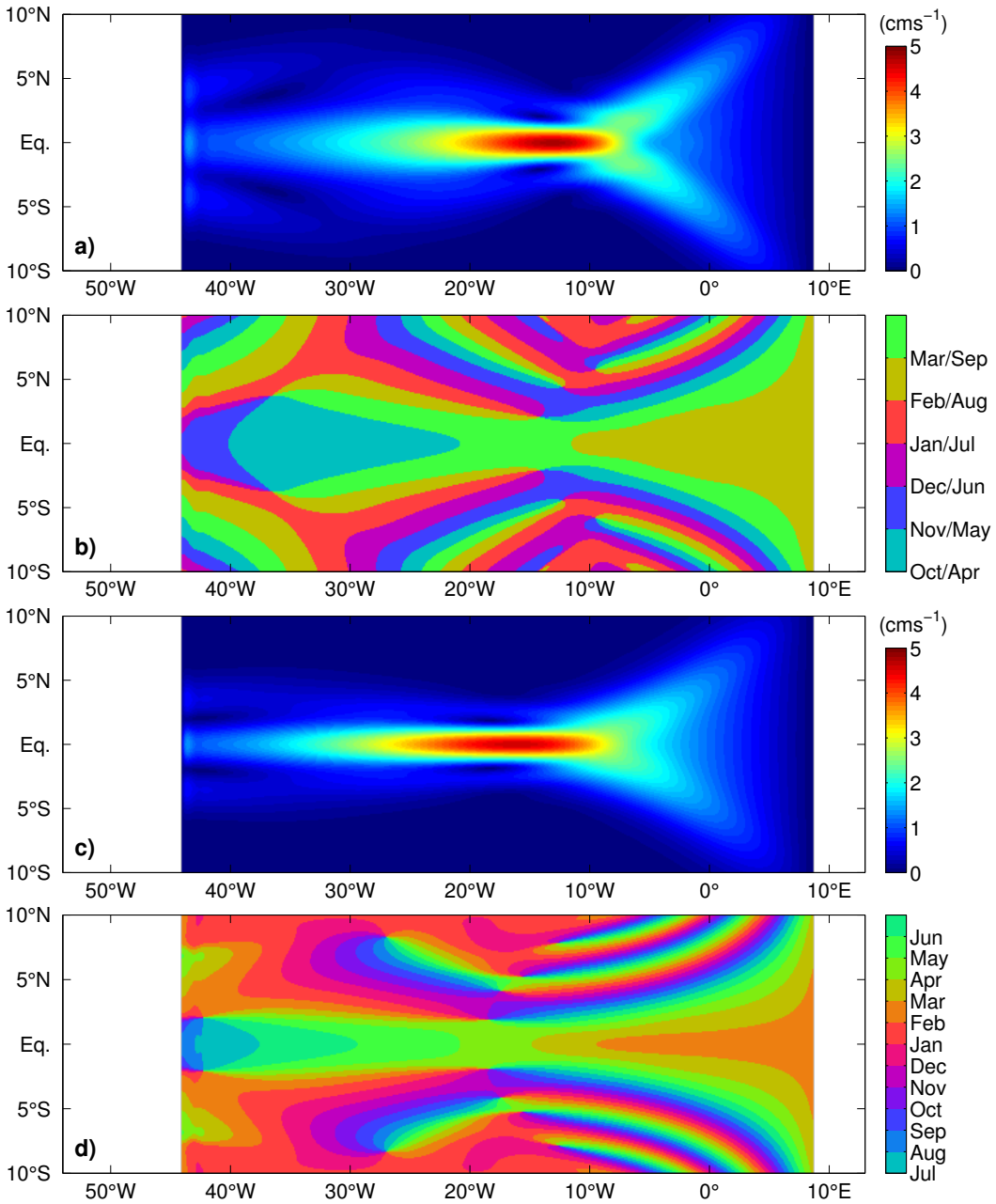

Figure 5.8: As in Figure 5.6, but simulated with the reduced-gravity model for the rectangular domain using a gravity wave speed $c = 1.32\,\mathrm{m\,s^{-1}}$ corresponding to the second baroclinic mode and $c = 0.74\,\mathrm{m\,s^{-1}}$ corresponding to the fourth baroclinic mode.

simulations that were forced with spatially uniform winds, we only adjusted the amplitude of the simulated basin mode in comparison to the moored observations on the equator at 23 °W. The simulated phase was unaltered, as we expect the phase of the oscillations to be well determined by the applied wind forcing. With the more realistic wind forcing, the second baroclinic mode, semiannual cycle, develops two separate amplitude maxima in space (Figure 5.10a): one centered on the equator at about 10 °W and the second slightly north of the equator west of 20 °W. A similar structure can be found in the TRATL01 simulation (Figure 5.6a). When changing from the reduced-gravity model simulations with spatially uniform to realistic wind forcing, the main difference for the fourth baroclinic mode, annual cycle, is a shift in the phase along the equator of

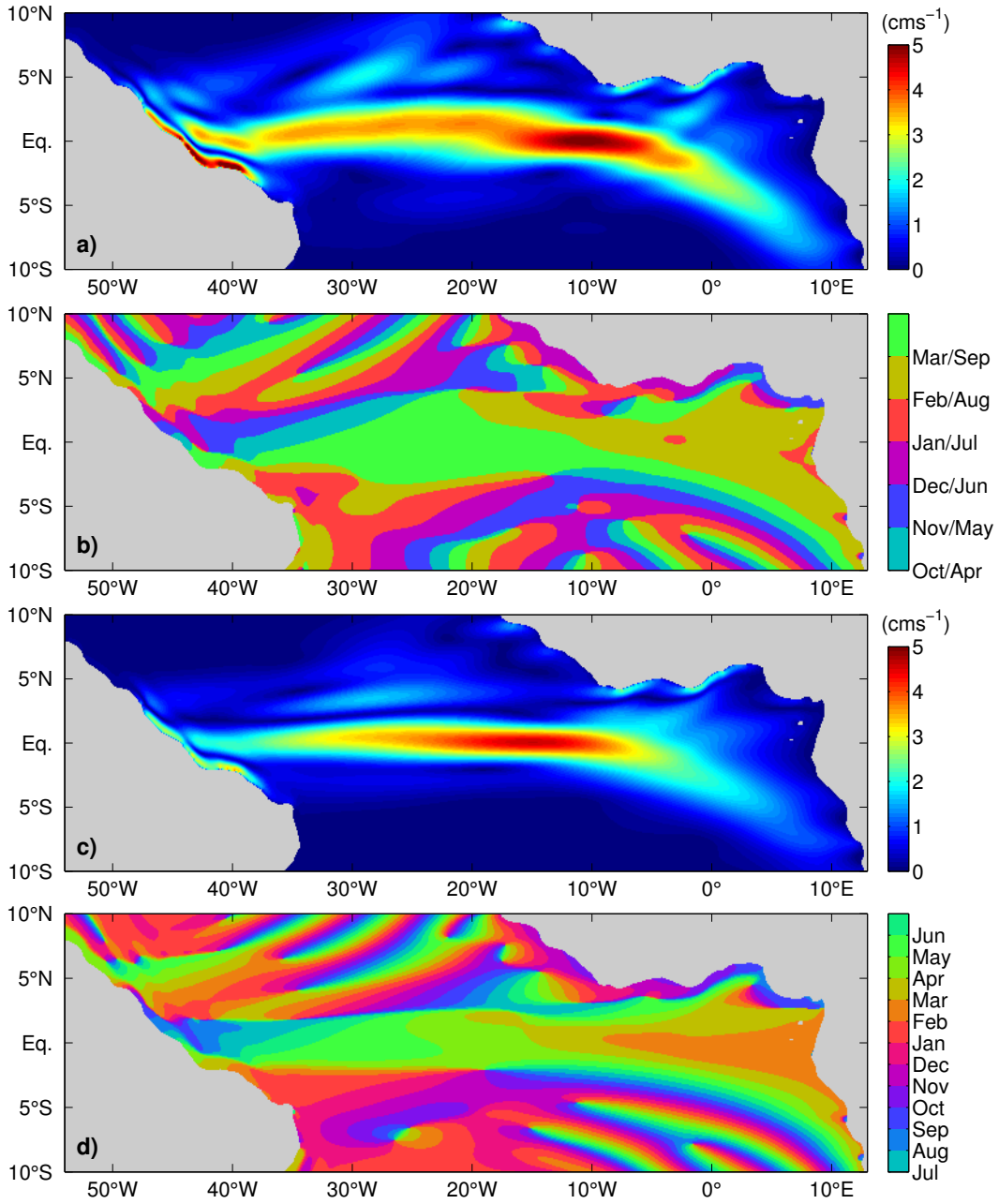

Figure 5.9: As in Figure 5.8, but for the realistic coastline domain.

up to 2 months, suggesting a deficiency of the reduced-gravity model in the most realistic setup with an unaltered phase. Again, there is good agreement between the linear, reduced-gravity model and the TRATL01 model in this case (Figure 5.10b,d and Figure 5.6b,d).

Overall, the regular oscillations produced by the reduced-gravity model are suggestive of equatorial basin modes. Realistic coastlines and realistic wind forcing both induce meridional asymmetry in the basin-mode structure, the influence being stronger for the lower baroclinic mode, semiannual cycle, compared to the annual cycle. Confirming previous results using models of different complexity applied to the Indian and Atlantic Oceans (*Thierry et al.*, 2004; *Han et al.*, 2011), our results also show that the general structure of a resonant equatorial basin mode is fairly

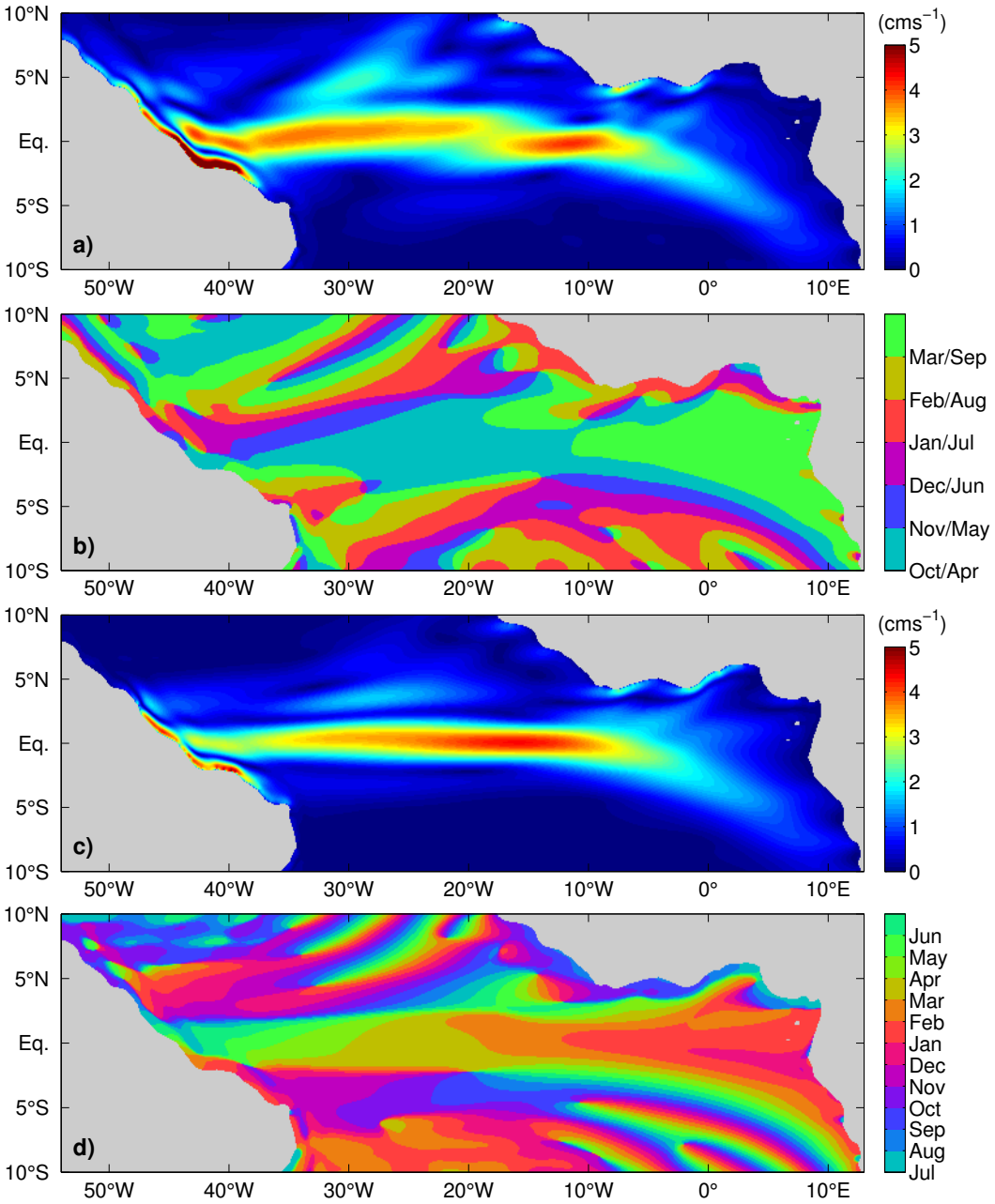

Figure 5.10: As in Figure 5.9, but with spatially varying wind forcing.

robust [similar structures are observed in the various reduced-gravity model simulations (Figure 5.8-Figure 5.10) as well as the GCM (Figure 5.6)].

5.4.3 EUC variability associated with equatorial basin modes

A question that arises from the above results is to what extent can the observed seasonal behavior of the EUC be explained by linear equatorial basin modes. Using the basin-mode solutions from the reduced-gravity model, we reconstruct the 3D structure of the velocity anomaly field by applying the vertical structure functions of the corresponding baroclinic modes (Figure 5.2). By adding the reconstructed simulated velocity anomalies to the mean velocity from meridional shipboard sections at different longitudes (*Johns et al.*, 2014),we obtain a time series of zonal velocity that can be analyzed in a similar fashion as the observed time series. In particular, EUC transports are calculated following *Johns et al.* (2014), that is, integrating only eastward velocities within the latitudinal range from 1°12′S to 1°12′N and the depth range from 0 to 300 m. Here, the reconstruction obtained from the reduced-gravity model simulations only includes the velocity variability associated with the second baroclinic mode, semiannual cycle, and the fourth baroclinic mode, annual cycle, and is derived for all three cases: the square basin, realistic geometry, and realistic wind forcing.

The comparison of observations with the reconstructed seasonal cycle (Figure 5.11a,b,c) shows that (i) at 23 °W, the observed EUC transport maximum of the seasonal cycle in September is found only slightly later in the reconstruction; (ii) at 10 °W, very good agreement is achieved with EUC transport maximum in August/September, a secondary maximum is in March/April, and the weakest EUC transport is in December; and (iii) there is only weak or no correspondence between observations and the reconstructions at 0 ° with the former exhibiting a spring transport maximum, whereas the reconstructions have a weak late boreal summer maximum, similar to what is found in TRATL01 (Figure 5.3c). The differences between the three different reduced-gravity model reconstructions, square basin, realistic coastlines, and realistic wind forcing, are relatively small, suggesting robust behavior of the equatorial basin modes. For the reconstructed seasonal cycle of the EUC transport at the three longitudes, the contributions of the annual harmonic cycle and the semiannual harmonic cycle are of similar importance (Figure 5.11d,e,f).

To further examine the vertical structure of the seasonal EUC transport variability, zonal transport profiles are calculated by integrating the reconstructed zonal velocity [only eastward velocities following *Johns et al.* (2014)] over the width of the EUC between 1°12′S and 1°12′N (Figure 5.12), which can be directly compared to the observations at 23 °W, 10 °W, and 0 ° shown in *Johns et al.* (2014), their Fig. 11). Here, we also include results regarding the western tropical Atlantic (i.e., 35 °W) to analyze the behavior of the EUC across the whole basin. While in general the three different reconstructions are very similar, we note the influence of realistic coastlines compared to the square basin in producing a well-separated and shallower transport maximum at 35 °W in boreal spring and a slight weakening of the semiannual transport maxima in the eastern

equatorial Atlantic when introducing realistic wind forcing. The reconstructed transport profiles obtained by using the second baroclinic mode, semiannual cycle, and the fourth baroclinic mode, annual cycle, show several similarities with the observed total transport profiles (*Johns et al.*, 2014) (i) there is a pronounced semiannual cycle in the shallow part of the transport profile (about upper 100 m), and (ii) the EUC is shallow in boreal spring and deep in boreal autumn. Differences between simulations with the reduced-gravity model and observations are particularly evident in the flow below the EUC core. In the simulations, it is the deep extension of the EUC during August/September at 0° (Figure 5.12) that is chiefly responsible for the EUC transport maximum during that period (Figure 5.11c). On the other hand, the observed deep extension of the EUC at 0° is strongest during May shortly after the shallow spring maximum, both together producing the EUC transport maximum in boreal spring (Figure 5.11c). The deep extension of the EUC at 10°W and at 23°W occurs about 1 month later in the simulations compared to the

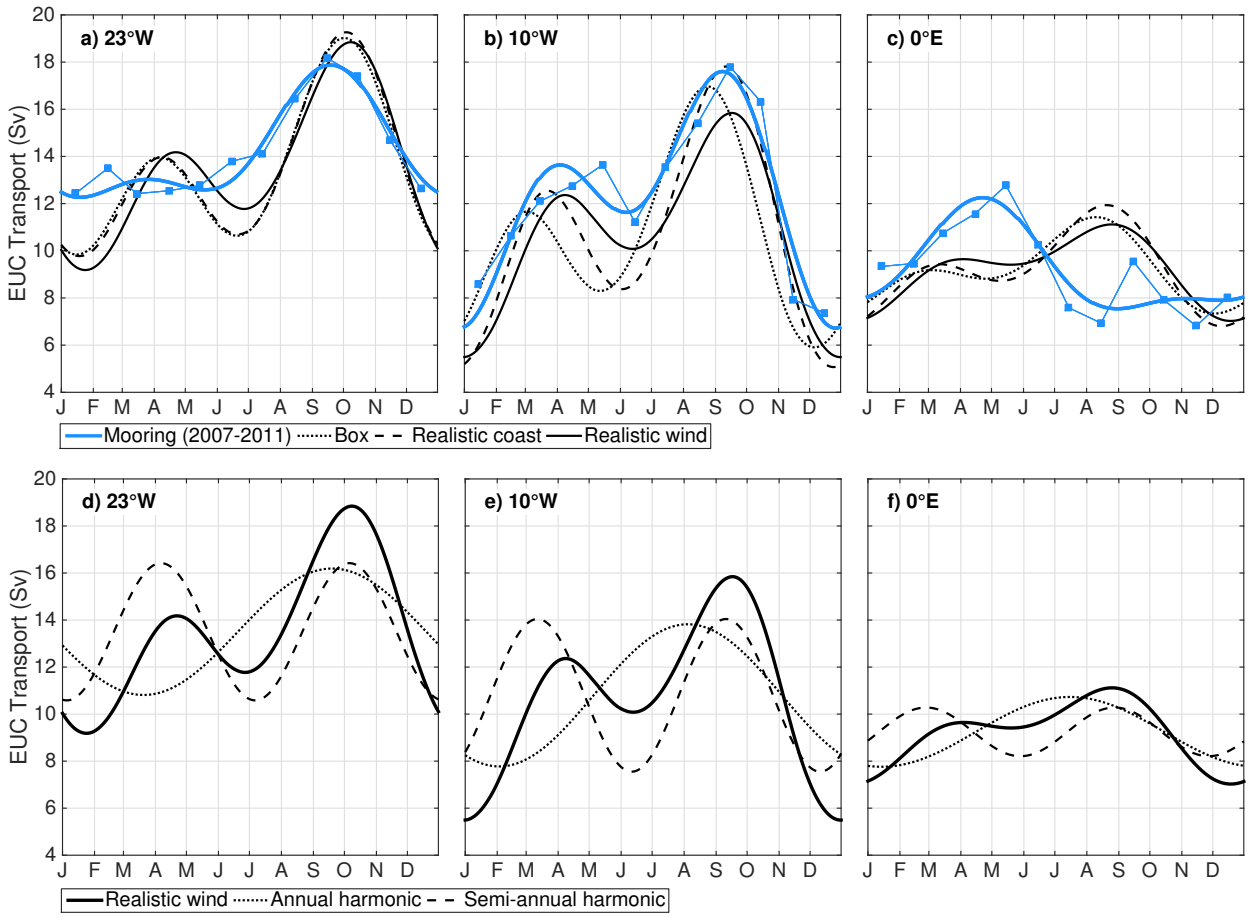

Figure 5.11: Monthly means (blue squares, thin blue lines) and annual plus semiannual harmonic cycle of the 30–300 m EUC eastward transport at (a) 23°W, (b) 10°W, and (c) 0° from observations taken from October 2007 to June 2011 (*Johns et al.* (2014), thick blue lines) and as reconstructed with the three different reduced-gravity model simulations: rectangular domain (dotted lines), realistic coastline domain (dashed lines), and realistic wind forcing (solid lines). The reconstructed annual plus semiannual harmonic cycle for the simulation with realistic wind forcing is repeated in (d),(e), and (f) (solid lines) with separate contributions from the annual harmonic (dotted lines) and semiannual harmonic cycle (dashed lines).

observations.

Other parameters that characterize the seasonal EUC variability are its core depth and latitude as well as its maximum velocity (Figure 5.13). These parameters were determined from moored observations at 23 °W by *Brandt et al.* (2014). Comparison of the reduced-gravity model reconstructed fields with the observational curves shows that the semiannual cycle of the EUC core velocity and the annual cycle of the EUC core depth can be largely reproduced by the superposition of the two dominant equatorial basin modes. Even though the vertically averaged annual cycle of the zonal velocity dominates the semiannual cycle (Figure 5.5), semiannual variability dominates the annual cycle for the EUC core velocity (Figure 5.13b). This is because the second baroclinic mode has a larger amplitude than the fourth baroclinic mode at the core depth of the mean EUC (Figure 5.2). At the same time, the fourth baroclinic mode, annual cycle, very

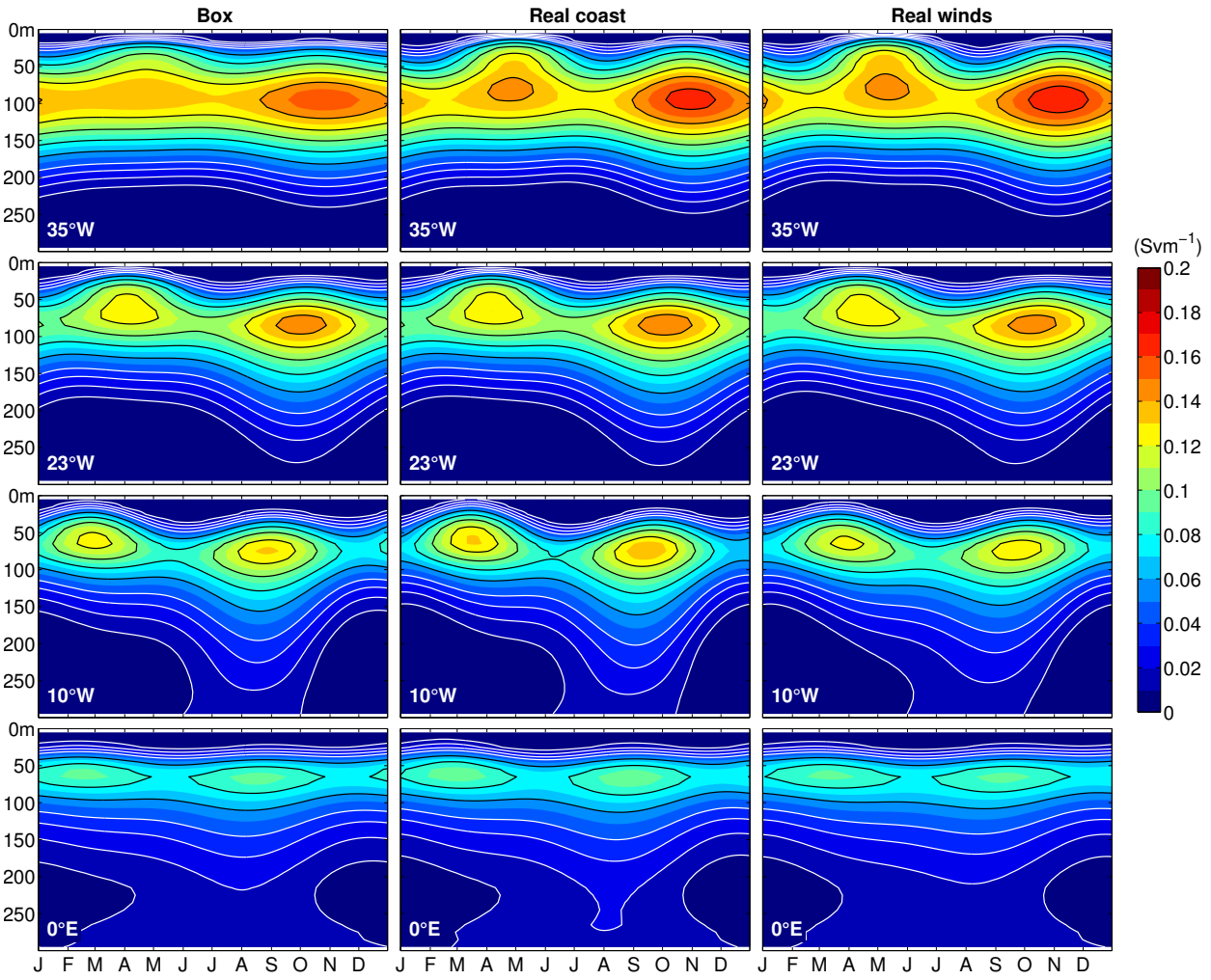

Figure 5.12: Monthly mean EUC transport profiles at 35 °W, 23 °W, 10 °W, and 0 ° for the three different reduced-gravity model simulations: (left) rectangular domain, (middle) realistic coastline domain, and (right) realistic wind forcing. White contour lines are included for transports between 0.01 and 0.04 Sv m^{-1} (1 Sv = 10^6 m^3 s^{-1}) with an increment of 0.01 Sv m^{-1} and black lines between 0.06 and 0.2 Sv m^{-1} with an increment of 0.02 Sv m^{-1}.

efficiently influences the seasonal cycle of the EUC core depth. With the first zero-crossing of the fourth baroclinic mode at about the core depth of the mean EUC (Figure 5.2), the strengthening/weakening above/below the EUC core during boreal spring and vice versa during boreal autumn (Figure 5.13d) results in a vertical movement of the EUC core during the annual cycle. The semiannual cycle does not change sign in the depth range of the EUC and thus does not contribute significantly to the vertical movement of the EUC core. The latitude of the EUC core is rather poorly represented by the simple basin modes. Other effects that might play a role in setting this parameter not accounted for in the simulations are the seasonally varying shallow meridional circulation forced by the meridional wind stress on the equator and the quasi-stationary meandering of the EUC east of the North Brazil Current retroflection, likely responding to the strong seasonal cycle of the retroflection.

5.5 Summary and discussion

We have analyzed a multiyear velocity time series from the equator, 23 °W, covering (with some gaps; see Figure 5.1) the whole water column with respect to the seasonal variations of the zonal velocity. Distinct peaks in frequency baroclinic mode space emerged, the most pronounced being the second baroclinic mode at the semiannual period and the fourth baroclinic mode at the annual period (Figure 5.5). Similar peaks are found in the TRATL01 simulation. The associated horizontal patterns as obtained from the TRATL01 model are consistent with the presence of equatorial basin modes, as confirmed using a linear, reduced-gravity model (Figure 5.7-Figure 5.10). The general agreement in the horizontal pattern as obtained from TRATL01 and the different runs with the reduced-gravity model also suggest that other effects not accounted for in the reduced-gravity model, such as the seasonal variability in the stratification associated with a vertical displacement of the mean zonal velocity profile, play only a minor role in producing zonal velocity anomalies of the specific baroclinic mode analyzed here.

By using a linear, reduced-gravity model for the simulation of equatorial basin modes for two different baroclinic modes, we were able to show that linear wave dynamics provide a simple explanation for several characteristics of the observed zonal velocity seasonal variability including that of the EUC. Besides equatorial beams that are often used to describe the seasonal variability in the equatorial ocean (*McCreary*, 1984; *Lukas and Firing*, 1985; *Thierry et al.*, 2004; *Brandt and Eden*, 2005), equatorial basin modes represent a powerful alternative means of describing equatorial ocean dynamics (*Cane and Moore*, 1981; *Jensen*, 1993; *Han et al.*, 1999; *Ding et al.*, 2009; *Han et al.*, 2011). Equatorial basin modes are associated with basin resonances occurring at periods defined by the phase speeds of equatorial Kelvin and long Rossby waves of specific baroclinic modes and the basin geometry. In conjunction with the characteristics of the wind forcing, basin resonance appears to explain the pronounced peaks in the frequency baroclinic mode space found in the moored observations. The simulations with the reduced-gravity model

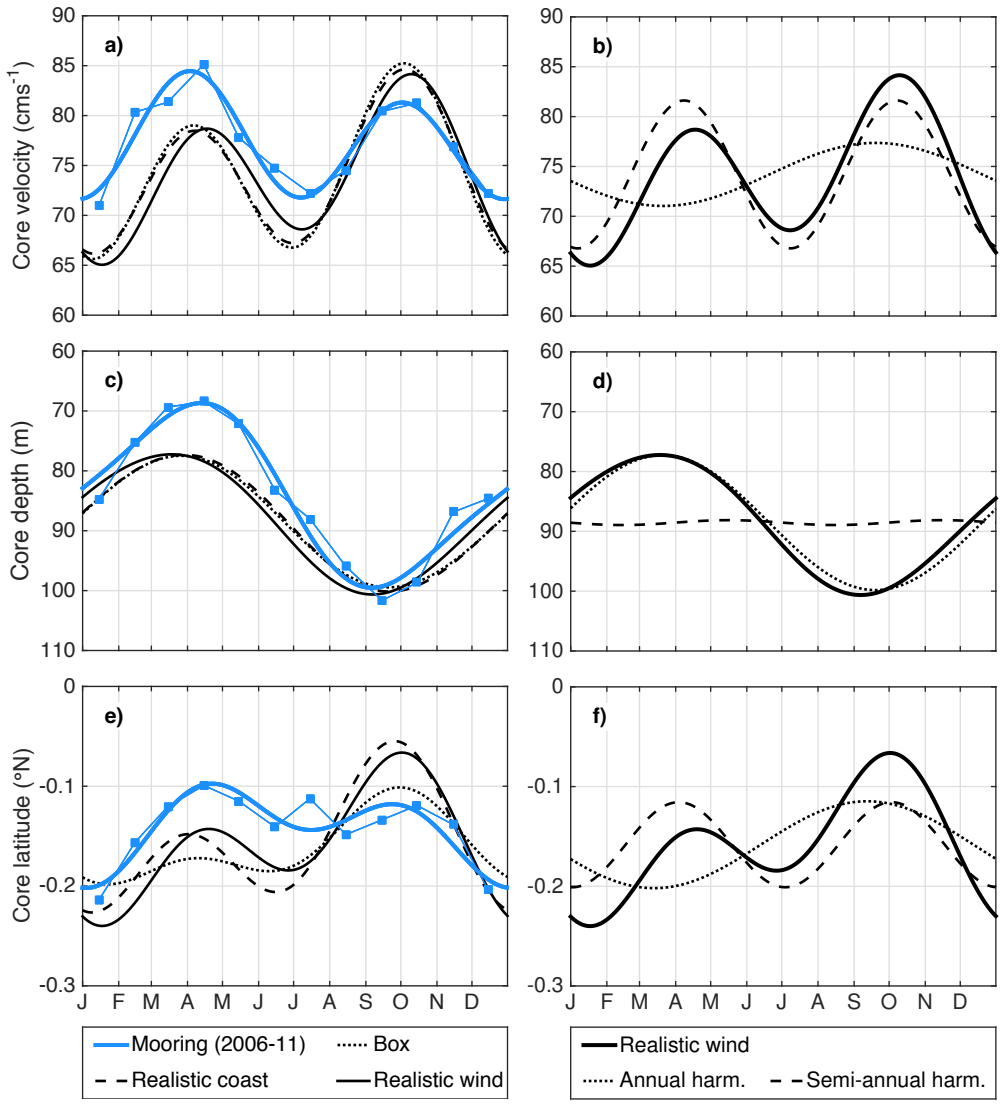

Figure 5.13: Monthly means (blue squares, thin blue lines) and annual plus semiannual harmonic cycle of the (a)EUC core velocity, (c) EUC core depth, and (e) EUC core latitude at 23 °W from observations taken from June 2006 to June 2011 (*Brandt et al.* (2014), thick blue lines) and as reconstructed with the three different reduced-gravity model simulations: rectangular domain (dotted lines), realistic coastline domain (dashed lines), and realistic wind forcing (solid lines). The reconstructed annual plus semiannual harmonic cycle for the simulation with realistic wind forcing is repeated in (b),(d), and (f) (solid lines) with separate contributions from the annual harmonic (dotted lines) and semiannual harmonic cycle (dashed lines).

in different configurations and the TRATL01 model confirm the result obtained by *Han et al.* (2011) and others that the resonant equatorial basin modes are robust features only weakly dependent on the structure of the equatorial basin and the wind forcing. *Thierry et al.* (2004) specifically analyzed the role of the Mid-Atlantic Ridge and found a negligible effect of this pronounced bathymetric feature, suggesting that a simple reduced-gravity model might be well suited for the simulation of equatorial basin modes.

While the resonance of the semiannual cycle in the Atlantic (as well as Indian) Ocean requires a phase speed close to the phase speed of the second baroclinic mode (*Thierry et al.*, 2004;

Ding et al., 2009), the resonance of the annual cycle is associated with a slower internal wave speed, which is achieved in the equatorial Atlantic by the fourth baroclinic mode. The higher baroclinic mode has a first zero-crossing of the associated vertical structure function (derived from observations) at about 65-m depth (Table 5.1), suggesting an opposing effect of the annual basin mode on the zonal flow above and below the mean EUC core, as seen in the observations (Figure 5.4a).

The seasonal cycle of the EUC reveals strong deviations from a simple local response to the wind forcing. Such deviation can be seen, for example, by the following: (i) the basinwide vertical migration of the EUC within the seasonal cycle cannot be in balance with the differing wind forcing in the eastern (predominantly semiannual forcing) and western (predominantly annual forcing) basin at the same time, and (ii) the maximum of the EUC core velocity during boreal spring is found during the period of weakest wind forcing (*Johns et al.*, 2014). Using the reduced-gravity model simulations, we show that the superposition of the two dominant basin modes, that is, the second baroclinic mode, semiannual cycle, and the fourth baroclinic mode, annual cycle, provide a simple explanation for a substantial part of the observed seasonal EUC variability. Particularly, the seasonal cycles of the EUC transport, core depth, and core velocity in the central equatorial Atlantic are well captured by the reconstructed velocity fields. However, the superposition of the two basin-mode solutions cannot account for the downward phase propagation of the annual cycle found below the EUC core (Figure 5.4), which must involve other baroclinic modes (*Brandt and Eden*, 2005). This discrepancy between the simulations and observations is probably responsible for the deviations in the transport profiles derived from the reconstructions (Figure 5.12) and observations (*Johns et al.*, 2014). It might also be the reason that although the amplitudes of the two basin modes are adjusted in comparison to the 23 °Wvelocity data, the reconstructed and observed EUC transport at 23 °W does not completely match (Figure 5.11a).

There is general disagreement between observations and the linear reduced-gravity model simulations as well as GCM simulations of the EUC in the eastern equatorial Atlantic, for example, at 0 °. *Philander and Chao* (1991) suggested that in the eastern equatorial Atlantic, the EUC acts as an inertial jet decelerated by lateral dissipation. As shown in satellite (*Athie and Marin*, 2008) and in situ observations (*Jouanno et al.*, 2013), there is a strong seasonal cycle of the amplitude of intraseasonal waves. Model simulations indicate that these waves, which are mainly wind generated by the high-frequency wind forcing, impact the seasonal cycle of turbulent mixing in the eastern equatorial Atlantic (*Jouanno et al.*, 2013). Through their effects on lateral dissipation and vertical mixing, the intraseasonal variability might influence the seasonal cycle of the zonal velocity in the eastern equatorial Atlantic. However, such effects might also play a role in the central equatorial Atlantic, which is also characterized by substantial seasonal cycles in the strengths of tropical instability waves (*Athie and Marin*, 2008) and vertical mixing (*Jouanno et al.*, 2013; *Hummels et al.*, 2014). These effects are not captured in the reduced-gravity model simulations. Besides the gravest equatorial basin modes discussed so far, we also want to mention a possible role of the second basin modes for the zonal velocity variability in the far eastern

equatorial Atlantic. In the case of the fourth baroclinic mode, the second basin mode has substantial oscillation energy at the semiannual period (Figure 5.7). The second basin mode likely has a stronger impact on the zonal velocity seasonal cycle east and west of the central equatorial Atlantic, which is dominated by the gravest basin mode. As the second basin mode typically has a reduced amplitude in the central equatorial Atlantic and is thus not well constrained by our observations on the equator at 23 °W, it is not included here, but it clearly deserves further study.

To correctly represent the seasonal variability of zonal velocity in GCMs, basin-mode resonance must be captured. As suggested by *Philander and Pacanowski* (1981), the evaluation of the seasonal cycle provides a sensitivity test of the different mixing parameterizations used in models. However, the response of the reduced-gravity model to varying frequencies of the wind forcing (Figure 5.7) indicates that the amplitude of the annual and semiannual oscillations crucially depends on the proximity of the resonance peaks to the annual and semiannual periods. The resonance periods of the second and fourth baroclinic modes as calculated using the mean Brunt–Väisälä frequency profile from TRATL01 are 185 and 339 days and as such are about 20 days shorter than the estimates obtained from observations (Table 5.1). In general, variations in the vertical density structure of GCMs compared to observations could enhance or reduce the wave speeds of the specific baroclinic modes and thus modify the amplitude of the corresponding basin modes by shifting the period of the resonance peaks. Particularly for coarse-resolution models, the vertical density structure could differ substantially from reality. The resulting alteration of the EUC transport seasonal cycle and in turn its associated supply to the equatorial upwelling has great potential to impact simulated sea surface temperature variability.

The analyzed simulation with the TRATL01 model show a deeper EUC (at 23 °W; 85 m in TRATL01 vs 70 m in the observations) and a deeper first zero-crossing of the fourth baroclinic mode when using the mean Brunt–Väisälä frequency profile from the model instead from the observations (77 vs 65 m). We also note a shift of the annual cycle to lower modes in the TRATL01 simulation compared to observations (Figure 5.5). A similar result can be conjectured from the GCM simulation studied by *Ding et al.* (2009), where it was found that the model solution is determined by the four gravest baroclinic modes with the second and third being dominant. Simulation of the seasonal cycle of equatorial zonal velocity thus requires, besides valid mixing parameterizations, a realistic representation of the vertical density structure and the mean flow field, both affecting the amplitudes of the annual and semiannual oscillations associated with the resonant basin modes.

6 Role of Basin-Mode Resonance for the Seasonal Variability of the Angola Current

The results from the previous chapter suggest some influence by the off-equatorial lobes of equatorial basin modes on the boundary circulation off Southwest Africa. Here, this impact and more generally the role of remote equatorial versus local forcing on the seasonality of the Angola Current is explored using again a composite of observational data and a suite of shallow water model simulations differing in the applied forcing.

The manuscript is currently under review for publication in *Journal of Physical Oceanography*.

Citation: Kopte, R., P. Brandt, M. Claus, R. J. Greatbatch, and M. Dengler, 2017: Role of Basin-Mode Resonance for the Seasonal Variability of the Angola Current. Submitted to J. Phys. Oceanogr.

The candidate carried out the analysis of observational data sets and model output. He performed all shallow water model runs using the model developed by Martin Claus. The candidate produced all figures and authored the manuscript from the first draft to the submitted version.

6.1 Introduction

In the southeastern tropical Atlantic, the Angola Current represents a major feature of the boundary circulation connecting the equatorial Atlantic with the coastal upwelling systems of Angola and Benguela (*Peterson and Stramma*, 1991; *Rouault et al.*, 2007; *Ostrowski et al.*, 2009). In the past, based exclusively on synoptic observations, the Angola Current had been assumed as a continuous poleward current, yet seasonally varying in strength, thereby advecting warm waters from the tropics southward (*Moroshkin et al.*, 1970; *Dias*, 1983a,b). Since July 2013, two current meters have been in place on the continental slope near 11 °S to investigate both advective and wave signals in the Angola Current. These direct velocity observations reveal a strongly variable alongshore flow in the depth range between 45 and 450 m with periodically alternating poleward and equatorward velocities in the range of $\pm 40\,\mathrm{cm\,s^{-1}}$. A weak southward mean flow was found in the upper 200 m with Angola Current core velocities of $8\,\mathrm{cm\,s^{-1}}$ at about 50 m depth and an associated southward mean transport of 0.32 Sv (*Kopte et al.*, 2017). Transport variability due to the semiannual and annual harmonics was determined to be of the same order as the mean Angola Current transport. The Angola Current converges with the northward flowing Benguela Current at about 16 °S, where a sharp, yet highly variable thermal front is formed known as the Angola-Benguela Frontal Zone (ABFZ) (*Meeuwis and Lutjeharms*, 1990).

On interannual time scales severe warm events, associated with the poleward intrusion of warm tropical waters across the ABFZ, appear to be primarily induced by a wave response via equatorial Kelvin waves (EKWs) and coastally trapped waves (CTWs) to the remote equatorial forcing (*Florenchie et al.*, 2003; *Lübbecke et al.*, 2010; *Bachèlery et al.*, 2016). Owed to their similarities to the El Niño phenomenon in the Pacific Ocean, these extreme warm events in the northern Benguela are referred to as Benguela Niños (*Shannon et al.*, 1986) and are known to have severe impact on the local marine ecosystem and rainfall variability affecting both fishery and agricultural sectors of the neighboring countries (*Gammelsrød et al.*, 1998). Based on regional modeling studies excluding the seasonal cycle in the analysis, *Bachèlery et al.* (2016) attributed intraseasonal variability in the upwelling system mainly to local forcing. Nonetheless, continuous and recurrent propagation of EKWs and CTWs from intraseasonal (*Polo et al.*, 2008) via seasonal (*Schouten et al.*, 2005; *Rouault*, 2012) to interannual time scales (*Bachèlery et al.*, 2016) are well documented from satellite altimetry data. Passages of these waves also imply modulations of the Angola Current strength through thermocline displacements (*Ostrowski et al.*, 2009). Likewise in the Pacific, semiannual oscillations of the Peru-Chile Undercurrent in the south and the California Undercurrent in the north have been associated with the passage of semiannual CTWs that are induced by semiannual EKWs (*Pizarro et al.*, 2002; *Gómez-Valdivia et al.*, 2017). Thermocline displacements associated with these dynamics have been verified as far south as 21 °S off the coast of Chile (*Ramos et al.*, 2006).

The main focus of the present study is the seasonal cycle of the Angola Current as observed by the moored current meters near 11 °S. As the equatorial and coastal wave-guides are well

connected, a question to be addressed is whether the variability seen in the Angola Current is linked to equatorial Atlantic variability particularly on seasonal time scales. A large fraction of the observed variability in equatorial Atlantic circulation is concentrated near resonance frequencies associated with equatorial basin modes (*Claus et al.*, 2016; *Brandt et al.*, 2016). Equatorial basin modes (*Cane and Moore*, 1981) represent low-frequency standing equatorial modes in a zonally bounded basin. Basin modes are composed of eastward propagating EKWs and westward propagating long equatorial Rossby waves with a given gravity wave speed associated with a specific baroclinic mode. Depending on the basin width L and the gravity wave speed c_n of the nth baroclinic mode, the resonance periods of the respective basin mode are given by $T_{n,m} = (4 \cdot L)/(m \cdot c_n)$, where m is a positive integer, and $m = 1$ corresponds to the gravest basin mode, while $m = 2$ describes a second basin mode having one mid-basin nodal point. Despite weak wind forcing at the semiannual time scale in the equatorial Atlantic, a considerable semiannual cycle in equatorial circulation is found, which is attributed to the resonance of the second baroclinic mode to semiannual wind forcing (*Thierry et al.*, 2004; *Ding et al.*, 2009; *Brandt et al.*, 2016). Likewise, the resonance period of the gravest basin mode for the fourth baroclinic mode is very close to the annual period, indicating resonance of this baroclinic mode to annual wind forcing (*Brandt et al.*, 2016). On interannual time scales, the correspondence between the Equatorial Deep Jets (EDJs) and equatorial basin modes for higher baroclinic modes has often been noted (*Ascani et al.*, 2006; *d'Orgeville et al.*, 2007; *Brandt et al.*, 2012; *Claus et al.*, 2016).

The large-scale structure of the basin modes themselves, but also their role in defining the phase for CTW propagation, suggests an impact of basin-mode-related dynamics on the boundary circulation off Angola. This topic is investigated in the present study by employing idealized simulations to reconstruct the observed seasonality of the Angola Current. Model-computed modal amplitudes are scaled to match modal amplitudes derived from velocity observations in the equatorial Atlantic. To do so, we primarily exploit a multi-year time series of top-to-bottom zonal velocity observations acquired at 23 °W-Equator. The mooring location appears advantageous for estimating the amplitudes of the gravest equatorial basin modes (*Brandt et al.*, 2016). However, similar studies conducted in the Indian Ocean have mentioned the potential importance of second basin modes, which are characterised by two amplitude maxima along the equator separated by a nodal point (*Han et al.*, 2011). Considering these second basin modes in the Atlantic, 23 °W is located in the proximity of their nodal point, which complicates the calculation of corresponding basin mode amplitudes. Therefore, complementary to 23 °W-Equator, we make use of zonal velocity observations available at 35 °W-Equator (*Send et al.*, 2002; *Hormann and Brandt*, 2009).

The paper is organized as follows: In section Section 6.2 the observational data sets used in this study are described. Section 6.3 introduces the basic equations, setup and forcing of the shallow water model experiments. The results section includes a brief description of the observed seasonal variability of the equatorial and eastern boundary circulation (Section 6.4.1), model validation (Section 6.4.2), a presentation of the horizontal structures of annual and semiannual oscillations associated with individual baroclinic modes (Section 6.4.3), as well as a description

of the reconstruction of the seasonal cycle of alongshore velocity off Angola using the shallow water model simulations (Section 6.4.4). A summary and discussion of the results is presented in Section 6.5.

6.2 Observational Data

In July 2013, a mooring array at ∼11 °S off Angola was deployed sampling velocity along the continental slope in the upper 500 m of the water column. The two most important components of the array, a mooring deployed at ∼1200 m depth (13°00'E, 10°50.0'S, Figure 6.1, termed "offshore" mooring in the following) and a bottom shield deployed at ∼500 m depth ("onshore" in the following) were recovered and redeployed in October 2015 (*Kopte et al.*, 2017). In October 2016, the 1200 m mooring was again recovered and redeployed, while the bottom shield was lost presumably due to elevated fishing activities. The mooring configuration was identical during both deployment periods. An upward-looking 75 kHz Teledyne RDI's Workhorse Long Ranger ADCP was mounted to the mooring cable at 500 m depth. The instrument measured velocity in the water column to about 45 m below the sea surface using 16 m bins.

As in *Kopte et al.* (2017), we use the delayed-time "all-sat-merged" data set of absolute geostrophic velocities derived from absolute dynamic topography as proxy for near-surface velocities (Figure 6.1). For this product multi-mission altimetry observations are mapped on a 0.25 ° × 0.25 ° grid provided on daily resolution (details on the mapping algorithm can be found in *Pujol et al.* (2016)). The data are distributed by the E.U. Copernicus Marine Service Information (`http://marine.copernicus.eu/`).

Additionally, for this study we make use of ocean velocity time series acquired along the equator at 23 °W and 35 °W. The 23 °W-Equator time series comprises a multi-year record of equatorial zonal velocity obtained from current meters deployed between 2004 and 2016. Merging nine

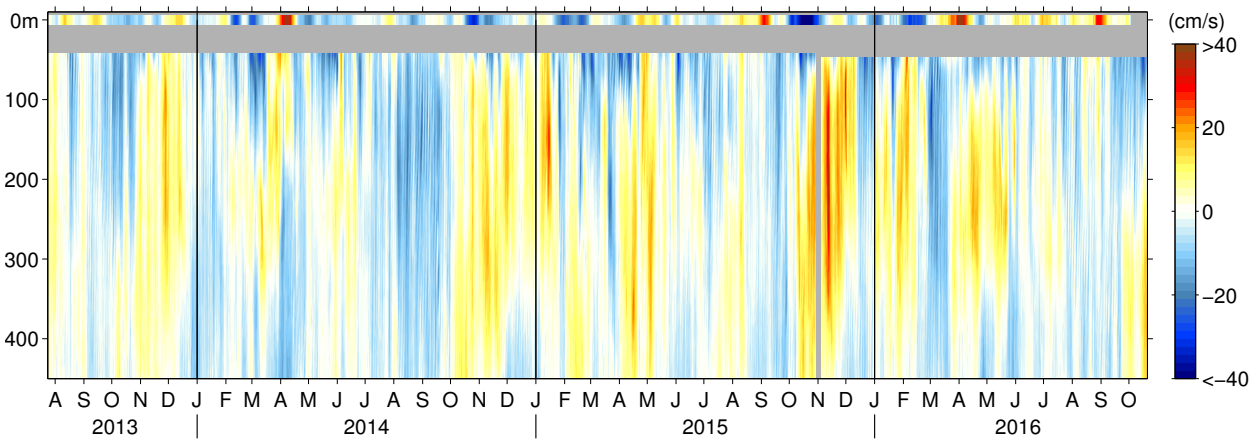

Figure 6.1: Time series of alongshore velocity (−34 °) as recorded by the moored ADCP located on the 1200 m isobath off Angola (13°00'E, 10°50.0'S). Positive values indicate equatorward and negative values indicate poleward flow. Surface values correspond to geostrophic alongshore velocities at the mooring location from altimetry.

successive deployment periods, this product is an updated version of the one presented in *Brandt et al.* (2016). It is composed of moored ADCPs profiling the upper 600 – 900 m of the water column, a few single-point current meters between 600 and 1000 m depth, as well as a McLane Moored Profiler (MMP) sampling between 1000 and 3500 m depth (for further details on the mooring setup see *Brandt et al.* (2016)). The time series used here also incorporates lowered-ADCP profiles taken during the mooring service cruises near the mooring position. Significantly fewer measurements are available at 35 °W-Equator. Here, the merged time series of zonal velocity contains moored ADCP data covering the upper 550 m depth between August 2004 and June 2006 (*Hormann and Brandt*, 2009) as well as data from three single-point current meters deployed at 652 m, 809 m, and 1107 m depth during the same period. Furthermore, deep velocity data are available recorded by four single-point current meters at 1290 m, 1490 m, 1690 m, and 1890 m depth between October 1992 and June 1994, that previously have been used to study the space-time structure of Equatorial Deep Jets (*Send et al.*, 2002). To improve the vertical coverage we incorporate nine lowered-ADCP as well as eight Pegasus profiles, that were acquired between 1 °N/S at 35 °W during several cruises and cover the seasonal cycle.

A 40-hour low pass filter was applied to all available ADCP data (sampling rates ranging from 0.5 h^{-1} to 3 day^{-1}), as well as to single-current meter data (sampling rate of 0.5 h^{-1}) to eliminate tidal currents. The MMP executed two successive profiles, an upcast followed by a downcast, every four or six days, with the two profiles separated by six hours. Here, no temporal filter was applied.

Finally, ADCP data from 11 °S-Angola were linearly interpolated on a 1-day × 5-m grid, while the velocity data acquired by different instrument types at 23 °W-Equator and 35 °W-Equator were merged on a regular 15-day × 10-m grid. Note the different total lengths of velocity time series obtained at the mooring locations, with the 23 °W-Equator mooring providing at least five years of zonal velocity data covering the whole water column, the 11 °S-Angola mooring yielding about three years of boundary current observations, while at 35 °W-Equator about two years of zonal velocity observations are available at distinct depth levels (Figure 6.2).

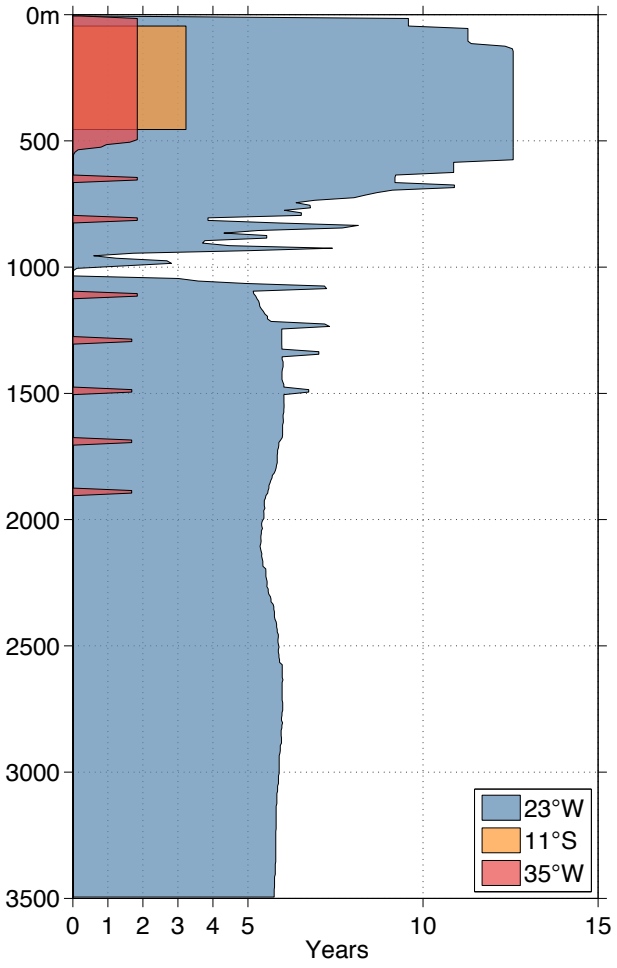

Figure 6.2: Length of the time series of available velocity data as function of depth for 23 °W-Equator (blue), 11 °S-Angola (orange), and 35 °W-Equator (red).

For the aspired decomposition of the velocity data from 23 °W-Equator and 35 °W-Equator into baroclinic modes we require a set of vertical structure functions. To obtain the latter, we first calculate buoyancy frequency profiles from shipboard CTD measurements acquired near 23 °W-Equator during the mooring service cruises. Vertical structure functions for an ocean depth of 4500 m are then derived from the averaged buoyancy frequency profile for the first five baroclinic modes (Figure 6.3a). These vertical modes are consistently used throughout our analysis.

6.3 Shallow water model simulations

To examine the role of remote equatorial versus local forcing as well as the potential impact of equatorial basin modes on the seasonality of the boundary circulation as observed at 11 °S-Angola, we employ a suite of linear shallow water models, each model representing the solution for a single baroclinic mode (e.g. *Gill* (1982)).

6.3.1 Basic equations

In spherical coordinates the governing equations associated with a particular baroclinic mode n are given by (see also *Greatbatch et al.* (2012); *Zhu et al.* (2017)):

$$\frac{\partial u_n}{\partial t} - f v_n = -\frac{g}{a\cos\theta}\frac{\partial \eta_n}{\partial \lambda} + \frac{\tau_s^x}{\rho H_E} G_n + F^u \tag{6.1a}$$

$$\frac{\partial v_n}{\partial t} + f u_n = -\frac{g}{a}\frac{\partial \eta_n}{\partial \theta} + \frac{\tau_s^y}{\rho H_E} G_n + F^v \tag{6.1b}$$

$$\frac{\partial \eta_n}{\partial t} + \frac{H_n}{a\cos\theta}\left[\frac{\partial u_n}{\partial \lambda} + \frac{\partial(\cos\theta v_n)}{\partial \theta}\right] = 0 \tag{6.1c}$$

where θ is latitude, λ is longitude, a is the radius of the earth, $f = 2\Omega\sin\theta$ is the Coriolis parameter with Ω being the angular speed of the earth, g is the acceleration due to gravity, ρ is a representative density for sea water. u and v correspond to the horizontal velocity components in the eastward and northward directions, respectively, while η represents the isopycnal displacement. (F^u, F^v) is the lateral mixing of momentum with horizontal eddy viscosity coefficient, A_h, given by

$$F^u = \frac{A_h}{a^2}\left[\frac{1}{\cos^2\theta}\frac{\partial^2 u}{\partial \lambda^2} + \frac{1}{\cos\theta}\frac{\partial}{\partial\theta}\left(\cos\theta\frac{\partial u}{\partial\theta}\right) + u\left(1-\tan^2\theta\right) - \frac{2\sin\theta}{\cos^2\theta}\frac{\partial v}{\partial\lambda}\right] \tag{6.2a}$$

$$F^v = \frac{A_h}{a^2}\left[\frac{1}{\cos^2\theta}\frac{\partial^2 v}{\partial \lambda^2} + \frac{1}{\cos\theta}\frac{\partial}{\partial\theta}\left(\cos\theta\frac{\partial v}{\partial\theta}\right) + v\left(1-\tan^2\theta\right) - \frac{2\sin\theta}{\cos^2\theta}\frac{\partial u}{\partial\lambda}\right] \tag{6.2b}$$

Furthermore, H_n is the equivalent depth set by the wave speed $c_n = \sqrt{gH_n}$ associated with baroclinic mode n. (τ_s^x, τ_s^y) typically (see details later) represents the surface wind stress vector that acts as a body force with vertical structure $G(z)$, where z is the vertical coordinate measured

positive upwards. $G_n = \frac{1}{H}\int_{-H}^{0} G(z)\hat{p}_n(z)\,dz$ is the dimensionless wind forcing profile projection factor, with $\hat{p}_n(z)$ representing the corresponding vertical structure function. Structure functions (Figure 6.3a) have been normalized so that $H = \int_{-H}^{0} (\hat{p}_n(z))^2\,dz$. Choosing an approach similar to *Zhu et al.* (2017), we first solve the equations for $G_n = 1$, and then obtain realistic projection coefficients by fitting model-computed modal amplitudes to modal amplitudes derived from observed velocities at 23 °W-Equator and 35 °W-Equator (see Section 6.3.3).

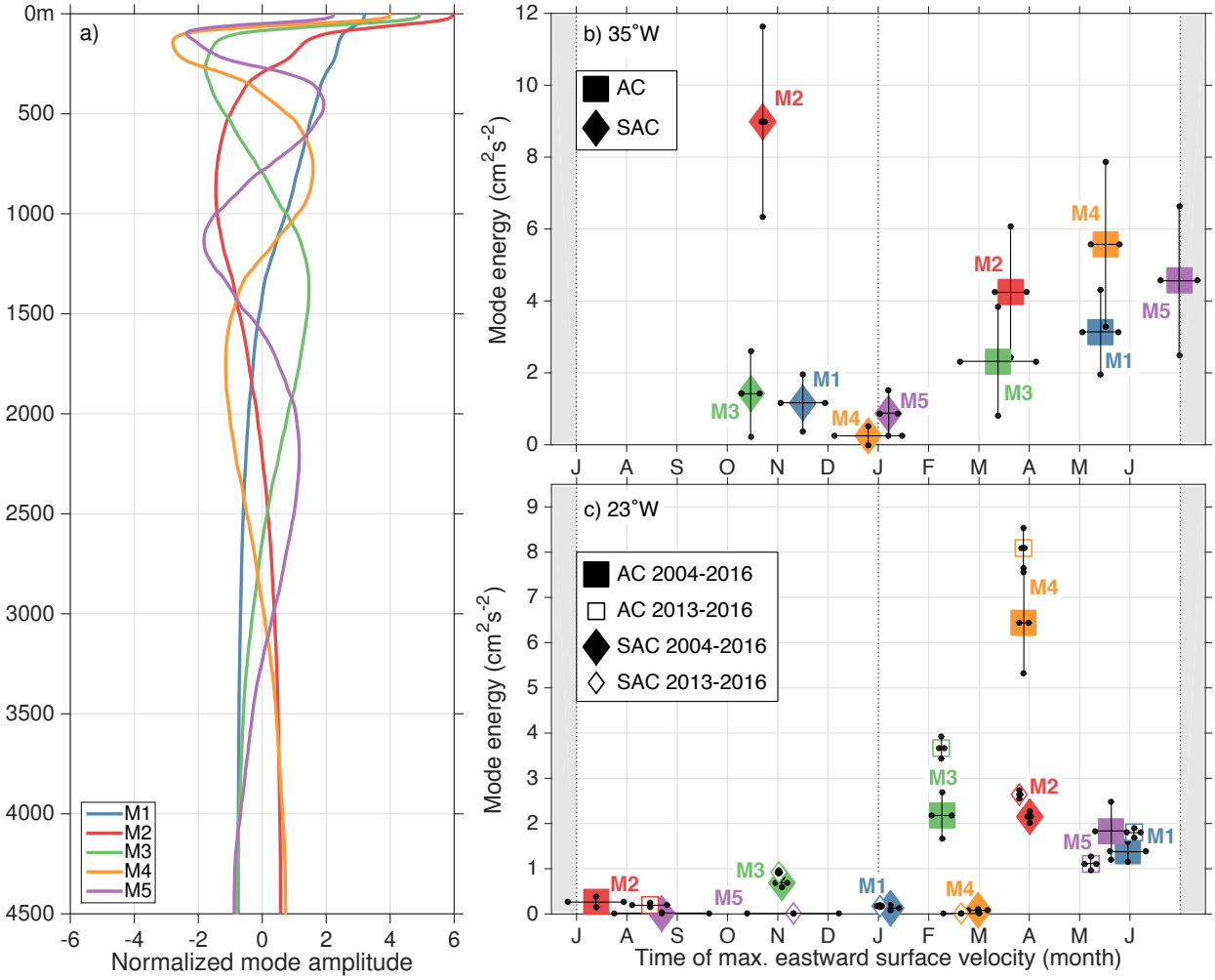

Figure 6.3: (a) Vertical structure functions of the first five baroclinic modes derived from a mean Brunt-Väisälä frequency profile calculated from CTD profiles near 23 °W-Equator. Normalization is carried out with respect to the standard deviations of the structure functions. Modal amplitudes of the energy of annual (squares) and semiannual (diamonds) cycles of the observed zonal velocity at 35 °W-Equator (b) and 23 °W-Equator (c) are plotted at the mode's time of maximum eastward surface velocity. Note that, for the sake of clarity, only one of the two maxima of the semiannual cycle is shown in (b) and (c). Errorbars correspond to standard deviations of energy and phase accounting for uncertainties due to incomplete data sets (for details on the mode projection see text). In (c) mode projection is carried out considering the full length of the time series (filled symbols) as well as a subset of the time series (open symbols) that corresponds to the period of moored observations at 11 °S-Angola (2013-2016).

6.3.2 Model setup and forcing

We set up a model domain for the Atlantic Ocean extending from 60 °W to 15 °E in the zonal and 34 °S to 25 °N in the meridional direction. The 1000 m isobath represents the coastline. Both model boundaries and coastlines are treated as solid walls. Along the northern and southern boundaries of the model domain sponge layers with e-folding scale of 2.5 ° latitude are applied to inhibit Kelvin wave propagation. The model has a horizontal resolution of 0.25 ° both in longitude and latitude. The scale depth H_E is chosen to be 500 m, which is an arbitrary choice, as the actual value of H_E will only affect the scaling factor G_n in the fitting procedure. Lateral eddy viscosity is set to $A_h = 300\,\mathrm{m^2\,s^{-1}}$ (*Claus et al.*, 2014; *Brandt et al.*, 2016).

Model simulations are carried out with varying gravity wave speeds representing the first five baroclinic modes. Either annually or semiannually oscillating forcing is applied to the momentum equations with each shallow water model being run for 11 years, which is sufficient for the model to reach equilibrium. The oscillating solution of the eleventh integration year is stored for further analysis. In order to distinguish between the role of the equatorial forcing that eventually excites resonant equatorial basin modes and the role of local forcing off Angola we carry out two sets of simulations that differ in the applied forcing.

In the first set of model simulations, the forcing is derived from oscillating wind stress (including both the zonal and meridional components) applied to the entire model domain. These runs therefore include the equatorial forcing potentially exciting equatorial basin modes as well as any local forcing that might be relevant at 11 °S-Angola (hereafter referred to as "EF+LF"). Equivalent runs are carried out using four different wind products with differing horizontal resolutions (Table 6.1). For consistency, annual and semiannual wind stress cycles are calculated from wind stress data between March 2007 and June 2016 for each wind product. As a starting point, a first realization of simulations driven by JRA-55 wind stress data *Japan Meteorological Agency* (2013) was obtained using gravity wave speeds as in *Brandt et al.* (2016). We then carried out sensitivity experiments by modifying the prescribed phase speeds for each baroclinic mode, aiming at improving the agreement between observed and model-computed phases at 23 °W-Equator (Figure 6.4 and Table 6.2). This approach is justified, as several factors not accounted for in the linear shallow-water model might affect the gravity wave speed such as background mean flow

Wind product	Horiz. resolution (°)	BF	Reference
JRA-55	0.5	x	*Japan Meteorological Agency* (2013)
Ascat	0.25	x	*Ricciardulli and Wentz* (2016)
ERA/INTERIM	0.25		*Berrisford et al.* (2009)
NCEP-DOE AMIPII	∼1.9	x	*Kanamitsu et al.* (2002)

Table 6.1: Wind products used for forcing the EF+LF shallow water model simulations. Crosses in column "BF" indicate when wind stress data was calculated based on available wind speed data via bulk formula $\vec{\tau} = \rho_a \cdot c_D \cdot \vec{u}_{10}^2$ with $\rho_a = 1.22\,\mathrm{kg\,m^{-3}}$ and $c_D = 0.0013$.

Baroclinic mode n	Gravity wave speed c_n ($\mathrm{m\,s^{-1}}$)
1	2.47 (2.47)
2	1.43 (1.32)
3	0.89 (0.95)
4	0.68 (0.74)
5	0.57 (0.57)

Table 6.2: Gravity wave speeds c_n ($\mathrm{m\,s^{-1}}$) for baroclinic modes 1-5 used in the shallow water model simulations. In brackets gravity wave speeds as used in *Brandt et al.* (2016) are shown. See also Figure 6.4.

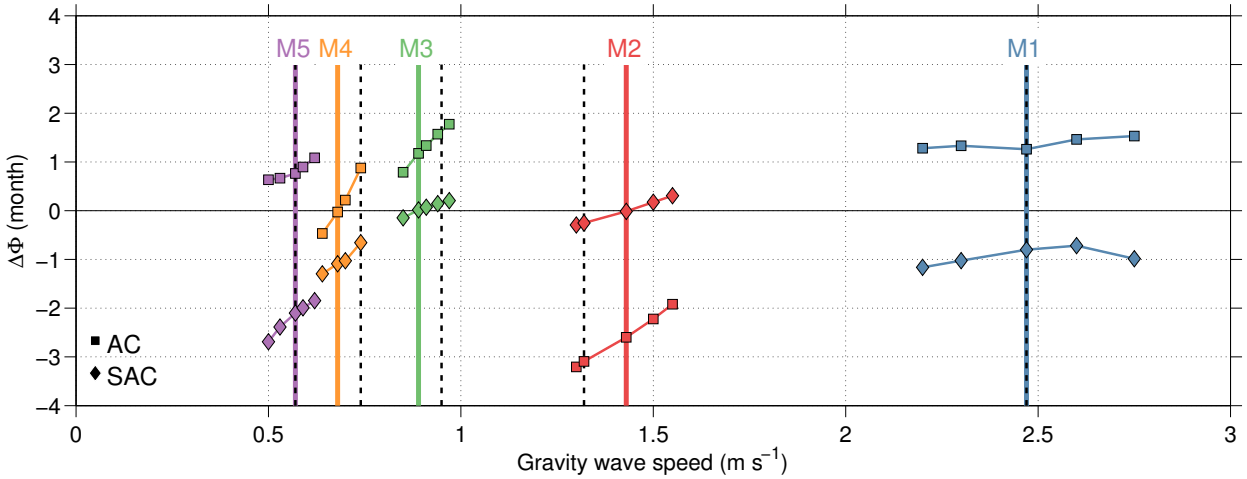

Figure 6.4: Local phase differences between observed and model-computed annual (squares) and semiannual (diamonds) cycles at 23 °W-Equator as function of the prescribed gravity wave speed for the first five baroclinic modes. Vertical solid colored lines correspond to gravity wave speeds used for the remainder of the study, vertical dashed black lines are associated with theoretical gravity wave speeds used in *Brandt et al.* (2016). See also Table 6.2.

and nonlinear effects. Moreover, the gravity wave speed is treated as being constant across the basin by our model – a simplification that cannot be met in reality due to large-scale changes in stratification and mean flow. Gravity wave speeds for the first and fifth baroclinic mode are left unchanged. An improved agreement of observed and model-computed semiannual cycle is found for the second baroclinic mode when increasing the gravity wave speed by $0.11\,\mathrm{m\,s^{-1}}$ and for third baroclinic mode when decreasing the gravity wave speed by $0.06\,\mathrm{m\,s^{-1}}$. These adjustments only marginally change the phase differences for the corresponding annual cycles. Likewise, decreasing the gravity wave speed of the fourth baroclinic mode by $0.06\,\mathrm{m\,s^{-1}}$ minimizes the phase difference for the annual cycle (Figure 6.4).

In a second set of simulations, the model is forced by a zonally uniform zonal forcing oscillating at either annual or semiannual frequency and restricted to the equatorial band (hereafter referred to as "EF-only"). Following *Greatbatch et al.* (2012), the forcing (τ_s^x in Equation (6.1a)) is given by

$$\tau_s^x = X_0 \exp\left(-\frac{\beta y^2}{2c_n}\right) \sin(\omega t) \tag{6.3}$$

where $y = a\theta$, $\beta = 2.3 \times 10^{-11}\,\mathrm{m^{-1}\,s^{-1}}$ is the meridional gradient of f at the equator, $\omega = 2\pi/T_B$ is the forcing frequency with T_B being either the annual or semiannual period, and X_0 being the amplitude. The results are independent of the choice of the amplitude, as the model-computed modal amplitudes (as well as the phases) from the EF-only runs are adjusted to reach agreement with the EF+LF runs at 23 °W-Equator. By excluding the local forcing at the eastern boundary, the EF-only runs assist in evaluating the relative importance of remote equatorial and local forcing for the seasonality of the eastern boundary circulation off Angola.

6.3.3 Scaling of model-computed modal amplitudes

As noted in Section 6.3.1, the forcing profile projection factors G_n are not assumed a priori, but remain to be determined through the fitting of model-computed modal amplitudes to suitable observations. As stated earlier, we primarily make use of a multi-year time series of top-to-bottom zonal velocity at 23 °W-Equator, which is most suitable for modal decomposition of the velocity signal. The decomposition is carried out by consecutively projecting the vertical structures associated with one particular baroclinic mode (Figure 6.3a) multiplied with either the annual or semiannual cycle onto the time series of observed zonal velocity. As the time series contains some gaps particularly at deeper levels, the orthogonality of the projected modes is not ensured. Therefore, the first 20 baroclinic modes are fitted in random order with the resulting contribution of the corresponding baroclinic mode being subtracted from the velocity signal before fitting the next mode. Repeating this procedure for 10000 random permutations of the fitting order yields estimates of the most probable mode energies and phases and associated uncertainties (Figure 6.3c). To test the robustness particularly with regard to the phase distribution, the modal decomposition is carried out once for annual and semiannual components derived using the total length of the time series and once using only the 2013-2016 period, with the latter corresponding to the mooring observation period at 11 °S-Angola. We note the dominance of the fourth baroclinic mode for the annual cycle and the second baroclinic mode for the semiannual cycle as discussed by *Brandt et al.* (2016), but also the stability of these modes in terms of energy and phase lock when comparing results from different observation periods (Figure 6.3c). However, a relative increase of the energy associated with the third and fourth baroclinic mode for the annual cycle is found when considering the 2013-2016 period. Here, an anomalously deep reaching Equatorial Undercurrent during the second half of 2015 (not shown) most likely results in an enhanced projection of the annual cycle onto these modes. Nevertheless, overall we find a consistent mode energy-phase distribution for both annual and semiannual cycles derived using different reference periods. Complementary, the modal decomposition is also carried out for the velocity time series acquired at 35 °W-Equator (Figure 6.3b). As the latter is limited both in temporal and vertical coverage, the modal characteristics are determined for the first

five baroclinic modes only, based on 120 random permutations of the fitting order. Similar to 23 °W-Equator, the fourth and second baroclinic modes are found to be dominating the annual and semiannual cycle, respectively. Interestingly, at 35 °W-Equator the second baroclinic mode at the semiannual period exhibits highest energy, while the dominance of the fourth baroclinic mode at the annual period seems not as striking as at 23 °W-Equator. However, given the comparably sparse sampling particularly of the deep ocean, uncertainties of derived amplitudes and phases are substantially larger at 35 °W than at 23 °W (Figure 6.3).

Oscillation amplitudes obtained from the modal decompositions at 23 °W-Equator and 35 °W-Equator are now used to quantify the forcing profile projection coefficients G_n. This is achieved by fitting model-computed modal amplitudes of the zonal velocity component from the EF+LF runs either at 23 °W-Equator or 35 °W-Equator to the corresponding modal amplitudes derived from observations. By fitting only the amplitudes but leaving model-computed phases unchanged, this approach is equivalent to a scaling of the model output with the ratio of observed and simulated amplitudes derived either at 23 °W-Equator or 35 °W-Equator.

To focus on the relative importance of equatorial and local forcing, modal amplitudes and phases from the EF-only runs are fitted to the scaled modal amplitudes and unaltered phases from the EF+LF runs at 23 °W-Equator. Following this approach, EF+LF and EF-only runs agree locally at 23 °W-Equator, and differences between EF+LF runs and EF-only runs at 11 °S-Angola can be related to the impact of local forcing that is retained in the EF+LF runs.

Amplitude-scaled shallow water model simulations from the EF+LF runs differing only by the applied forcing product are assessed in terms of their capability to reproduce the annual and semiannual cycles as observed at the equatorial mooring positions (Section 6.4.2). EF+LF simulations with the best-suited forcing product are then used, in comparison to the corresponding EF-only runs, to investigate the contribution of single baroclinic modes to annual and semiannual cycles at 11 °S off Angola. However we note, although the model-computed modal amplitudes are scaled to match observed modal amplitudes either at 23 °W-Equator or 35 °W-Equator, elsewhere they do depend on several aspects of the model configuration, such as the applied damping or the capture of the resonance characteristics as a function of basin geometry and chosen phase speeds.

6.4 Results

6.4.1 Frequency spectra of observed velocity fields at 23 °W-Equator and 11 °S-Angola

As noted by *Brandt et al.* (2016) the zonal velocity field at 23 °W-Equator is dominated by the seasonal cycle as well as interannual variations associated with the Equatorial Deep Jets. Here we focus on the seasonal cycle in the upper 450 m depth, chosen as a consistent depth range in which velocity observations are also available off Angola. As the longest time series at 11 °S-Angola

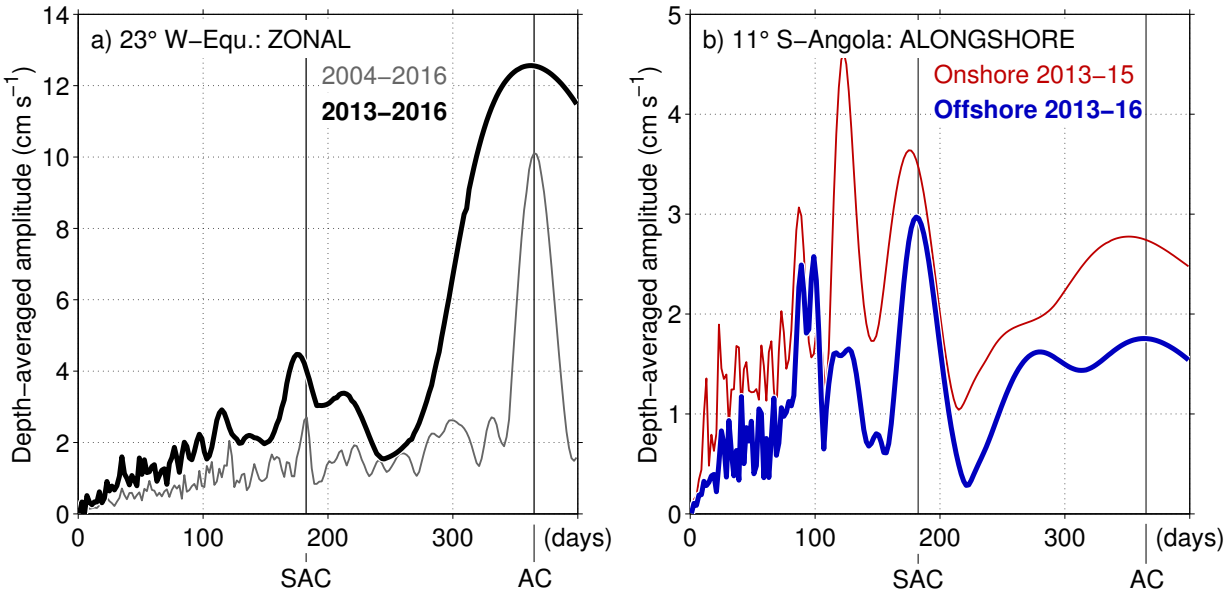

Figure 6.5: Mean frequency spectra in the 45 – 450 m depth range of observed (a) zonal velocity at 23 °W-Equator and (b) alongshore velocity at 11 °S-Angola for different moorings and/or time spans. Spectra are calculated by fitting harmonic functions to the time series at each depth level between 45 and 450 m followed by vertical averaging.

covers only about 3.25 years (Figure 6.2), consistent frequency spectra are obtained by applying harmonic fits to the zonal and alongshore velocity time series for each depth level at 23 °W-Equator and 11 °S-Angola, respectively, followed by vertical averaging of harmonic amplitudes over the chosen depth range (Figure 6.5). While the annual component clearly is the main contributor to the seasonal cycle of zonal velocity at 23 °W-Equator (Figure 6.5a), at 11 °S-Angola the relative importance of the semiannual compared to the annual cycle of alongshore velocity is strongly enhanced (Figure 6.5b). Furthermore, the frequency spectra derived from the first deployment period of the onshore ADCP off Angola reveals a strong component near 120 days. However, this peak is neither as pronounced in the spectra calculated from the first deployment period for the offshore ADCP (not shown) nor in the spectra for the offshore ADCP when combining both deployment periods. Here, distinct peaks are found near 90 and 100 days, most likely associated with a period of enhanced intraseasonal variability in the alongshore flow between December 2015 and April 2016 (Figure 6.1). As the permanence and recurrence of these intraseasonal oscillations as well as their associated forcing mechanisms are difficult to assess with the available data set, in the following we restrict our analysis to annual and semiannual oscillations.

6.4.2 Reconstruction of annual and semiannual cycles of zonal velocity at the equator using shallow water model simulations

As described in Section 6.3.3, model-computed amplitudes are scaled against amplitudes derived from modal decompositions of the annual and semiannual cycles of the observed zonal velocity at

23 °W-Equator or 35 °W-Equator. A set of equivalent EF+LF shallow water model simulations is carried out differing only by the applied wind forcing product (Table 6.1) in order to assess the dependency of the model runs on the chosen forcing product to reproduce the seasonal cycle of zonal velocity along the equator. The projection coefficients G_n, which correspond to the scaling factor for model-computed modal amplitudes, provide a measure on how much energy input is needed to reproduce observed amplitudes of annual and semiannual oscillations. Therefore, G_n is not only a function of the wind energy input, but also depends critically on how realistically the model reproduces the resonance characteristics (see also *Greatbatch et al.* (2012); *Brandt et al.* (2016)). The latter depend on several parameters of the model configuration such as basin geometry, dissipation and gravity wave speeds. A comparison of projection coefficients depending on the wind forcing product and the oscillation period does reveal a clustering for coefficients derived from scaling model-computed modal amplitudes at 23 °W-Equator for similar baroclinic modes and oscillation periods (Figure 6.6a). In general, there is only a weak dependence on the chosen forcing product. However, some larger differences between the products for particular baroclinic modes should be noted. For example, the coefficients for the second baroclinic mode, annual cycle or the fourth baroclinic mode, semiannual cycle associated with ERA/INTERIM forcing are about a factor three smaller or larger compared to the corresponding coefficients associated with the other forcing products. This means that a different energy input is necessary to reproduce the observed amplitudes for the corresponding baroclinic modes when forcing the model with oscillating wind stress derived from ERA/INTERIM compared to the other wind products. As our EF+LF model simulations differ only in the applied wind forcing, the findings demonstrate the uncertainties in the representation of specific aspects of the equatorial Atlantic circulation when forcing ocean models with one particular wind-forcing product. Similar projection coefficients are derived from scaling model-computed amplitudes at 35 °W-Equator, which can differ significantly from their counterparts at 23 °W-Equator (Figure 6.6a). These differences might result partly from the less robust modal decomposition at 35 °W-Equator. Furthermore, 35 °W-Equator might not be ideal in representing the large-scale basin mode structure of the gravest basin mode, as the mooring position is located either within an area of strongly changing or low amplitudes.

Model-computed phases from EF+LF runs are not fitted to observations. Therefore, the difference of observed and simulated phases represents another indicator on how well the models are able to reproduce observed annual and semiannual oscillations locally at 23 °W-Equator depending on the applied wind-forcing product (Figure 6.6b). Again, concerning the phase differences only minor dependencies on the applied wind forcing are found at least for baroclinic modes with significant energy at 23 °W-Equator (compare Figure 6.3c). Phase differences at 35 °W-Equator are generally larger (Figure 6.6b), as expected keeping in mind that gravity wave speeds are optimized for local agreement at 23 °W-Equator. Yet again, smallest phase differences are observed for the dominant baroclinic modes that are close to equatorial resonance. For the remainder of the study we decided on comparing simulations forced by annual and semiannual oscillations

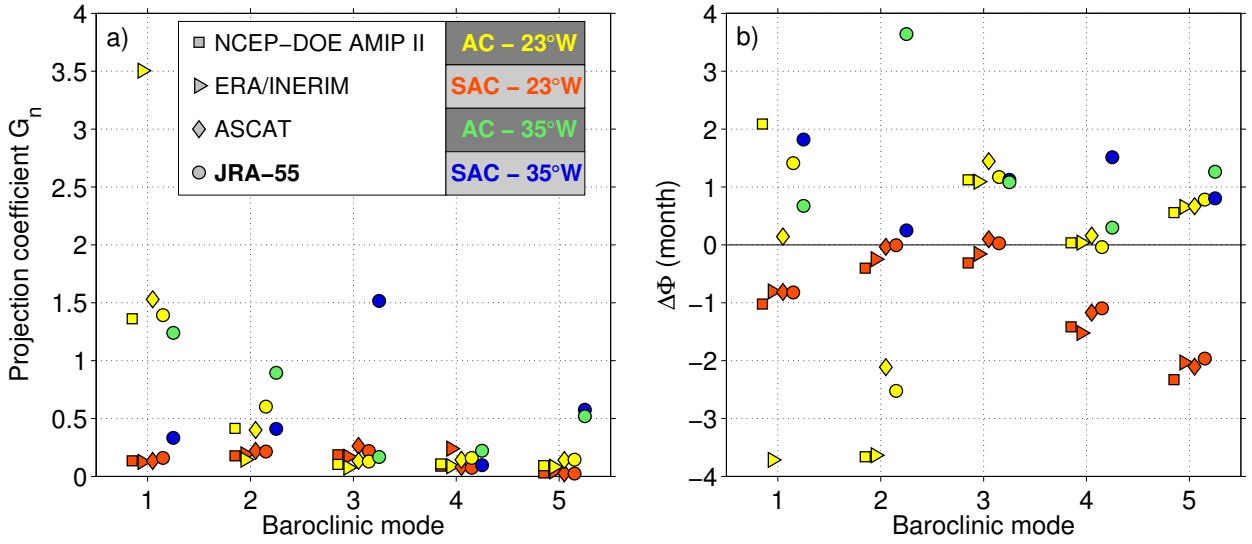

Figure 6.6: (a) Dimensionless projection coefficients G_n for EF+LF simulations being forced by different wind products. Projection coefficients are computed by fitting model-computed amplitudes to amplitudes derived from projecting the corresponding baroclinic mode on annual and semiannual cycles of observed zonal velocity at 23 °W-Equator (yellow and red, respectively), and 35 °W-Equator (only shown for JRA55 forcing, green and blue, respectively). Model-computed phases are not fitted but remain solely determined by the applied wind forcing and model characteristics. In (b) local phase differences between EF+LF shallow water model simulations and observed modal semiannual and annual cycles are shown; colors and symbols as given in (a).

Baroclinic mode n	G_n - Annual cycle	G_n - Semiannual cycle
1	1.39 (1.24)	0.16 (0.33)
2	0.60 (0.89)	0.21 (0.41)
3	0.13 (0.17)	0.22 (1.51)
4	0.16 (0.22)	0.07 (0.09)
5	0.14 (0.52)	0.02 (0.57)

Table 6.3: Dimensionless projection coefficients G_n for EF+LF simulations being forced by Fourier components of JRA-55 wind stress data corresponding to annual (middle column) and semiannual (right column) oscillations as obtained from scaling model-computed amplitudes locally at 23 °W-Equator. In brackets corresponding projection coefficients derived from scaling model-computed amplitudes locally at 35 °W-Equator are displayed.

derived from the JRA-55 wind stress data and scaled locally at 23 °W-Equator to our observations from the equatorial moorings and 11 °S-Angola, as these simulations generally yield best phase agreement to the observations at 23 °W-Equator (for corresponding projection coefficients see Table 6.3).

As a first test for our chosen set of EF+LF simulations, we compare the observed vertical structure of annual and semiannual cycles both at 35 °W-Equator and 23 °W-Equator to the linear superposition of shallow water model simulations of the first five baroclinic modes with wind forcing of the corresponding oscillation period (Figure 6.7). The observed annual cycle of zonal velocity at 23 °W-Equator (Figure 6.7c) is characterized by a phase jump at 70 to

80 m depth accompanied by maximum annual amplitudes above and below, mirroring the annual cycle in EUC core depth (*Brandt et al.*, 2016). Deeper in the water column, significant annual amplitudes are found down to about 2500 m water depth. The superposition of annually oscillating shallow water model simulations for the first five baroclinic modes reveals a very similar behavior, showing zero amplitude at 70 – 80 m depth surrounded by maxima above and below, however not as vertically confined as in the observations (Figure 6.7d). According to Figure 6.3c the pattern of annual amplitudes is mainly determined by the fourth baroclinic mode. However, due to discrepancies in the model-computed phases particularly for the third and fifth baroclinic mode (Figure 6.6b), a phase shift in the distribution of annual amplitudes is clearly visible compared to the observations. The observed vertical structure of semiannual amplitudes at 23 °W-Equator (Figure 6.7g) is dominated by the second baroclinic mode (Figure 6.3c, *Brandt et al.* (2016)) and

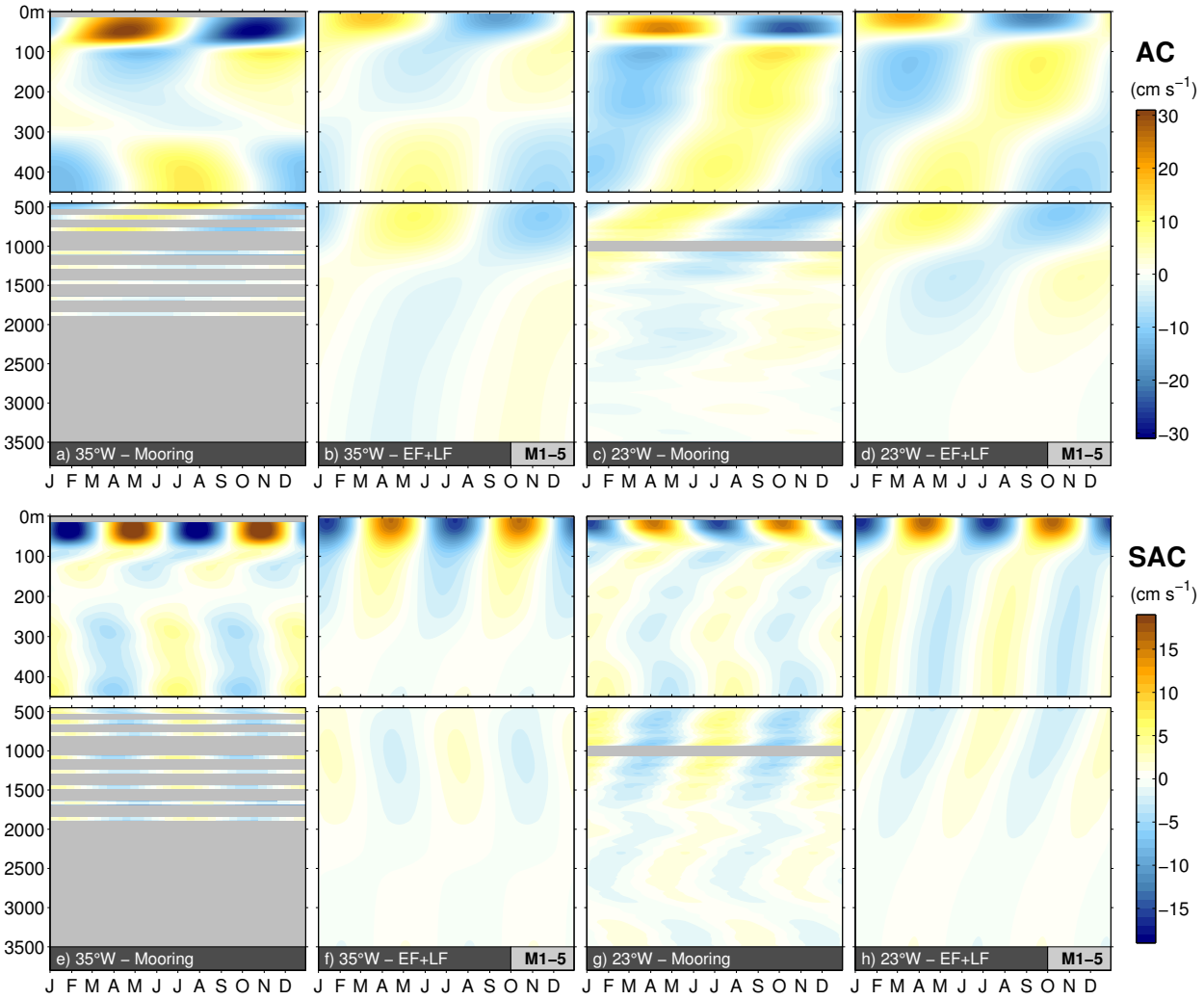

Figure 6.7: Annual and semiannual cycles of zonal velocity (cm s^{-1}) at 35 °W-Equator and 23 °W-Equator as reconstructed by fitting annual (a and c) and semiannual (e and g) harmonics to the observed velocity field, and by superposition of the first 5 baroclinic modes from the EF+LF shallow water model simulations forced with annually (b and d) and semiannually (f and h) oscillating wind stress. Model-computed amplitudes are scaled with respect to observations obtained at 23 °W-Equator.

accordingly is characterized by near-surface amplitude maxima. Below, compared to the annual cycle, the vertical structure is less complex, consistent with the dominance of lower baroclinic modes. The reconstruction using semiannually oscillating shallow water model simulations shows a very similar amplitude distribution compared to the observations both in magnitude and phase. This is attributable to the precise simulation of the second baroclinic mode with the remaining modes having only minor influence on the semiannual cycle. In fact, for the semiannual cycle baroclinic modes 1, 3, 4, and 5 are characterized by energies of less than $0.7\,\mathrm{cm^2\,s^{-2}}$, while the second baroclinic mode exhibits about $2.3\,\mathrm{cm^2\,s^{-2}}$ (Figure 6.3c). Nevertheless, we note that the reconstructed semiannual cycle from shallow water model simulations lacks amplitude and structure in the deep ocean below 2000 m depth. The same comparison is carried out for annual and semiannual components in zonal velocity at 35 °W-Equator (Figure 6.7 a, b and e, f, respectively). Note again that projection coefficients obtained at 23 °W-Equator are used for scaling of model-computed modal amplitudes. For the annual cycle this results in a slightly weaker simulated annual cycle, although observed and simulated baroclinic structures bear important similarities. The semiannual cycle at 35 °W-Equator is well reproduced by our simulations in terms of amplitude. Here the largest differences are found in the depth range between 100 and 300 m depth, where the semiannual cycle reconstructed from observations shows stronger baroclinicity. Observed and reconstructed vertical structures at 35 °W-Equator still look rather similar, although overall larger discrepancies are found compared to 23 °W-Equator. These discrepancies might be explained with generally larger differences between observed and model-computed phases at 35 °W-Equator (Figure 6.6b). Nonetheless, the results from the reconstruction of annual and semiannual cycles of zonal velocity at 23 °W-Equator and 35 °W-Equator encourages us to evaluate the models further for their basin-wide structures and particularly at 11 °S-Angola.

6.4.3 Horizontal structure of annual and semiannual oscillations

In a next step we explore the horizontal distribution of amplitude (Figure 6.8) and phase (Figure 6.9) of simulated annual and semiannual oscillations in order to identify baroclinic modes relevant at 11 °S off Angola. For this purpose we use the EF-only simulations that show the impact of purely equatorial forcing off the coast of Angola. The horizontal structures are generally characterized by elongated amplitude maxima along the equator; in the eastern part of the basin regions of enhanced amplitude are partly being deflected to the south. Largest amplitudes are obtained for the second baroclinic mode, semiannual cycle and the fourth baroclinic mode, annual cycle showing maximum amplitude of zonal velocity oscillation at the equator in mid-basin. As discussed in *Brandt et al.* (2016), for these combinations of baroclinic mode and forcing period the equatorial ocean is close to resonance, thus forming equatorial basin modes. Similar simulations for a rectangular ocean basin resulted in symmetric amplitude structures (*Brandt et al.*, 2016; *Han et al.*, 2011). Including a realistic coastline generates the effect of asymmetric structures due to the presence of the Gulf of Guinea and the northwestward slanted

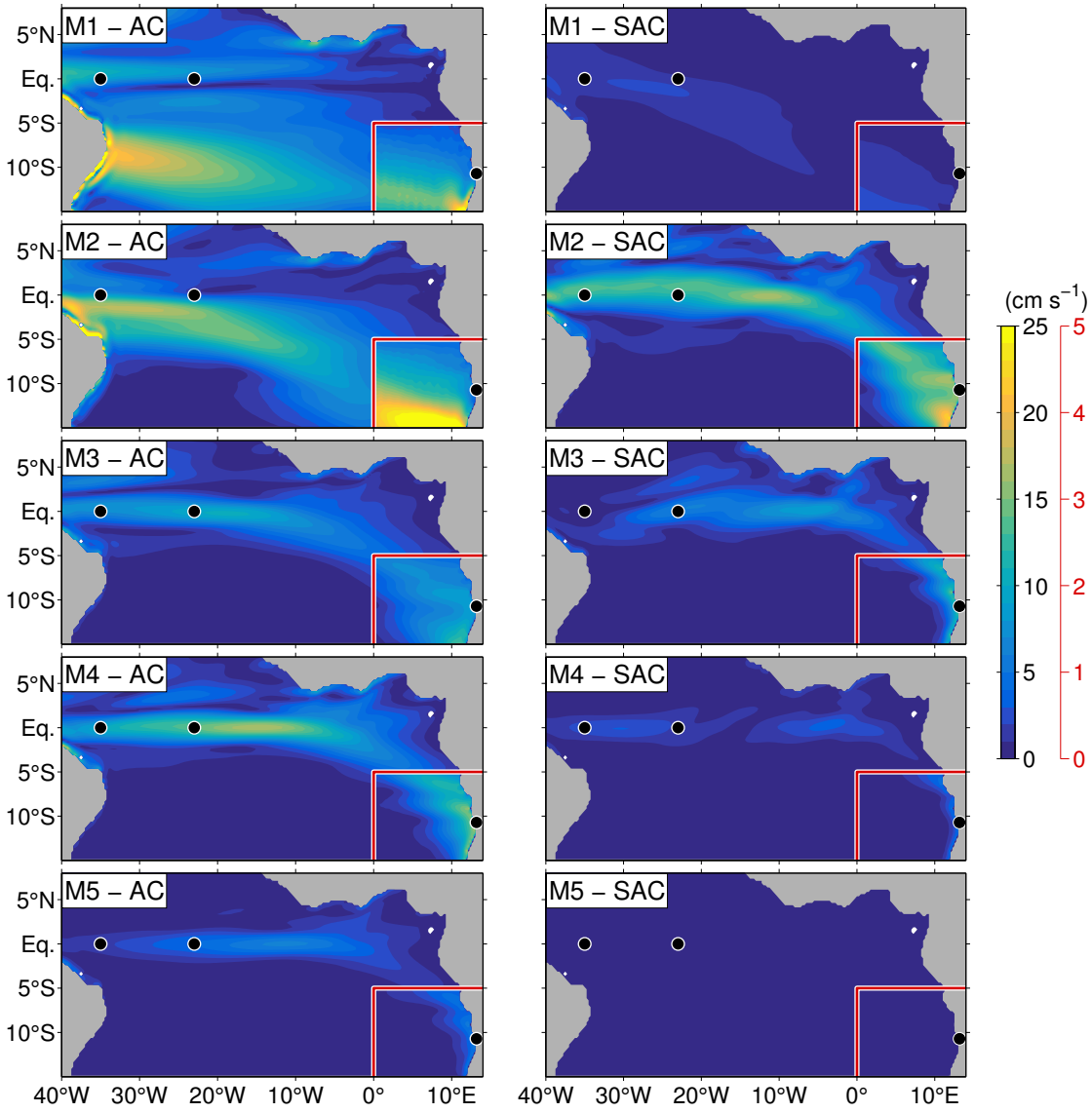

Figure 6.8: Amplitudes of annual (left) and semiannual (right) cycles of surface zonal velocities for baroclinic modes 1-5 from the EF-only runs. Within the rectangle in the southeastern corner of the domain corresponding amplitudes of meridional velocity are shown (associated with the red color scale). Black dots denote mooring locations at 35 °W-Equator, 23 °W-Equator, and 11 °S-Angola.

coastline of equatorial Brazil. The horizontal structures of the amplitude and phase for other combinations of baroclinic mode and forcing period can strongly deviate from the basin mode structure (see, e.g., patterns of the first baroclinic mode). For the fourth baroclinic mode, semiannual cycle a different pattern is found, which is characterized by two amplitude maxima along the equator separated by a nodal point in mid-basin. It can be associated with a second basin mode. In any case, enhanced amplitudes of higher baroclinic modes are more confined to the equator in their meridional extent (Figure 6.8). Note that Figure 6.8 displays the amplitudes of the modes' surface velocity, where the second baroclinic mode has the largest expression (compare Figure 6.3a). In the subsurface the relative importance of different baroclinic modes varies depending on their vertical structure. The corresponding phase distributions reveal generally

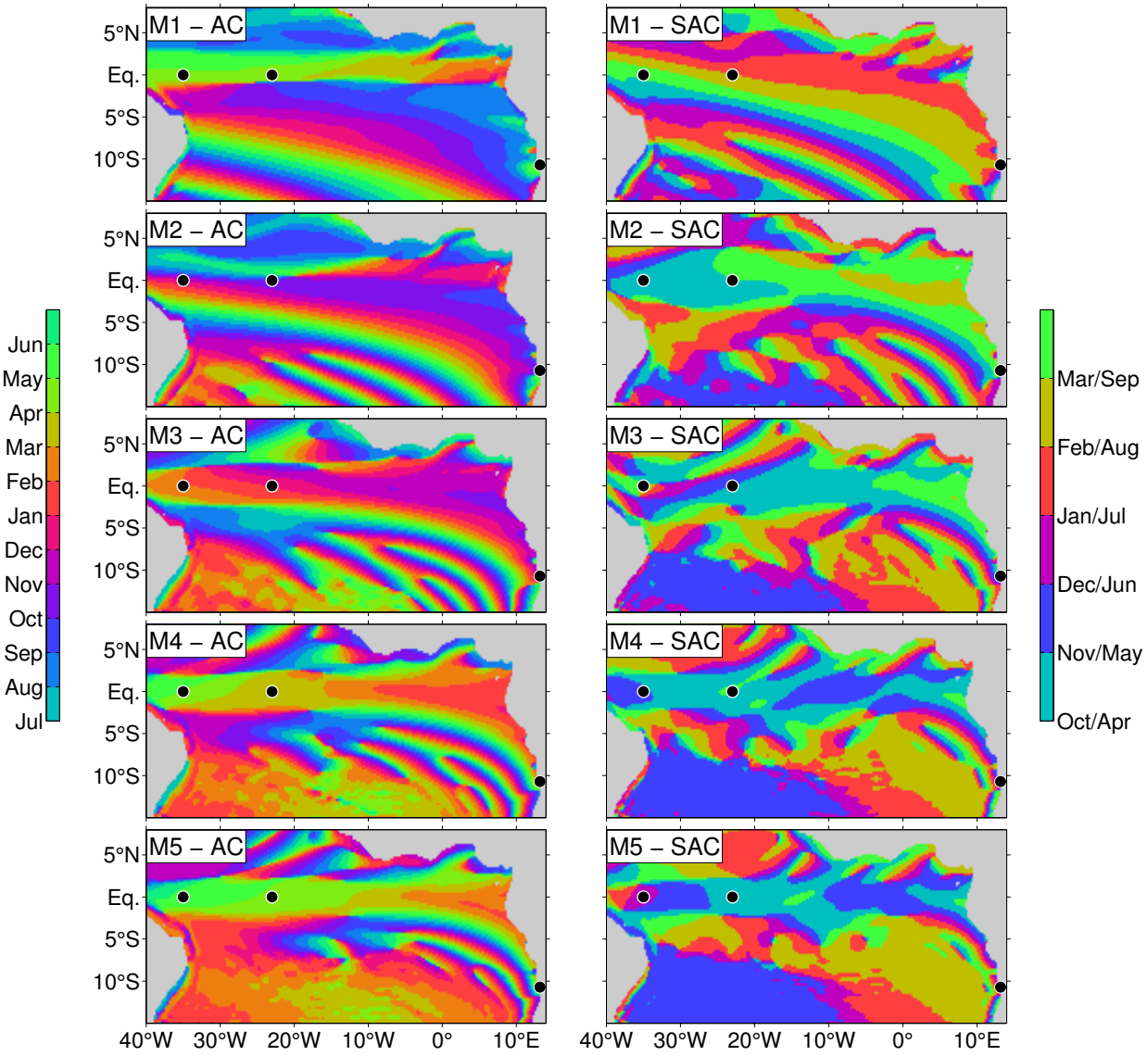

Figure 6.9: Month of maximum eastward surface velocity of annual (left) and semiannual (right) cycles for baroclinic modes 1-5 from the EF-only runs associated with amplitude patterns shown in Figure 6.8). Within the rectangle in the southeastern corner of the domain corresponding times of maximum southward surface meridional velocity are shown. Black dots denote mooring locations at 35 °W-Equator, 23 °W-Equator, and 11 °S-Angola.

westward phase propagation (Figure 6.9). The patterns of both amplitude and phase distributions indicate that velocity oscillations induced by the purely equatorial forcing have a role to play at the coast off Southwest Africa. There, alongshore velocities have a dominant meridional component. Therefore, the amplitude of the meridional velocity is displayed in the southeastern corner of the domain in Figure 6.8. Whether a particular baroclinic mode affects the velocity at 11 °S-Angola apparently depends on the meridional extent and associated shape of the southward deflection of the amplitude maximum as well as on the mode's energy as determined at 23 °W-Equator. The fourth and second baroclinic modes, being found to dominate the annual and semiannual cycles in zonal velocity both at 23 °W-Equator and 35 °W-Equator, respectively, also appear to dominate the annual and semiannual cycles in meridional velocity at 11 °S-Angola. Simulations

for baroclinic modes closest to equatorial resonance are generally found to exhibit appropriate amplitudes to influence the meridional velocity near the coast at 11 °S, i.e. baroclinic modes 3-5 and 1-3 for the annual and semiannual cycle, respectively. However, for the semiannual cycle the near-coastal amplitude maximum of meridional velocity is located south of 11 °S-Angola for the first and second baroclinic modes suggesting an even stronger impact of the equatorial forcing further away from the equator. Particularly the first baroclinic mode exhibits low amplitude at the semiannual period at 11 °S-Angola. Instead, the second basin mode of the fourth baroclinic mode is likely to play a role.

6.4.4 Observed and reconstructed annual and semiannual cycles of alongshore velocity at 11 °S-Angola

The annual and semiannual components at 11 °S-Angola are derived by fitting annual and semiannual harmonics to the time series of alongshore velocity at each depth level (Figure 6.10a and e, respectively). Here, the semiannual cycle shows higher amplitudes (in agreement with Figure 6.5b) along with a reduced baroclinicity compared to the annual cycle. Annual and semiannual components derived from the corresponding time series of altimetry-based geostrophic velocities allow for the interpretation of near-surface baroclinic structures. For the annual cycle the flow reverses direction between the surface and the depth of the uppermost ADCP measurements (about 50 m). The semiannual cycle of the alongshore velocity is instead characterized by a more gradual change with depth, indicating the dominance of lower baroclinic modes compared to the annual cycle.

In a next step, we extract zonal and meridional velocities at the first model grid point at 11 °S off the coast of Angola from the EF-only simulations corresponding to the observations at 11 °S-Angola. The alongshore velocity component at 11 °S is calculated for each baroclinic mode and multiplied with the corresponding vertical structure function. The resulting time series of velocity profiles associated with each baroclinic mode are summed up to reconstruct the annual and semiannual cycles of alongshore velocity. For the purely equatorial forcing (Figure 6.10b and f, respectively), the reconstructed annual cycle agrees well with the observations in terms of both amplitude and phase. Thus, the annual cycle of alongshore velocity at 11 °S-Angola appears to reflect primarily the response to the remote equatorial forcing. The purely equatorial forcing also generates a semiannual cycle at 11 °S-Angola with an amplitude comparable to the observed one. However, the reconstructed semiannual cycle from the EF-only simulations reveals substantial differences in the baroclinic structure with too-strong velocities near the surface and too-weak velocities at depth being also phase-shifted relative to the observed semiannual cycle. This indicates that the remote equatorial forcing alone is not sufficient to set up the baroclinic structure of the semiannual cycle as observed, but rather local forcing might play a role as well. Therefore, a similar extraction is carried out for the EF+LF simulations that include also the local forcing along the eastern boundary. Again, using the first five baroclinic modes for

the reconstruction we find a good agreement between the summed-up model output and the observations for the annual cycle (Figure 6.10c). The reconstructed baroclinic structure of the semiannual cycle bears more similarities with the observed one (Figure 6.10g), indicating the importance of local forcing for the semiannual cycle. Nevertheless, the reconstruction still lacks amplitude at mid-depth.

To further evaluate the importance of the remote equatorial forcing for the annual and semiannual cycles at 11 °S-Angola, the amplitude and phase of the individual modal contributions to the oscillations can be compared between the simulations driven with equatorial forcing and those simulations driven with full forcing. With few exceptions modal phase differences for the two sets of simulations are within less than one month and modal amplitude differences are smaller than $0.1\,\mathrm{cm\,s^{-1}}$ (Table 6.4). These minor differences underline the dominance of the remote equatorial forcing for the annual cycle at 11 °S-Angola. The larger discrepancy between the reconstructions of the forcing-dependent semiannual cycles is largely associated with the third baroclinic mode, which is phase-shifted by about one month, and, more importantly, stronger in amplitude by about $0.23\,\mathrm{cm\,s^{-1}}$ in the simulation with equatorial forcing only. Multiplied with the corresponding vertical structure function (Figure 6.3a), this difference in amplitude is sufficient to explain the intensification near the surface and concurrent reduction at depth in the semiannual cycle reconstructed from simulations based on equatorial forcing compared to the simulations with realistic forcing (Figure 6.10f).

As Figure 6.8 suggests, in general only baroclinic modes with basin mode resonance periods

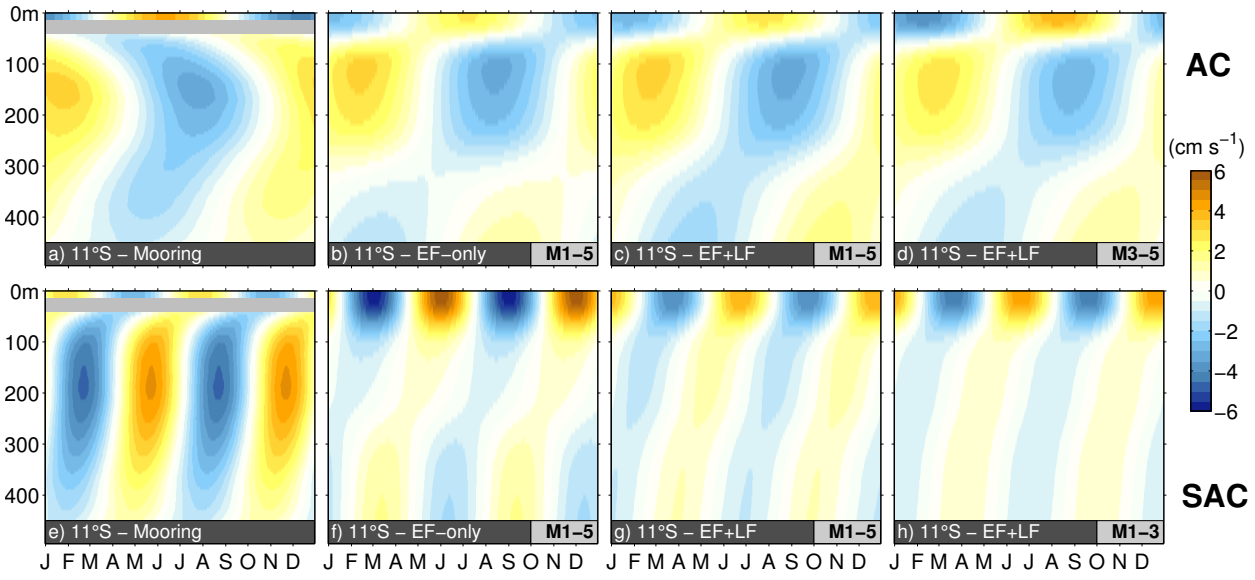

Figure 6.10: Baroclinic structures of observed (a) annual and (e) semiannual oscillations of alongshore velocity at 11 °S-Angola derived by fitting harmonic functions at each depth level. At the surface corresponding oscillations derived from AVISO geostrophic velocities are shown. Shown to the right are corresponding baroclinic structures obtained from linear superposition of the first five baroclinic modes from the EF-only simulations driven (b, f) and the EF+LF simulations (c, g). In (d) and (h) only EF+LF simulations for baroclinic modes with their resonance periods closest to either the annual or semiannual cycle are considered for superposition.

Baroclinic mode n	Annual cycle		Semiannual cycle	
	ΔAmp. ($cm\,s^{-1}$)	ΔPhase (month)	ΔAmp. ($cm\,s^{-1}$)	ΔPhase (month)
1	-0.021	+5.6	+0.081	+0.11
2	+0.081	-2.3	+0.071	-0.32
3	+0.043	-0.3	+0.227	-1.0
4	-0.016	-0.4	+0.108	+0.4
5	-0.072	-1.0	+0.027	-0.2

Table 6.4: Amplitude and phase differences between EF-only and EF+LF simulations for individual baroclinic modes at 11 °S-Angola. Positive/negative differences correspond to a stronger/weaker response to EF-only forcing compared to the EF+LF forcing, with the former inducing a southward maximum of surface alongshore velocity later/earlier, respectively. To obtain depth-dependent differences, the amplitude difference needs to be multiplied with the corresponding vertical structure function (Figure 6.3a).

close to either the annual or semiannual cycles are likely to influence the alongshore velocity off the coast of Angola. Therefore, we repeat the reconstruction using EF+LF simulations summing up only the relevant baroclinic modes, which are modes 3-5 and 1-3 for the annual and semiannual cycles, respectively (Figure 6.10d and h). As expected from Figure 6.8, the annual cycle is only little changed compared to the reconstruction using five modes, stressing the importance of the fourth baroclinic mode for the annual cycle with contributions from both the third and fifth baroclinic modes especially in setting up the phases. For the semiannual cycle, the restriction to the first three baroclinic modes results in even less amplitude at mid-depth. Together with Figure 6.8, this indicates the influence of higher baroclinic modes in generating the observed baroclinic structure of the semiannual cycle in alongshore velocity at 11 °S-Angola and thus, besides the gravest basin mode, also a potential impact of the second basin mode for the fourth baroclinic mode.

6.5 Summary and discussion

We have analyzed the seasonal cycle of alongshore velocity measured by a moored ADCP at 11 °S-Angola between July 2013 and October 2016. Pronounced peaks in the spectra at annual and semiannual frequencies (Figure 6.5b) were found to be associated with distinct baroclinic structures (Figure 6.10a, e). In the equatorial Atlantic resonant basin modes (*Cane and Moore*, 1981) have been found to represent robust features that can explain pronounced spectral peaks in the zonal velocity field at the annual and semiannual frequencies (*Claus et al.*, 2016; *Brandt et al.*, 2016; *Thierry et al.*, 2004; *Ding et al.*, 2009). Equatorial basin modes are composed of equatorial Kelvin and long equatorial Rossby waves for a particular baroclinic mode, with basin resonances found at characteristic periods depending on both gravity wave speed and basin geometry. Given the link between the equatorial and coastal wave-guides, we examine the relative importance of remote equatorial forcing including potential basin mode resonances versus the local forcing off

Angola for the observed annual and semiannual cycle of alongshore velocity at 11 °S-Angola.

A suite of shallow water model simulations is employed, forced either by zonally uniform oscillating zonal forcing restricted to the equator (EF-only runs) or by the Fourier components of several wind products corresponding to the annual and semiannual periods (EF+LF runs). Model-computed modal amplitudes are fitted to modal amplitudes derived from mooring data at 23 °W-Equator (Figure 6.6a and Table 6.3). Note that the resulting forcing profile projection may differ for annual and semiannual frequencies for the same baroclinic mode. As noted earlier, it is crucial how well our simulations capture the resonance characteristics of the equatorial Atlantic (*Greatbatch et al.*, 2012; *Brandt et al.*, 2016). The resonance frequency in the model depends mainly on the combination of chosen gravity wave speed and model geometry. Furthermore, dissipation of wave energy could be different for the annual and semiannual cycle, but is prescribed and fixed in the shallow water model simulations. Therefore, the projection coefficients do not so much mirror the wind energy input (and are therefore not necessarily similar for different oscillation periods), but rather indicate how much energy input is required to establish similar modal amplitudes as observed at a given oscillation period, given the model-inherent resonance characteristics.

The large-scale horizontal structures of the amplitude of annual and semiannual oscillations for different baroclinic modes suggest their dynamic influence on the boundary circulation off Angola (Figure 6.8, Figure 6.9). In model simulations driven with zonally uniform zonal forcing restricted to the equator (EF-only) the observed annual cycle of alongshore velocity at 11 °S-Angola is already well reproduced, suggesting remote equatorial forcing as the major driver for annual oscillations of the eastern boundary circulation off Angola (Figure 6.10b). Although the remote equatorial forcing also generates a semiannual cycle of comparable amplitude, the model-computed semiannual cycle is significantly different from the observed one (Figure 6.10f). Some improvement in terms of the vertical structure and phase of the reconstructed semiannual cycle is achieved when including local forcing along the eastern boundary (EF+LF runs, Figure 6.10g). Furthermore, it could be shown that both annual and semiannual oscillations appear to be primarily determined by those baroclinic modes being close to equatorial resonance either for the annual or semiannual frequency (Figure 6.10d, h).

Nevertheless, while amplitudes of model-derived and observed annual cycles are very similar, the model-derived semiannual cycle lacks amplitude at mid-depth. Given the vertical structure of the baroclinic modes (Figure 6.3a), contributions of higher baroclinic modes seem to be underestimated for the semiannual cycle. Here we want to note that our approach for scaling model-computed modal amplitudes relies on one particular location in the central equatorial Atlantic, where an observational data set of top-to-bottom ocean velocities is available to allow for baroclinic mode decomposition. However, owing to the differences in the spatial distribution of the amplitude for different baroclinic modes, a locally confined scaling might be problematic, as seen for example for the fourth baroclinic mode, semiannual cycle. The corresponding basin mode represents the structure of a second basin mode, which is characterized by two velocity

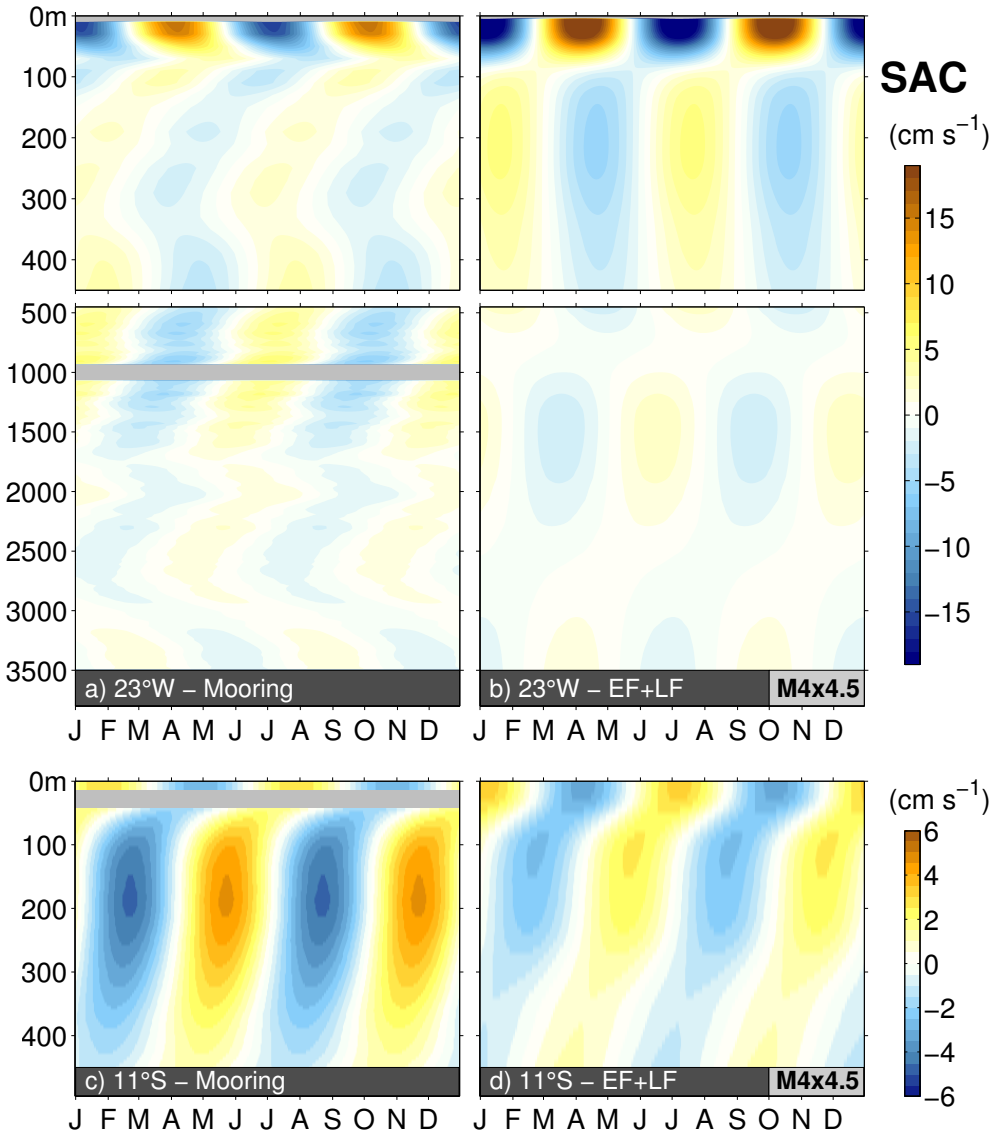

Figure 6.11: Similar to Figure 6.7 and Figure 6.10, this time comparing the vertical structure of the observed semiannual cycles with the model-computed semiannual cycles, where the amplitude of the fourth baroclinic mode has been enhanced by a factor 4.5 for 23 °W-Equator (a and b), and 11 °S-Angola (c and d).

maxima along the equator (Figure 6.8). 23 °W-Equator is located close to the nodal point of the second basin mode, which complicates the determination of the corresponding modal amplitude and thus adds uncertainty to the scaling of model-computed modal amplitudes. In fact, when artificially enhancing the amplitude of the fourth baroclinic mode, semiannual cycle by a factor 4.5 the model-computed semiannual cycle becomes similar to the observed one (Figure 6.11c, d). Therefore, a limiting factor for a realistic reconstruction of the semiannual cycle at 11 °S-Angola appears to be the amplitude of the fourth baroclinic mode. Here, the modal decomposition derived from zonal velocity data at 35 °W-Equator yields another estimate of the strength of the second basin mode associated with the fourth baroclinic mode, semiannual cycle. Indeed, the mode energy for this particular basin mode is found to be significantly larger at 35 °W-Equator compared to 23 °W-Equator (0.25 cm^2 s^{-2} vs. 0.08 cm^2 s^{-2}). However, the corresponding scaling

coefficients for the shallow water model simulations derived independently at the two locations are very similar (0.09 at 35 °W-Equator vs. 0.07 at 23 °W-Equator, compare Table 6.3). Hence, the strength of the simulated basin mode associated with the fourth baroclinic, semiannual cycle would change only marginally, if we scaled our simulations at 35 °W-Equator and thus cannot explain the too-weak amplitude at 11 °S-Angola. Interestingly, the reconstructed semiannual cycle in zonal velocity at 23 °W-Equator does not change drastically, when equivalently increasing the amplitude of the fourth baroclinic mode by a factor of 4.5 (Figure 6.11a and b). The most notable differences to the observed semiannual cycle at 23 °W-Equator are absent amplitudes in the depth range between 600 and 1000 m on the one hand, but a more realistic amplitude structure close to the ocean floor on the other hand. Apparently, observed amplitudes in the depth range between 600 and 1000 m prevent a stronger projection of the fourth baroclinic mode onto the semiannual cycle of zonal velocity at 23 °W-Equator. However, several other factors potentially influence the model-computed amplitude at 11 °S-Angola. Among them are model-inherent characteristics such as the applied damping and the efficiency of basin mode resonance depending on model geometry and chosen phase speeds. Furthermore, our model setup does not contain topographic features like the mid-Atlantic ridge and treats coastlines as solid walls. Therefore, any interaction of a baroclinic mode with the topography that could foster the transfer of energy between baroclinic modes is not included in our model. Linear models also do not include nonlinear processes like a potential nonlinear interaction of the annual cycle with itself that could shift energy to the semiannual cycle. In this way, the dominant basin mode of the annual cycle, being of fourth baroclinic mode, might feed energy into the second basin mode of the semiannual cycle, providing one potential explanation for the missing strength of the fourth baroclinic mode in the semiannual cycle in our linear model. Nevertheless, given the simplicity of our model, it seems even more remarkable how much of the annual and semiannual oscillations discussed here appear to be governed essentially by linear dynamics.

While investigating the seasonal cycle of equatorial Atlantic circulation, *Brandt et al.* (2016) compared their shallow water, basin mode simulations to the ocean general circulation model (OGCM) TRATL01 (*Duteil et al.*, 2014), noting similarities in the representation of the dominant basin modes for the annual and semiannual cycles. TRATL01 constitutes a 0.1 ° resolution nest between 30 °S and 30 °N in the Atlantic Ocean, that is embedded in a global ORCA05 configuration at 0.5 ° resolution via two-way-nesting (*Debreu and Blayo*, 2008). The configuration is forced by interannually varying atmospheric data provided by the Coordinated Ocean-Ice Reference Experiments (CORE) v2 reanalysis data (*Griffies et al.*, 2009) over the period 1948-2007. Extracting the annual and semiannual cycles of alongshore velocity at 11 °S-Angola from TRATL01 reveals very similar baroclinic structures compared to the observations (Figure 6.12). Just like *Brandt et al.* (2016) noted for the annual cycle in zonal velocity at 23 °W-Equator, we also find a slightly deeper depth of the phase jump in the annual cycle of alongshore velocity at 11 °S-Angola in TRATL01 (Figure 6.12b), pointing again to a too-strong vertical diffusion in the model. Considering baroclinic mode contributions, this would result in a stronger projection of

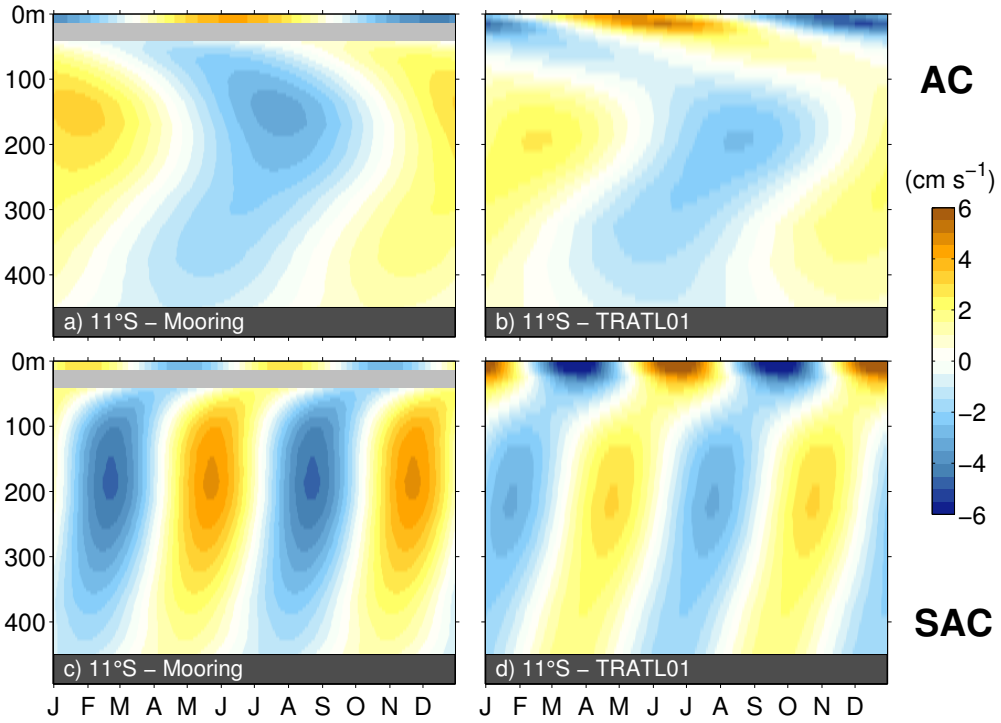

Figure 6.12: Similar to Figure 6.10, this time comparing observed annual (a) and semiannual (c) oscillations of alongshore velocity to annual (b) and semiannual (d) oscillations extracted from the TRATL01 model at 11 °S-Angola. For both data sets annual and semiannual components were reconstructed by fitting corresponding harmonic functions at each depth level.

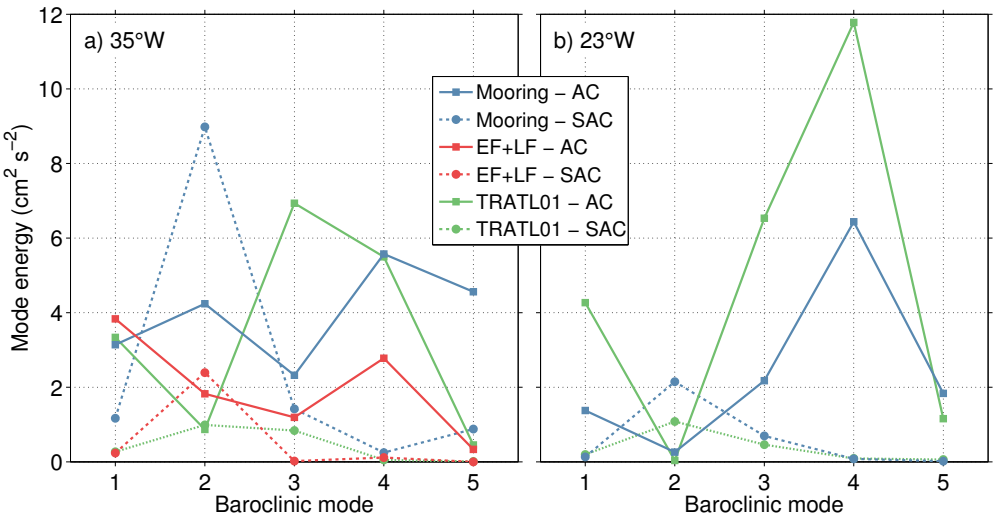

Figure 6.13: Baroclinic mode spectra of the annual (solid) and semiannual (dashed) cycles for 35 °W-Equator (a) and 23 °W-Equator (b) derived from moored velocity observations (blue), EF+LF shallow water model simulations (red), and the TRATL01 model (green). In b) mode spectra of the shallow water model are identical to the one derived from observations as model-computed modal amplitudes are scaled locally at 23 °W-Equator.

the annual cycle onto the third baroclinic mode (not shown). The semiannual cycle derived from TRATL01 (Figure 6.12d) does reveal a mid-depth maximum in alongshore velocity, although slightly deeper and weaker compared to the observations. However, keeping in mind possibly

too-strong vertical diffusion in TRATL01, it still confirms the potential importance of a fourth baroclinic mode in setting up the semiannual cycle of alongshore velocity at 11 °S-Angola. A modal decomposition of zonal velocity from TRATL01 at 23 °W-Equator shows similar relative weights of the baroclinic modes compared to observations, although the annual cycle seems more energetic while the semiannual cycle seems less energetic in TRATL01 (Figure 6.13b). Similar to 11 °S-Angola, the relative contribution of the third baroclinic mode to the annual cycle is larger in TRATL01 compared to the observations at 23 °W-Equator. At 35 °W-Equator the third baroclinic mode is the largest contributor to the annual cycle in TRATL01, while the modal decomposition of the observed time series suggests local dominance of the fourth baroclinic mode followed by the second baroclinic mode (Figure 6.13a). Considering the semiannual cycle at 35 °W-Equator, the large amplitude of the second baroclinic mode derived from observations is mirrored neither by TRATL01 nor by the EF+LF shallow water model simulations scaled at 23 °W-Equator. Overall, mode energy spectra derived from observations, the EF+LF shallow water model runs, and TRATL01 agree less well at 35 °W-Equator compared to 23 °W-Equator. As noted earlier, the uncertainties associated with the modal decomposition of the zonal velocity observations at 35 °W-Equator are rather large and might be one of the factors accounting for the differences between mode spectra. Furthermore, for a realistic representation of the seasonal cycle of the equatorial circulation by an OGCM it seems crucial that resonance characteristics are captured correctly. To achieve the latter, a realistic representation of the stratification along the equator is essential, as this specifies corresponding gravity wave speeds. While our shallow water model simulations assume constant phase speeds across the basin, TRATL01 does account for changes in stratification. Consequently, the basin-wide structures of the annual and semiannual cycles for a specific baroclinic mode can look significantly different in TRATL01 compared to our idealized simulations (Figure 6.14). Comparably small shifts in the location of local maxima thus can result in rather large discrepancies in the modal amplitude at one particular location, as seen for example in the annual cycle of the second baroclinic mode near 35 °W (compare Figure 6.8 and Figure 6.14). Also the location of local maxima associated with the semiannual cycle of the fourth baroclinic mode is significantly different between the shallow water model simulations and TRATL01, underlining the problematic nature of correctly scaling modal amplitudes relying on individual locations, where suitable observations are available.

The wave response of the coastal upwelling regions off Angola and Namibia to the remote equatorial wind forcing has previously been discussed mainly with respect to the intermittent occurrence of warm Benguela Niño events (*Florenchie et al.*, 2003, 2004; *Rouault et al.*, 2007; *Huang et al.*, 2007; *Lübbecke et al.*, 2010; *Richter et al.*, 2010; *Bachèlery et al.*, 2016) developing in the northern Benguela. Carrying out a set of regional model simulations for the Southeast Atlantic intentionally excluding the seasonal cycle in the analysis, *Bachèlery et al.* (2016) noted the dominance of remote equatorial forcing on interannual time scales while on intraseasonal time scales local forcing prevailed. However, for seasonal time scales particularly the importance of the semiannual cycle as contributor to upwelling and downwelling seasons off Angola has been

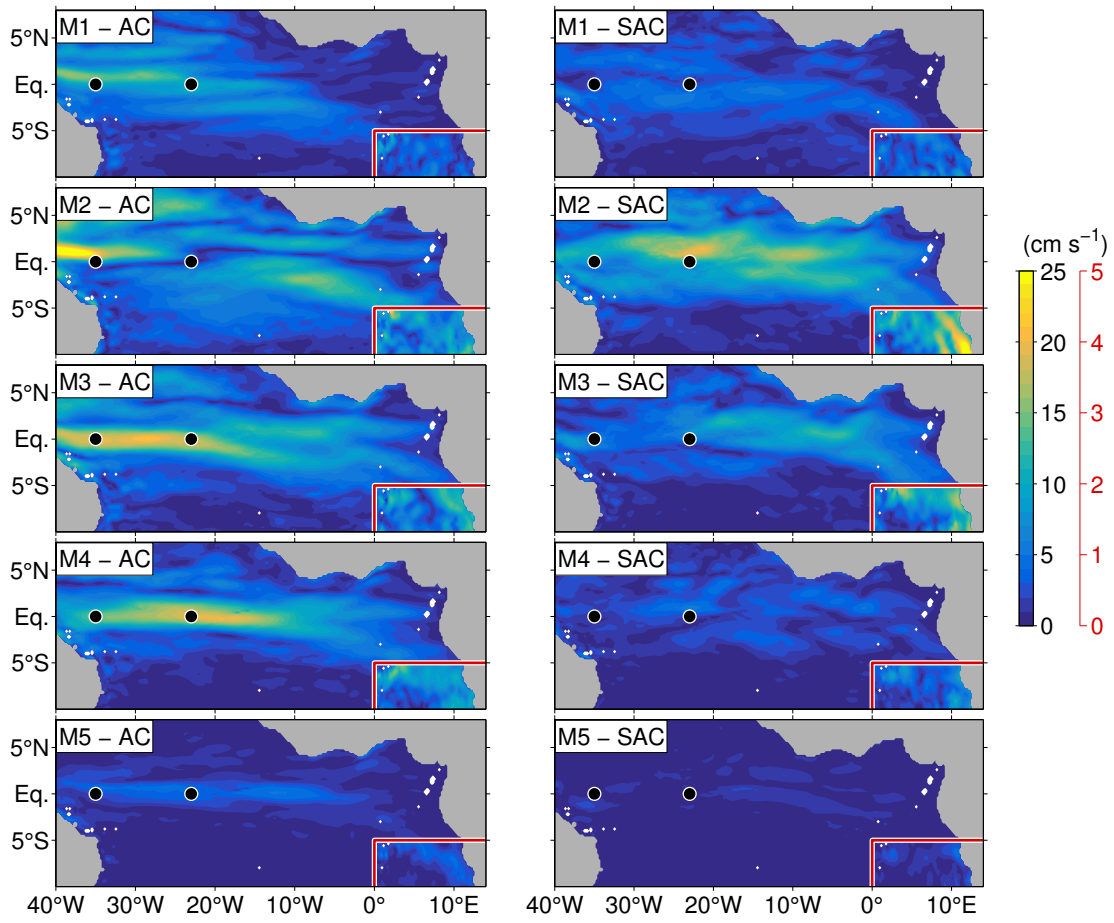

Figure 6.14: As Figure 6.8, but from the TRATL01 model. Mode projection is carried out at model grid points with water depth larger than 1000 m.

underlined (*Ostrowski et al.*, 2009; *Rouault*, 2012; *Kopte et al.*, 2017). The mooring observations off Angola (Figure 6.1) for the first time reveal the baroclinic structures of both the annual and semiannual cycle and our results appear to confirm that equatorial dynamics play a crucial role for the eastern boundary circulation variability on these time scales.

As noted in Section 6.4.1 on intraseasonal time scales a pronounced peak in the velocity spectra is found near 120 days for the onshore ADCP (Figure 6.5b). The persistence of this oscillation cannot be verified with the available data. Nevertheless, elevated energy near 120 days is also found in the zonal velocity time series at 23 °W-Equator, which might be associated with resonance of either the gravest basin mode of the first baroclinic mode or the second basin mode of the second baroclinic mode. The vertical structure of the 120-day oscillation at 11 °S-Angola indeed suggests the dominance of low baroclinic modes. Superposition of the shallow water model simulations forced with the Fourier component of wind stress data corresponding to 120 days confirm the low-baroclinic mode nature of this oscillation, although being phase-shifted and too weak (not shown). Interestingly, a basin mode resonance at 120-day period has been described for the Caribbean Sea (*Hughes et al.*, 2016), that could impact also equatorial Atlantic circulation via CTW and EKW response and potentially even the boundary circulation off Angola.

However, the isolation of the corresponding signatures in the velocity data at 23 °W-Equator was hindered by several interfering, stronger signals that are associated with a diversity of forcing mechanisms. Thus, the possible equatorial forcing of intraseasonal variability in the boundary circulation off Angola remains an open question.

7 Synthesis

In this thesis the characteristics of the boundary current flow and hydrography within the seasonal upwelling system off Angola are examined. Multi-year velocity observations acquired near 11 °S off Angola for the first time give insight into the mean strength and baroclinic structure as well as the intraseasonal to seasonal variability of the Angola Current (AC). Additionally, an extensive data set of shipboard velocity and hydrographic observations, obtained in the framework of a long-term joint initiative by the Norwegian Agency for Development Cooperation (NORAD), the Food and Agricultural Organization of the United Nations (FAO), and West African coastal countries, is explored in cooperation with the Angolan partners. The data reveal the mean structures of ocean currents and hydrography along the entire Angolan coastline separately for austral summer and austral winter. In light of the presence of large biases in coupled climate simulations particularly in the Southeast Atlantic Ocean (*Davey et al.*, 2002; *Richter et al.*, 2014; *Toniazzo and Woolnough*, 2014) the new insights into the current and thermal structures off Angola might turn out very valuable for model validation purposes.

The wave response of the coastal upwelling regions off Angola and Namibia to the remote equatorial forcing has received considerable attention in the past, mainly with respect to the intermittent occurrence of oceanic warm events centered near the Angola-Benguela Frontal Zone (ABFZ) known as Benguela Niños (*Shannon et al.*, 1986; *Florenchie et al.*, 2003; *Lübbecke et al.*, 2010; *Bachèlery et al.*, 2016). On interannual time scales these anomalous warm events are known to have severe consequences both for the marine ecosystem but also for rainfall variability over the adjacent land masses (*Gammelsrød et al.*, 1998; *Rouault et al.*, 2003). Temperature anomalies are triggered by anomalous thermocline displacements in response to the propagation of Equatorial Kelvin Waves (EKWs) and Coastally Trapped Waves (CTWs) (*Pizarro et al.*, 2002; *Ramos et al.*, 2006; *Gómez-Valdivia et al.*, 2017). The present study focuses on the connection of equatorial and coastal wave-guides as well, but with emphasis on the seasonal cycle. In this context, not only the pure propagation of EKWs and CTWs is considered, in addition the role of resonant equatorial basin-modes (*Cane and Moore*, 1981) for the seasonality of both the equatorial circulation and the boundary circulation off Angola is explored. Resonant equatorial basin-modes represent an oscillation composed of eastward propagating EKWs and westward propagating Equatorial Rossby Waves (ERWs) of a particular baroclinic mode with the corresponding oscillation period being close to some forcing period to give rise to resonance. Linear superposition of the dominant equatorial basin-modes thereby can explain large fractions of the seasonal cycle of the equatorial Atlantic circulation. Furthermore, the off-equatorial lobes of the basin-modes also influence

meridional velocity oscillations at the eastern boundary and therefore also impact the seasonal cycle of the AC flow.

In the following the progress on the scientific key question raised in Chapter 1 will be discussed in light of the results presented in the preceding chapters and integrated in the current level of knowledge.

- **What are the characteristics of the boundary current flow off Angola locally at 11 °S and along the entire Angolan coastline?** (Chapter 3 and Chapter 4):

  The moored velocity measurements acquired near 11 °S off Angola do not show a persistent southward flow of the AC during the observation period. Instead, the velocity time series of about 2.5 years duration reveal strong intraseasonal to seasonal variability, with periodically alternating southward and northward velocities in the range of $\pm 40\,\mathrm{cm\,s^{-1}}$. Overall, a weak southward mean flow is found in the upper 200 m depth, associated with an AC core located at about 50 m depth and centered over the 500 m-isobath with velocities not exceeding $8\,\mathrm{cm\,s^{-1}}$. The mean southward volume transport of the AC during the period of moored observations is estimated to be 0.32 ± 0.05 Sv. Transport fluctuations range from 2.2 Sv southward to 1.2 Sv northward. Thus, the multi-year measurements of the alongshore flow off Angola correct our view of an AC permanently flowing southward, which was based on historical synoptic measurements. While the previously reported values (*Moroshkin et al.*, 1970; *Dias*, 1983a,b; *Mohrholz et al.*, 2001) are within the range of the AC strength derived from moored observations, all these early measurements had apparently been obtained during episodes of southward velocity by chance.

  An extensive in-situ dataset of shipboard velocity observations was acquired within the EAF-Nansen program. The data was post-processed and analyzed in the framework of a capacity building effort with Angolan partners. For the first time, the large-scale mean structure of the AC is revealed based on observational data. It generally is characterized by a downstream strengthening of the poleward flow along the Angolan coastline. Maximum velocities exceeding $30\,\mathrm{cm\,s^{-1}}$ during austral summer are reached just north of the ABFZ. During austral summer, corresponding to the main downwelling season, the AC is confined to the upper 120 m in the north, gradually deepening to 200 m depth at about 17 °S in the south. The downstream flow divergence indicates that the poleward current cannot solely be supplied from the north. Instead, waters from offshore must be entrained, for instance as part of an offshore recirculation cell. During austral winter, coinciding with the major upwelling season, poleward velocities of the AC are weaker along the entire coastline. Maximum southward velocities do not exceed $15\,\mathrm{cm\,s^{-1}}$. However, the poleward flow extends to greater depth during austral winter. The reduced/enhanced poleward flow found during upwelling/downwelling periods thereby is in agreement with the passage of upwelling/downwelling CTWs, which induce equatorward/poleward velocity anomalies (*Ostrowski et al.*, 2009; *Rouault*, 2012). The results constitute an important milestone

also for the modeling community, as they will enable the validation of ocean models and reanalysis products in terms of their representation of the boundary current flow off Angola. In the past, model inter-comparison studies evaluating model biases in the region were forced to select one reference product that was assumed to have the best representation of the alongshore currents off Angola, as no appropriate observational reference was available (e.g. *Xu et al.* (2014)). Nonetheless, it certainly is encouraging that the alongshore current structure derived from the observations agrees to a large extent with results obtained from several ocean reanalysis products (*Xu et al.*, 2014). In addition, a first evaluation of ocean reanalysis products with the moored velocity observations obtained at 11 °S reveals simulated AC transports that are comparable to the estimate derived from the observations, despite with a disagreement concerning the seasonality (Chapter 3). Clearly more thorough assessments of the observed and simulated current structure are necessary and will follow in the future, with the results presented here even facilitating comparisons accounting for the seasonal differences of the AC flow.

Seasonally averaged profiles of alongshore velocity extracted from the Nansen shipboard velocity data near the mooring position at 11 °S compare well with the corresponding velocity profiles derived from the mooring data. Both data sets independently show the seasonal differences in the baroclinic structure of the flow as well as in maximum southward velocity. However, the generally stronger flow in the shipboard observations, which represent the period from 2005 to 2016 suggests that the moored observations from 2013 to 2015 might cover a period of an anomalously weak Angola Current. Furthermore, the AC transport during the period of moored observations ranges at the lower end of previously reported AC transport estimates (*Dias*, 1983a; *Mercier et al.*, 2003). In particular, it should be noted that the observation period did not include any significant Benguela Niño event. As the AC is supposed to be anomalously strong during such an event, the mean transport estimate derived for the period of moored observations is expectedly smaller than the AC transport of 11 Sv (*Mercier et al.*, 2003) reported during the major Benguela Niño in 1995 (*Gammelsrød et al.*, 1998).

- **How is the seasonal upwelling off Angola reflected in the seasonal cycle of temperature and salinity?** (Chapter 3 and Chapter 4):

  A strong seasonality in near-surface temperature and salinity is found off Angola based on an extensive set of shipboard hydrographic data supplemented by autonomous glider measurements. With the combination of historic and recent measurements on the continental slope near 11 °S it was possible to construct a mean seasonal cycle of temperature and salinity for the upper 500 m depth in which the major downwelling (austral summer: March/April) and upwelling (austral winter: July/August) seasons are well represented. Furthermore, there are indications for a secondary upwelling period in December/January. Cooling during the secondary upwelling is weaker compared to the major upwelling season, nonetheless isopy-

cnals in the near-surface layers are displaced upward, bringing colder, more saline waters closer to the surface. The secondary upwelling thereby separates the major downwelling in March/April from the secondary downwelling in October. Concerning the meridional distribution of temperature and salinity, a thin surface layer with extremely warm and fresh waters spreads southward along the Angolan coastline to about 13 °S during austral summer, being absent during austral winter. Below the thermocline only minor changes in the water mass composition are found between the seasons. Nonetheless, a seasonal vertical migration of the central water body is observed, associated with the dynamical response to the passage of downwelling and upwelling CTWs. Based on the analysis of temperature time series data obtained on the Angolan shelf, *Berrit and Dias* (1977) already mentioned the existence of a secondary upwelling period off Angola during December/January in an early study. With the advent of satellite remote sensing techniques, the propagation of four seasonal CTWs per year could be evidenced along the Angolan coastline (*Schouten et al.*, 2005; *Ostrowski et al.*, 2009; *Rouault*, 2012), contributing to the interpretation of the seasonal occurrence of upwelling in the tropical Angolan system. The results presented here confirm the existence of a regular seasonal cycle with alternating seasons of down- and upwelling, which are in agreement with both the seasonal cycle derived from time series data (*Berrit and Dias*, 1977) and the passing times of semiannual down- and upwelling CTWs. Both the derived seasonality of temperature and salinity at 11 °S off Angola and the alongshore summer and winter averages of the hydrographic properties will become very useful to the scientific community, as they can be used for the validation of the simulated thermal structure off Angola, where the sources for existing biases in coupled climate simulations are still under debate (*Richter et al.*, 2014; *Toniazzo and Woolnough*, 2014). Particularly the contribution of systematic errors in the ocean models to the bias problem can be verified as observations of the currents and thermal structure off Angola become available (*Xu et al.*, 2014). The freshwater anomaly in the surface layer of the northern parts of Angola's coastline during austral summer is most likely associated with the annual cycle in river runoff (*Mohrholz et al.*, 2001). In fact, a study employing a high-resolution numerical model attributes most of the regional Sea Surface Salinity (SSS) structure and seasonality to the discharge of the Congo river (*Berger et al.*, 2014), which is the most significant source of freshwater in the region. The Congo outflow peaks between December and January (*Dai et al.*, 2009), inducing a freshwater anomaly spreading from the north to the south in the following months. Excess evaporation over precipitation, that is present off Angola year round (*Praveen Kumar et al.*, 2013; *Lüdke*, 2016), degrades the freshwater anomaly during austral autumn. Overall, the seasonal cycle of temperature and salinity off Angola in the surface layer and upper thermocline appears to be governed by a combination of CTW dynamics, continental river discharge, mixing, and surface heat and freshwater fluxes. Yet, a full explanation of how the coastal upwelling is fueled in the absence of alongshore winds and thus wind-driven Ekman divergence is still missing.

- **What is the importance of basin-mode resonance for the seasonal cycle of the equatorial circulation in the Atlantic?** (Chapter 5):

  The circulation in the equatorial Atlantic is dominated by alternating zonal currents, the most prominent and strongest feature being the eastward flowing Equatorial Undercurrent (EUC). Seasonal variability of the circulation is dominated by the annual cycle. However, although the forcing at the semiannual frequency is weak, a pronounced semiannual cycle of zonal velocity is found along the equator. A modal decomposition of a multi-year, full-depth velocity time series from the central equatorial Atlantic shows that the annual cycle is dominated by the fourth baroclinic mode, while the semiannual cycle is dominated by the second baroclinic mode. Their corresponding horizontal patterns show a structural robustness being derived from either an Ocean General Circulation Model (OGCM) or linear Shallow Water Model (SWM) simulations of varying basin geometry and/or forcing. These patterns are associated with resonant equatorial basin modes, that are composed of eastward propagating EKWs and westward propagating ERWs. Previous studies already linked the semiannual cycle of the equatorial Atlantic circulation to the resonance of the second baroclinic mode to the weak semiannual wind forcing (*Thierry et al.*, 2004; *Ding et al.*, 2009). Due to the comparable basin width, a similar importance of the second baroclinic mode for the semiannual cycle in the equatorial Indian Ocean circulation has been noted (*Han et al.*, 1999, 2011). Making use of the unique time series of full-depth velocity observations at 23 °W, which allows the decomposition of the velocity signal into baroclinic modes, it is now possible to reveal the dominance of the fourth baroclinic mode for the annual cycle, suggesting resonance of this mode to the annual wind forcing. The modal decomposition in fact shows that a large fraction of the observed variability in the equatorial Atlantic circulation is concentrated near resonance frequencies associated with particular baroclinic modes (*Claus et al.*, 2016). These include also higher baroclinic modes at a time scale of about 4.5 years, verifying the often noted correspondence between the Equatorial Deep Jets and equatorial basin-modes (*Ascani et al.*, 2006; *d'Orgeville et al.*, 2007; *Brandt et al.*, 2012; *Greatbatch et al.*, 2012). Regarding the seasonal cycle, the superposition of the two dominant basin-modes as obtained from the SWM can explain substantial parts of the observed seasonal EUC variability, i.e. zonal transport, core velocity, core latitude. In this way, equatorial basin-modes (*Cane and Moore*, 1981; *Han et al.*, 1999; *Ding et al.*, 2009; *Han et al.*, 2011; *Claus et al.*, 2016) provide a powerful alternative to equatorial beams (*McCreary*, 1984; *Lukas and Firing*, 1985; *Thierry et al.*, 2004; *Brandt and Eden*, 2005) that are often used to describe seasonal variability in the equatorial oceans.

- **Given the connection of equatorial and coastal wave-guides, what is the importance of resonant equatorial basin-modes (and remote equatorial forcing in general) for the seasonal cycle of the Angola Current?** (Chapter 6):

  Similar to the seasonality of zonal velocity in the equatorial Atlantic, alongshore veloc-

ity off Angola shows distinct peaks at the annual and semiannual periods. The results from Chapter 5 suggest the potential impact of the off-equatorial lobes of the equatorial basin-modes on meridional velocity oscillations at the eastern boundary and thus on the seasonality of the alongshore flow off Angola. By designing a suite of SWM simulations differing in the applied forcing, the remote equatorial forcing is isolated and its impact on the boundary current seasonality is investigated. The observed annual cycle of alongshore velocity at 11 °S off Angola is well reproduced by the remote equatorial forcing. The inclusion of the local forcing results only in minor modifications of the model-computed annual cycle. The remote equatorial forcing also induces a semiannual cycle at 11 °S off Angola with an amplitude that is comparable to the observed one. However, observed and model-computed baroclinic structures and phases disagree substantially. The inclusion of local forcing improves the agreement of observed and simulated semiannual velocity oscillations at 11 °S compared to the purely equatorial forcing. Thus, the semiannual cycle of the Angola Current appears to be strongly modified by local winds at the eastern boundary. However, even the semiannual cycle derived from simulations including the local forcing lacks amplitude at mid-depth. This could be the result of underestimating the strength of the second equatorial basin-mode of the fourth baroclinic mode in the model simulations, as the corresponding basin-mode represents a second basin-mode. Second basin-modes in the Atlantic are generally not well-constrained by the mooring data from the equatorial mooring at 23 °W, which are used to obtain realistic modal amplitudes from the SWM simulations.

For the first time the investigation of the wave response off Angola to the remote equatorial and local forcing is no more limited to either satellite observations (*Schouten et al.*, 2005; *Polo et al.*, 2008; *Ostrowski et al.*, 2009) or pure model studies (*Rouault*, 2012; *Bachèlery et al.*, 2016). Instead, the acquired moored velocity observations off Angola reveal distinct baroclinic structures for the annual and semiannual cycle, that are associated with the oscillation-period-dependent dominance of particular baroclinic modes. Previous studies focused mainly on the propagation of an anomalously strong pair of EKW and CTW that triggered Benguela Niño events (*Shannon et al.*, 1986) for example in 1995 or 2001 (*Gammelsrød et al.*, 1998; *Florenchie et al.*, 2003; *Rouault et al.*, 2007). In a regional modeling study, which intentionally excludes the seasonal cycle in the analysis, the dominance of the remote equatorial forcing for the variability in the coastal upwelling regions off Angola and northern Namibia is noted (*Bachèlery et al.*, 2016). Here it is shown, that also the annual cycle of alongshore velocity off Angola can be essentially reproduced with purely equatorial forcing. In this context it should be noted that not only the simple propagation of an EKW that transmits part of their energy into a poleward propagating CTW needs to be considered. Results from Chapter 5 and Chapter 6 rather suggest that EKWs and ERWs of particular baroclinic modes can build up (quasi-)resonant zonal oscillations for matching

forcing periods. The linear superposition of these resonant equatorial basin-modes can not only explain a large part of the seasonality of the equatorial Atlantic circulation, furthermore the basin-modes also represent the dominant contributors to the observed baroclinic structures of annual and and partly semiannual oscillations at 11 °S off Angola. Although the observed semiannual cycle of the AC cannot yet be fully explained, it is remarkable how much of the annual and semiannual oscillations observed at 11 °S off Angola appear to be governed essentially by linear wave dynamics. On intraseasonal time scales *Bachèlery et al.* (2016) noted the dominance of local forcing over remote equatorial forcing for the variability in the upwelling region. This is in agreement with the results presented here in so far as local forcing is already essential to reproduce the observed semiannual cycle of the AC and might become increasingly important on shorter time scales. In the intraseasonal range alongshore velocity at 11 °S shows a distinct peak near 120 days, associated with a baroclinic structure indicating the dominance of low baroclinic modes. Equivalent SWM simulations as for the annual and semiannual cycles confirm the low-baroclinic nature of this oscillation, despite being phase-shifted and too weak. This indicates that remote equatorial forcing most likely is not the main driver for the observed intraseasonal variability. On the other hand, continuous and recurrent propagation of EKWs and CTWs have been evidenced from altimetry data particularly for intraseasonal time scales (*Polo et al.*, 2008). Furthermore, basin-mode resonance at the 120 day period has recently been described for the Caribbean Sea (*Hughes et al.*, 2016). The verification of a potential impact of this oscillation on the equatorial Atlantic circulation via CTW and EKW response and possibly on the boundary circulation off Angola was hindered by the impossibility to isolate the signal from several interfering, stronger signals in the equatorial Atlantic. Thus, the potential role of remote equatorial forcing for the intraseasonal variability in the boundary circulation off Angola remains an open question.

7.1 Outlook

The results of the present study have substantially enhanced our knowledge of the tropical Angolan system, particularly with regard to the boundary current circulation and its variability, but also in terms of the relation between seasonal wave propagation and seasonally occurring upwelling. Yet, many gaps in our understanding of this highly productive marine ecosystem still remain.

As discussed here as well as in previous studies (*Ostrowski et al.*, 2009; *Rouault*, 2012), upwelling and downwelling seasons off Angola are primarily associated with the propagation of CTWs. Alongshore winds off Angola are weak throughout the year (Figure 1.1). In fact, the seasonal minimum of alongshore winds coincides with the major upwelling season, ruling out wind-driven Ekman divergence as driving force for the coastal upwelling. Other processes like internal wave induced mixing might instead contribute to the nutrient supply to the near-surface

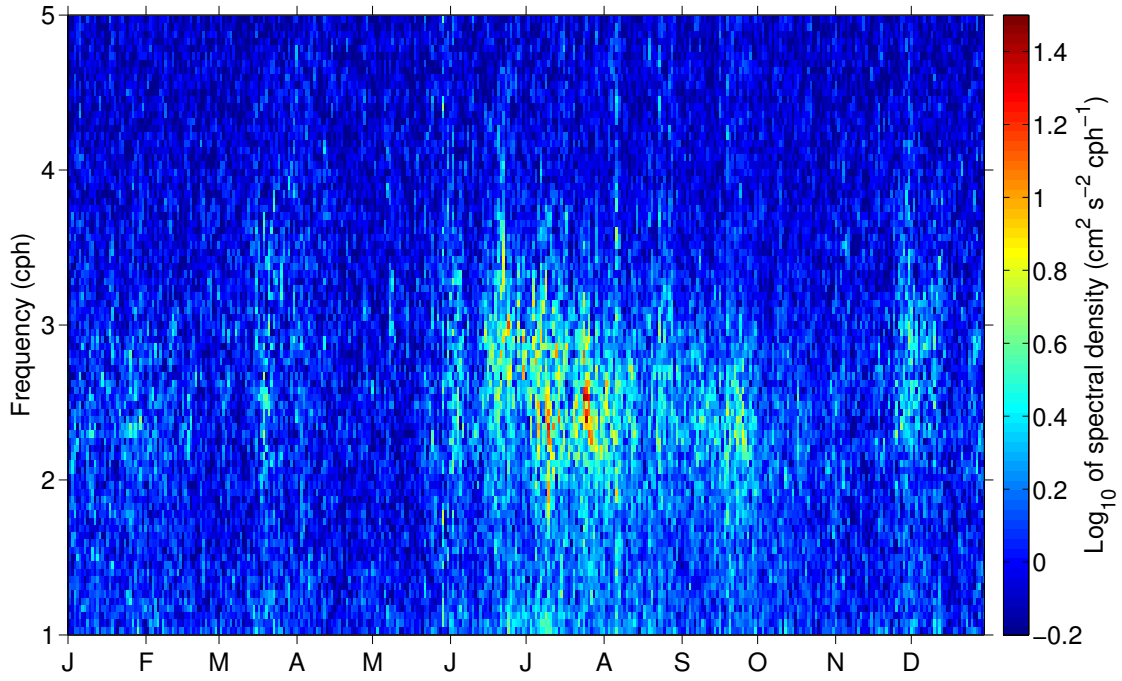

Figure 7.1: The spectral density distribution of internal wave energy in the high frequency range (close to the buoyancy frequency $N_0 \sim 3$ cph) during the year computed from moored velocity data at 11 °S off Angola. The spectral distribution is derived from observations of crossshore velocity at the shelf in 500 m water depth for the depth range between 300 and 150 m.

layers and thus foster primary production in the euphotic zone. However, the impact of the CTW propagation on these processes remains unclear. Hydrographic data off Angola do suggest a seasonal change in the stratification of the deeper waters on the continental slope, that most likely is induced by CTW propagation. Stratification over the shelf break and continental slope controls the transfer of tidally induced internal wave energy onto the shelf (*Hall et al.*, 2013), which in turn is capable to fuel the diapycnal nutrient fluxes on the shelf (*Schafstall et al.*, 2010). By impacting stratification, CTW propagation might therefore essentially control the amount of internal wave energy reaching the Angolan shelf where it induces diapycnal mixing. Spectral analysis of the crossshore velocity component measured by the onshore Acoustic Doppler Current Profiler (ADCP) of the 11 °S array (located on the continental slope at about 500 m water depth) indeed suggests a seasonal cycle in internal wave energy with elevated energy levels during the major upwelling season (Figure 7.1), supporting this hypothesis. Unfortunately, a similar instrument moored at about 200 m water depth could not be retrieved. Thus, a similar analysis, which would reveal how much internal wave energy actually enters the Angolan shelf, has not been possible. Further studies are required in the future to enhance the understanding of these processes.

Another unresolved issue regards the exact role of the AC for the anomalously strong southward advection of warm tropical waters during Benguela Niño events. *Mercier et al.* (2003) report an AC transport of about 11 Sv during the major Benguela Niño event in February/March 1995, which

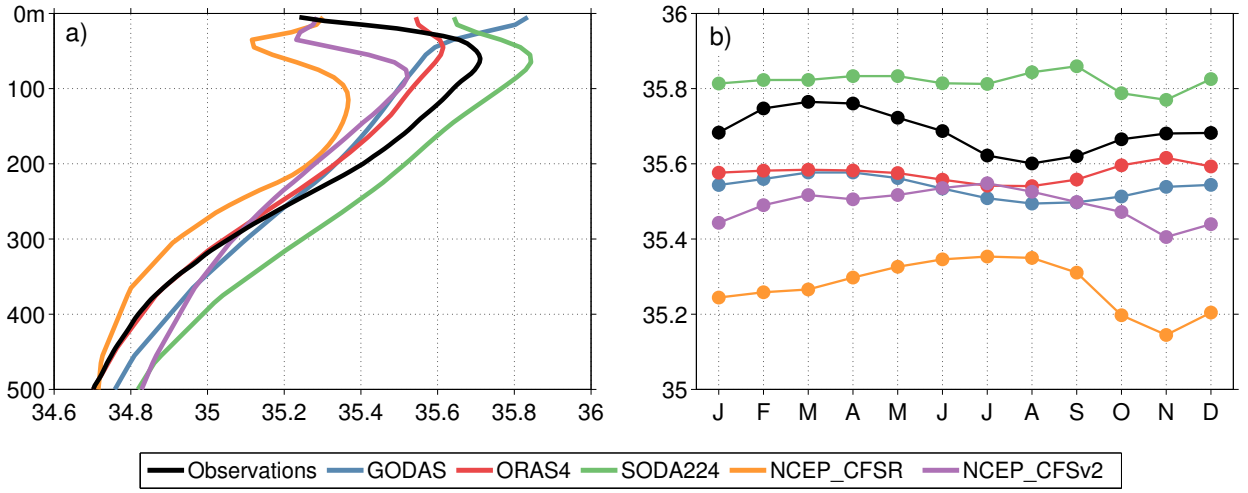

Figure 7.2: (a) Profiles of mean salinity from observations (black) and various reanalysis products (colors). In (b) the corresponding mean seasonal cycles of salinity averaged over 50–100 m depth are shown for observations (black) reanalysis products.

was based on an inverse study making use of World Ocean Circulation Experiment (WOCE) line A13. Given the AC mean transport of about 0.3 Sv derived from the moored velocity observations, this would imply a massive transport anomaly during a Benguela Niño event. As the mooring array off Angola is still in place, chances to capture the AC flow during such an event are still given. This would yield a direct estimate of the associated transport anomaly and would help to interpret the previously reported value by *Mercier et al.* (2003) for the Benguela Niño 1995.

On interannual time scales, the hydrographic data from the EAF-Nansen program revealed strong variability of the subsurface ocean heat content in the depth range of the AC. Warm and cold periods can persist for several years most likely associated with interannual transport variability of the AC. Interestingly, the heat content anomalies in the subsurface usually precede Sea Surface Temperature (SST) anomalies of the same sign in the Angola-Benguela Area, which are used as an indicator for Benguela Niño/Niña events. This suggests potential preconditioning of these events by subsurface heat content anomalies building up over years and would require forcing mechanisms different from the often proposed direct wave response to zonal wind anomalies in the western equatorial Atlantic.

Nonetheless, the recent efforts in collecting new in-situ measurements off Angola as well as making already existing observational data available to the scientific community have contributed to the ongoing progress in process understanding in a highly important yet so far generally undersampled region of the World Oceans. The collected data will become very valuable particularly for the assessment of still existing serious biases in coupled climate simulations and ocean reanalysis products in the near future. First assessments of the representation of current strength and thermal structure off Angola in widely-used ocean reanalysis products have already been undertaken as part of this thesis (Chapter 3). The results show encouraging similarities in the observed and simulated AC strength and thermal structure, besides strong differences in the seasonality

of the AC transport. The comparison of observed and simulated subsurface salinity constitutes another indicator on how well relevant physical processes for the Angolan system, such as horizontal advection, vertical mixing, and continental river discharge, are represented in the models. Tremendous differences between observed and simulated salinity are found at 11 °S particularly in the upper 100 m of the water column (Figure 7.2), based on a similar assessment as carried out in Section 3.4. The misrepresentation of both the near-surface salinity and subsurface salinity in the depth range of the AC core underline the need for a better understanding of the processes at work. Ongoing efforts to sustain and perhaps even extend existing observing systems in the region will be crucial for further scientific progress just as much as the further development of capacities in Angola and the neighboring countries to observe the ocean and analyze obtained measurements.

Bibliography

Anderson, D. L., and A. Gill (1975), Spin-up of a stratified ocean, with applications to upwelling, *Deep Sea Research and Oceanographic Abstracts*, *22*(9), 583–596, doi:10.1016/0011-7471(75)90046-7.

Ascani, F., D. Wang, and E. Firing (2006), Equatorial deep jets in a simple ocean generation circulation model, *Eos Trans. AGU*, *87*(36), Ocean Sci. Meet. Suppl., Abstract OS33C–05.

Ascani, F., E. Firing, J. P. McCreary, P. Brandt, and R. J. Greatbatch (2015), The Deep Equatorial Ocean Circulation in Wind-Forced Numerical Solutions, *Journal of Physical Oceanography*, *45*(6), 1709–1734, doi:10.1175/JPO-D-14-0171.1.

Athie, G., and F. Marin (2008), Cross-equatorial structure and temporal modulation of intraseasonal variability at the surface of the Tropical Atlantic Ocean, *Journal of Geophysical Research: Oceans*, *113*(C8), C08,020, doi:10.1029/2007JC004332, c08020.

Bachèlery, M.-L., S. Illig, and I. Dadou (2016), Interannual variability in the South-East Atlantic Ocean, focusing on the Benguela Upwelling System: Remote versus local forcing, *Journal of Geophysical Research-Oceans*, *121*(1), 284–310, doi:10.1002/2015JC011168.

Balmaseda, M. A., K. Mogensen, and A. T. Weaver (2013), Evaluation of the ECMWF ocean reanalysis system ORAS4, *Quarterly Journal of the Royal Meteorological Society*, *139*(674), 1132–1161, doi:10.1002/qj.2063.

Barnett, T. P. (1983), Interaction of the Monsoon and Pacific Trade Wind System at Interannual Time Scales Part I: The Equatorial Zone, *Monthly Weather Review*, *111*(4), 756–773, doi:10.1175/1520-0493(1983)111⟨0756:Iotmap⟩2.0.Co;2.

Berger, H., A. M. Treguier, N. Perenne, and C. Talandier (2014), Dynamical contribution to sea surface salinity variations in the eastern Gulf of Guinea based on numerical modelling, *Climate Dynamics*, *43*(11), 3105–3122, doi:10.1007/s00382-014-2195-4.

Berrisford, P., D. P. Dee, K. Fielding, M. Fuentes, P. W. Kallberg, S. Kobayashi, and s. Uppala (2009), *The ERA-Interim archive*, ECMWF.

Berrit, G. R. (1976), Les eaux froides côtières du Gabon à L'Angola sont-elles dues à un upwelling d'Ekman, *Cahiers ORSTROM, Séries Océanographie*, *14*, 473–478.

Berrit, G. R., and C. Dias (1977), Hydroclimatologie des Régions Côtières de L'Angola, *Cahiers ORSTROM, Séries Océanographie*, *15*, 181–196.

Bianchi, G., A. Bjordal, K. A. Koranteng, M. Tandstad, B. Sambe, and T. Stromme (2016), Collaboration between the Nansen Programme and the Large Marine Ecosystem Programmes, *Environmental Development*, *17*, 340–348, doi:10.1016/j.envdev.2015.11.003, thematic Issue - Ecosystem Based Management of Large Marine Ecosystems.

Boyd, J. P. (1980), Equatorial Solitary Waves. Part I: Rossby Solitons, *Journal of Physical Oceanography*, *10*(11), 1699–1717, doi:10.1175/1520-0485(1980)010⟨1699:ESWPIR⟩2.0.CO;2.

Brandt, P., and C. Eden (2005), Annual cycle and interannual variability of the mid-depth tropical Atlantic Ocean, *Deep Sea Research Part I: Oceanographic Research Papers*, *52*(2), 199 – 219, doi:10.1016/j.dsr.2004.03.011.

Brandt, P., F. A. Schott, C. Provost, A. Kartavtseff, V. Hormann, B. Bourlès, and J. Fischer (2006), Circulation in the central equatorial Atlantic: Mean and intraseasonal to seasonal variability, *Geophysical Research Letters*, *33*(7), L07,609, doi:10.1029/2005GL025498, l07609.

Brandt, P., A. Funk, V. Hormann, M. Dengler, R. J. Greatbatch, and J. M. Toole (2011), Interannual atmospheric variability forced by the deep equatorial Atlantic Ocean, *Nature*, *473*(7348), 497–500, doi:10.1038/nature10013.

Brandt, P., et al. (2012), Ventilation of the equatorial Atlantic by the equatorial deep jets, *Journal of Geophysical Research: Oceans*, *117*(C12), C12,015, doi:10.1029/2012JC008118, c12015.

Brandt, P., A. Funk, A. Tantet, W. Johns, and J. Fischer (2014), The Equatorial Undercurrent in the central Atlantic and its relation to tropical Atlantic variability, *Climate Dynamics*, *43*(11), 2985–2997, doi:10.1007/s00382-014-2061-4.

Brandt, P., M. Claus, R. J. Greatbatch, R. Kopte, J. M. Toole, W. E. Johns, and C. W. Böning (2016), Annual and Semiannual Cycle of Equatorial Atlantic Circulation Associated with Basin-Mode Resonance, *Journal of Physical Oceanography*, *46*(10), 3011–3029, doi:10.1175/JPO-D-15-0248.1.

Cane, M. A., and P. R. Gent (1984), Reflection of low-frequency equatorial waves at arbitrary western boundaries, *Journal of Marine Research*, *42*(3), 487–502, doi:10.1357/002224084788505988.

Cane, M. A., and D. W. Moore (1981), A Note on Low-Frequency Equatorial Basin Modes, *Journal of Physical Oceanography*, *11*(11), 1578–1584, doi:10.1175/1520-0485(1981)011⟨1578:ANOLFE⟩2.0.CO;2.

Carr, M.-E., and E. J. Kearns (2003), Production regimes in four Eastern Boundary Current systems, *Deep Sea Research Part II: Topical Studies in Oceanography*, *50*(22–26), 3199–3221, doi:10.1016/j.dsr2.2003.07.015.

Carton, J. A., and B. S. Giese (2008), A Reanalysis of Ocean Climate Using Simple Ocean Data Assimilation (SODA), *Monthly Weather Review*, *136*(8), 2999–3017, doi:10.1175/2007MWR1978.1.

Charney, J. G. (1959), Non-linear theory of a wind-driven homogeneous layer near the equator, *Deep Sea Research (1953)*, *6*, 303 – 310, doi:10.1016/0146-6313(59)90089-9.

Chassignet, E. P., H. E. Hurlburt, O. M. Smedstad, G. R. Halliwell, P. J. Hogan, A. J. Wallcraft, R. Baraille, and R. Bleck (2007), The {HYCOM} (HYbrid Coordinate Ocean Model) data assimilative system, *Journal of Marine Systems*, *65*(1–4), 60–83, doi:10.1016/j.jmarsys.2005.09.016, marine Environmental Monitoring and PredictionSelected papers from the 36th International Liège Colloquium on Ocean Dynamics36th International Liège Colloquium on Ocean Dynamics.

Chavez, F. P., and M. Messié (2009), A comparison of Eastern Boundary Upwelling Ecosystems, *Progress in Oceanography*, *83*(1–4), 80–96, doi:10.1016/j.pocean.2009.07.032.

Claus, M., R. J. Greatbatch, and P. Brandt (2014), Influence of the Barotropic Mean Flow on the Width and the Structure of the Atlantic Equatorial Deep Jets, *Journal of Physical Oceanography*, *44*(9), 2485–2497, doi:10.1175/JPO-D-14-0056.1.

Claus, M., R. J. Greatbatch, P. Brandt, and J. M. Toole (2016), Forcing of the Atlantic Equatorial Deep Jets Derived from Observations, *Journal of Physical Oceanography*, *46*(12), 3549–3562, doi:10.1175/JPO-D-16-0140.1.

Crépon, M., C. Richez, and M. Chartier (1984), Effects of Coastline Geometry on Upwellings, *Journal of Physical Oceanography*, *14*(8), 1365–1382, doi:10.1175/1520-0485(1984)014⟨1365:EOCGOU⟩2.0.CO;2.

Dai, A., T. Qian, K. E. Trenberth, and J. Milliman (2009), Changes in continental freshwater discharge from 1948-2004, *Journal of Climate*, *22*, 2773–2791, doi:10.1175/2008JCLI2592.1.

Davey, M., et al. (2002), STOIC: a study of coupled model climatology and variability in tropical ocean regions, *Climate Dynamics*, *18*(5), 403–420, doi:10.1007/s00382-001-0188-6.

Debreu, L., and E. Blayo (2008), Two-way embedding algorithms: a review, *Ocean Dynamics*, *58*(5), 415–428, doi:10.1007/s10236-008-0150-9.

Diakhaté, M., G. de Coëtlogon, A. Lazar, M. Wade, and A. T. Gaye (2016), Intraseasonal variability of tropical Atlantic sea-surface temperature: air–sea interaction over upwelling fronts,

Quarterly Journal of the Royal Meteorological Society, *142*(694), 372–386, doi:10.1002/qj.2657.

Dias, C. (1983a), Note on the evidence of a permanent southward flow of the upper oceanic tropospheric waters off Angola at 12°S, *Collection of Scientific Papers International Commission for the Southeast Atlantic Fisheries*, *10*, 99–102.

Dias, C. (1983b), Preliminary report on the physical oceanography off southern Angola, March and July 1971, *Collection of Scientific Papers International Commission for the Southeast Atlantic Fisheries*, *10*, 103–116.

Ding, H., N. S. Keenlyside, and M. Latif (2009), Seasonal cycle in the upper equatorial Atlantic Ocean, *Journal of Geophysical Research: Oceans*, *114*(C9), C09,016, doi:10.1029/2009JC005418, c09016.

d'Orgeville, M., B. L. Hua, and H. Sasaki (2007), Equatorial deep jets triggered by a large vertical scale variability within the western boundary layer, *Journal of Marine Research*, *65*(1), 1–25, doi:10.1357/002224007780388720.

Durgadoo, J. V., B. R. Loveday, C. J. C. Reason, P. Penven, and A. Biastoch (2013), Agulhas Leakage Predominantly Responds to the Southern Hemisphere Westerlies, *Journal of Physical Oceanography*, *43*(10), 2113–2131, doi:10.1175/JPO-D-13-047.1.

Duteil, O., F. U. Schwarzkopf, C. W. Böning, and A. Oschlies (2014), Major role of the equatorial current system in setting oxygen levels in the eastern tropical Atlantic Ocean: A high-resolution model study, *Geophysical Research Letters*, *41*(6), 2033–2040, doi:10.1002/2013GL058888, 2013GL058888.

Fennel, W. (1999), Theory of the Benguela Upwelling System, *Journal of Physical Oceanography*, *29*(2), 177–190, doi:10.1175/1520-0485(1999)029⟨0177:TOTBUS⟩2.0.CO;2.

Florenchie, P., J. R. E. Lutjeharms, C. J. C. Reason, S. Masson, and M. Rouault (2003), The source of Benguela Niños in the South Atlantic Ocean, *Geophysical Research Letters*, *30*(10), doi:10.1029/2003GL017172.

Florenchie, P., C. J. C. Reason, J. R. E. Lutjeharms, M. Rouault, C. Roy, and S. Masson (2004), Evolution of Interannual Warm and Cold Events in the Southeast Atlantic Ocean, *Journal of Climate*, *17*(12), 2318–2334, doi:10.1175/1520-0442(2004)017⟨2318:EOIWAC⟩2.0.CO;2.

Food and Agricultural Organization of the United Nations (FAO) (2014), The state of World Fisheries and Agriculture.

Fu, L.-L. (2007), Intraseasonal Variability of the Equatorial Indian Ocean Observed from Sea Surface Height, Wind, and Temperature Data, *Journal of Physical Oceanography*, *37*(2), 188–202, doi:10.1175/JPO3006.1.

Gammelsrød, T., C. H. Bartholomae, D. C. Boyer, V. L. L. Filipe, and M. J. O'Toole (1998), Intrusion of warm surface water along the Angolan-Namibian coast in February–March 1995: the 1995 Benguela Niño, *South African Journal of Marine Science*, *19*(1), 41–56, doi:10.2989/025776198784126719.

Gill, A. E. (1982), *Atmosphere-Ocean Dynamics*, Academic Press, 662 pp.

Goubanova, K., S. Illig, E. Machu, V. Garçon, and B. Dewitte (2013), SST subseasonal variability in the central Benguela upwelling system as inferred from satellite observations (1999–2009), *Journal of Geophysical Research: Oceans*, *118*(9), 4092–4110, doi:10.1002/jgrc.20287.

Greatbatch, R. J. (1985), Kelvin wave fronts, Rossby solitary waves and the nonlinear spin-up of the equatorial oceans, *Journal of Geophysical Research: Oceans*, *90*(C5), 9097–9107, doi:10.1029/JC090iC05p09097.

Greatbatch, R. J., P. Brandt, M. Claus, S.-H. Didwischus, and Y. Fu (2012), On the Width of the Equatorial Deep Jets, *Journal of Physical Oceanography*, *42*(10), 1729–1740, doi:10.1175/JPO-D-11-0238.1.

Griffies, S. M., et al. (2009), Coordinated Ocean-ice Reference Experiments (COREs), *Ocean Modelling*, *26*(1–2), 1 – 46, doi:10.1016/j.ocemod.2008.08.007.

Grodsky, S. A., J. A. Carton, S. Nigam, and Y. M. Okumura (2012), Tropical Atlantic Biases in CCSM4, *Journal of Climate*, *25*(11), 3684–3701, doi:10.1175/JCLI-D-11-00315.1.

Gruber, N., Z. Lachkar, H. Frenzel, P. Marchesiello, M. Munnich, J. C. McWilliams, T. Nagai, and G.-K. Plattner (2011), Eddy-induced reduction of biological production in eastern boundary upwelling systems, *Nature Geosciences*, *4*(11), 787–792, doi:10.1038/ngeo1273.

Gómez-Valdivia, F., A. Parés-Sierra, and A. Laura Flores-Morales (2017), Semiannual variability of the California Undercurrent along the Southern California Current System: A tropical generated phenomenon, *Journal of Geophysical Research: Oceans*, *122*(2), 1574–1589, doi:10.1002/2016JC012350.

Hall, R. A., J. M. Huthnance, and R. G. Williams (2013), Internal Wave Reflection on Shelf Slopes with Depth-Varying Stratification, *Journal of Physical Oceanography*, *43*(2), 248–258, doi:10.1175/JPO-D-11-0192.1.

Han, W., J. P. M. Jr., D. L. T. Anderson, and A. J. Mariano (1999), Dynamics of the Eastern Surface Jets in the Equatorial Indian Ocean, *Journal of Physical Oceanography*, *29*(9), 2191–2209, doi:10.1175/1520-0485(1999)029⟨2191:DOTESJ⟩2.0.CO;2.

Han, W., J. P. McCreary, Y. Masumoto, J. Vialard, and B. Duncan (2011), Basin Resonances in the Equatorial Indian Ocean, *Journal of Physical Oceanography*, *41*(6), 1252–1270, doi:10.1175/2011JPO4591.1.

Harlaß, J., M. Latif, and W. Park (2015), Improving Climate Model Simulation of Tropical Atlantic Sea Surface Temperature: The Importance of Enhanced Vertical Atmosphere Model Resolution, *Geophysical Research Letters*, *42*(7), 2401–2408, doi:10.1002/2015GL063310.

Hazeleger, W., and P. de Vries (2003), Fate of the equatorial undercurrent in the Atlantic, in *Interhemispheric water exchange in the Atlantic ocean*, vol. 68, edited by G. J. Goni, pp. 175–191, Elsevier Oceanography.

Hazeleger, W., P. de Vries, and Y. Friocourt (2003), Sources of the Equatorial Undercurrent in the Atlantic in a High-Resolution Ocean Model, *Journal of Physical Oceanography*, *33*(4), 677–693, doi:10.1175/1520-0485(2003)33⟨677:SOTEUI⟩2.0.CO;2.

Hellerman, S. (1980), Charts of the variability of the wind stress over the tropical Atlantic, in *Oceanography and Surface Layer Meteorology in the B/C Scale*, edited by G. Siedler, J. D. Woods, and W. Düing, pp. 63–75, Pergamon, doi:10.1016/B978-1-4832-8366-1.50022-4.

Holton, J. R. (2004), *An Introduction to Dynamic Meteorology*, vol. 88, 4 ed., Elsevier, Amsterdam, 535 pp.

Hormann, V., and P. Brandt (2009), Upper equatorial Atlantic variability during 2002 and 2005 associated with equatorial Kelvin waves, *Journal of Geophysical Research: Oceans*, *114*(C3), C03,007, doi:10.1029/2008JC005101, c03007.

Huang, B., Z.-Z. Hu, and B. Jha (2007), Evolution of model systematic errors in the Tropical Atlantic Basin from coupled climate hindcasts, *Climate Dynamics*, *28*(7), 661–682, doi:10.1007/s00382-006-0223-8.

Hughes, C. W., J. Williams, A. Hibbert, C. Boening, and J. Oram (2016), A Rossby whistle: A resonant basin mode observed in the Caribbean Sea, *Geophysical Research Letters*, *43*(13), 7036–7043, doi:10.1002/2016GL069573, 2016GL069573.

Hummels, R., M. Dengler, P. Brandt, and M. Schlundt (2014), Diapycnal heat flux and mixed layer heat budget within the Atlantic Cold Tongue, *Climate Dynamics*, *43*(11), 3179–3199, doi:10.1007/s00382-014-2339-6.

Hurlburt, H. E., and J. D. Thompson (1973), Coastal Upwelling on a β-Plane, *Journal of Physical Oceanography*, *3*(1), 16–32, doi:10.1175/1520-0485(1973)003⟨0016:CUOAP⟩2.0.CO;2.

Japan Meteorological Agency (2013), *JRA-55: Japanese 55-year Reanalysis, Daily 3-Hourly and 6-Hourly Data*, doi:10.5065/D6HH6H41.

Jarre, A., et al. (2015), Synthesis: climate effects on biodiversity, abundance and distribution of marine organisms in the Benguela, *Fisheries Oceanography*, *24*, 122–149, doi:10.1111/fog.12086.

Jensen, T. G. (1993), Equatorial variability and resonance in a wind-driven Indian Ocean model, *Journal of Geophysical Research: Oceans*, *98*(C12), 22,533–22,552, doi:10.1029/93JC02565.

Johns, W. E., P. Brandt, B. Bourlès, A. Tantet, A. Papapostolou, and A. Houk (2014), Zonal structure and seasonal variability of the Atlantic Equatorial Undercurrent, *Climate Dynamics*, *43*(11), 3047–3069, doi:10.1007/s00382-014-2136-2.

Johnson, G. C., and D. Zhang (2003), Structure of the Atlantic Ocean Equatorial Deep Jets, *Journal of Physical Oceanography*, *33*(3), 600–609, doi:10.1175/1520-0485(2003)033⟨0600:SOTAOE⟩2.0.CO;2.

Jouanno, J., F. Marin, Y. du Penhoat, and J.-M. Molines (2013), Intraseasonal Modulation of the Surface Cooling in the Gulf of Guinea, *Journal of Physical Oceanography*, *43*(2), 382–401, doi:10.1175/JPO-D-12-053.1.

Kanamitsu, M., W. Ebisuzaki, J. Woollen, S.-K. Yang, J. J. Hnilo, M. Fiorino, and G. L. Potter (2002), NCEP–DOE AMIP-II Reanalysis (R-2), *Bulletin of the American Meteorological Society*, *83*(11), 1631–1643, doi:10.1175/BAMS-83-11-1631.

Kopte, R., P. Brandt, M. Dengler, P. C. M. Tchipalanga, M. Macuéria, and M. Ostrowski (2017), The Angola Current: Flow and hydrographic characteristics as observed at 11°S, *Journal of Geophysical Research: Oceans*, *122*(2), 1177–1189, doi:10.1002/2016JC012374.

Kostianoy, A. G., and J. R. E. Lutjeharms (1999), Atmospheric effects in the Angola-Benguela frontal zone, *Journal of Geophysical Research-Oceans*, *104*(C9), 20,963–20,970, doi:10.1029/1999JC900017.

Lamb, K. G. (2014), Internal Wave Breaking and Dissipation Mechanisms on the Continental Slope/Shelf, *Annual Review of Fluid Mechanics*, *46*(1), 231–254, doi:10.1146/annurev-fluid-011212-140701.

Large, W. G., and G. Danabasoglu (2006), Attribution and Impacts of Upper-Ocean Biases in CCSM3, *Journal of Climate*, *19*(11), 2325–2346, doi:10.1175/JCLI3740.1.

Lass, H. U., M. Schmidt, V. Mohrholz, and G. Nausch (2000), Hydrographic and Current Measurements in the Area of the Angola–Benguela Front, *Journal of Physical Oceanography*, *30*(10), 2589–2609, doi:10.1175/1520-0485(2000)030⟨2589:HACMIT⟩2.0.CO;2.

Lazar, A., I. Polo, S. Arnault, and G. Mainsant (2006), Kelvin Waves Activity in the eastern Tropical Atlantic, in *Proceedings of the Symposium on 15 Years of Progress in Radar Altimetry (ESA SP-614, July 2006)*.

Lehodey, P., et al. (2006), Climate Variability, Fish, and Fisheries, *Journal of Climate*, *19*(20), 5009–5030, doi:10.1175/JCLI3898.1.

Lübbecke, J. F., C. W. Böning, N. S. Keenlyside, and S.-P. Xie (2010), On the connection between Benguela and equatorial Atlantic Niños and the role of the South Atlantic Anticyclone, *Journal of Geophysical Research-Oceans*, *115*(C9), doi:10.1029/2009JC005964.

Lüdke, J. (2016), Seasonal Mixed Layer Heat and Salinity Budget in the South Eastern Tropical Atlantic Ocean, Master's thesis, Christian-Albrechts-Universität zu Kiel.

Lukas, R., and E. Firing (1985), The Annual Rossby Wave in the Central Equatorial Pacific Ocean, *Journal of Physical Oceanography*, *15*(1), 55–67, doi:10.1175/1520-0485(1985)015⟨0055:TARWIT⟩2.0.CO;2.

Madec, G. (2008), NEMO ocean engine. Note du pole de modélisation, Institut Pierre-Simon Laplace (IPSL), France, No 27, p. 300 pp.

Matsuno, T. (1966), Quasi-Geostrophic Motions in the Equatorial Area, *Journal of the Meteorological Society of Japan. Ser. II*, *44*(1), 25–43, doi:10.2151/jmsj1965.44.1_25.

McCreary, J. P. (1981a), A Linear Stratified Ocean Model of the Coastal Undercurrent, *Philosophical Transactions of the Royal Society of London A: Mathematical, Physical and Engineering Sciences*, *302*(1469), 385–413, doi:10.1098/rsta.1981.0176.

McCreary, J. P. (1981b), A Linear Stratified Ocean Model of the Equatorial Undercurrent, *Philosophical Transactions of the Royal Society of London A: Mathematical, Physical and Engineering Sciences*, *298*(1444), 603–635, doi:10.1098/rsta.1981.0002.

McCreary, J. P. (1984), Equatorial beams, *Journal of Marine Research*, *42*(2), 395–430, doi:10.1357/002224084788502792.

McCreary, J. P., and S.-Y. Chao (1985), Three-dimensional shelf circulation along an eastern ocean boundary, *Journal of Marine Research*, *43*(1), 13–36, doi:doi:10.1357/002224085788437316.

Meeuwis, J., and J. R. E. Lutjeharms (1990), Surface thermal characteristics of the Angola-Benguela front, *South African Journal of Marine Science*, *9*(1), 261–279, doi:10.2989/025776190784378772.

Mercier, H., M. Arhan, and J. R. E. Lutjeharms (2003), Upper-layer circulation in the eastern Equatorial and South Atlantic Ocean in January–March 1995, *Deep Sea Research Part I: Oceanographic Research Papers*, *50*(7), 863–887, doi:10.1016/S0967-0637(03)00071-2.

Milinski, S., J. Bader, H. Haak, A. C. Siongco, and J. H. Jungclaus (2016), High atmospheric horizontal resolution eliminates the wind-driven coastal warm bias in the southeastern tropical Atlantic, *Geophysical Research Letters*, *43*(19), 10,455–10,462, doi:10.1002/2016GL070530, 2016GL070530.

Mohrholz, V., M. Schmidt, and J. R. E. Lutjeharms (2001), The hydrography and dynamics of the Angola-Benguela Frontal Zone and environment in April 1999, *South African Journal of Science*, *97*(May/June 2001), 199–208.

Mohrholz, V., C. H. Bartholomae, A. K. van der Plas, and H. U. Lass (2008), The seasonal variability of the northern Benguela undercurrent and its relation to the oxygen budget on the shelf, *Continental Shelf Research*, *28*(3), 424–441, doi:10.1016/j.csr.2007.10.001.

Mohrholz, V., A. Eggert, T. Junker, G. Nausch, T. Ohde, and M. Schmidt (2014), Cross shelf hydrographic and hydrochemical conditions and their short term variability at the northern Benguela during a normal upwelling season, *Journal of Marine Systems*, *140, Part B*, 92–110, doi:10.1016/j.jmarsys.2014.04.019.

Monteiro, P., A. van der Plas, J.-L. Mélice, and P. Florenchie (2008), Interannual hypoxia variability in a coastal upwelling system: Ocean–shelf exchange, climate and ecosystem-state implications, *Deep Sea Research Part I: Oceanographic Research Papers*, *55*(4), 435–450, doi:10.1016/j.dsr.2007.12.010.

Moroshkin, K. V., V. Bunov, and R. Bulatov (1970), Water circulation in the eastern South Atlantic Ocean, *Oceanology*, *10*, 27–34.

Ostrowski, M., J. C. B. da Silva, and B. Bazik-Sangolay (2009), The response of sound scatterers to El Niño- and La Niña-like oceanographic regimes in the southeastern Atlantic, *ICES Journal of Marine Science: Journal du Conseil*, *66*(6), 1063–1072, doi:10.1093/icesjms/fsp102.

Parrish, Schwing, and Mendelssohn (2000), Mid-latitude wind stress: the energy source for climatic shifts in the North Pacific Ocean, *Fisheries Oceanography*, *9*(3), 224–238, doi:10.1046/j.1365-2419.2000.00136.x.

Patricola, C. M., M. Li, Z. Xu, P. Chang, R. Saravanan, and J.-S. Hsieh (2012), An investigation of tropical Atlantic bias in a high-resolution coupled regional climate model, *Climate Dynamics*, *39*(9), 2443–2463, doi:10.1007/s00382-012-1320-5.

Pedlosky, J. (1987), *Geophysical Fluid Dynamics*, 2 ed., Springer-Verlag.

Peterson, R. G., and L. Stramma (1991), Upper-level circulation in the South Atlantic Ocean, *Progress in Oceanography*, *26*(1), 1–73, doi:10.1016/0079-6611(91)90006-8.

Philander, S. G. (1990), *El Niño, La Niña, and the Southern Oscillation*, *International Geophysics Series*, vol. 46, Academic Press, 293 pp.

Philander, S. G. H., and Y. Chao (1991), On the Contrast between the Seasonal Cycles of the Equatorial Atlantic and Pacific Oceans, *Journal of Physical Oceanography*, *21*(9), 1399–1406, doi:10.1175/1520-0485(1991)021⟨1399:OTCBTS⟩2.0.CO;2.

Philander, S. G. H., and R. C. Pacanowski (1981), Response of equatorial oceans to periodic forcing, *Journal of Geophysical Research: Oceans*, *86*(C3), 1903–1916, doi:10.1029/JC086iC03p01903.

Philander, S. G. H., and R. C. Pacanowski (1986), A model of the seasonal cycle in the tropical Atlantic Ocean, *Journal of Geophysical Research: Oceans*, *91*(C12), 14,192–14,206, doi:10.1029/JC091iC12p14192.

Philander, S. G. H., and J.-H. Yoon (1982), Eastern Boundary Currents and Coastal Upwelling, *Journal of Physical Oceanography*, *12*(8), 862–879, doi:10.1175/1520-0485(1982)012⟨0862:EBCACU⟩2.0.CO;2.

Picaut, J. (1983), Propagation of the Seasonal Upwelling in the Eastern Equatorial Atlantic, *Journal of Physical Oceanography*, *13*(1), 18–37, doi:10.1175/1520-0485(1983)013⟨0018:POTSUI⟩2.0.CO;2.

Pizarro, O., G. Shaffer, B. Dewitte, and M. Ramos (2002), Dynamics of seasonal and interannual variability of the Peru-Chile Undercurrent, *Geophysical Research Letters*, *29*(12), 22–1–22–4, doi:10.1029/2002GL014790.

Polo, I., A. Lazar, B. Rodriguez-Fonseca, and S. Arnault (2008), Oceanic Kelvin waves and tropical Atlantic intraseasonal variability: 1. Kelvin wave characterization, *Journal of Geophysical Research-Oceans*, *113*(C7), 18, doi:10.1029/2007jc004495.

Poole, R., and M. Tomczak (1999), Optimum multiparameter analysis of the water mass structure in the Atlantic Ocean thermocline, *Deep Sea Research Part I: Oceanographic Research Papers*, *46*(11), 1895–1921, doi:10.1016/S0967-0637(99)00025-4.

Praveen Kumar, B., J. Vialard, M. Lengaigne, V. S. N. Murty, M. J. McPhaden, M. F. Cronin, F. Pinsard, and K. Gopala Reddy (2013), TropFlux wind stresses over the tropical oceans: evaluation and comparison with other products, *Climate Dynamics*, *40*(7), 2049–2071, doi:10.1007/s00382-012-1455-4.

Pujol, M. I., Y. Faugère, G. Taburet, S. Dupuy, C. Pelloquin, M. Ablain, and N. Picot (2016), DUACS DT2014: the new multi-mission altimeter data set reprocessed over 20 years, *Ocean Sci.*, *12*(5), 1067–1090, doi:10.5194/os-12-1067-2016.

Qiao, L., and R. H. Weisberg (1997), The Zonal Momentum Balance of the Equatorial Undercurrent in the Central Pacific, *Journal of Physical Oceanography*, *27*(6), 1094–1119, doi:10.1175/1520-0485(1997)027⟨1094:TZMBOT⟩2.0.CO;2.

Ramos, M., O. Pizarro, L. Bravo, and B. Dewitte (2006), Seasonal variability of the permanent thermocline off northern Chile, *Geophysical Research Letters*, *33*(9), n/a–n/a, doi:10.1029/2006GL025882, l09608.

Reason, C. J. C., and D. Jagadheesha (2005), Relationships between South Atlantic SST Variability and Atmospheric Circulation over the South African Region during Austral Winter, *Journal of Climate*, *18*(16), 3339–3355, doi:10.1175/JCLI3474.1.

Ricciardulli, L., and F. J. Wentz (2016), *Remote Sensing Systems ASCAT C-2015 Daily Ocean Vector Winds on 0.25 deg grid, Version 02.1*, Remote Sensing Systems.

Richter, I., and S.-P. Xie (2008), On the origin of equatorial Atlantic biases in coupled general circulation models, *Climate Dynamics*, *31*(5), 587–598, doi:10.1007/s00382-008-0364-z.

Richter, I., S. K. Behera, Y. Masumoto, B. Taguchi, N. Komori, and T. Yamagata (2010), On the triggering of Benguela Niños: Remote equatorial versus local influences, *Geophysical Research Letters*, *37*(20), L20,604, doi:10.1029/2010GL044461.

Richter, I., S.-P. Xie, S. K. Behera, T. Doi, and Y. Masumoto (2014), Equatorial Atlantic variability and its relation to mean state biases in CMIP5, *Climate Dynamics*, *42*(1), 171–188, doi:10.1007/s00382-012-1624-5.

Rouault, M. (2012), Bi-annual intrusion of tropical water in the northern Benguela upwelling, *Geophysical Research Letters*, *39*(12), L12,606, doi:10.1029/2012GL052099.

Rouault, M., P. Florenchie, N. Fauchereau, and C. J. C. Reason (2003), South East tropical Atlantic warm events and southern African rainfall, *Geophysical Research Letters*, *30*(5), 8009, doi:10.1029/2002GL014840.

Rouault, M., S. Illig, C. Bartholomae, C. J. C. Reason, and A. Bentamy (2007), Propagation and origin of warm anomalies in the Angola Benguela upwelling system in 2001, *Journal of Marine Systems*, *68*(3–4), 473–488, doi:10.1016/j.jmarsys.2006.11.010.

Saetelsdal, G., G. Bianchi, and T. Stromme (1999), The Dr. Fridtjof Nansen Programme 1975-1993. Investigations of fishery resources in developing regions. History of the programme and review of results, *FAO Fisheries Technical Paper 391. Rome*, 434 pp.

Schafstall, J., M. Dengler, P. Brandt, and H. Bange (2010), Tidal-induced mixing and diapycnal nutrient fluxes in the Mauritanian upwelling region, *Journal of Geophysical Research: Oceans*, *115*(C10), C10,014, doi:10.1029/2009JC005940, c10014.

Schmidtko, S., G. C. Johnson, and J. M. Lyman (2013), MIMOC: A global monthly isopycnal upper-ocean climatology with mixed layers, *Journal of Geophysical Research-Oceans*, *118*(4), 1658–1672, doi:10.1002/jgrc.20122.

Schmidtko, S., L. Stramma, and M. Visbeck (2017), Decline in global oceanic oxygen content during the past five decades, *Nature*, *542*(7641), 335–339, doi:10.1038/nature21399.

Schopf, P. S., D. L. Anderson, and R. Smith (1981), Beta-dispersion of low-frequency Rossby waves, *Dynamics of Atmospheres and Oceans*, *5*(3), 187–214, doi:10.1016/0377-0265(81)90011-7.

Schott, F. A., J. P. McCreary, and G. C. Johnson (2004), *Earth Climate: The Ocean-Atmosphere Interaction*, chap. Shallow Overturning Circulations of the Tropical-Subtropical Oceans, pp. 261–304, Geophysical Monograph 147, American Geophysical Union, doi:10.1029/147GM15.

Schott, F. A., M. Dengler, R. Zantopp, L. Stramma, J. Fischer, and P. Brandt (2005), The Shallow and Deep Western Boundary Circulation of the South Atlantic at 5∘sS–11∘S, *Journal of Physical Oceanography*, *35*(11), 2031–2053, doi:10.1175/JPO2813.1.

Schouten, M. W., R. P. Matano, and T. P. Strub (2005), A description of the seasonal cycle of the equatorial Atlantic from altimeter data, *Deep Sea Research Part I: Oceanographic Research Papers*, *52*(3), 477 – 493, doi:10.1016/j.dsr.2004.10.007.

Send, U., C. Eden, and F. Schott (2002), Atlantic Equatorial Deep Jets: Space–Time Structure and Cross-Equatorial Fluxes, *Journal of Physical Oceanography*, *32*(3), 891–902, doi:10.1175/1520-0485(2002)032⟨0891:AEDJST⟩2.0.CO;2.

Shankar, D., J. P. McCreary, W. Han, and S. R. Shetye (1996), Dynamics of the East India Coastal Current: 1. Analytic solutions forced by interior Ekman pumping and local alongshore winds, *Journal of Geophysical Research: Oceans*, *101*(C6), 13,975–13,991, doi:10.1029/96JC00559.

Shannon, L. V., A. J. Boyd, G. B. Brundrit, and J. Taunton-Clark (1986), On the existence of an El Niño-type phenomenon in the Benguela System, *Journal of Marine Research*, *44*(3), 495–520, doi:10.1357/002224086788403105.

Shannon, L. V., J. J. Agenbag, and M. E. L. Buys (1987), Large- and mesoscale features of the Angola-Benguela front, *South African Journal of Marine Science*, *5*(1), 11–34, doi:10.2989/025776187784522261.

Stommel, H. (1959), Wind-drift near the equator, *Deep Sea Research (1953)*, *6*, 298 – 302, doi:10.1016/0146-6313(59)90088-7.

Stramma, L., G. C. Johnson, J. Sprintall, and V. Mohrholz (2008), Expanding Oxygen-Minimum Zones in the Tropical Oceans, *Science*, *320*(5876), 655–658, doi:10.1126/science.1153847.

Strub, P. T., V. Combes, F. A. Shillington, and O. Pizarro (2013), Currents and Processes along the Eastern Boundaries, *International Geophysics*, *103*, 339–384, doi:10.1016/B978-0-12-391851-2.00014-3, ocean Circulation and Climate.

Suginohara, N., and Y. Kitamura (1984), Long-Term Coastal Upwelling over a Continental Shelf–Slope, *Journal of Physical Oceanography*, *14*(6), 1095–1104, doi:10.1175/1520-0485(1984)014⟨1095:LTCUOA⟩2.0.CO;2.

Thierry, V., A.-M. Treguier, and H. Mercier (2004), Numerical study of the annual and semi-annual fluctuations in the deep equatorial Atlantic Ocean, *Ocean Modell.*, *6*(1), 1–30, doi: 10.1016/S1463-5003(02)00054-9.

Thomsen, S., T. Kanzow, G. Krahmann, R. J. Greatbatch, M. Dengler, and G. Lavik (2016), The formation of a subsurface anticyclonic eddy in the Peru-Chile Undercurrent and its impact on the near-coastal salinity, oxygen, and nutrient distributions, *Journal of Geophysical Research-Oceans*, *121*(1), 476–501, doi:10.1002/2015JC010878.

Toniazzo, T., and S. Woolnough (2014), Development of warm SST errors in the southern tropical Atlantic in CMIP5 decadal hindcasts, *Climate Dynamics*, *43*(11), 2889–2913, doi: 10.1007/s00382-013-1691-2.

Wacongne, S., and B. Piton (1992), The near-surface circulation in the northeastern corner of the South Atlantic ocean, *Deep Sea Research Part A. Oceanographic Research Papers*, *39*(7–8), 1273–1298, doi:10.1016/0198-0149(92)90069-6.

Wahl, S., M. Latif, W. Park, and N. Keenlyside (2011), On the Tropical Atlantic SST warm bias in the Kiel Climate Model, *Climate Dynamics*, *36*(5), 891–906, doi:10.1007/s00382-009-0690-9.

Wattenberg, H. (1938), *Die Verteilung des Sauerstoffs im Alantischen Ozean*, de Gruyter, 132 pp.

Wunsch, C., and A. Gill (1976), Observations of equatorially trapped waves in Pacific sea level variations, *Deep Sea Research and Oceanographic Abstracts*, *23*(5), 371–390, doi:10.1016/0011-7471(76)90835-4.

Wüst, G. (1935), *Die Stratosphäre des Atlantischen Ozeans*, 288 pp.

Xu, Z., M. Li, C. M. Patricola, and P. Chang (2014), Oceanic origin of southeast tropical Atlantic biases, *Climate Dynamics*, *43*(11), 2915–2930, doi:10.1007/s00382-013-1901-y.

Yoon, J. H., and S. G. H. Philander (1982), The generation of coastal undercurrents, *Journal of the Oceanographical Society of Japan*, *38*(4), 215–224, doi:10.1007/BF02111104.

Zhu, X., R. J. Greatbatch, and M. Claus (2017), Interannual variability of tropical Pacific sea level from 1993 to 2014, *Journal of Geophysical Research: Oceans*, *122*(1), 602–616, doi: 10.1002/2016JC012347.

Zuidema, P., et al. (2016), Challenges and Prospects for Reducing Coupled Climate Model SST Biases in the Eastern Tropical Atlantic and Pacific Oceans: The U.S. CLIVAR Eastern Tropical Oceans Synthesis Working Group, *Bulletin of the American Meteorological Society*, *97*(12), 2305–2328, doi:10.1175/BAMS-D-15-00274.1.

Own Publications

Brandt, P., M. Claus, R. J. Greatbatch, **R. Kopte**, J.M. Toole, W.E. Johns, and C.W. Böning, 2016: Annual and Semiannual Cycle of Equatorial Atlantic Circulation Associated with Basin-Mode Resonance. J. Phys. Oceanogr., 46, 3011–3029, doi: 10.1175/JPO-D-15-0248.1.

Kopte, R., P. Brandt, M. Dengler, P. C. M. Tchipalanga, M. Macuéria, and M. Ostrowski (2017), The Angola Current: Flow and hydrographic characteristics as observed at 11 °S, J. Geophys. Res. Oceans, 122, 1177–1189, doi:10.1002/2016JC012374.

Kopte, R., P. Brandt, M. Claus, R. J. Greatbatch, and M. Dengler, 2017: Role of Basin-Mode Resonance for the Seasonal Variability of the Angola Current. Submitted to J. Phys. Oceanogr.

Tchipalanga, P. C. M., M. Dengler, P. Brandt, **R. Kopte**, M. Macuéria, P. Coelho, M. Ostrowski, and N. S. Keenlyside, 2017: Eastern boundary circulation and hydrography off Angola – building oceanographic capacities in Southwestern Africa. To be submitted to Bulletin of American Meteorological Society.

Danksagung

An erster Stelle möchte ich mich bei Peter Brandt bedanken. Für all seine Geduld und Unterstützung in den letzten Jahren, für die Vermittlung seines Fachwissens und seine Fähigkeit für mich höchst verworren scheinende Probleme so schnell zu analysieren und auf das Wesentliche zu reduzieren. Ausserdem für seine Weitsicht, Verlässlichkeit, Hilfsbereitschaft und den Optimismus, speziell in der Zeit als es dieser Arbeit noch an der notwendigen Datengrundlage mangelte.

Des Weiteren danke ich Richard Greatbatch und Martin Claus für wertvolle Diskussionen über die äquatoriale Wellendynamik und wie diese mit einem einfachen Flachwassermodel untersucht werden kann, sowie die hilfreichen Hinweise zu dem Manuskript. Spezieller Dank gilt Martin Claus für seine Geduld bei meinen Fragen, was beim Starten eines Modelllaufes alles zu beachten ist und wie die Parameter eines Sponge Layers eingestellt werden müssen.

Danke auch an alle Co-Autoren der hier gezeigten Publikationen, sowie an all die hilfsbereiten Wissenschaftler und Techniker unserer Arbeitsgruppe.

Spezieller Dank geht an meine Freunde und Kollegen in der PO für die gute Zeit sowohl im Büro als auch in der Freizeit, für hilfreiche und oft auch nicht ganz so hilfreiche (dafür umso lustigere) Unterhaltungen ("ä bissl Zirkuläähschn"), Korrekturlesungen, Tipps, und und und: Flo ("Sitznachbar und Freund", oder wie war das?), Rebecca, FPT, Thilo, Yao, Kristin, Tim. Vielen Dank auch an Robin für die Kaffeepausen auf der Dachterasse und an Kerstin und Julian für die Freundschaft und Unterstützung während des Studiums und besonders auch in der letzten Zeit.

Ein besonderer Dank gilt Henrike für ihren moralischen Beistand, die stetige Motivation und all die Aufmunterung und Ablenkung während unseres langen gemeinsamen Weges.

Ausserdem möchte ich meiner Familie, insbesondere meinen Eltern und meinem Bruder für ihre großartige Unterstützung aller meiner Vorhaben danken sowie für ihr Mitfiebern ab der ersten Minute.

Erklärung

Hiermit erkläre ich, dass ich die vorliegende Arbeit - abgesehen von der Beratung durch meinen Betreuer Prof. Dr. Peter Brandt - unter Einhaltung der Regeln guter wissenschaftlicher Praxis der DFG sebstständig erarbeitet und verfasst habe. Diese Arbeit hat weder ganz, noch zum Teil, an anderer Stelle im Rahmen eines Prüfungsverfahrens vorgelegen, ist nicht veröffentlicht und auch nicht zur Veröffentlichung eingereicht.

Kiel, 2017

Robert Kopte